Quantum Metric and Topology in the exploration of photonic Dirac systems

Charly Leblanc

University Clermont Auvergne
Institut Pascal - CNRS
ecole doctorale des sciences fondamentales

Quantum Metric and Topology in the exploration of photonic Dirac systems

prepared in the team of Quantum Optoelectronics and Nanophotonics

Dissertation for the Degree of Doctor of Philosophy

CHARLY LEBLANC

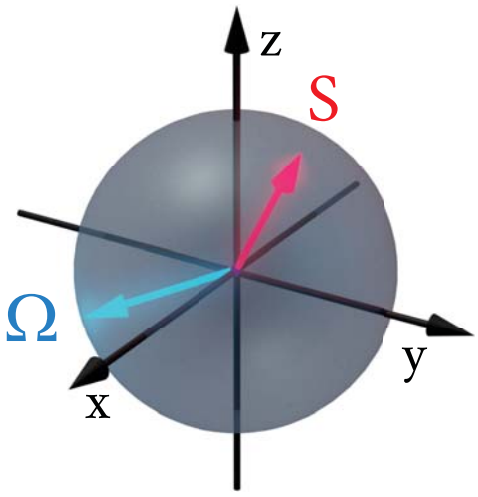

Supervisors: Prof. Dmitry Solnyshkov, Dr. Guillaume Malpuech

Referees: Prof. Päivi Törmä, Prof. Fabrice Mortessagne

Examiners: Prof. Daniele Sanvitto (chairman), Dr. Alberto Amo, Dr. Sarah Porteboeuf-Houssais

Clermont-Ferrand, 14^{th} of October 2022

Résumé

Cette thèse est dédiée à l'étude des systèmes photoniques de Dirac, le rôle de leur topologie et Métrique Quantique, et leur comportement vis-à-vis de la non-Hermiticité.

Après des chapitres introductifs sur ces sujets, nous étudions d'abord les points de Dirac dans les microcavités. En excitant de manière cohérente deux bandes proche d'un point de Dirac, nous démontrons expérimentalement que le paquet d'onde polaritonique présente des oscillations de Zitterbewegung. Cet effet peut être compris avec une théorie de Yang-Mills non-Abélienne, qui couple la précession du spin à la dynamique spatiale.

Ensuite, nous présentons un ancien travail, décrivant l'effet Hall anormal photonique dans le régime opposé, lorsqu'une seule bande est excitée de manière adiabatique. Après, nous démontrons que ces deux régimes peuvent être décrits dans un formalisme unique, prenant la forme d'équations semi-classiques utilisant uniquement des paramètres statiques des bandes, à savoir la dispersion et la Métrique Quantique.

Suite à cela, nous présentons un travail expérimental sur un régime de couplage fort lumière-matière sélectif en spin qui se traduit par une non-linéarité optique exceptionnellement forte et un effet Zeeman géant, qui permet d'ouvrir une bande interdite au point de Dirac dans les systèmes polaritoniques, et qui a des applications directes en physique topologique.

Dans le dernier chapitre, nous démontrons qu'en présence de non-Hermiticité, un point de Dirac se transformera en une paire de points exceptionnels, reliés par un arc de Fermi. Nous montrons que la Métrique Quantique diverge au voisinage d'un point exceptionnel. Cette divergence permet de comprendre le comportement complexe d'un paquet d'onde centré sur ce point.

Enfin, nous présentons la première extraction expérimentale de la Métrique Quantique dans un système non-Hermitien, présentant des points exceptionnels. Cette thèse se termine sur l'observation de la divergence de la Métrique Quantique aux points exceptionnels, en accord avec la théorie.

Keywords

Topologie, Métrique Quantique, Tenseur Géométrique Quantique, physique non-Hermitienne, points de Dirac, points exceptionnels, équations semiclassiques, dynamique d'un paquet d'onde, photonique, microcavités, exciton-polaritons, couplage spin-orbite, théorie de Yang-Mills, monocouche de semiconducteur, Zitterbewegung, Zeeman géant.

Abstract

This thesis is dedicated to the study of photonic Dirac systems, the role of their associated topology and Quantum Metric, and their behavior with respect to non-Hermiticity.

After introductory chapters on these subjects, we first study Dirac points in microcavities. By exciting coherently two bands near a Dirac point, we experimentally demonstrate Zitterbewegung oscillations from a polariton wavepacket. The dynamics can be fully understood thanks to a non-Abelian Yang-Mills theory, which couple the precession of the spin to the spatial dynamics.

Then we introduce a previous work, describing the photonic anomalous Hall effect in the opposite regime, when a single band is excited adiabatically. Afterwards, we demonstrate that both of these regime can be described in a single formalism, taking the form of semiclassical equations using only static band parameters, namely the dispersion and the Quantum Metric.

Following this, we present an experimental work about a spin-selective strong light-matter coupling regime which results in unusually strong optical nonlinearity and a giant Zeeman effect, which allows to open a gap at the Dirac point in polaritonic systems, and which has direct applications in topological physics.

In the last chapter, we demonstrate that in presence of non-Hermiticity, a Dirac point will transform into a pair of exceptional points, linked by a Fermi arc. We show theoretically that the Quantum Metric diverges at the vicinity of an exceptional point. This divergence allows to understand the complex behavior of a wavepacket centered at this point.

Lastly, we present the first experimental extraction of the Quantum Metric in a non-Hermitian system, exhibiting exceptional points. This thesis ends with the observation of the divergence of the Quantum Metric at the vicinity of exceptional points, accordingly with the theory.

Keywords

Topology, Quantum Metric, Quantum Geometric Tensor, non-Hermitian physics, Dirac points, exceptional points, semiclassical equations, wavepacket dynamics, photonics, microcavities, exciton-polaritons, spin-orbit coupling, Yang-Mills theory, monolayer semiconductor, Zitterbewegung, giant Zeeman.

My contributions

I will present here my contributions to all my published articles.

E.1 1^{st} author articles

- High-frequency exciton polariton clock generator.

- Universal semiclassical equations based on the QM for a two-band system.

For both of these theoretical articles, I did the analytics under the guidance of my advisors. I also performed the numerical simulations both with the semi-classical equations and with the Schrodinger equation. Finally, I wrote the draft versions of the manuscript and worked on their improvement together with my supervisors.

- Experimental measurement of the divergent quantum metric of an Exceptional point.

In this experimental paper, in collaboration with a Chinese group, I performed the full treatment of the raw experimental data that we received. I extracted and analyzed the data to obtain the experimental dispersion for each polarization. With a double Lorentzian fit, I extracted the real and imaginary part of the modes, which allowed us to demonstrate the presence of an EP in the cavity. I extracted the Stokes vectors and finally the QM in the 2D reciprocal space. I precisely extracted the QM behavior along a line which crosses the EP, demonstrating the divergence of the metric. With the guidance of my advisors, I developed a Hamiltonian describing the system to fit the dispersion, and to model theoretically the Stokes vector and the QM. Finally, I made all the 14 panels in the main article, wrote the draft of the manuscript and worked on its improvement.

- Giant effective Zeeman splitting in a monolayer semiconductor realized by spin-selective strong light–matter coupling.

This experimental paper is a collaboration with a lot of experimental groups. With the group of A. I. Tartakovskii, we discussed the bare flake and cavity spectroscopy data. With the help of my advisors, I developed the cavity fitting model accounting for the Stokes shift (fig. 1.D), that I used to extract the main result of this article: a giant Zeeman splitting (fig. 2.b). I also developed a rate equation model, which I used to fit the Rabi splitting (fig. 3.c), the DOCP versus the pumping power (fig. S4), and the blueshift of the LPB (fig. 3.c). From the fits I extracted the important parameters to model the effective interaction between trion-polariton. I showed that we obtain strong nonlinearities at low pumping, the second main result of this article. I wrote with my advisors the section 2 of the supplementary, and I made all the figures in this section. During this collaboration, I was exchanging directly with the other first author Tomas P. Lyons about the data analysis, the fits, and the improvements of the figures and the manuscript.

E.2 Other articles

- Quantum metric and wave packets at exceptional points in non-Hermitian systems.

My main contribution to this article is the derivation of the QM at the vicinity of an EP, showing the divergence of 1/q. I also participated in the discussion and interpretation of the wavepacket behavior. I took part in the search for ideas about the possible interesting consequences of the divergence of the QM. I participated in the testing of these ideas and the selection of the best ones for the paper.

- Domain-Wall topology induced by spontaneous symmetry breaking in polariton graphene.

I participated in the discussion and interpretation of the numerically observed phenomena all along the development of this work. I suggested several ideas concerning the possible applications of the chiral domain wall currents. I made an aesthetic and clear 3D figure showing the polariton graphene, the domain walls excited by lasers, and the topological current at the interface (fig. 3.a. and fig. S1). I wrote a part of the supplementary.

- Experimental investigation of a non-Abelian gauge field in 2D perovskite photonic platform.

Right from the start, I studied the Yang-Mills theory together with my supervisors. I derived the equations of motion in a non-Abelian field (the classical chromodynamics equations), and I simulated this spin-dependent trajectory in real space with these equations (fig. 2.J). I also made 3D figures representing the system (fig. 2.A and fig. 3.A.).

- Quantum analogue of a Kerr black hole and the Penrose effect in a Bose-Einstein condensate.

In this article, I showed that the Bose-Einstein condensate's metric is equivalent to the Kerr's one. I derived theoretically the wavefunction of an acoustic Kerr (rotating) black hole. I have shown that the black hole exhibits two limits: the event horizon and the ergosphere. I demonstrated the validity of this result by performing numerical simulations, solving the Gross-Pitaevskii equation. I was also involved in the simulations of the Penrose effect in the ergoregion, using vortices with quantized angular momentum in the condensate.

Acknowledgements

Si j'avais un unique conseil à donner à quelqu'un qui voudrait se lancer dans une thèse, ce serait probablement de bien choisir ses encandrants de thèse. Bien avant le sujet de thèse. C'est ce que je pensais au début de ma thèse, au milieu de celle-ci, et c'est ce que je pense encore maintenant. Si cette thèse est un succès, c'est avant tout parce que j'ai eu la chance d'avoir des encadrants passionés, passionants, et qui ont su être là dans des moments difficiles, aussi. Ce sont devenus des modèles pour moi, chacun avec ces particularités. Dmitry, avec son efficacité, ses idées originales et brillantes, et qui ne ménage jamais ses efforts; et Guillaume, avec sa rigueur et ses connaissances, et qui a le super pouvoir de comprendre des sujets complexes et de les retranscrire de façon très simple, afin qu'un pauvre doctorant comme moi puisse les comprendre. Ce serait dur de résumer ce que j'ai vécu et appris dans cette équipe pendant ces 3 ans de thèse et ces 8 mois de stage, et c'est bien sûr avec une légère pointe au coeur que je vais quitter ce bureau. Merci pour tout, Dmitry et Guillaume.

A l'Institut Pascal, je voudrais aussi remercier chaleureusement Ismaël, dont les interactions m'ont beaucoup aidées, tant sur le point scientifique que humain. Merci à Pavel, pour ces questions toujours pertinentes, et sa fascinante culture russe. Je n'ai aucun doute sur votre réussite future. Merci à Léo et Gabin pour ces moments amicaux. Biensûr je remercie aussi l'équipe spectroscopie optique pour nos échanges, ainsi que Guy et Hiba pour ces petites pauses hebdomadaires. Merci à Francoise, Vanessa et Sabrina pour mes démarches administratives qui me perdent tant.

Je voudrais témoigner ma reconaissance aux différents collègues expérimentateurs avec qui j'ai eu la chance de collaborer. Tout d'abord, je remercie l'équipe de Sheffield dirigée par Alexander Tartakovskii, et en particulier merci à Tom pour ces interactions tout le long de cette collaboration, j'ai beaucoup appris. Merci aussi à l'équipe de Lecce dirigée par Daniele Sanvitto, c'était un réel plaisir de travailler sur un article aussi ambitieux.

Merci à mes amis, que j'ai cité ou non, et qui constituent une partie importante de mon bien-être. Ces soirées jeux, ces soirées TdV, ces moments de sport, de randonnée, de musique, des débats animés. Ces sorties loin de tout, à Saint-Désiré, dans le Jura, dans l'Aubrac, mais aussi au fameux festival du Roi de l'Oiseau. Merci pour ces souvenirs, merci d'avoir répondu présent, et j'espère tous vous revoir très bientôt.

Merci à Lauriane, qui a réussi à alleger mes soucis et tracas pendant cette thèse. Merci pour ton support et ton aide, qui m'ont été très précieux.

Évidemment, merci à ma famille, et particulèrement à mon père et ma mère, pour m'avoir accompagné tout au long de mes études. Je n'aurais pas réussi sans vous. Votre fils va enfin finir ses études!

Charly Leblanc

Contents

Topology is a field of Mathematics. In Physics, it allowed the description of materials beyond the Fermi level model. Indeed, before the 80s and the discovery of the Quantum Hall effect, a material was described as a conductor or insulator based on its electronic band structure, the position of the gaps and the Fermi level (see fig. 1). The Quantum Hall Effect revealed that a material can be an insulator in the bulk, but still conduct on its surface, leading to a new classification of materials. Topology was found to be an adequate tool to describe these new properties, and so now in order to fully understand a material we need to study the behavior of the eigenstates along the bands.

The Quantum Geometric Tensor is a matrix introduced in the 80s which contains all the information needed. This matrix is built with eigenstates and their derivatives in the reciprocal space. The imaginary part of this matrix is linked to the Berry Curvature, and by integrating it along the bands we will obtain an integer topological invariant, the so-called Chern number. If this integer is non-zero the material is said to be topologically non-trivial (see fig. 1). Since then, the field of topological physics has been growing exponentially. It found potential applications in quantum computing where "topological protection" is expected to strongly limit qubits decoherence. In photonics, topologically-protected unidirectional edge states are very appealing in order to build integrated photonic circuits. On another side, the real part of the Quantum Geometric Tensor is linked to the Quantum Metric. Initial understanding of the Quantum Metric is that it permits the calculation of quantum distances between eigenstates. In recent years, it has appeared that the Quantum Metric describes non-adiabatic corrections of effects mostly explained by the Berry curvature, such as the Anomalous Hall Effect.

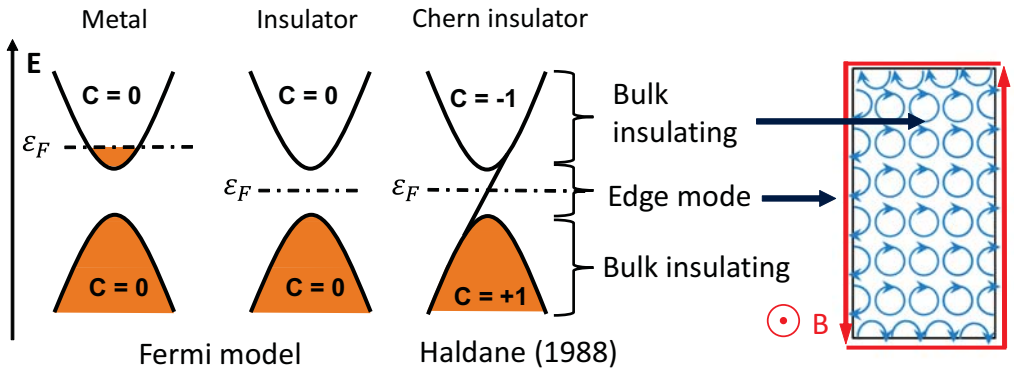

Figure 1: *Classification of materials. Chern insulators insulate in the bulk and conduct on the edge, a property well explained by topology.*

This thesis also focuses on a specific type of bands singularity: 2D Dirac points. Dirac points are linear crossing points carrying a singular Berry curvature distribution. They appear in the 2D band structure of graphene (see fig. 2). An interesting property is that when a gap opens at Dirac points due to time-reversal breaking, the two bands that split acquire nonzero Chern numbers, and so the bands become topologically non-trivial. We will

use this property not with graphene, but by implementing Dirac points in photonic systems. A convenient way to do so is by using microcavities (planar Fabry-Perot resonators). These microcavities display a series of modes with quasi-parabolic dispersion, each one of these modes being a doublet of polarization, TE and TM. If we focus on the dispersion, we will see that if there is presence of birefringence in the cavity, the doublet will split at $k = 0$, and because their effective mass is different the bands will cross in two points of the reciprocal space. The crossings are linear, meaning we have Dirac points in the system (see fig. 2).

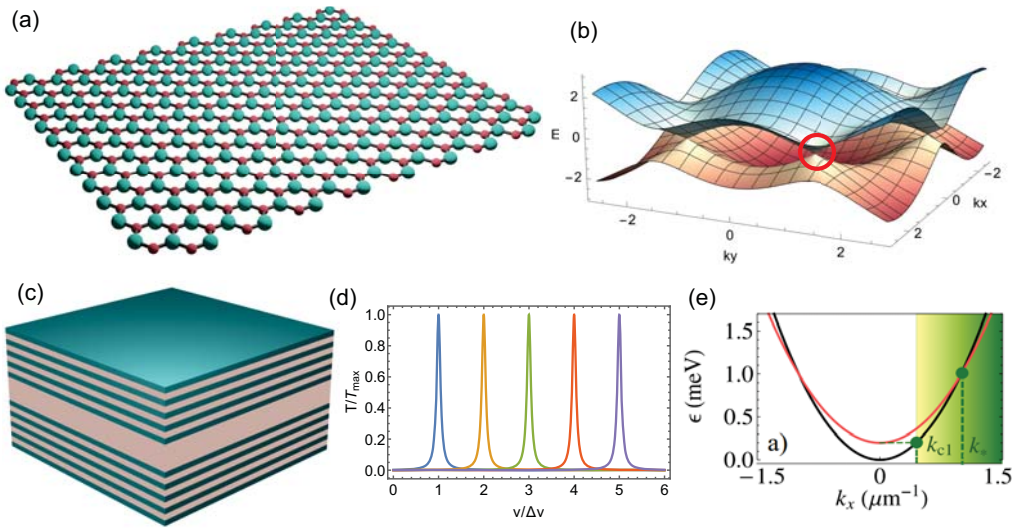

Figure 2: *(a) A sheet of graphene, which is made of carbon atoms arranged into a 2D honeycomb lattice composed of two triangular sublattices (blue and red). (b) Graphene dispersion displaying 6 Dirac points. (c) Fabry-Pérot cavity. (d) Series of modes of the cavity. (e) Dirac points in presence of birefringence in the cavity.*

In order to get more control of the light in the microcavity we will use light-matter interaction. For example we can insert a semiconductor slab in the microcavity so there will be a coupling between the photonic modes and the excitations of the semiconductor, called excitons. A quasiparticle arises from this coupling, part matter and part light, which we call exciton-polariton, or polariton. This quasi-particle has already demonstrated superfluidity, Bose-Einstein condensation and also appears to be an interesting candidate to study room temperature photonics and analogue physics.

In this thesis, we will present in the 1^{st} chapter some historical viewpoints about Dirac physics, starting from graphene, its topology and how the electrons are solution to a massless Dirac equation near the Dirac points. In the 2^{nd} chapter, we will study Dirac points in simple optical systems, such as crystals and microcavities, and crucial effects that allow to obtain these points in microcavities, namely linear birefringence and TE-TM splitting. A more versatile photonic platform, known as microcavity exciton-polaritons, will be introduced in the 3^{rd} chapter. The Quantum Geometric tensor, giving both topology and the Quantum Metric, is at the heart of this thesis, and will be presented in the 4^{th} and last introductory chapter. Generally, systems which display Dirac points can be described at the vicinity of the latter by a superposition of eigenstates, with a (pseudo)spin coupled with the spatial

dynamics, which can be interpreted as an effect of a non-Abelian gauge field. Oscillations, known as Zitterbewegung oscilattions, can be observed owing to the pseudospin precession. A theoretical formalism presented in the 5^{th} chapter describing both the adiabatic limit, with the anomalous Hall effect, and the opposite limit of coherent band superposition, with this Zitterbewegung motion, can be exactly defined with Quantum Metric terms. These effects and the first extraction of the Quantum Metric have been realized recently in exciton-polariton microcavities. This chapter will end with the study of an experimental work on a semiconductor monolayer embedded in a microcavity. We show that a spin-selective strong light-matter coupling regime results in unusually strong optical nonlinearity and a giant Zeeman effect, which has direct applications in topological physics. The 6^{th} and last chapter will be devoted to non-Hermitian physics. In photonic systems, losses appear quite naturally, and different losses for different eigenstates transform a Dirac point into a pair of exceptional points linked with a Fermi arc. The effective Hamiltonian becomes non-Hermitian. We will demonstrate that if we send a wavepacket (a light beam) near an exceptional point, the dynamics of this wavepacket can be expressed with Quantum Metric terms. Finally, we will present the first experimental measurement of the Quantum Metric in a non-Hermitian system, more precisely near an exceptional point.

Chapter 1: Dirac points in graphene

Contents

In the 1^{st} introductory chapter, we present the most famous system displaying Dirac points, namely the graphene. After introducing the pseudospin model, which is a crucial tool with respect to this thesis, we study how to develop a tight-binding Hamiltonian for graphene, and how to use it to describe the topology of Dirac points. A link is made between the equation describing electrons at the vicinity of Dirac points and the well-known relativistic Dirac equation. Finally, we investigate how to develop Dirac physics for massive particles.

1.1 Pseudospin model

In this thesis and in a substantial part of our work, we are dealing with physical systems with two states, represented by a two-by-two matrix. A geometrical representation of the Schrödinger equation for solving two-level quantum systems has been developed by Richard Feynman in the 50s [1]. In this section, I will first summarise these results with notations consistent with the rest of this manuscript, then I will explain why this model is of crucial interest for our works.

We consider a general superposition of two eigenstates which can be written as

$$|\psi(t)\rangle = c_1(t)\,|\psi_1\rangle + c_2(t)\,|\psi_2\rangle \tag{1.1}$$

From this point, we usually solve the Schrödinger equation with a perturbation V for the coefficients $c_{1,2}(t)$, which allow to compute the population of the eigenstates, and deduce the physical properties of the system from them [2]. Here the idea is different, considering that the phase of $|\psi(t)\rangle$ does not play any role, only three real numbers are needed to completely define the wavefunction. We then construct a 3-component vector $\mathbf{S}$ with three real functions S_1, S_2, and S_3 depending on $c_{1,2}(t)$

$$\begin{aligned} S_1 &= c_1 {c_2}^* + {c_2}^* c_1 \\ S_2 &= i(c_1 {c_2}^* - {c_2}^* c_1) \\ S_3 &= c_1 {c_1}^* - c_2 {c_2}^* \end{aligned}$$

where $c_{1,2}^*$ is the complex conjugate of $c_{1,2}$. The time dependence of $\mathbf{S}$ can be obtain from

the Schrödinger equation which gives for c_1

$$i\hbar\frac{dc_1}{dt} = c_1\left(E_0/2 + V_{11}\right) + c_2 V_{12} \tag{1.2}$$

where E_0 is the energy splitting of the two levels. Similar equations for c_2 and $c_{1,2}^*$ can be derived. Usually V_{11} and V_{22} are negligible compared to E_0. From eq. 1.2 we find the differential equation for $\mathbf{S}$ [1]

$$\frac{d\mathbf{S}}{dt} = \mathbf{\Omega} \times \mathbf{S} \tag{1.3}$$

where $\mathbf{\Omega}$ is a 3-component vector with real values Ω_i defined by

$$\begin{aligned} \Omega_1 &= \tfrac{1}{\hbar}\left(V_{12} + V_{21}\right) \\ \Omega_2 &= \tfrac{i}{\hbar}\left(V_{12} - V_{21}\right) \\ \Omega_3 &= E_0/\hbar \end{aligned} \tag{1.4}$$

The remaining combination $c_1{c_1}^* + c_2{c_2}^*$ is equal to the length of the vector $\mathbf{S}$, which is equal to 1 when $|\psi(t)\rangle$ is normalised to unity. The eq. 1.3 describes the precession motion of a spin in a constant magnetic field [3]. Hence one should expect that in the case of the transitions between the two magnetic levels of a spin 1/2 particle, the component S_1, S_2 and S_3 would be proportional with μ_x, μ_y and μ_z, and Ω_1, Ω_2 and Ω_3 would be proportional with the magnetic field components H_x, H_y and H_z respectively. By analogy, any two-state transition described by equation 1.3 can be thought in terms of the classical vector model for spin precession. In this case, $\mathbf{S}$ describe not a spin but a pseudospin, and $\mathbf{\Omega}$ describe not a magnetic field but an effective magnetic field. Feynman wrote about this model: "*Although the approach does not obtain results inaccessible to straight-forward calculation, the simplicity of the pictorial representation enables one to gain physical insight and to obtain results quickly which display the main features of interest*".

Indeed, any two-level quantum system can be represented geometrically on a Bloch sphere [4, 5] as shown in fig. 1.1. This representation is massively used in modern physics thanks to the development of quantum computing and more precisely the concept of qubit [6]. Knowing the effective magnetic field acting on the system, and knowing the precession equation, there is no apparent difficulties to understand geometrically the possible states of the system. An analogue of the Bloch sphere is the Poincaré sphere, more used to represent polarisation of light. In the Poincaré sphere, the states are the six polarisation states of light (H,V,D,A,R,L). In this thesis, we are using microcavities, whose eigenstates are characterized by polarisation [7] represented on the Poincaré sphere by the so-called Stokes vectors (an analogue of the pseudospin). Feynman developed this model to described two quantum levels in presence of a perturbation $\mathbf{\Omega}$, but his work is actually more general than that, and successfully describe systems where the effective field is similar or greater than the splitting between the two states. Also, we will be dealing mostly with two-level systems, such as two coupled modes or two levels of a micropillar. Consequently, we will use the Bloch sphere representation with the pseudospin model.

For the practical point of view, we can rewrite any two-by-two Hermitian matrix H under

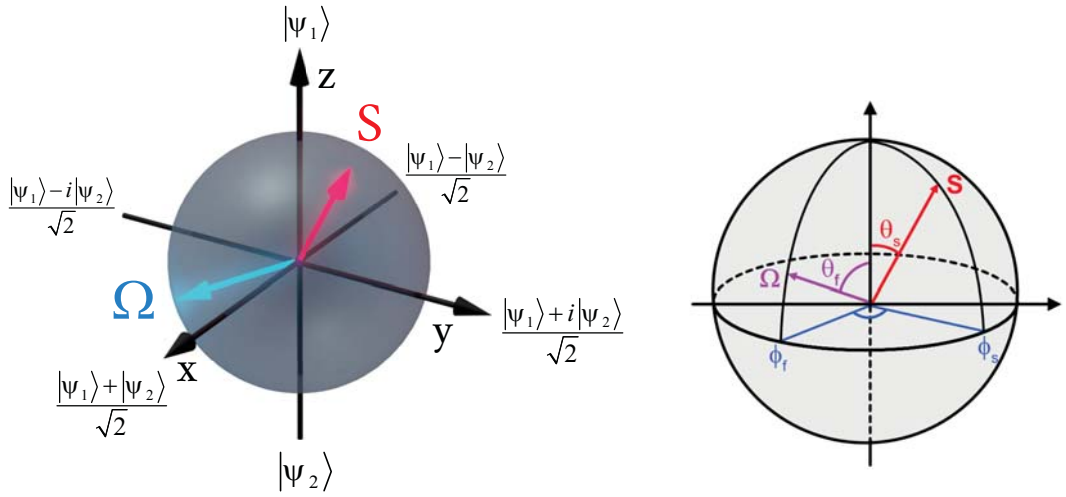

Figure 1.1: *Bloch sphere representation of a two-level quantum system. The position of the pseudospin* $\boldsymbol{S}$ *and the effective magnetic field* $\boldsymbol{\Omega}$ *is given by the polar and azimuthal angles* $\theta_{S,f}$ *and* $\phi_{S,f}$ *respectively, where* f *means field.*

the form

$$H = \begin{pmatrix} H_0(k) - \frac{\Omega_z(k)}{2} & -\frac{\Omega_x(k) - i\Omega_y(k)}{2} \\ -\frac{\Omega_x(k) + i\Omega_y(k)}{2} & H_0(k) + \frac{\Omega_z(k)}{2} \end{pmatrix} = H_0 I_2 - \boldsymbol{\Omega}_{eff}(k) \cdot \boldsymbol{\sigma} \tag{1.5}$$

where $\boldsymbol{\sigma} = (\sigma_x, \sigma_y, \sigma_z)$ represents the Pauli vector composed of Pauli matrices, I_2 is the identity matrix, and $\boldsymbol{\Omega}$ is the effective magnetic field. The eigenstates are parallel or anti-parallel to this effective field. Moreover, considering ψ_+ and ψ_- are the two eigenstates, the pseudospin $\boldsymbol{S} = (S_x, S_y, S_z)$ is given by

$$S_i = (\psi_+ \ \ \psi_-)^* \sigma_i \begin{pmatrix} \psi_+ \\ \psi_- \end{pmatrix} = \langle \sigma_i \rangle \tag{1.6}$$

This geometrical representation of the Hamiltonian as an effective magnetic field acting on a pseudospin will be extensively used in the following of this thesis. The pseudospin precession is not needed in the adiabatic approximation where the system stays in a single eigenstate, in a single band. However, it will be used when bands are coherently excited, something that we will study in chapter 5.

1.2 Tight-binding Hamiltonian of graphene

Graphene is made of carbon atoms arranged in a 2D honeycomb lattice. A lot of structures are made with graphene. For instance graphite, used in pencils since 1960, is a stack of graphene layers [8]. Also carbon nanotubes are made of rolled-up cylinders of graphene. More recently a stack of rotated layers of graphene led to a promising structure, moiré graphene [9], with interesting properties such as superconductivity and Mott insulating. K. Novoselov and A. Geim first isolated graphene sheets using scotch tape in 2004 [10, 11], and got the Nobel prize for it in 2010. Since then, the properties of graphene have been heavily studied [12, 13, 14]. In this chapter we will study the graphene dispersion using the

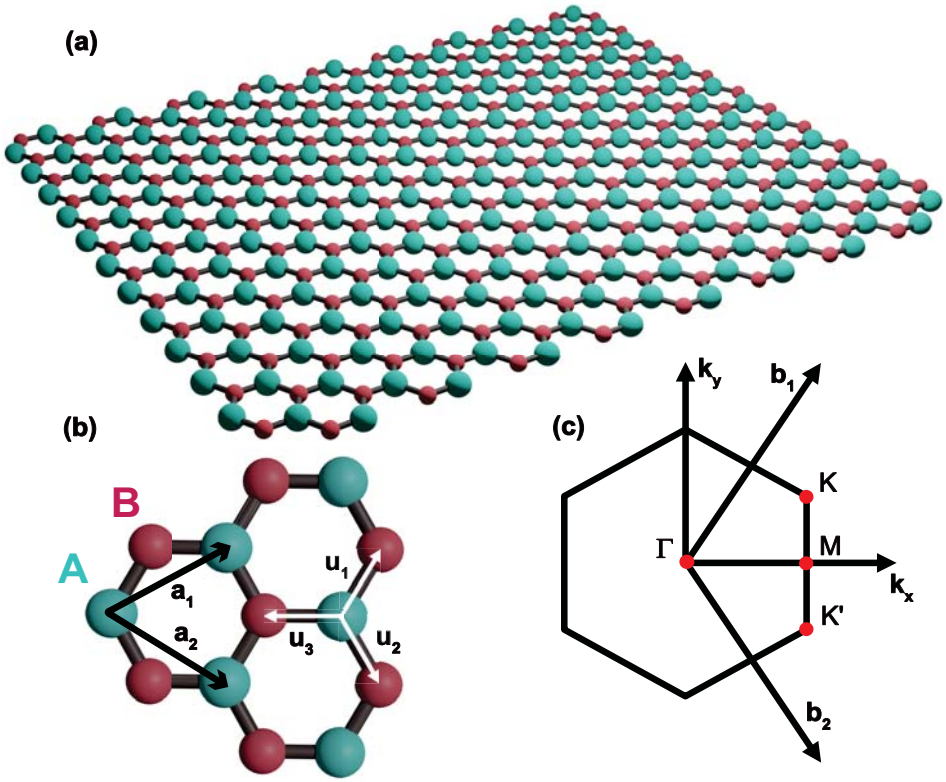

Figure 1.2: *(a) Graphene sheet. (b) Lattice structure of graphene, a honeycomb lattice made of 2 triangular sublattices. For graphene, the atoms A and B are the same, but for hexagonal Boron Nitride, they are different. (c) First Brillouin zone of graphene.*

tight-binding model. This model is useful to describe the case where atomic wavefunctions are overlapping enough that there is a need to correct the description of an isolated atom, but not overlapping too much, so this is still only a correction. A comprehensive description of the tight-binding model can be found in the well written book Ashcroft and Mermin [15]. The unit cell of graphene, shown in fig. 1.2, is composed of two atoms, which we will call A (cyan) and B (magenta) atoms. These atoms form a honeycomb lattice. Each type of atom forms a triangular lattice, and its unit vectors are:

$$\mathbf{a_1} = \frac{a}{2}\left(3, \sqrt{3}\right)$$
$$\mathbf{a_2} = \frac{a}{2}\left(3, -\sqrt{3}\right)$$

where a is the distance between nearest neighbours (A and B). The first Brillouin zone of graphene is shown in the panel (c) of fig. 1.2. The K and K' points are at the corners of this zone, and represent Dirac points, which will be one of the central objects of interest in this thesis. Considering only nearest-neighbour hopping, the tight-binding Hamiltonian for graphene is:

$$\hat{H} = -t \sum_i \sum_j \left(\hat{a}_i^\dagger \hat{b}_j + \hat{b}_j^\dagger \hat{a}_i\right) \tag{1.7}$$

where i and j correspond to sites in A and B sublattices, $\hat{a}_i^\dagger$ and $\hat{a}_i$ correspond to fermionic operators which create and annihilate electrons on the sites in A sublattice, and $\hat{b}_i^\dagger$ and $\hat{b}_i$ are

doing the same for the sites of B sublattice. The term t corresponds to the overlap between the p_z orbitals of adjacent carbon atoms and is known to be approximately $t \simeq 2.7\ eV$ [14]. In the honeycomb lattice, one atom has three nearest neighbours. The three corresponding vectors are (in the case of A atom):

$$\begin{aligned}\mathbf{u_1} &= \tfrac{a}{2}\left(1, \sqrt{3}\right)\\ \mathbf{u_2} &= \tfrac{a}{2}\left(1, -\sqrt{3}\right)\\ \mathbf{u_3} &= a\left(-1, 0\right)\end{aligned}$$

We can then rewrite the sum over the nearest neighbours:

$$\sum_i \sum_j \left(\hat{a}_i^\dagger \hat{b}_j + \hat{b}_j^\dagger \hat{a}_i\right) = \sum_{i\in A} \sum_u \left(\hat{a}_i^\dagger \hat{b}_{i+u} + \hat{b}_{i+u}^\dagger \hat{a}_i\right) \tag{1.8}$$

The A sublattice sites (noted i) are at the position $\mathbf{r_i}$, and $\hat{b}_{i+u}^\dagger$ and $\hat{b}_{i+u}$ respectively creates and annihilates an electron on the B neighbours sites (noted $i+u$) at position $\mathbf{r_i} + \mathbf{u}$ ($\mathbf{u_1}$, $\mathbf{u_2}$ or $\mathbf{u_3}$). The operator can be written in the tight-binding approximation [16] such as

$$\hat{a}_i^\dagger = \frac{1}{\sqrt{N/2}} \sum_{\mathbf{k}} e^{i\mathbf{k}\cdot\mathbf{r_i}} \hat{a}_k^\dagger \tag{1.9}$$

where N is the number of atoms, therefore $N/2$ is the number of A sites. Using the same property for $\hat{b}_i^\dagger$, eq. 1.7 becomes

$$\hat{H} = \frac{-t}{N/2} \sum_{i\in A} \sum_u \sum_{\mathbf{k}} \sum_{\mathbf{k}'} \left(e^{i(\mathbf{k}-\mathbf{k}')\cdot\mathbf{r_i}} e^{-i\mathbf{k}'\cdot\mathbf{u}} \hat{a}_{\mathbf{k}}^\dagger \hat{b}_{\mathbf{k}'} + h.c.\right) \tag{1.10}$$

Using the fact that $\sum_{i\in A} e^{i(\mathbf{k}-\mathbf{k}')\cdot\mathbf{r}_i} = \frac{N}{2}\delta_{\mathbf{k}\mathbf{k}'}$, we can rewrite the Hamiltonian:

$$\hat{H} = -t \sum_u \sum_{\mathbf{k}} e^{i\mathbf{k}\cdot\mathbf{u}} \hat{a}_{\mathbf{k}}^\dagger \hat{b}_{\mathbf{k}} + h.c. \tag{1.11}$$

In this thesis, we will usually express the Hamiltonian in the matrix representation, using the Pauli matrices basis. Hence the Hamiltonian reads:

$$\hat{H} = \sum_{\mathbf{k}} \Psi^\dagger h(\mathbf{k}) \Psi \tag{1.12}$$

where

$$\Psi = \begin{pmatrix} \hat{a}_{\mathbf{k}} \\ \hat{b}_{\mathbf{k}} \end{pmatrix}, \Psi^\dagger = \begin{pmatrix} \hat{a}_{\mathbf{k}}^\dagger & \hat{b}_{\mathbf{k}}^\dagger \end{pmatrix} \tag{1.13}$$

and h is the matrix representation of the Hamiltonian:

$$h(\mathbf{k}) = -t \sum_u \begin{pmatrix} 0 & \cos\left(\mathbf{k}\cdot\mathbf{u}\right) + i\sin\left(\mathbf{k}\cdot\mathbf{u}\right) \\ \cos\left(\mathbf{k}\cdot\mathbf{u}\right) - i\sin\left(\mathbf{k}\cdot\mathbf{u}\right) & 0 \end{pmatrix} \tag{1.14}$$

As mentioned, the two-by-two form of the matrix allows to express it as an effective magnetic field acting on the pseudospin of the lattice. This pseudospin is a degree of freedom describing the orbital wave functions positioned in two different sublattices of the honeycomb lattice. Using the Pauli matrices basis:

$$h(\mathbf{k}) = -t \sum_u \left(\cos\left(\mathbf{k}\cdot\mathbf{u}\right)\sigma_x - \sin\left(\mathbf{k}\cdot\mathbf{u}\right)\sigma_y\right) \tag{1.15}$$

The eigenvalues of this matrix can be written as:

$$E_\pm(\mathbf{k}) = \pm t\sqrt{3 + f(\mathbf{k})} \tag{1.16}$$

where

$$f(\mathbf{k}) = 2\cos\left(\sqrt{3}k_y a\right) + 4\cos\left(3/2k_x a\right)\cos\left(\sqrt{3}/2k_y a\right) \tag{1.17}$$

The energy bands are plotted in fig. 1.3. The top and lower bands are touching in six points which are the Dirac points. Using eq. 1.16, we can compute the position of these points in the momentum space, with two of them given by the formulas:

$$\mathbf{K} = \left(\frac{2\pi}{3a}, \frac{2\pi}{3\sqrt{3}a}\right), \quad \mathbf{K}' = \left(\frac{2\pi}{3a}, -\frac{2\pi}{3\sqrt{3}a}\right) \tag{1.18}$$

We want to emphasize that not any linear crossing of two bands is a Dirac point, these points are also characterized by a topological quantity named the winding number which will be introduced later.

1.3 Effective Hamiltonian at the Dirac point

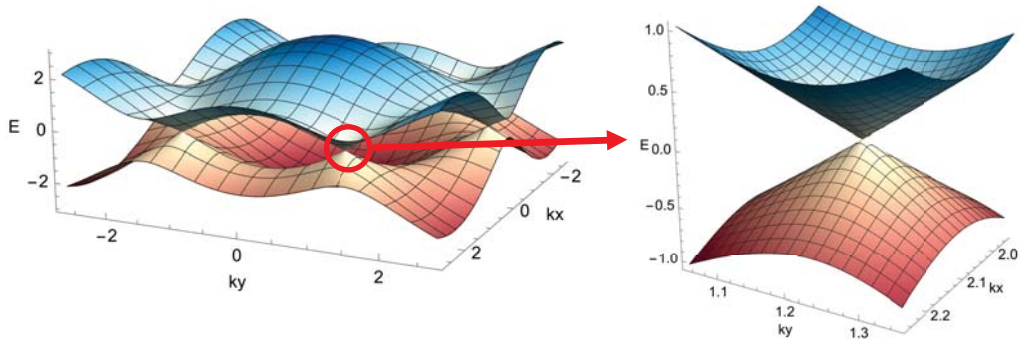

Figure 1.3: *(a) Graphene dispersion in the 2D reciprocal space with $a = 1$ and $t = 3$. (b) Zoom on the Dirac point, the crossing is linear.*

We are interested in the behavior of the system near the Dirac points. We can define the relative wavevector near one Dirac point positioned in K' as: $\mathbf{q} = \mathbf{k} - \mathbf{K}'$ where $\mathbf{K}'$ is the wavevector of the Dirac point. The series expansion of the Hamiltonian h near the Dirac

point reads [14]:

$$h_{K'}(\mathbf{q}) = \hbar v_f \begin{pmatrix} 0 & q_x - iq_y \\ q_x + iq_y & 0 \end{pmatrix} = \hbar v_f \left(q_x \sigma_x + q_y \sigma_y\right) \tag{1.19}$$

It can be written under the form

$$h_{K'} = \hbar v_f \mathbf{q} \cdot \boldsymbol{\sigma} \tag{1.20}$$

with $\mathbf{q} = (q_x, q_y)$. We remark that this Hamiltonian is similar to a Rashba Hamiltonian [17, 18]. Close to the Dirac point, the eigenvalues given by eq. 1.16 become

$$E_{\pm}(\mathbf{q}) = \hbar v_f \left|\mathbf{q}\right| \tag{1.21}$$

where v_f is the Fermi velocity given by $v_f = 3/2at$. We observe that the dispersion is linear near the Dirac point, so it forms a cone in the reciprocal space (see fig. 1.3.b). This result was obtained the first time by Wallace in 1947 [16]. In the same manner, we can obtain the effective Hamiltonian near the **K** point

$$h_K(\mathbf{q}) = \hbar v_f \begin{pmatrix} 0 & q_x + iq_y \\ q_x - iq_y & 0 \end{pmatrix} = \hbar v_f \mathbf{q}^* \cdot \boldsymbol{\sigma} \tag{1.22}$$

with $\mathbf{q}^* = (q_x, -q_y)$. This time, we observe that this Hamiltonian is similar to the Dresselhaus Hamiltonian [19]. It gives the same dispersion as the one in the **K'** point, but not the same eigenvectors. The two Hamiltonians can be distinguished by a winding number – a topological invariant that we introduce below.

1.4 Topology of graphene

Topology was first a field of Mathematics studying topological invariants. These are quantities which do not change under continuous transformations. For example, the number of holes in an object is a topological invariant. The cube and the polyhedron in fig. 1.4 have both zero holes, and hence they are considered as topologically trivial objects. It is different for the torus and the cup which have one hole, and hence are topologically non-trivial objects. It is possible to transform the cube into the polyhedron with a continuous transformation, but not into the torus [20]. The first applications of topology in physics date from the 18^{th} century [21, 22], but began to gain prominence with the work of Poincaré in 1895, who was studying celestial mechanics [23]. Interest in topology has grown exponentially in recent times in physics since the discovery of the quantum Hall effect in the 1980s by K. von Klitzing, work which earned him the Nobel Prize in 1985 [24]. The topology underneath this effect is linked with the famous Chern number, which characterises the topology of the bands. The Chern number will be one of the subjects of interest in this thesis. It will be explained in the chapter 4.

The topology of the Dirac points in graphene can be described by another topological invariant – the winding number. This number describes the winding of the phase of the wavefunction around a point. Let us find the winding number of the Dirac point. We start

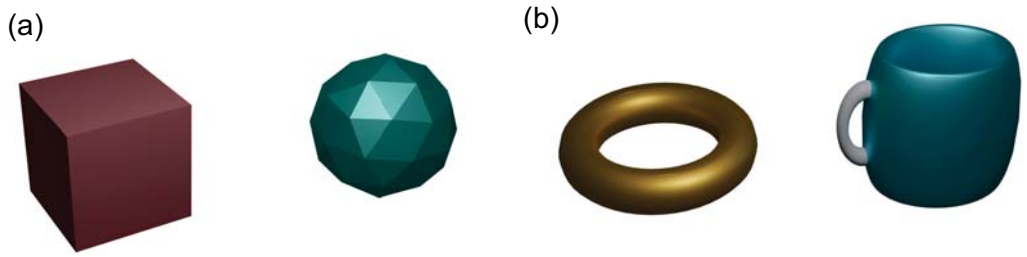

Figure 1.4: *The number of holes in a object is a topological invariant. (a) The cube and the spherical polyhedron have both zero holes. (b) The torus and the cup have one hole.*

by expressing the effective Hamiltonian of graphene at the **K** point 1.19 under the form [25]

$$H_D = \hbar \nu_f q \begin{pmatrix} 0 & e^{-i\theta_q} \\ e^{i\theta_q} & 0 \end{pmatrix} \tag{1.23}$$

where ν_f is the Fermi velocity and θ_q corresponds to the angle between the $+k_x$ direction and $\mathbf{q} = (q_x, q_y)$ in the 2D reciprocal space (that is, the polar angle determining the orientation of the wave vector). The resulting wavefunction written as a spinor is

$$\psi_{\pm} = \frac{1}{\sqrt{2}} \begin{pmatrix} \pm e^{-i\theta_q} \\ 1 \end{pmatrix} \tag{1.24}$$

The winding number of the Dirac point corresponds to the number of rotations that the pseudospin performs when the wavevector fully rotates once around this point. It is expressed as [26]

$$\omega = \frac{1}{2\pi} \oint \nabla \Phi(\mathbf{q}) d\mathbf{q} \tag{1.25}$$

where $\Phi(\mathbf{q})$ is the relative phase between the two components of the spinor. As we see, the winding number is an integral value, which is usually the case for topological numbers. This expression is strongly related to the Berry connection (phase) and the Berry curvature, which will be discussed in detail in chapter 4. In our case, $\Phi(\mathbf{q}) = \theta_q$ and eq. 1.25 can be written as

$$\omega = \frac{1}{2\pi} \oint \frac{1}{q} \frac{\partial \theta_q}{\partial \theta_q} q d\theta_q = 1 \tag{1.26}$$

In the same manner, the winding number at the **K'** point is $\omega = -1$, meaning that the pseudospin is rotating in the other direction. A representation of the pseudospin texture[1] is given in fig. 1.5 around two Dirac points with opposite winding numbers. The non-zero winding numbers mean that the Dirac points are topologically non-trivial. They are stable in the sense that they can be moved, e.g. by deformation of the lattice, but they can't be easily destroyed. The only way to annihilate a Dirac point is through a topological phase transition, by merging two Dirac points of opposite winding numbers [27, 28].

[1] Example of computation of pseudospin textures in Appendix A.

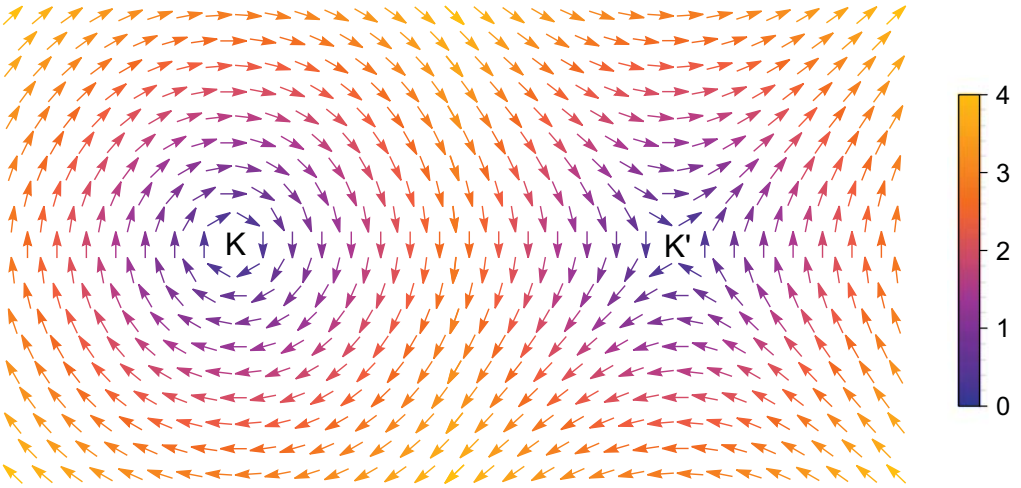

Figure 1.5: *Representation of the pseudospin texture in the 2D reciprocal space. The winding number is $\omega = +1$ at the **K** point, and $\omega = -1$ at the **K'** point. Color, in arbitrary unit, represents the intensity of the field.*

1.5 Dirac equation: relativistic physics and graphene

But why is it called Dirac point exactly? To answer this question, we need first to take a look at the Dirac equation, introduced by one of the most famous physicists of his time, Paul Dirac, in 1928 [29]. This equation was derived in the framework of relativistic quantum mechanics, and it describes particles with spin 1/2:

$$H = c\boldsymbol{\alpha} \cdot \mathbf{p} + mc^2\beta \tag{1.27}$$

where m is the rest mass of a particle and c the speed of light. α_i and β are the Dirac matrices which must satisfy

$$\begin{aligned} {\alpha_i}^2 &= \beta^2 = 1 \\ \alpha_i\alpha_j + \alpha_j\alpha_i &= 0 \\ \alpha_i\beta + \beta\alpha_i &= 0 \end{aligned} \tag{1.28}$$

In 3D, these matrices can be expressed in term of Pauli matrices σ_i $(i = x, y, z)$ such as

$$\alpha_i = \begin{pmatrix} 0 & \sigma_i \\ \sigma_i & 0 \end{pmatrix}, \quad \beta = \begin{pmatrix} \sigma_0 & 0 \\ 0 & -\sigma_0 \end{pmatrix} \tag{1.29}$$

with σ_0 the identity matrix. The matrices are of dimension four because there are two degrees of freedom to consider: the spin $\pm 1/2$ and the particle/antiparticle. The eigenvalues of eq. 1.27 are $E^2 = m^2c^4 + p^2c^2$, which ultimately gives the stunning result that there should exist the antiparticles with negative energy. Owing to this result, Paul Dirac predicted the existence of positron [30], the electron's antiparticle.

In this thesis, we are more interested in 2D systems, because we are using microcavities which confine the particles in one direction (generally z). In this case, one obtains a simpler

two-by-two Hamiltonian

$$H = hc\mathbf{k} \cdot \boldsymbol{\sigma} + mc^2\sigma_z \tag{1.30}$$

which can be interpreted as fixing the spin in eq. 1.27 while keeping the particle/antiparticle degree of freedom. In this equation, $\mathbf{k} = (k_x, k_y)$ and $\boldsymbol{\sigma} = (\sigma_x, \sigma_y)$ is a vector of Pauli matrices. We see that without the second term, which is the term corresponding to the mass, this equation is similar to eq. 1.20. So the 2D massless Dirac equation is similar to the equation describing graphene near the K points. The differences are in the values of the parameters, for instance the Fermi velocity in graphene is approximately 300 times slower than the speed of light. The eigenvalues of this Hamiltonian are plotted in fig. 1.6, and we observe that without a mass (left panel, $m = 0$), the dispersion is similar to the dispersion of graphene at the Dirac point. The first analogy between graphene and the Dirac equation was noticed by Semenoff in 1984 [31]. We can also get the dispersion of a massive Dirac Hamiltonian (right panel, $m \neq 0$). In this case, the bands are not crossing and we observe the emergence of a gap $2mc^2$ proportional to the mass.

To focus on graphene again, the effective mass m^* of a particle in a solid, meaning the mass the particle seems to have in the material, is given by the equation

$$\frac{1}{{m_{ij}}^*} = \frac{1}{\hbar^2}\frac{\partial^2 E}{\partial k_i \partial k_j} \tag{1.31}$$

We understand from eq. 1.31 that a massless particle has a linear dispersion. So near the Dirac cones in graphene the electrons behave like particles with no mass! Using this property, a 2D massless electron gas has been realized experimentally in 2005 [10]. The outstanding properties of graphene have made this material useful for many applications [32]. For instance, the high conductivity and capacity of graphene make it a great candidate for electronics [33], such as electronic batteries [34, 35], which are expected to be industrialized in the close future, owing to the recent improvements for scalable production of the material [36, 37, 38]. Also, the high ratio of surface over volume and the low density of defects of the material is interesting for sensors, for example to detect single molecules [39].

1.6 Staggered honeycomb lattice

Note that in this chapter we focused on graphene, but it is only a particular case among all possible honeycomb lattices. For instance, the Boron Nitride [40] is still a honeycomb lattice, but with different atoms in the two sublattices A and B, as shown in fig. 1.2.a.b (with colors now meaning different atoms). It appears to behave differently near the **K** and **K'** points [41, 42]. Indeed, the staggering[2] of the lattice adds a term in the effective Hamiltonian proportional to σ_z, which reads

$$h_{BN,K'}(\mathbf{q}) = \hbar v_f (q_x\sigma_x + q_y\sigma_y) + \chi\sigma_z \tag{1.32}$$

[2]Meaning the difference of neighbour atoms.

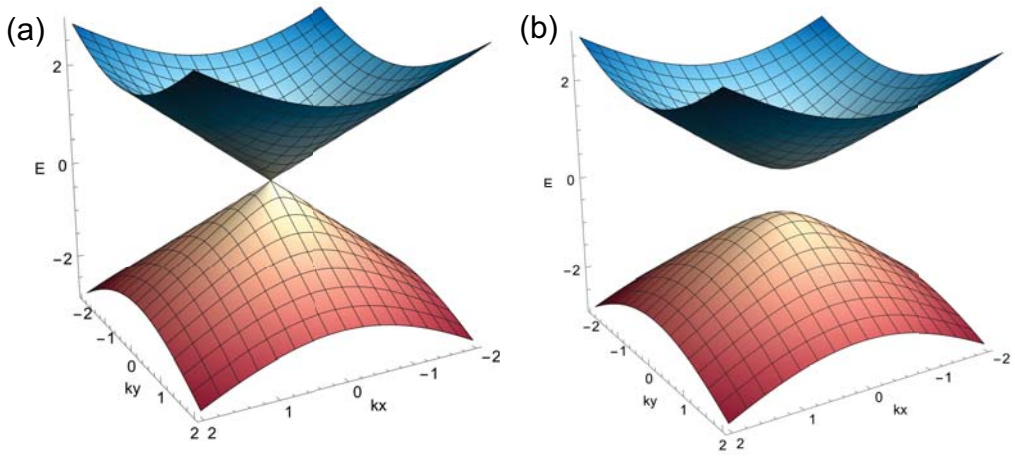

Figure 1.6: *Dispersion of the 2D Dirac Hamiltonian (a) without mass $m = 0$ (b) with a non-zero mass $m \neq 0$. The gap is proportional to the mass.*

Owing to this term, the dispersion near the **K'** now becomes

$$E_{BN,K'}(\mathbf{q}) = \pm\hbar v_f \sqrt{{q_x}^2 + {q_y}^2 + \chi^2} \tag{1.33}$$

and the plot of this dispersion is similar to the panel b of fig. 1.6. We remark that it opens a gap at the **K'** point, proportional to χ. We can demonstrate that it does the same at the **K** point. It means that, contrary to the case with the linear crossing of the bands, the electrons near this points have an effective mass. Consequently, in the following, we will call this type of Hamiltonian "massive Dirac Hamiltonian".

Chapter 2: Singularities in optical systems

Contents

In the 2^{nd} introductory chapter, we study simple optical systems where Dirac points have been predicted theoretically and then observed. First, we investigate crystal optics which displays Dirac points in presence of linear birefringence, which is an effect demonstrated more than a hundred years ago. Then we study microcavities, which are more contemporary systems and are the central platform of the works done in this thesis. We develop the cavity formalism, and finally we demonstrate how with only a few ingredients we can obtain Dirac points.

2.1 Dirac points in crystal optics

In this part we will study electromagnetic waves in crystals, which are anisotropic media. The properties of such media are given by the permittivity and permeability tensors, which are respectively $\epsilon_{ij}(\omega)$ and $\mu_{ij}(\omega)$. The most common case is where the medium is a non-magnetic transparent biaxial dielectric [43]. The constitutive equations for such crystals can be written as

$$\mathbf{E} = \boldsymbol{\varepsilon}^{-1}\mathbf{D},\ \mathbf{B} = \mu_0\mathbf{H} \tag{2.1}$$

where ε^{-1} is the inverse dielectric tensor, which can be expressed as

$$\boldsymbol{\varepsilon}^{-1} = \frac{1}{\varepsilon_0}\begin{pmatrix} 1/\epsilon_x & 0 & 0 \\ 0 & 1/\epsilon_y & 0 \\ 0 & 0 & 1/\epsilon_z \end{pmatrix} \tag{2.2}$$

In the case of a biaxial crystal, all the principal components are different. We will take $\epsilon_x < \epsilon_y < \epsilon_z$. Also, the Maxwell's curl equations for a monochromatic wave are:

$$\omega\mathbf{D} = -\mathbf{k}\times\mathbf{H},\ \mathbf{B} = \mu_0\mathbf{H} \tag{2.3}$$

We can define a vector $\mathbf{n}$ such as

$$\mathbf{k} = \omega\mathbf{n}/c \tag{2.4}$$

We see that, contrary to the case of an isotropic medium where $n = \sqrt{\varepsilon}$ depends only on the frequency, here the magnitude of this vector depends on its direction. Substituting 2.1

in 2.3 and using the last equation we obtain

$$\mathbf{D} = \mathbf{n} \times (\mathbf{E} \times \mathbf{n}) = n^2\mathbf{E} - (\mathbf{n} \cdot \mathbf{E})\,\mathbf{n} \tag{2.5}$$

which forms a set of three linear homogeneous equations for the three components of $\mathbf{E}$: $n^2 E_i - n_i n_k E_k = \varepsilon_{ij} E_k$. These equations are compatible only if the following condition is fulfilled [44]

$$\det \left| n^2 \delta_{ik} - n_i n_k - \varepsilon_{ik} \right| = 0 \tag{2.6}$$

We consider the case of the section with the xy-plane, hence we take $n_z = 0$ in equation 2.6 which cancels lot of terms and the equation now reads:

$$\left(n^2 - \varepsilon_z\right)\left(\varepsilon_x {n_x}^2 + \varepsilon_y {n_y}^2 - \varepsilon_x \varepsilon_y\right) = 0 \tag{2.7}$$

The cancellation of the first term of the product gives the equation of a circle

$$n^2 = \varepsilon_z \tag{2.8}$$

and for the second term it gives the equation of an ellipse

$$\frac{{n_x}^2}{\varepsilon_y} + \frac{{n_y}^2}{\varepsilon_x} = 0 \tag{2.9}$$

which is inside the circle because $\epsilon_x < \epsilon_y < \epsilon_z$. We can find in the same way the section with the yz and xz-planes. In this case in the yz-plane the circle is inside the ellipse. Finally, in the xz-plane they intersect, as shown is the figure 2.1; indeed the plane wave exhibits four degeneracy points which are actually Dirac points, which were named Diabolocial points at the time of the discovery of the conical refraction in biaxial crystals, first theoretically by Hamilton in 1837 [45] and shortly after experimentally by Lloyd [46]. Hamilton asked himself what would happen if a wavepacket or a light beam was sent near the degeneracy points. He realised that a ray cone would appear inside a crystal slab, as shown in fig. 2.2.d., which is peculiar, because an incident beam in any other direction would give a double refraction. The conical refraction effect was getting attention because it was one of the first, if not the very first, mathematical prediction of a physical effect. Airy said that conical refraction was "perhaps the most remarkable prediction that has ever been made". The relation of the linear energy crossing exhibited by the diabolical points to the Dirac Hamiltonian can be understood from the polarization of the different wave surfaces crossing at this point. The full theory of the intensity evolution in such systems was developed relatively recently [47].

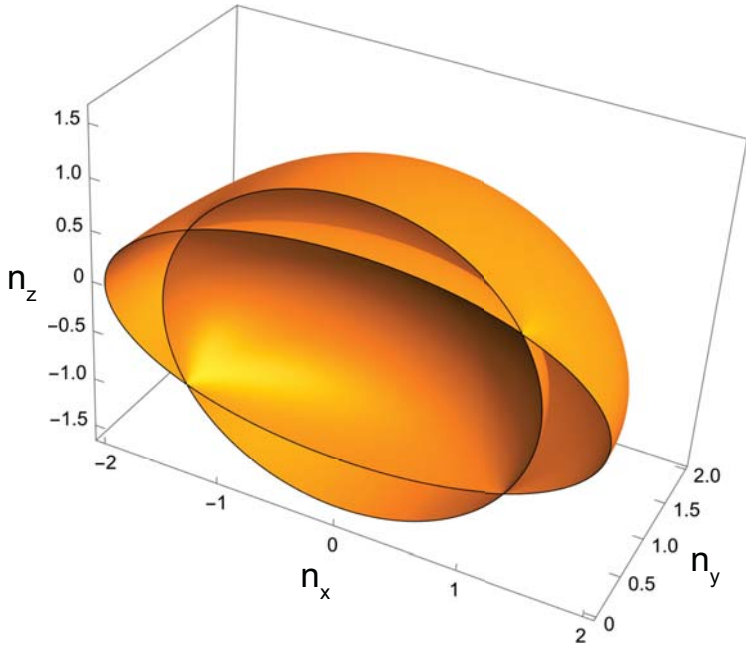

Figure 2.1: *Wave surface for* $\epsilon_x = 1$, $\epsilon_y = 2.25$ *and* $\epsilon_z = 4$, *displaying four Dirac points.*

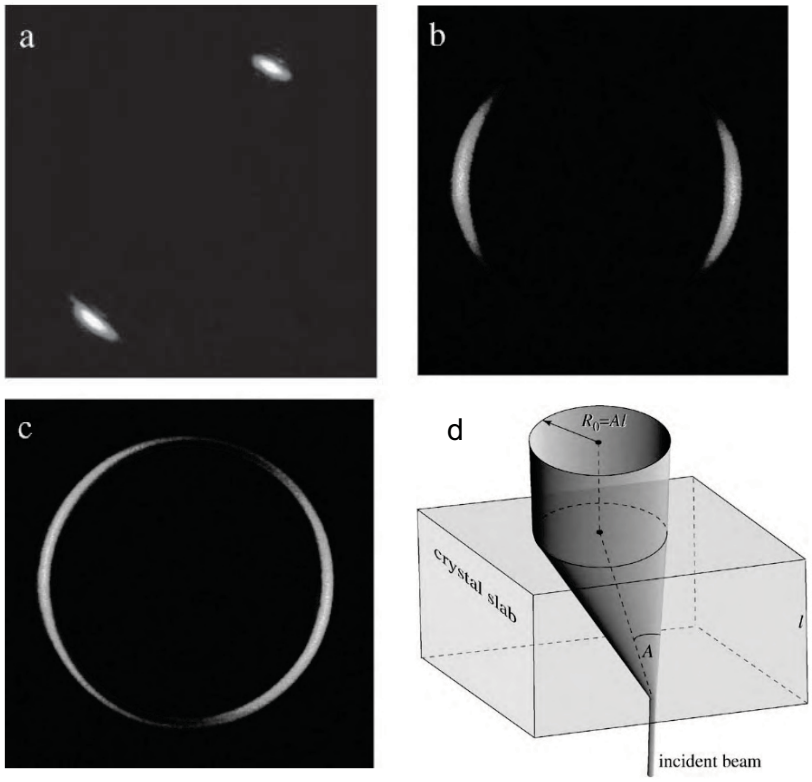

Figure 2.2: *(a-c) Transition from double refraction to conical refraction as the light beam approaches the Dirac point. (d) Schematic of internal conical refraction predicted by Hamilton. These figures are taken from Berry and Jeffrey [43]*

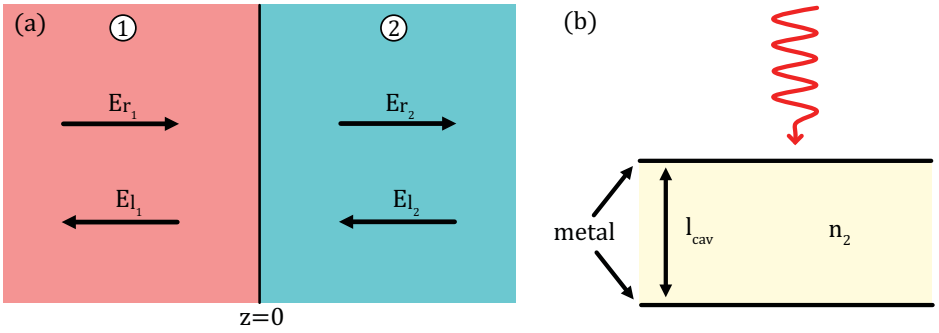

Figure 2.3: *(a) Wave propagation at an interface. (b) Fabry-Pérot cavity made of vacuum-metal-dielectric-metal-vacuum.*

2.2 Dirac points in microcavities

2.2.1 Formalism

Let us consider an electromagnetic wave propagating in two media noted 1 and 2 on fig 2.3, separated by an interface at $z = 0$. The amplitudes of the wave are given by $\mathrm{Re}\left(E_i(z)e^{i\omega t}\right)$ where

$$E_i(z) = E_{r_i}e^{-jk_iz} + E_{l_i}e^{jk_iz} \tag{2.10}$$

with j the complex number $j = \sqrt{-1}$ and $\omega = 2\pi\nu$ the angular frequency. E_r is the part of the wave going from left to right (e^{-jk_iz}) and E_l is going in the opposite direction. We write Fresnel conditions, which express the continuity of the electric and magnetic field at the interface

$$\begin{cases} E_{r_1} + E_{l_1} = E_{r_2} + E_{l_2} \\ B_{r_1} + B_{l_1} = B_{r_2} + B_{l_2} \end{cases} \tag{2.11}$$

and using the third Maxwell equation in the reciprocal space $\mathbf{B} = \mathbf{k} \times \mathbf{E}/\omega$, equations 2.11 become

$$\begin{cases} E_{r_1} + E_{l_1} = E_{r_2} + E_{l_2} \\ k_1\left(E_{r_1} - E_{l_1}\right) = k_2\left(E_{r_2} - E_{l_2}\right) \end{cases} \tag{2.12}$$

In a realistic experiment, a wave is coming from one particular direction. We suppose it comes from the left, meaning $E_{l_2} = 0$. Because $k_i = 2\pi n_i/\lambda_0$, the equations 2.12 give

$$\begin{cases} E_{r_2} = \tau_{12}E_{r_1} \\ E_{l_1} = \rho_{12}E_{r_1} \end{cases} \tag{2.13}$$

where

$$\begin{cases} \tau_{12} = \frac{2n_1}{n_1+n_2} \\ \rho_{12} = \frac{n_1-n_2}{n_2+n_2} \end{cases} \tag{2.14}$$

τ_{12} is the transmission coefficient of the wave from the medium 1 to the medium 2. ρ_{12} is the reflection coefficient of the wave from the medium 1 on the medium 2. We observe that $\tau_{12} \neq \tau_{21}$ and $\rho_{12} = -\rho_{21}$. Also, we see that $\tau_{12}\tau_{21} + {\rho_{12}}^2 = 1$. These results are very general and can be extended to an arbitrary number of media and interfaces, using the so-called

S-matrix formalism [48]. In the case of N layers of dielectric, the electric field of the first medium is connected to the N medium with the formula

$$\left[E_1{}'\right] = P_{12}D_2P_{12}\dots D_{N-1}P_{N-1}\left[E_N\right] = S_{1,N}\left[E_N\right] \tag{2.15}$$

where $[E_1] = (E_{r_1}\ E_{g_1})$ is the matrix representation of the electric field, S is the propagation matrix, P is a transition matrix, and D is a dephasing matrix defined by

$$P_{i-1,i} = \frac{1}{\tau_{i-1,i}}\begin{bmatrix} 1 & \rho_{i-1,i} \\ \rho_{i-1,i} & 1 \end{bmatrix},\ D_i = \begin{bmatrix} e^{-j\varphi_i} & 0 \\ 0 & e^{j\varphi_i} \end{bmatrix} \tag{2.16}$$

with $\varphi_i = k_i l_i$ correspond to the phase-shift of the wave in the layer number i of thickness l. To obtain the transmission and reflection coefficient of the whole structure, we need to consider a wave coming from the left for instance, meaning $E_{r_N} = 0$, which gives

$$\rho_{1N} = \frac{S_{12}}{S_{22}},\ \tau_{1N} = \frac{1}{S_{22}} \tag{2.17}$$

2.2.2 Fabry-Pérot cavities

In this section I will present microcavities (cavities operating in a micrometer range), which are one of the main platforms used in this thesis. Microcavities are optical microresonators close to or below the dimension of the wavelength of light, and are used to confine light. Different types of microcavities exist. For instance, metallic cavities that use the reflection from a single metallic interface, planar multilayer Bragg reflectors with high reflectivity or photonic crystals. Historically, optical microcavities are also called Fabry-Pérot cavities or Fabry–Pérot interferometers, because they were used for calibration of optical systems. A cavity in vacuum can be considered as a sequence of 5 layers represented in fig. 2.3: vacuum, metal, dielectric, metal, vacuum. This problem can be treated as a 3 media problem if we describe the metallic mirrors with transition matrices given by

$$P_{12} = \frac{1}{\tau_{12}}\begin{pmatrix} 1 & \rho_0 e^{j\theta} \\ \rho_0 e^{j\theta} & 1 \end{pmatrix},\ P_{21} = \frac{1}{\tau_{21}}\begin{pmatrix} 1 & \rho_0 e^{-j\theta} \\ \rho_0 e^{-j\theta} & 1 \end{pmatrix} \tag{2.18}$$

with $e^{j\theta}$ corresponding to the phase shift due to the metallic interface, and ρ_0 is the reflection coefficient close to unity which takes into account the high reflectivity of the mirrors. The propagation matrix $S_{13} = P_{12}D_2P_{23}$ can be easily obtained

$$S_{13} = \frac{1}{\tau_{12}\tau_{21}}\begin{pmatrix} e^{-j\varphi} + {\rho_0}^2 e^{j\varphi} & \rho_0(e^{-j(\varphi-\theta)} + e^{j(\varphi-\theta)}) \\ \rho_0(e^{-j(\varphi-\theta)} + e^{j(\varphi-\theta)}) & e^{j\varphi} + {\rho_0}^2 e^{-j\varphi} \end{pmatrix} \tag{2.19}$$

which gives the transmittance T_{cav} of the Fabry-Pérot cavity

$$T_{cav} = \frac{\left|\tau_{12}\tau_{21}\right|^2}{\left|1 - {\rho_0}^2 e^{-2j(\varphi-\theta)}\right|^2} \tag{2.20}$$

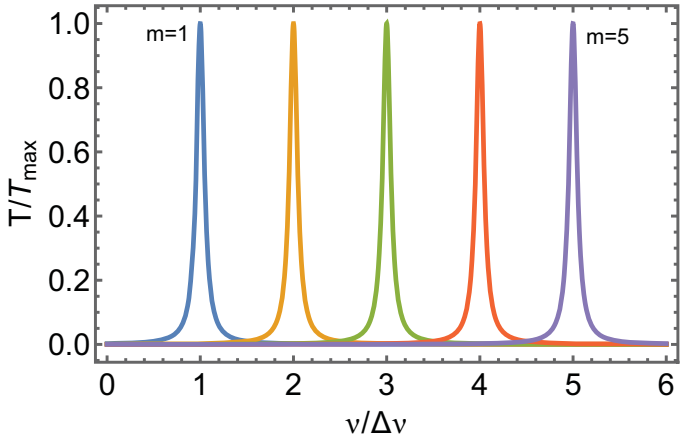

Figure 2.4: *Normalized transmittance of Fabry-Pérot cavity modes for m equal 1 to 5.*

Depending on the wavelength of the incident beam, the transmittance oscillates between T_{min} and T_{max}. It can be shown [48] that close to the resonance of the cavity the transmittance can be written as

$$T_{cav} \approx T_{\max} \frac{1}{1 + (2F/\pi)^2[(\nu/\Delta\nu - j)\pi - \theta]^2} \tag{2.21}$$

where $\Delta\nu = c/(2n_{res}L)$ is the separation between the cavity modes (free spectral range) and F is the finesse of the cavity given by $F = \pi\sqrt{R}/(1-R)$. The full width at half maximum is $\delta = \Delta\nu/F$. We understand why F was named finesse: it defines how fine a mode is. The normalized transmittance from eq. 2.21 is plotted in fig. 2.4 and we observe that a Fabry-Pérot cavity displays a series of modes. An important parameter of these cavities is the thickness L, because the resonances are obtained for $L = j\lambda_0/(2n_{res})$ ($j \in \mathcal{N}$), meaning they are half-wave type cavities.

2.2.3 Photonic cavity modes

In this part we will consider a Fabry-Pérot cavity excited by a laser (see fig. 2.5.a) with a small angle θ with respect to the normal of the mirrors. In this case, light will slowly propagate in the cavity plane, which means $k_z \gg k_{/\!/}$ with $k_{/\!/} = \sqrt{k_x^2 + k_y^2}$. The wavector k_z is quantized. It is defined by the thickness and refractive index of the cavity L and n_c respectively, and the number j ($j \in$ N) of the mode considered $k_z = j\pi/n_cL$. Since the energy is given by

$$E = \hbar ck = \hbar c\sqrt{{k_{/\!/}}^2 + {k_z}^2}, \tag{2.22}$$

its Taylor expansion gives:

$$E = \hbar ck_z \left(1 + \frac{{k_{/\!/}}^2}{2{k_z}^2}\right) \tag{2.23}$$

which means that the in-plane dispersion depends quadratically on the wavevector. The dispersion is plotted in fig. 2.5.b, and we observe an interesting property of these cavities which is that we can obtain a massive dispersion for light! Indeed, in our case, from 2.23 we

write

$$E = \hbar c k_z + \frac{c}{\hbar k_z}\frac{\hbar^2 k_{/\!/}^2}{2} \tag{2.24}$$

which, using the definition of k_z, can be put in the simple form

$$E = \frac{\hbar c j \pi}{n_c L} + \frac{\hbar^2 k_{/\!/}^2}{2m^*} \tag{2.25}$$

where $m^* = \hbar\pi j/(cLn_c)$ is the effective mass of the photonic mode number j. It is also possible to obtain the effective mass using eq. 1.31 which is useful in many cases where the equation of the dispersion is not known, for instance from experimental data. The two consequences of eq. 2.25 are the massive behavior of photons as mentioned above, and also the presence of a photonic ground state.

2.2.4 TE-TM splitting

The in-plane wavevector $k_{/\!/}$ is given by the angle of the incoming beam: $k_{/\!/} = \omega c^{-1} \sin\theta$. Actually the in-plane photonic modes of the cavity are a doublet of polarisation called transverse-electric (TE) and transverse-magnetic (TM) modes. The reflectance and transmittance of the cavity are polarization-dependent. Because of that, a splitting occurs between these two polarizations [49, 50, 51] which can be described by a 2×2 Hamiltonian in the linear polarisation basis $(\psi_{TE}, \psi_{TM})^T$

$$H_{lin} = \begin{pmatrix} \frac{\hbar^2 k_{/\!/}^2}{2m_{TE}} & 0 \\ 0 & \frac{\hbar^2 k_{/\!/}^2}{2m_{TM}} \end{pmatrix} \tag{2.26}$$

We can rewrite this Hamiltonian in the circular basis $(\psi^+, \psi^-)^T$ using

$$\begin{pmatrix} \psi_{TE} \\ \psi_{TM} \end{pmatrix} = \frac{1}{\sqrt{2}} \begin{pmatrix} e^{i\phi} & e^{-i\phi} \\ ie^{i\phi} & -ie^{-i\phi} \end{pmatrix} \begin{pmatrix} \psi_+ \\ \psi_- \end{pmatrix} \tag{2.27}$$

which gives

$$H_{circ} = \begin{pmatrix} \frac{\hbar^2 k_{/\!/}^2}{2m^*} & -\beta k_{/\!/}^2 e^{-2i\varphi} \\ -\beta k_{/\!/}^2 e^{2i\varphi} & \frac{\hbar^2 k_{/\!/}^2}{2m^*} \end{pmatrix} \tag{2.28}$$

where $\varphi = \arctan(k_y/k_x)$ is the in-plane polar angle of the wavevector, β is the strength of the TE-TM splitting and m^* the effective mass of the modes defined by

$$\frac{1}{m^*} = \frac{1}{2}\left(\frac{1}{m_{TE}} + \frac{1}{m_{TM}}\right), \ \beta = \frac{\hbar^2}{4}\left(\frac{1}{m_{TE}} - \frac{1}{m_{TM}}\right) \tag{2.29}$$

We see that the sign of the off-diagonal term, which depends on φ, changes twice in a full circle in the reciprocal space, which is the reason why there is a winding number two [52] as shown in fig. 2.6.c. The splitting is zero at $k_{/\!/} = 0$ and increases with $k_{/\!/}$, as shown in the dispersion plotted in fig. 2.6.a-b. It shows a cut of the 2D dispersion in two perpendicular directions; k_x and k_y. We observe that the TE-TM splitting changes the effective mass of the

TE and TM modes. As we will see later, the TE and TM bands carry a Berry topological charge of opposite sign at $k_{/\!/} = 0$.

2.2.5 Linear Birefringence and Dirac points

Now we need to add an interesting ingredient to these microcavities to modify the band geometry: the linear birefringence [53]. This birefringence comes from the anisotropic properties of particular materials, for instance perovskite [54], or liquid-crystal microcavities [55] which display high birefringence. These birefringent materials will be inserted inside the cavity. From the theoretical point of view, the Hamiltonian now reads [18]

$$H_{circ} = \begin{pmatrix} \frac{\hbar^2 k_{/\!/}^2}{2m^*} & \beta_0 - \beta k_{/\!/}^2 e^{-2i\varphi} \\ \beta_0 - \beta k_{/\!/}^2 e^{2i\varphi} & \frac{\hbar^2 k_{/\!/}^2}{2m^*} \end{pmatrix} \tag{2.30}$$

where β_0 is the birefringence term. This term splits the linearly-polarized modes at $k_{/\!/} = 0$ as shown in fig. 2.6.d-e. Because the effective masses of the two modes are different, they cross in two points in the 2D reciprocal space [18]. The crossing is linear and we are in the presence of a pair of tilted Dirac points (with winding number 1) replacing the touching parabola singularity (with winding number 2) induced by TE-TM splitting, as shown in the fig. 2.6.f. Indeed, it is not obvious from the fig. 2.6.d but we can [18], like in the chapter 1, describe the system near this degeneracy point with an effective Hamiltonian which reads

$$H_D(\mathbf{q}) = \begin{pmatrix} 0 & q_x + iq_y \\ q_x - iq_y & 0 \end{pmatrix} = (q_x\sigma_x - q_y\sigma_y) \tag{2.31}$$

where $q = \sqrt{q_x^2 + q_y^2}$ is small and is defined by $k_{/\!/} = K_D + q$, with K_D the position of the Dirac point in the reciprocal space. We remark that this Hamiltonian is similar to the Dirac Hamiltonian in graphene presented in chapter 1, and consequently will give the same winding number $\omega = 1$ and the same dispersion which is plotted in fig. 1.3.b. However, contrary to graphene, both Dirac points in a cavity have the same winding. The band topology is not modified by the birefringence, but the geometry is [56]. This aspect will be discussed later in detail. Cavities are one of the simplest optical systems to obtain Dirac points, considering also the high tunability of these structures. For instance, liquid crystal microcavities [55] have tunable birefringence depending on the electric field applied in the z direction. It allows a certain control of the position of the Dirac point in the reciprocal space, since the position of the these points is given by $\mathbf{k_D} = \left\{0, \pm\sqrt{\beta_0/\beta}\right\}$, which means that $k_{D,y}$ increases with the birefringence β_0.

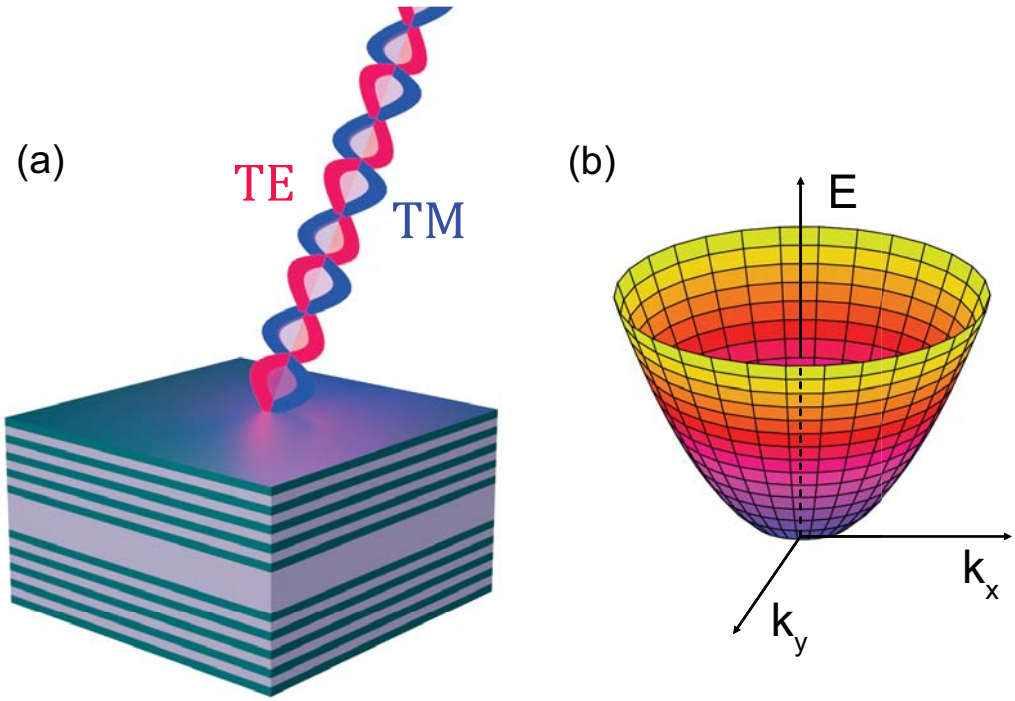

Figure 2.5: *(a) Microcavity composed of two DBRs of semiconductor and a spacer. The in-plane dispersion depends on the angle θ of the incident light. (b) In-plane dispersion of the cavity modes.*

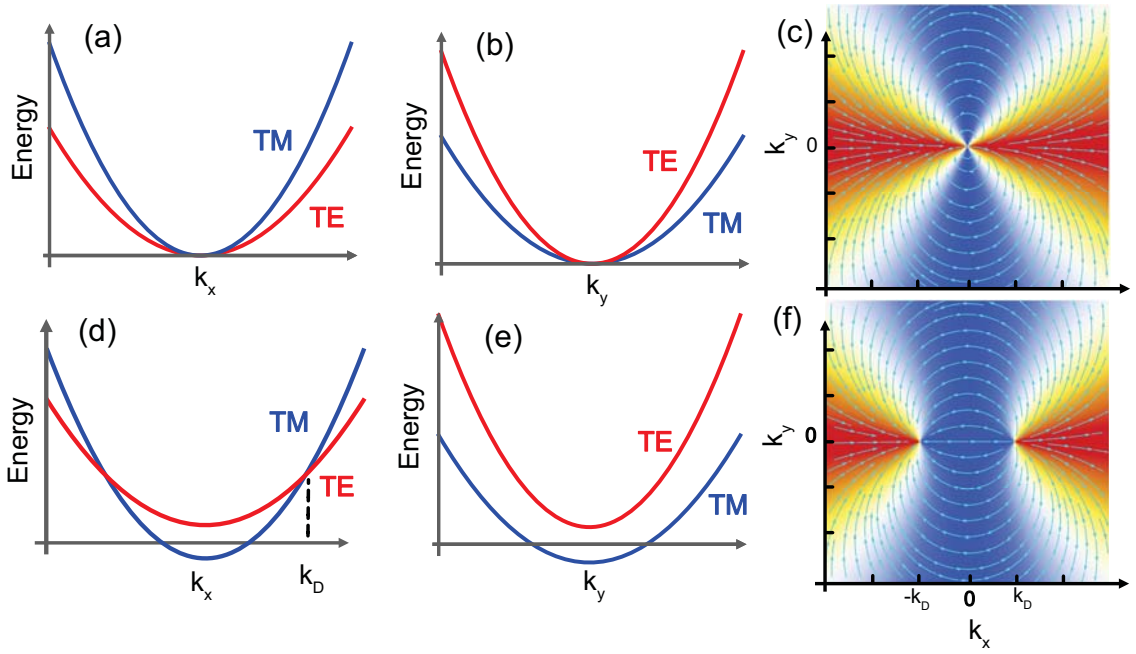

Figure 2.6: *(a-b) Dispersion of TE-TM modes in k_x and k_y direction passing by $k_{/\!/} = 0$. (c) Pseudospin texture with only TE-TM splitting. We observe the texture of a monopole, with a winding number 2. The background density plot shows the linear polarization. (d-e) Dispersion of TE-TM modes in k_x and k_y direction with linear birefringence $\beta_0 \neq 0$. A Dirac point is present at $k_{/\!/} = k_D$. (f) Pseudospin texture with linear birefringence and TE-TM splitting. The monopole of winding number 2 splitted into two monopoles (at the position of the Dirac points) of winding number 1. The background density plot shows the linear polarization.*

Chapter 3: Microcavity polaritons

Contents

In the 3^{rd} introductory chapter, we present a general description of exciton-polaritons, and then we focus on microcavity exciton-polaritons. We describe the key phenomena observed with polaritons, such as Bose-Einstein condensation and superfluidity. We investigate the optical spin-Hall effect, which can be viewed as the starting point of topological polaritonics. Lastly, we study magnetism effects on polaritons, and particularly the Zeeman effect which has direct applications in topological physics.

3.1 Exciton-polaritons

3.1.1 Introduction

A quasiparticle is an object which behaves like a particle. They can be both solutions of the same equations (e.g. Schrödinger equation), they have a mass, a momentum, a position, a charge, a spin, etc... The difference between a particle and a quasiparticle is a more complex question that it seems at first glance [57]. The notion of quasiparticle was first implemented by Lev Landau to describe helium superfluidity [58], and a common definition is that quasiparticles are used to describe collective phenomena in a underlying medium. For instance, a hole in a semiconductor comes from the collective behavior of electrons moving in this semiconductor. We can understand that the concept of quasiparticles is a useful simplification, reducing drastically the number of objects to study to understand the behavior of the system.

A polariton is another quasiparticle, resulting from the strong-coupling of a photonic mode and matter. Numerous types of polaritons exist. For instance, the coupling of a photonic mode and a surface plasmon in a metal is called a surface plasmon polariton. There is also phonon-polaritons, resulting from the coupling of a photon with an optical phonon. What will interest us in this thesis are exciton-polaritons, arising from the strong

coupling of light and excitons in a semiconductor, and more precisely in microcavity exciton-polaritons. Bulk exciton-polaritons have been discovered by Hopfield [59] and Agranovich [60] independently in the late 50's, and 2D cavity exciton-polaritons have been realised in 1992 by Arakawa [61]. Even if this thesis is not dedicated only to microcavity exctiton-polaritons, the expertise of our group [7, 62] on the matter has made these quasiparticles a natural platform to explore new ideas and projects [63, 2, 64].

Polaritons obtain properties from both of their composite parts. From the photonic part the polaritons get a small effective mass, for instance $m^* = 5 \times 10^{-5}\ m_0$ is a typical polariton mass, with m_0 the free electron mass. From their excitonic part, the polaritons inherit the possibility to interact with each other. These interactions can be neglected only for the case of weak polariton density. Signatures of polariton-polariton interactions have been demonstrated, as optical parametric oscillations [65] and bistability [66] in polariton systems have been observed. Moreover, excitons possess a real spin, which is sensitive to an external magnetic field via a Zeeman splitting. Another property of polaritons is that since excitons and photons are bosons, polaritons are bosons too. Hence it is possible to achieve Bose-Einstein condensation with polaritons, something that will be more studied later in this chapter. All these properties make polaritonic an exciting field in order to implement optical devices, like all-optical polariton transistor [67], high-frequency polariton clock generator [2], or polariton lasers [68, 69] to cite a few [70].

3.1.2 2D polaritons

In the following, microcavity exciton-polaritons will be noted simply polaritons, and since we will be working exclusively in $2D$, $k_{/\!/}$ will be noted k. Polaritons arise from the strong coupling of excitons confined in a quantum well and photons confined in the cavity. An illustration of a possible system, composed of a semiconductor slab placed in a Fabry-Perot cavity, is shown in fig. 3.1.a The polariton modes can be described by the Hamiltonian

$$H_{pol} = \begin{pmatrix} E_C(k) & \hbar\Omega_R/2 \\ \hbar\Omega_R/2 & E_X(k) \end{pmatrix} \tag{3.1}$$

where Ω_R is the strength of the exciton-photon coupling, named Rabi splitting, $k = \sqrt{k_x^2 + k_y^2}$ is the in-plane wavevector and E_X and E_C are the bare exciton and photon energies, respectively. These energies are given by the relations

$$E_X(k) = E_X(0) + \frac{\hbar^2 k^2}{2m_X}, \quad E_C(k) = \frac{\hbar c j \pi}{n_c L} + \frac{\hbar^2 k^2}{2m^*} \tag{3.2}$$

with m_X the mass of the exciton, typically of order of magnitude of the electron mass, $m^* = \hbar\pi j/(cLn_c)$ the effective mass of the photon, typically 10^5 order of magnitude lower than the electron mass, and L the width of the cavity, n_c its refractive index, and j the number of the cavity mode. The eigenvalues of H_{pol} are the lower and upper polariton modes given by

$$E_{U/L} = \frac{1}{2}\left(E_X + E_C \pm \sqrt{(E_C - E_X)^2 + \hbar^2\Omega_R^2}\right) \tag{3.3}$$

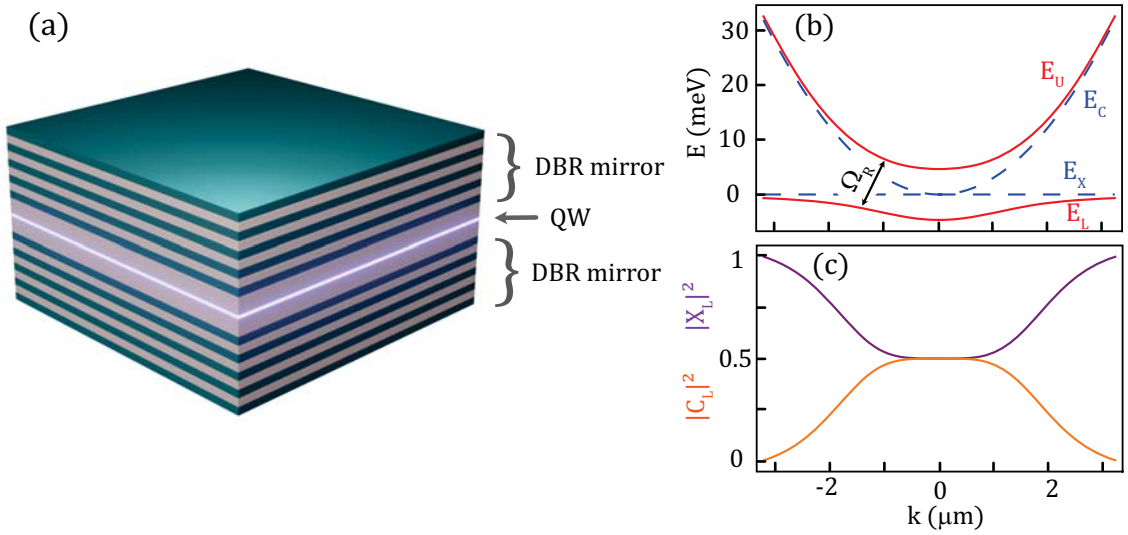

Figure 3.1: *(a) Fabry-Perot microcavity with quantum wells (QW) inserted in it. The photonic modes are confined between the two DBRs and the excitons are confined in the QW. (b) Dispersion of polaritons (upper and lower branches) in red and dispersion of non-interacting photonic and excitonic modes in blue. Parameters:* $E_C = E_X = 0$ *meV,* $\Omega_R = 5$ *meV,* $m_X = 0.4\ m_0$, $m_C = 10^{-5}\ m_0$ *with* m_0 *the free electron mass. (c) Photonic and excitonic fraction of the lower polariton branch. It is the opposite for the upper branch.*

The dispersion is plotted in fig. 3.1.b. The upper and lower polariton branches are in red, and the bare photon and exciton dispersions are in dashed blue. The interaction between the two polariton branches is determined by the Rabi splitting Ω_R, which can be found graphically from the minimum distance between the two branches. In the experiments, the Rabi splitting needs to be larger than the linewidths of the modes, which are induced by the losses, in order to consider the system in the strong coupling regime. The eigenstates of H_{pol} are

$$P_U = \begin{pmatrix} X_U(k) \\ C_U(k) \end{pmatrix}, \quad P_L = \begin{pmatrix} X_L(k) \\ C_L(k) \end{pmatrix} \tag{3.4}$$

with $X_{U/L}$ and $C_{U/L}$ the Hopfield's coefficients satisfying the relation $|X_U|^2 + |C_U|^2 = 1$, and which are defined by

$$X_U(k) = \frac{E_U(k) - E_L(k)}{\sqrt{\hbar^2\Omega_R^2 + (E_U(k) - E_L(k))^2}}, \quad C_U(k) = \frac{\hbar\Omega_R}{\sqrt{\hbar^2\Omega_R^2 + (E_U(k) - E_L(k))^2}} \tag{3.5}$$

$|X_U|^2$ and $|C_U|^2$ correspond to the excitonic and photonic fraction of the mixed upper polariton state at a particular k. The lower polariton state fractions are plotted in fig. 3.1.c. We observe that far away from $k = 0$ the polariton states are pure states, and in vicinity of $k = 0$ these states are close to be 50% mixed.

3.2 Bose-Einstein condensation

3.2.1 Definition

Bose-Einstein condensation (BEC) is a phenomenon studied by Einstein [71] and Bose [72] which were working on the statistics of gas of bosons. Bosons, contrary to fermions, are not subject to the Pauli exclusion principle. Hence they can accumulate in the same quantum state. Einstein's idea was to consider an ideal gas of bosons, which allowed him to predict a new kind of phase transition. We consider an ideal gas of N bosons, without interaction and at a temperature T. The total number of particles N is described according to the Bose-Einstein distribution f_{BE} by:

$$N = \sum_i f_{BE}(\epsilon, \mu, T) = \sum_i \frac{1}{\exp\left(\beta(\epsilon_i - \mu)\right) - 1} \tag{3.6}$$

where $\beta = 1/k_B T$, with k_B The Boltzmann's constant, E_i the energy of the i-th state, and μ the chemical potential. We can separate particles in two groups: those in the ground state and those in the excited states:

$$N = N_0 + N_T = \frac{1}{\exp\left(\beta(\epsilon_0 - \mu)\right) - 1} + \sum_{i \neq 0} \frac{1}{\exp\left(\beta(\epsilon_i - \mu)\right) - 1} \tag{3.7}$$

Since the number of particles in a state has to be positive, necessarily $\epsilon_0 > \mu$. When the chemical potential has a value close to the energy of the ground state, the number of particles in this state becomes very large, it is the mechanism at the base of the Bose-Einstein condensation. Nevertheless, without taking into account the interaction between the particles, the compressibility of the system becomes infinite [73]. The solution to this problem came from Bogoliubov and his model of weakly interactive boson gas. By introducing an interaction between particles, Bogoliubov solves the main problem of the theory describing the ideal boson gas, and thus lays the foundation for a modern theory that can accurately describe the Bose-Einstein condensation [74]. Nevertheless, to make the problem more simple and solvable, some approximations are necessary. Thus, interactions between more than two particles are neglected. The interaction considered has a range less than the average distance between the particles : $d = n^{-1/3} = (N/V)^{-1/3}$. We start by writing the equation for the field operator in the Heisenberg representation [73]

$$i\hbar \frac{\partial \Psi}{\partial t} = \left(-\frac{\hbar^2 \nabla^2}{2m} + V_{ext}(\mathbf{r}, t) + \int \Psi^\dagger(\mathbf{r}', t) V_{int}(\mathbf{r}' - \mathbf{r}) \Psi(\mathbf{r}', t) d\mathbf{r}' \right) \Psi(\mathbf{r}, t) \tag{3.8}$$

with Ψ the field operator, and where the first term represents a free particle without external potential, V_{ext} is an external potential and V_{int} is the interaction potential between two particles. In order to obtain the equation that we want, two approximations are necessary. First, we consider the boson gas dilute enough to deal only with the contact interactions: $V_{int} = \alpha\delta(\mathbf{r}' - \mathbf{r})$. Second, we assume that $T = 0$ and all the particles of the system are in the ground state, then the field operator Ψ can be replaced by $\psi(\mathbf{r}, t) = \langle \Psi(\mathbf{r}, t) \rangle$, which means we are in the mean-field approximation. This allows to obtain the so-called Gross-Pitaveskii

equation

$$i\hbar\frac{\partial\psi(\mathbf{r},t)}{\partial t} = \left(-\frac{\hbar^2\boldsymbol{\nabla}^2}{2m} + V_{ext} + \alpha|\psi|^2\right)\psi(\mathbf{r},t) \tag{3.9}$$

which is also called the non-linear Schrödinger equation, due to the interaction term between particles. If we set the interaction constant $\alpha = 0$, we obtain the Schrödinger equation. This equation was derived independently by Gross [75] and Pitaevskii [76] in 1961. Coherence and interaction are important effects that can be studied starting from the Gross-Pitaevskii equation. Bose-Einstein condensates are a rich platform to investigate experimental and theoretical physics [73, 77].

3.2.2 Quantum fluid of light

Experimentally, two types of excitations are possible to obtain polaritons. First is the off-resonant excitation consisting by exciting a reservoir, which is a large number of excitons at high-energy, excitons which will then relax to the lower polariton state at $k = 0$ via phonon emission, forming a BEC. This process is shown in the fig. 3.2.a. In 1997, Imamoglu demonstrated that to obtain a BEC of polaritons was equivalent to obtain a polariton laser [78], which was experimentally demonstrated few years later [79]. The simulation of the polariton relaxation and condensation under non-resonant pumping, neglecting polarisation effects, can be described by the damping GPE [80, 64]

$$i\hbar\frac{\partial\psi}{\partial t} = -\left(1 - i\Lambda\right)\frac{\hbar^2}{2m^*}\Delta\psi + \alpha|\psi|^2\psi + \left(U_0 + U_R + i\gamma(n_{tot}) - i\Gamma\right)\psi \tag{3.10}$$

with m^* the polariton effective mass, α is the interaction constant, U_0 an external potential, and U_R is the repulsive potential created by the reservoir. The satured gain term is given by $\gamma(n_{tot}) = \gamma_0(n_R)\exp(-n_{tot}/n_s)$, where $n_{tot} = \int|\psi|^2 dxdy$ is the total particle density, and n_s and n_R are respectively the saturation density and the reservoir density. The decay time of polaritons is given by Γ. Finally, the Λ term is a small dimensionless coefficient, which was introduced by Pitaevskii to describe energy relaxation [81], and here it describes the effect of the scattering rates between the condensate and its excited states and the reservoir.

If we consider the spin degree of freedom, one can write a spinor GPE, written in the circular polarization basis which is the true spin projection basis $\boldsymbol{\psi} = (\psi_+, \psi_-)^T$. The kinetic term written in this basis is described by real space operators $k_{x,y} \to -i\partial_{x,y}$ [82, 83]

$$\begin{aligned} i\hbar\tfrac{\partial\psi_+}{\partial t} &= -\tfrac{\hbar^2}{2m^*}\Delta\psi_+ + \beta(\partial_y + i\partial_x)^2\psi_- + \alpha_1|\psi_+|^2\psi_+ + \alpha_2|\psi_-|^2\psi_+ \\ i\hbar\tfrac{\partial\psi_-}{\partial t} &= -\tfrac{\hbar^2}{2m^*}\Delta\psi_- + \beta(\partial_y - i\partial_x)^2\psi_+ + \alpha_1|\psi_-|^2\psi_- + \alpha_2|\psi_+|^2\psi_- \end{aligned} \tag{3.11}$$

These equations differ from the ones which describe a condensed binary mixture of cold atoms [84, 85] because of the additional TE-TM spin-orbit coupling term. An interesting property is the strong anisotropy of the interaction constants $\alpha_1 \gg \alpha_2$, which means they are miscible condensates. The first demonstration of polariton BEC was done at low temperature [68], as shown in fig. 3.2.b.c. The authors observed the condensation occurring when the power of the pump P exceeded a threshold P_{thr}. The first polariton condensates were achieved using CdTe and later GaAs semiconductor quantum well microcavities , which are limited to cryogenic

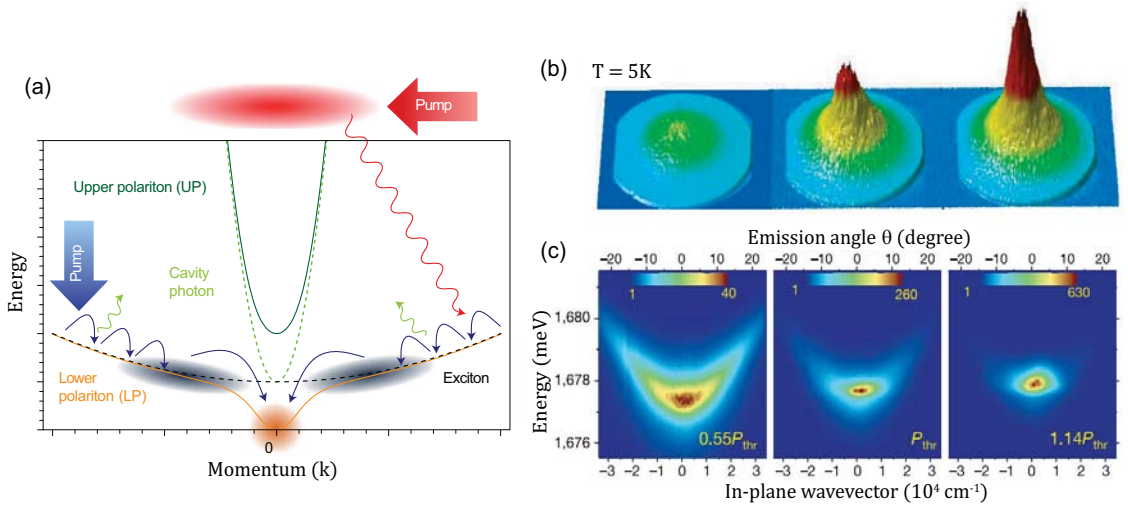

Figure 3.2: *(a) Polariton dispersion, with the pump laser exciting high-energy excitons in the reservoir, which then relax in the ground state at $k = 0$ via phonon emission, creating a polariton BEC. (b-c) Experimental dispersion demonstrating polariton condensation at low temperature. Figures from this review on polariton BEC [101].*

temperature. Since then, wide bandgap semiconductors[86] and organic microcavities[87] (owing to the high binding-energy of organic materials [88]) have shown the possibility to obtain a polariton BEC at room temperature. Another interesting property of these polariton BEC is that they are an ideal platform to study quantum fluids [89], meaning fluids displaying macroscopic quantum effects such as superfluidity [90, 91], optically controllable [92] and even at room temperature [93]. These fluids can host qualitatively different excitations, such as linear small perturbations of the condensate known as bogolons, but also non-linear solutions of the GPE known as solitons in 1D and quantum vortices in 2D [94, 95]. Some crucial advantages of polariton quantum fluids is the possibility to create metastable flows of particles, and also a full experimental access to the wavefunction, in real, reciprocal space, frequency, time domain, and also to the pseudo-spin degree of freedom. This allowed to investigate quantum fluids effects not easily achieved in other platforms, such as oblique solitons [96, 97]. Very recently, Kardar–Parisi–Zhang universality was demonstrated in a 1D polariton condensate [98]. It also allows to investigate analogue gravity [99, 100] in quantum systems, like 2D rotating black holes with a quantized angular momentum [63].

3.3 Resonant pumping

Another way of obtaining polaritons is quasi-resonant injection, which means to create macroscopically occupied and coherent states at a given energy, wavector, density and even pseudospin, by a direct laser excitation fixing all these parameters. In this case, and for relatively low wavevectors, the polariton wavefunction $\psi(r, t)$ can be described by the GPE with a pump and a decay term. We also neglect the polarization degree of freedom [102] to

simplify the theoretical description, hence the equation reads

$$i\hbar\frac{\partial\psi}{\partial t} = \left[-\frac{\hbar^2}{2m^*}\nabla^2 + \alpha|\psi|^2 - i\frac{\hbar}{2\tau}\right]\psi + Pe^{-i\omega_p t} \tag{3.12}$$

where the chosen parameters are from GaAs samples: $m^* = 5\times10^{-5}\ m_0$ is the polariton mass, $\alpha = 5\ \mu eV\ \mu m^2$ is the coefficient of polariton-polariton interactions [103], $\tau \sim 100\ ps$ is the polariton lifetime [56], and $P(\mathbf{r})$ is the pump, exciting the system at a certain energy $E_P = \hbar\omega_p$. The confinement potential term U can describe particular structures which can be obtained by lithography. These structures can be for instance micropillars [104, 105], where polaritons are also confined in the x and y directions, making the confinement $0D$. Quasi-resonant excitation is mandatory to obtain effects such as bistability [66] and optical parametric oscillations [65].

3.4 Optical Spin Hall effect

The TE-TM splitting of photonic cavity modes, explained in the previous chapter, gives rise to a TE-TM splitting of polariton modes. This TE-TM splitting can be seen as an effective magnetic field Ω_{TE-TM} acting on the pseudospin of polaritons. Their spin (i.e. the angular momentum) has a ±1 projection in the growth direction of the microcavity (usually z), so the polariton can be considered as a two-level system with an effective pseudospin $S = 1/2$. We consider here polaritons described by a spinor $(\Psi^+, \Psi^-)^T$. The propagation of polaritons in a microcavity can be described by an effective Hamiltonian, which is a reformulation of 2.28 and reads [52]

$$H_{eff} = \frac{\hbar^2k^2}{2m^*} + \hbar\boldsymbol{\sigma}\cdot\boldsymbol{\Omega}_{TE-TM} \tag{3.13}$$

with $\boldsymbol{\sigma} = (\sigma_x, \sigma_y, \sigma_z)$ the Pauli matrix vector, $\Omega = (\Delta_{TE-TM}(k)\cos2\varphi, \Delta_{TE-TM}(k)\sin2\varphi, 0)$ the effective magnetic field, where Δ_{TE-TM} is the TE-TM splitting term and m^* the effective mass of the polaritons. The pseudospin obeys the precession equation[1]

$$\frac{d\mathbf{S}}{dt} = \mathbf{S}\times\boldsymbol{\Omega}_{TE-TM} \tag{3.14}$$

where $S_i = (\psi^+\ \psi^-)^*\sigma_i\begin{pmatrix}\psi^+\\ \psi^-\end{pmatrix} = \langle\sigma_i\rangle$ is the polariton pseudospin, and $\boldsymbol{\Omega}_{TE-TM} = (\Omega_x, \Omega_y)$ is defined by

$$\Omega_x = \frac{\Delta_{TE-TM}}{\hbar k^2}\left({k_x}^2 - {k_y}^2\right),\quad \Omega_y = \frac{2\Delta_{TE-TM}}{\hbar k^2}k_xk_y \tag{3.15}$$

So let's stop a few seconds here and look at the value of the effective magnetic field along a circle in the 2D reciprocal space of radius 1 (a.u.) and center at $\mathbf{k} = 0$

- If $(k_x, k_y) = (1,0)$ or $(-1,0)$ then $\Omega_x = \frac{\Delta_{TE-TM}}{\hbar k^2}$, $\Omega_y = 0$

[1] Note that the crossover product is not in the same order as in Feyman's description [1] described in chapter 1. It's actually a matter of convention [106, 107].

- If $(k_x, k_y) = (0, 1)$ or $(0, -1)$ then $\Omega_x = -\frac{\Delta_{TE-TM}}{\hbar k^2}$, $\Omega_y = 0$
- If $(k_x, k_y) = \left(\frac{1}{\sqrt{2}}, \frac{1}{\sqrt{2}}\right)$ or $\left(\frac{-1}{\sqrt{2}}, \frac{-1}{\sqrt{2}}\right)$ then $\Omega_x = 0$, $\Omega_y = \frac{\Delta_{TE-TM}}{\hbar k^2}$
- If $(k_x, k_y) = \left(\frac{1}{\sqrt{2}}, \frac{-1}{\sqrt{2}}\right)$ or $\left(\frac{1}{\sqrt{2}}, \frac{-1}{\sqrt{2}}\right)$ then $\Omega_x = 0$, $\Omega_y = \frac{-\Delta_{TE-TM}}{\hbar k^2}$

It is represented the fig 3.3.a, and we observe that the effective magnetic field is rotating twice for a single rotation in the reciprocal space. When we excite coherently the TE and TM modes at a given frequency, as shown in fig 3.3.b., we obtain a circular cross section, with a circle centered at $k = 0$, and along this cross section the effective magnetic field will behave the same way. Now, for the pseudospin $\mathbf{S}$ we start by getting in the polarization of light, which can be totally determined by the Stokes parameters which correspond to the following polarization degrees

$$\rho_L = \frac{I_H - I_V}{I_H + I_V}, \quad \rho_D = \frac{I_D - I_A}{I_D + I_A}, \quad \rho_C = \frac{I_+ - I_-}{I_+ + I_-} \tag{3.16}$$

where H, V, D, A, $+$ and $-$ note for horizontal, vertical, diagonal, antidiagonal, circular right and left respectively. There is a strict correspondance between the polarization of light emitted from the cavity and the polariton pseudospin, meaning $S_x = \rho_L$, $S_y = \rho_D$ and $S_z = \rho_C$. Now we can fully understand the system using the Bloch sphere representation on fig. 3.3.c. When the TM polarized incident light oscillates in the (x, z) plane, it excites a polariton state in the reciprocal space along the S_x vector. In this case, the effective magnetic field and the pseudospin are aligned and the cross product of the two vectors is zero, meaning there will be no precession of the pseudospin. It is true for the four only configurations where the pseudospin are aligned or anti-aligned with either S_x or S_y. Every other possible configuration will make the pseudospin rotate around the effective magnetic field. Since the latter is in the (S_x, S_y) plane, the pseudospin will acquire a S_z component, and hence the polariton will be circularly polarized. Indeed, if we excite with a laser polarized linearly, it has been demonstrated theoretically [52] and experimentally [108] that the photons coming out of the cavity along diagonal directions in the k-space are circularly polarized. This polarization depends fully on the emission angle $\theta = arctan(k_y/k_x)$, as shown in the fig. 3.3.d., where the red color means it is polarized circular right and blue left respectively. Hence, the polarization of light absorbed and re-emitted by the cavity is different due to the pseudospin precession. This effect is called the Optical Spin Hall Effect, and it is the starting point of topological polaritonics [62].

3.5 Interaction with a magnetic field

3.5.1 Zeeman effect

As mentioned before, one important property of polaritons is their (pseudo)spin inherited from the spins of excitons and cavity photons, which gives the polarization of the emitted photons. The optical spin Hall effect allows to tune the spin of the polaritons owing to their photonic part. We will study in this section how to control the polariton spin using its

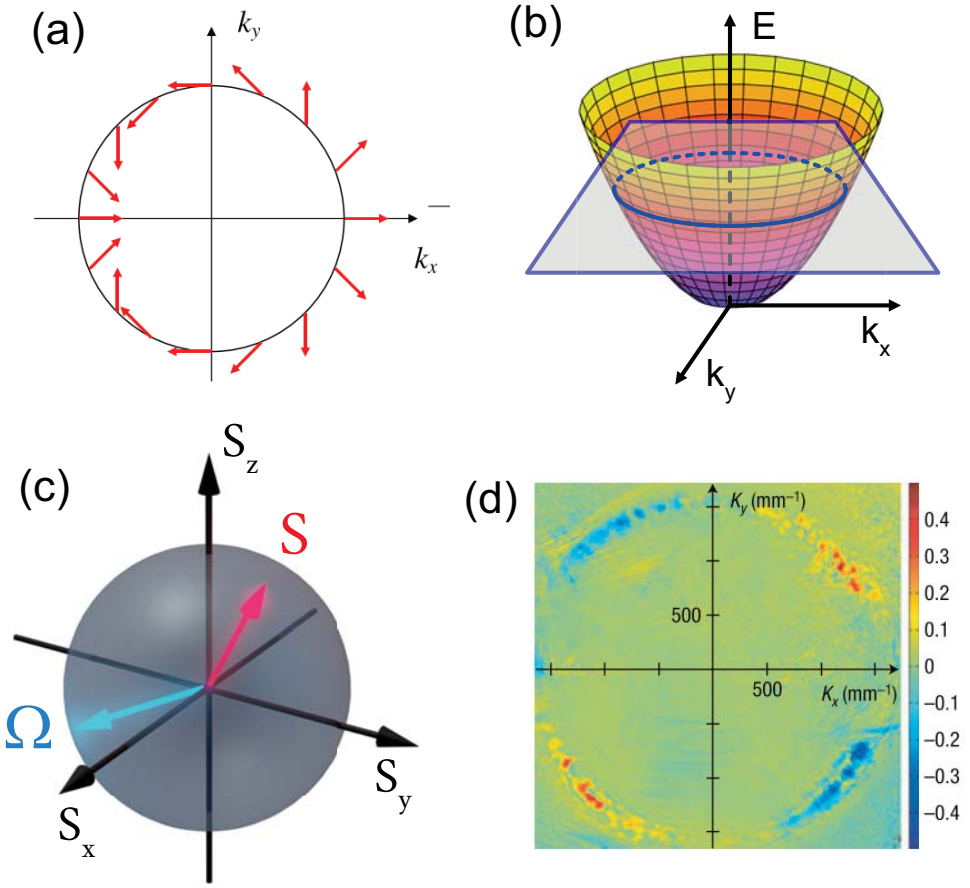

Figure 3.3: *(a) Double rotation of the effective magnetic field $\mathbf{\Omega}_{TE-TM}$ in the 2D reciprocal space. (b) Cross section of a parabolic TE or TM mode. (c) Bloch sphere with polarization of light as states: linear polarization (S_x, S_y) and circular one S_z. (d) Experimental measurment of the intensity of the circular degree of polarization. Color red means circular right, color blue means circular left.*

excitonic part. Indeed, one big advantage of polaritons with respect to other optical systems is the possibility to interact with them with an electromagnetic field [109, 62]. For instance, the excitonic part of polaritons are sensitive to a Zeeman splitting [110]. The exciton energy splits into two levels in a magnetic field according to the equation

$$E_X(B) = E_X(0) + \frac{\hbar^2 k^2}{2m_X} + \Delta_Z(B)/2 \tag{3.17}$$

where m_X is the exciton mass and Δ_Z is the Zeeman splitting term, with g the g-factor, and μ_B the Bohr magneton. The second term, meaning the exciton dependence on the wavevector $\mathbf{k}$, is usually negligeable compared to the Zeeman effect. The excitons with a total angular momentum $\mathbf{J}$ couple with light following the rules

- the excitons with $J_z = -1$ couple with σ^- photons, creating spin-down polaritons
- the excitons with $J_z = +1$ couple with σ^+ photons, creating spin-up polaritons

Due to that, polaritons demonstrate also a Zeeman splitting, which will split the two circular polarized polariton modes. This effect is represented in the fig. 3.4.a. At $B = 0\ T$, the two branches are degenerate, but at $B = 4T$ we observe a splitting of the two modes and of the exciton energy [111]. This splitting was found to be larger that the linewidth of the modes with an applied magnetic field of a few Tesla in GaAs- and CdTe-based microcavities [112, 113]. The Hamiltonian describing the polaritons under magnetic field was introduced for the first time in 2009 [114], and is composed of the Hamiltonian of polaritons with TE-TM splitting 3.13 and a Zeeman term, in the circular polarization basis

$$H = \begin{pmatrix} \frac{\hbar^2 k^2}{2m^*} + \frac{\Delta_Z}{2} & \frac{\Delta_{TE-TM}(k)}{2} e^{-2i\varphi} \\ \frac{\Delta_{TE-TM}(k)}{2} e^{-2i\varphi} & \frac{\hbar^2 k^2}{2m^*} - \frac{\Delta_Z}{2} \end{pmatrix} = \frac{\hbar^2 k^2}{2m^*} + \hbar \boldsymbol{\sigma} \cdot \boldsymbol{\Omega} \tag{3.18}$$

with $\boldsymbol{\sigma}$ the Pauli matrix vector, $\boldsymbol{\Omega} = (\Delta_{TE-TM}(k)\cos 2\varphi, \Delta_{TE-TM}(k)\sin 2\varphi, \Delta_Z)$ the effective magnetic field, Δ_{TE-TM} the TE-TM splitting term, m^* the effective mass of polaritons and Δ_Z the Zeeman splitting term. The importance of the Zeeman effect on polariton stems from the fact that this Hamiltonian was shown to be sufficient to study topological photonics [114]. Note that this effect has been predicted [112] and experimentally demonstrated [111] to disappear in the case where polaritons form a BEC. Starting from the left of the panel b of fig 3.4, the system is under constant magnetic field $B = 4\ T$ and we see a clear Zeeman splitting. It is at low power of the pump, $P = 8\ \mu W$. As the power increases, we observe the formation of the polariton BEC at $k = 0$. When the BEC is fully formed, at $P = 171\ \mu W$, there is no presence of the Zeeman splitting anymore. It is known as the Mesner effect.

3.5.2 Diamagnetic effect

It has been demonstrated that the exciton energy under a magnetic field not only splits due to the Zeeman effect, but there were also an overall blue shift of the energy [115] which increases quadratically with B

$$E_X(B) = E_X(0) + \frac{\hbar^2 k^2}{2m_X} + \Delta_Z(B)/2 + \gamma B^2 \tag{3.19}$$

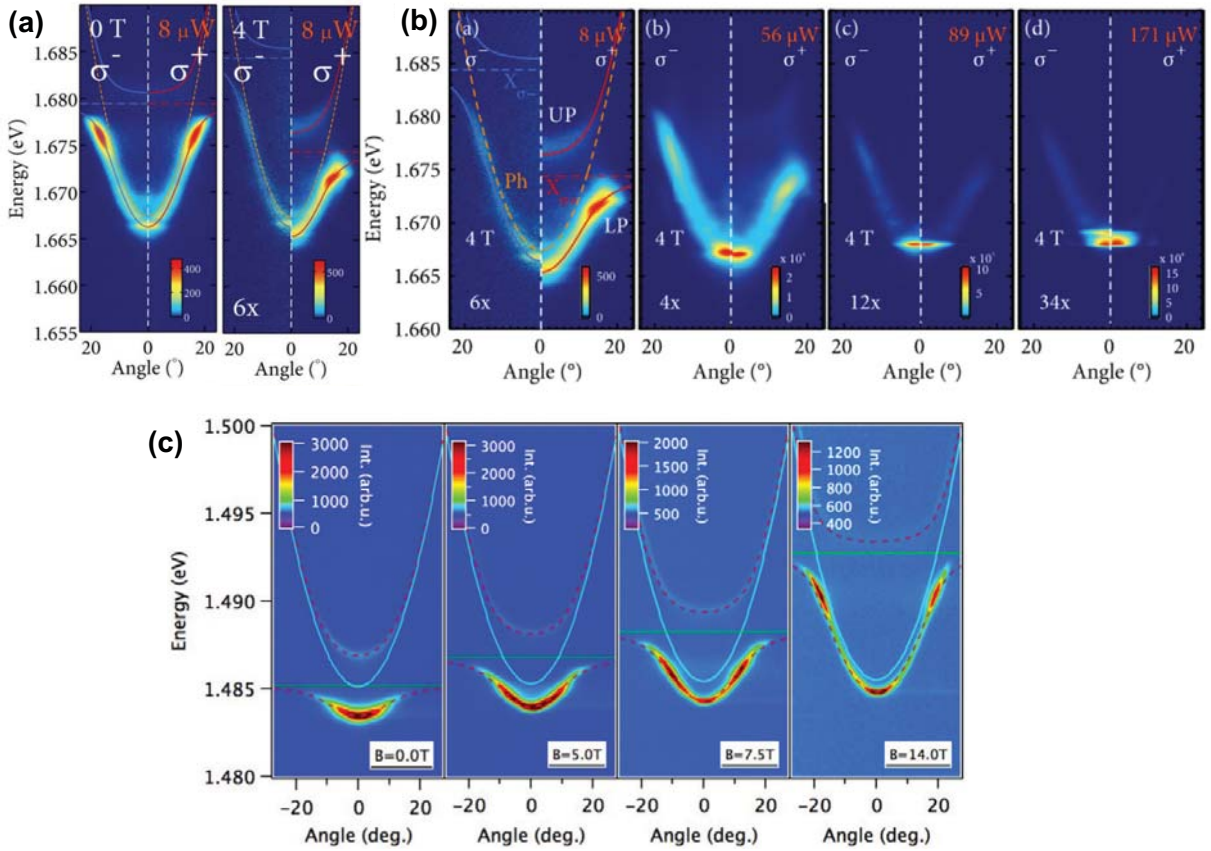

Figure 3.4: ***Experimental demonstration of the Zeeman effect, Mesner effect, and diamagnetic effect.*** *We consider only the lower polariton branch (a) σ^+ and σ^- polarized polariton dispersion with no applied magnetic field (left panel) and under a magnetic field of 4T (right panel). We observe a splitting of the two polarizations. (b) σ^+ and σ^- polarized polariton dispersion under a constant 4T magnetic field, but with a ramping power of the pump, from $P = 8\ \mu W$ to $P = 171\ \mu W$. As the polariton BEC forms, we observe a supression of the Zeeman splitting. (c) In some materials, the Zeeman effect is negligeable compared to the diamagnetic shift. We observe the blue shift of the exciton energy as the magnetic field increases.*

where γ is the diamagnetic term, and $\Delta_Z(B) = g\mu_B B$ is the Zeeman splitting, with g the g-factor, and μ_B the Bohr magneton. Depending on the material used to build the microcavity, the diamagnetic effect can be negligible, comparable, or far greater than the Zeeman effect. The latter [116] is shown on the panel c of fig 3.4. At constant pumping power, as the magnetic field B increases, we observe a blue shift of the exciton energy, from $E_X = 1485\ meV$ at $B = 0\ T$ to $E_X = 1493\ meV$ at $B = 14\ T$.

Chapter 4: Quantum Geometric Tensor

Contents

In the 4^{th} and last introductory chapter, we investigate the properties of the Quantum Geometric Tensor, which is at the heart of topological physics. It allows to compute the Berry curvature and the Quantum Metric. We develop the notions of Berry phase, of the so-called Chern number, and of bulk-boundary correspondence. We study one of the simplest topological systems, known as the Jackiw-Rebbi interface state, then we talk about the development of topological photonics in the last two decades. The last part of this chapter is dedicated to metrics, and more precisely to the properties of different known metrics such as the Riemannian and Minkowski metrics. Finally, the Quantum Metric, its applications and its relation with the Chern number is discussed.

4.1 Definition

As mentioned earlier, the story of topological physics date from the 18^{th} century [21, 22]. For instance, the geometria situs, which is the latin term for topology, took an important part in the works of Gauss. The field began to gain prominence with the work of Poincaré in 1895, who was studying celestial mechanics [23]. The analysis of magnetic monopoles by Dirac in the 30s was of the topological nature [30], and in the 60s, Gell-Mann and Lévy have created the non-linear sigma model in the quantum field theory, which incorporates the concepts of topology [117]. Interest in topology has grown exponentially in recent times in physics since the discovery of the quantum Hall effect in the 1980s by K. von Klitzing, work which earned him the Nobel Prize in 1985 [24]. This effect unravelled the necessity to develop a description beyond the Fermi level model. We will not develop here a band theory of crystals, starting from the Bloch theorem [15], but we will rather consider the dispersion relation as a known entity. A dispersion links the energy of a particle to its wavevector. Theoretically, the dispersion is given by the eigenvalues of the Hamiltonian describing the system. Another important quantity is the Fermi level, describing the highest occupied single particle state. In graphene, for instance, it corresponds to the energy of the Dirac point, meaning that the bands below the Dirac point are fully occupied, and the bands above are

empty. This band model for materials was sufficient until the rise of topological physics, which expresses the fact that not only the dispersion and the Fermi level are important, but also the geometry of the eigenstates along these bands over the Brillouin zone.

The Quantum Geometric Tensor (QGT) is a complex tensor introduced by Provost and Vallée in the 1980 [118], that is composed of eigenstates and their derivatives in a parameter space (in our case it will be the reciprocal space)

$$T_{ij} = \left\langle \frac{\partial\psi}{\partial k_i} \middle| \frac{\partial\psi}{\partial k_j} \right\rangle - \left\langle \psi \middle| \frac{\partial\psi}{\partial k_j} \right\rangle \left\langle \frac{\partial\psi}{\partial k_i} \middle| \psi \right\rangle \tag{4.1}$$

From this matrix, two quantities of interest can be derived

- The antisymmetric imaginary part which defines the Berry Curvature. It is given by $F_{ij} = -2\mathrm{Im}(T_{ij})$
- The symmetric real part which determines the Quantum Metric[1]. It is given by $g_{ij} = \mathrm{Re}(T_{ij})$

This chapter is dedicated to explaining these two concepts, their fundamental interest and their applications.

4.2 Berry curvature and Chern number

4.2.1 Berry phase and related quantities

Berry phase is an example of a geometric phase appearing in quantum mechanics [119]. Other examples include the Pancharatnam phase in optics [120, 121, 122] or the Hannay angle in classical mechanics [123], including the Foucault pendulum [124].

We start by considering an Hamiltonian H changing slowly over time, meaning in an adiabatic process. A particle in the n^{th} eigenstate ψ_n is described by the equation

$$H(t)\psi_n(\mathbf{r},t) = E_n\psi_n(\mathbf{r},t) \tag{4.2}$$

where the eigenstate can be written under the form

$$\psi_n(\mathbf{r},t) = \psi_n(\mathbf{r})e^{-iE_nt/\hbar} \tag{4.3}$$

The adiabatic theorem says that if H changes adiabatically, then the particle in the n^{th} will remain in this state during the evolution of the system. However, the eigenstate will acquire a time-dependant phase

$$\Psi_n(\mathbf{r},t) = \psi_n(\mathbf{r},t)e^{-t\theta_n(t)/\hbar}e^{i\gamma_n(t)} \tag{4.4}$$

where γ_n is called the geometric phase and θ_n is called the dynamic phase and is described by

$$\theta_n(t) = -\frac{1}{\hbar}\int_0^t E_n(t')dt' \tag{4.5}$$

[1] It is also called the Fubini-Study metric.

It generalizes the $E_n t/\hbar$ term when E_n is changing over time. Note that the energy is not conserved here, which is a direct consequence to the evolution in time of the Hamiltonian. If we use the eigenfunction form in eq. 4.4 into the time-dependant Schrödinger equation

$$i\hbar\frac{\partial\psi_n}{\partial t} = H(t)\psi_n \tag{4.6}$$

we will observe the annihilation of the energy E_n term and it leads to an equation for the geometric phase γ_n

$$\frac{d\gamma_n}{dt} = i\left\langle \psi_n \middle| \frac{\partial\psi_n}{\partial t} \right\rangle \tag{4.7}$$

The Hamiltonian changes over time because of some parameter which does so. We consider $\mathbf{k}(t)$ as a time-dependant function, and we use the simple fact that the derivative of ψ_n can be written as

$$\frac{\partial\psi_n}{\partial t} = \frac{\partial\psi_n}{d\mathbf{k}}\frac{d\mathbf{k}}{dt} \tag{4.8}$$

A careful derivation [125] allows to obtain the following expression

$$\gamma_n(t) = i\int_{k_i}^{k_f} \langle\psi_n\,|\nabla_k\psi_n\rangle\cdot d\mathbf{k} \tag{4.9}$$

Now, of course the Hamiltonian can describe a loop and returns to its original form after a time t_L. In this case, the geometric phase takes the form

$$\gamma_n(t_L) = i\oint \langle\psi_n\,|\nabla_k\psi_n\rangle\cdot d\mathbf{k} \tag{4.10}$$

which is known as the Berry phase, derived by Berry the first time in 1984 [126], and usually takes a non-zero value. According to the Stokes' theorem, it can be written as an integral of a curl of the same scalar product over the surface encircled by the contour:

$$\gamma_n = \iint_S \nabla\times i\,\langle\psi_n|\nabla\psi_n\rangle\,d^2k \tag{4.11}$$

Berry noticed the analogy with the magnetic field: the expression of the Berry phase is similar to the one of a magnetic flux in terms of vector potential $\mathbf{A}$ whose curl appears in the latter expression. Indeed, let us define a curve C around a surface S, and B is a magnetic field. The flux Φ through this surface can be written as

$$\Phi = \int_S \mathcal{B}\cdot d\mathbf{a} \tag{4.12}$$

and of course if we write the magnetic field under the form $\mathbf{B} = \boldsymbol{\nabla}\times\mathbf{A}$ and use the Stokes' theorem the equation takes the form

$$\Phi = \int_S (\nabla\times\mathbf{A})\cdot d\mathbf{a} = \oint_C \mathbf{A}\cdot d\mathbf{r} \tag{4.13}$$

If we want to study the n^{th} band of periodic system, we can generalize the results above with

a periodic Hamiltonian, thus a periodic eigenstate [15]. The latter can be written under the form $\psi_{n,\mathbf{k}}(\mathbf{r}) = e^{i\mathbf{k}\cdot\mathbf{r}}u_{n,\mathbf{k}}(\mathbf{r})$, with $u_{n,\mathbf{k}}$ the Bloch state of the n^{th} band considered. In this case, the Berry phase of this band can be described as a flux of an analogue of a magnetic field $\mathcal{B}$, called Berry curvature and which is defined by the following equation

$$\mathcal{B}_n = i\nabla_k \times \langle \psi_n | \nabla_k \psi_n \rangle = \boldsymbol{\nabla}_k \times \mathcal{A}_n(\mathbf{k}) \tag{4.14}$$

where $\mathcal{A}$ is the analogue of the vector potential $\mathbf{A}$. It is called the Berry connection and can be written under the form

$$\mathcal{A}_n(\mathbf{k}) = i \langle u_{n,\mathbf{k}} | \boldsymbol{\nabla}_{\mathbf{k}} | u_{n,\mathbf{k}} \rangle \tag{4.15}$$

Using this notation the Berry phase γ can be re-expressed as

$$\gamma_n = \oint \mathcal{A}_n(\mathbf{k}) \cdot d\mathbf{k} \tag{4.16}$$

The Berry connection, phase, and curvature are key concepts in topological physics [127, 128]. We note that, under a gauge transformation $|u_{n,\mathbf{k}}\rangle \to e^{i\nu(\mathbf{k})}|u_{n,\mathbf{k}}\rangle$, the Berry connection $\mathcal{A}$ is not gauge invariant [129] and transforms as $\mathcal{A}_n(\mathbf{k}) \to \mathcal{A}_n(\mathbf{k}) - \nabla_{\mathbf{k}}\nu(\mathbf{k})$. In contrary, the Berry curvature $\mathcal{B}$, as a magnetic field, appears naturally as gauge invariant under this transformation.

4.2.2 Bulk-boundary correspondence

One can compute the flux of $\mathcal{B}$ on a surface S in the reciprocal space to obtain the Berry flux

$$\iint_S \mathcal{B}(\mathbf{k}) \cdot d\mathbf{s} \tag{4.17}$$

This flux is equal to $2\pi n$ on a closed surface, where n is an integer, simply because it corresponds to a Berry phase on a vanishingly small contour (Eq. 4.10), which is necessarily equal to 0 modulo 2π. The 2D Brillouin zone is geometrically equivalent to a torus, as shown in fig. 4.1.a. The Chern number C is defined as the Berry flux on a closed surface divided by 2π and so it is an integer

$$C = \frac{1}{2\pi} \oiint_S \mathcal{B}(\mathbf{k}) \cdot d\mathbf{s} \tag{4.18}$$

It can be viewed as the number of charges[2] of the gauge field represented by the Berry curvature, located inside the torus, as shown in the fig. 4.1.b-d. The Chern number is defined in a band, and the sum of the Chern numbers over all the bands is equal to zero. It allows to describe topological insulators: insulating materials with topological gaps. Since the Chern number is a topological invariant, it can't change its value under continuous transformations, meaning without the gap closing. A peculiar phenomenon happens at the interface between two materials with different topological invariants. In this case, the topology allows these different Chern numbers to connect only through a topological transition which happens at the interface. This transition requires the energy gap to close at the interface, nullify the

[2]The topological charge can be seen as a monopole of the Berry flux.

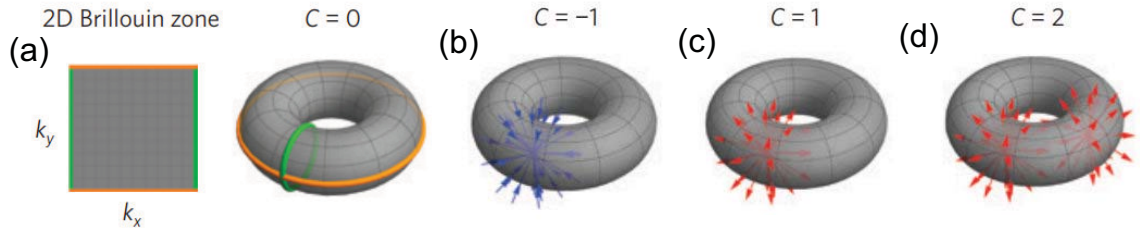

Figure 4.1: *The arrows represent the Berry curvature, from positive to negative charge (a) Mapping between the 2D Brillouin zone and a torus. Without topological charge (monopole of Berry flux) inside the closed surface, the system is topological trivial, meaning the Chern number C is equal to zero. (b) Presence of negative charge of Berry flux. The Chern number of the system is equal to $C = -1$. (c) Positive charge of Berry flux: $C = 1$ (d) The Chern number is equal to the number of the charges. $C = 2$.*

Chern number, then re-open the gap, as shown in the fig. 4.2.b. This is called the bulk-edge correspondence: the number of the states at the interface is determined by the topology of the bulk on both sides. The resulting state, localized at the interface, stems from the difference of topology of the different materials and hence is called topological edge state. The interface between a topologically non-trivial insulator and a trivial one, like vacuum, is sufficient to assure the existence of a topological edge state.

4.2.3 Example: the Jackiw-Rebbi interface state

In this section, we will study a famous example of topological interface, known as Jackiw-Rebbi interface [130]. Even if this effect stems from particle physics, it is nowadays more studied in condensed matter physics because there exist real implementations of this effect [64, 131], especially in topological photonics [132]. We consider a 2D massive Dirac Hamiltonian, which reads

$$H(\mathbf{q}) = \hbar\nu_f \mathbf{q}\cdot\boldsymbol{\sigma} + m\sigma_z \tag{4.19}$$

where ν_f is the Fermi velocity, m the mass of the particle, $\mathbf{q} = (q_x, q_y)$ is the 2D wavevector and $\boldsymbol{\sigma} = (\sigma_x, \sigma_y)$ is the Pauli matrix vector. As mentioned in previous chapters, the gap opens because of the σ_z term, and this gap is proportional to the mass. It has been shown that the corresponding Berry curvature reads

$$\mathcal{B}_z = \frac{\alpha^2 m}{2(m^2 + \alpha^2 k^2)^{3/2}} \tag{4.20}$$

with $\mathcal{B} = (0, 0, \mathcal{B}_z)$, meaning the Berry curvature is oriented perpendicularly with respect to the 2D wavevector $\mathbf{q}$. We remark that the sign of the Berry curvature is controlled by the sign of the mass. Thus, if we consider two half-spaces with opposite signs of the mass, they will be characterized by opposite Berry curvatures and opposite Chern numbers $\pm 1/2$ (the Chern numbers here can be different from 1, because the integration surface is not a closed manifold). The interface Chern number is the difference of these Chern numbers, and in this case it is equal to one. It means that the existence of one localized state is guaranteed at this interface. This configuration is particularly interesting, because it has an analytical

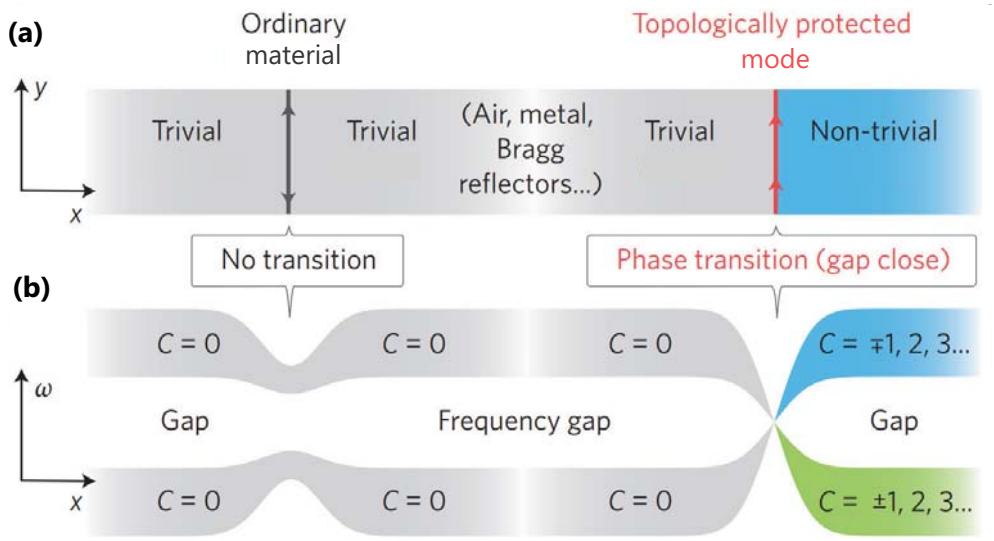

Figure 4.2: *(a) A topologically protected edge mode appears at the interface of systems with different topology (i.e. different Chern number). (b) Dispersion of systems (e.g. waveguides) with different topology cannot transition into each other without closing the energy gap. A topological phase transition happens on the right, but not on the left. Figures from [128].*

solution for the interface state [127, 130].

4.2.4 Topological photonics

The theoretical possibility to obtain one-way edge modes in photonics was proposed by Haldane in 2005 [133], and, as we see, it took three years to be published because it was too difficult to believe. Almost at the same time, topological effects started to be studied in polaritonics [114]. Quite rapidly after the initial proposal, Wang realized in 2009 a photonic analogue of the quantum Hall effect in a gyromagnetic photonic crystal [134], utilizing a square lattice, as shown in fig. 4.4.a, and breaking the time-reversal symmetry[3] by applying a magnetic field. As we see in the fig. 4.4.b, the edge state whose dispersion is shown in red, possesses a unidirectional group velocity $v_g = (1/\hbar)\partial E/\partial k$. This edge state is also isolated in energy from the bulk modes, hence exciting this mode will result in one-way propagation without the possibility for the particles to backscatter into another edge mode or bulk mode: this one-way edge mode is said to be topologically protected against backscattering. It allows the propagation in a unique direction even in presence of minor defects, which naturally appear in the growth of microstructures. This is shown in fig. 4.4.c: the authors excite the photonic crystal at the point A, and apply a magnetic field B perpendicular to the plane of the crystal. We observe that the mode is propagating to the right. Below, we see that the wave gets around the defect without any backscattering, and continues its propagation to the right. This effect has numerous applications for integrated photonics, such as optical insulators and topological lasers, the latter combining in a single component the laser and the topological insulator. Topological optical isolating behavior has already been demonstrated [135], and topological lasers have first been theoretically suggested [136]

[3] More details about symmetries in appendix B.

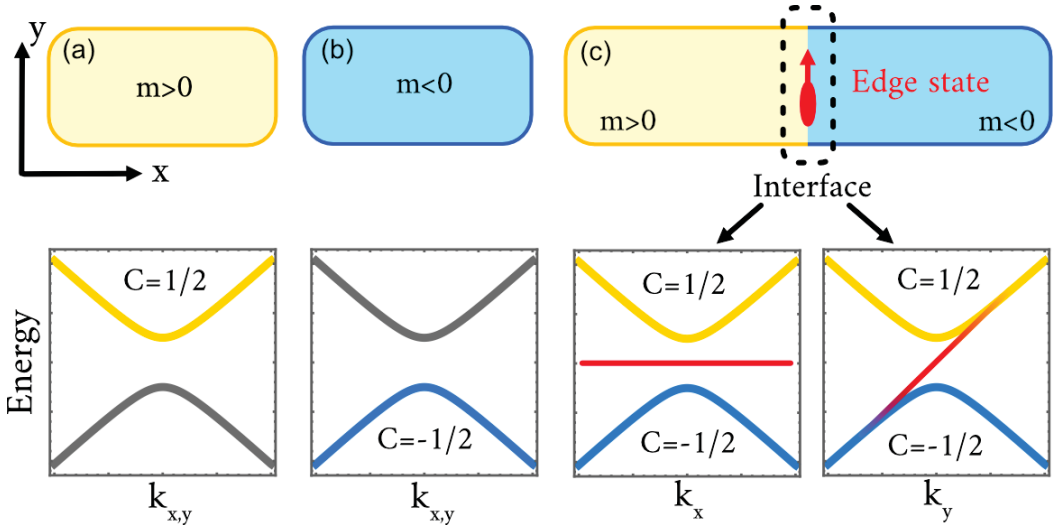

Figure 4.3: ***Scheme of the implementation of a Jacky-Rebbi interface state.*** *We consider a massive Dirac Hamiltonian (a) with a particle with a positive mass, exhibiting a positive Chern number (b) with a particle with a negative mass, exhibiting a negative Chern number. (c) We join these two spaces. The bulk-boundary correspondence says that the gap should close at the interface. The interface state (in red) is exponentially localized in the x direction, and is unidirectional in the y direction, due to its unique velocity in the dispersion along k_y.*

and experimentally [137] demonstrated in 1D, then demonstrated in 2D in the same year [138]. For the last two decades the studies of non-trivial topological structures, such as analogue graphene [139, 140, 141, 142], and their applications have exhibited an exponential growth [128, 129, 143, 144].

4.3 Metrics

4.3.1 Riemannian metric

A metric, as we can guess, allows to define the distances between different objects. Most of metrics used in Physics are Riemannian metrics, which is the reason why we will focus on this particular metric in this section. A Riemannian metric is a metric tensor field on a manifold[4] M, making the latter a Riemannian manifold [145]. The metric tensor $\mathbf{g}$ can be expressed in terms of coordinate differential forms [146]

$$\mathbf{g} = g_{ij} dx^i \otimes dx^j \tag{4.21}$$

where dx^i are infinitesimal real numbers and $g_{ij} = g_{ji} = \mathbf{g}(\partial_i, \partial_j)$. It allows also to define infinitesimal displacement ds^2, called elementary arc length, which reads

$$ds^2 = g_{ij} dx^i dx^j \tag{4.22}$$

[4]Definition of a manifold in Appendix B.2.

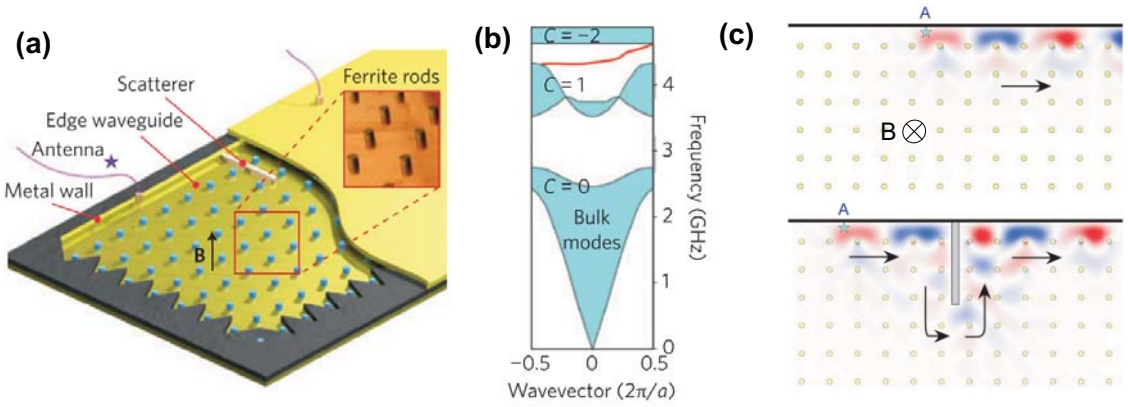

Figure 4.4: *(a) Experimental setup to observe a one-way edge state in a square gyromagnetic photonic crystal (b) Dispersion of the photonic crystal. One-way edge mode (in red) joining the second and third bands, which are topologically non-trivial. (c) Simulated field propagation of the one-way edge mode and its topological protection against backscattering in the presence of a defect. Figures from [134].*

The equivalence between these two forms is the reason why we use the elementary arc length in general. The latter allows to obtain all the metric components g_{ij} and to compute all the relevant geometric quantities from it.

4.3.2 Minkowski metric

For exemple, the well-known Minkowski metric is a Riemannian metric. Classical non-relativistic physics is based on a three-dimensional affine space on $\mathbb{R}$, which is called "space", and manipulates vectors $\vec{v}$ of the associated vector space $\mathbb{R}^3$. On this vector space, a very important structure is the scalar product of two vectors

$$\vec{u}.\vec{v} = u^1v^1 + u^2v^2 + u^3v^3 \tag{4.23}$$

where the u^i and v^i are the components of $\vec{u}$ and $\vec{v}$ in an orthonormal base. The scalar product describes all the geometry. It allows in particular to define the norm of a vector, and the angle between two vectors. Relativistic physics has some particularities :

- The space is not $\mathbb{R}^3$ anymore but $\mathcal{E}$ of dimension 4 : it unites time and space, and it is now called spacetime.
- The scalar product is not euclidean : for each point $p \in \mathcal{E}$, a vector space basis exists where it can be written

$$\vec{u}.\vec{v} = -u^0v^0 + u^1v^1 + u^2v^2 + u^3v^3 \tag{4.24}$$

More specifically, for each point $p \in \mathcal{E}$, one can provide [147] a bilinear form g (associated to the tangent vector space), which is symmetrical, not degenerate[5] and of signature

[5]Clear definitions are given in appendix B.1.

$(-,+,+,+)$:

$$g(\vec{u},\vec{v}) = -u^0v^0 + u^1v^1 + u^2v^2 + u^3v^3 \tag{4.25}$$

The bilinear form g defined above is called a metric tensor. Thanks to this metric, we can now define different types of 4-vectors[6]. If $\vec{u}$ is a non-trivial 4-vector, we observe that it can only be one of 3 types :

- a timelike $\iff g(\vec{u},\vec{u}) < 0$
- a spacelike $\iff g(\vec{u},\vec{u}) > 0$
- a lightlike $\iff g(\vec{u},\vec{u}) = 0$ with $(\vec{u} \neq 0)$

Another important feature of this metric, hence its name, is the measure of distance. If we consider two points P and P' infinitely close, we can associate an infinitesimal separation 4-vector $\overrightarrow{dP}$ and define the square of the distance by:

$$ds^2 = g(\overrightarrow{dP},\overrightarrow{dP}) \tag{4.26}$$

Given a coordinate system (x^α) near P, if dx^α is the difference of coordinates between P and P', then 4.26 can be written [148]

$$ds^2 = g_{\alpha\beta}dx^\alpha dx^\beta \tag{4.27}$$

For example, for a flat spacetime, the metric is given by : $ds^2 = \eta_{\alpha\beta}dx^\alpha dx^\beta$ where $\eta_{\alpha\beta}$ is the Minkowski matrix:

$$\eta_{\alpha\beta} = \begin{pmatrix} -c^2 & 0 & 0 & 0 \\ 0 & 1 & 0 & 0 \\ 0 & 0 & 1 & 0 \\ 0 & 0 & 0 & 1 \end{pmatrix} \tag{4.28}$$

i.e. in Cartesian coordinates the metric can be written

$$ds^2 = -c^2dt^2 + dx^2 + dy^2 + dz^2 \tag{4.29}$$

4.3.3 Quantum metric

Definition

The Quantum Metric (QM) is a gauge-invariant tensor which allows to compute the quantum distance between states

$$ds^2 = g_{ij}dk_idk_j = 1 - |\langle\psi(\mathbf{k})|\psi(\mathbf{k}+\boldsymbol{\delta}\mathbf{k})\rangle|^2 \tag{4.30}$$

where ds is an infinitesimal distance between two points in the reciprocal space, g_{ij} is the QM term, and $\psi(\mathbf{k})$ and $\psi(\mathbf{k}+\boldsymbol{\delta}\mathbf{k})$ are the two states. We remark that if these two states are the same, the distance is equal to zero, but if they are orthogonal, the distance is maximal, equal

[6] Meaning a vector with 3 spatial components and 1 time component.

to one. In our case, the states of our system will correspond to the polarization of light, that we can experimentally extract from a cavity. A distance $ds^2 = 1$ at a particular point in the reciprocal space means that at this point the polarization changes abruptly to orthogonal if we move by $\boldsymbol{\delta}\mathbf{k}$ from this point, and a distance $ds^2 = 0$ means that the polarization remains still.

It is also a quantity that has been studied in Quantum Information [149], in topological physics [150], in Moiré materials [151, 152, 153], in flat bands [154, 155] and more specifically in the study of superfluidity in flat band systems [156, 157, 158] by Päivi Törmä. For instance, the square root of the Quantum Metric appears as a fundamental criterion to understand the stability of Bose-Einstein condensates [159]. What will interest us more in this thesis is the possibility to describe interband transitions between two quantum levels with the QM. Indeed, it has been shown that the QM allows the description of small nonadiabatic corrections to the Anomalous Hall Effect [160]. As we will see in the next chapters, the QM term can even dominate the dynamics in non-Hermitian systems [161], and also totally describe the semiclassical trajectories of a wavepacket [162]. The interest for the QM stems also from the fact that its experimental measurements have been recently achieved in microcavities, in Hermitian [56] and non-Hermitian [163] systems.

Relations between Quantum Metric and Chern number

It has been proved relatively recently that many properties of the Chern number and the QM are linked [164, 165, 166]. For instance, let us consider a 2D parameter space, such as a 2D reciprocal space formed by k_x, k_y. The Chern number C is the integral of the Berry curvature $\mathcal{B}$

$$C = \frac{1}{2\pi} \iint \mathcal{B}(k_x, k_y) dk_x dk_y \tag{4.31}$$

and the quantum volume vol_g is the volume of the parameter space computed by the metric, and is defined by

$$vol_g = \int \sqrt{\det(g)} dk_x dk_y \tag{4.32}$$

where $\det(g) = g_{ij} g^{ij}$ is the determinant of the Quantum Metric tensor. In this case, a theorem says that [150, 164]:

$$vol_g \geq \pi \left| C \right| \tag{4.33}$$

which means that if there is no QM or if the QM is too small, it assured the non-existence of the Chern number. Moreover, it has been shown that one can compute the Berry curvature from the QM [167, 168]. The relation reads

$$\mathcal{B}^2 = 4 \det(g) = 4 g_{ij} g^{ij} \tag{4.34}$$

One result of this equation is that there is more information in the QM than in the Berry curvature. Very recently the Quantum Metric has been shown to dictate the Chern number and the Winding number of Dirac Hamiltonian [166]. These works are the examples of the rising interest in the QM.

Chapter 5: Wavepacket dynamics

Contents

In the 5^{th} chapter, we investigate the dynamics of particles described as wavepackets. By exciting coherently two bands near a Dirac point, we experimentally demonstrate that the polariton wavepacket exhibits Zitterbewegung oscillations. It can be understood with a non-Abelian Yang-Mills theory, which couple the precession of the spin to the spatial dynamics. Then we introduce a previous work, describing the photonic anomalous Hall effect in the opposite regime, when a single band is excited adiabatically. Afterwards, we demonstrate that both of these regime can be described in a single formalism, taking the form of semiclassical equations using only static band parameters, namely the dispersion and the Quantum Metric. Following this, we present an experimental work about a spin-selective strong light-matter coupling regime which results in unusually strong optical nonlinearity

and a giant Zeeman effect, which allows to open a gap at the Dirac point in polaritonic systems, and which has direct applications in topological physics

5.1 Experimental investigation of a non-Abelian gauge field in a 2D perovskite photonic platform

5.1.1 Context

Electromagnetism is the first and simplest gauge theory, introduced in 1865 by Maxwell [169]. A gauge theory means that different configurations of the gauge potential yield similar observations. This inherent vagueness in the physical description gives us the choice about which formulation to use in a particular situation. We can use what is called a gauge transformation to switch from one description to another, and the underlying invariance is called a gauge invariance. Starting from a massive scalar field Lagrangian [170]

$$\mathcal{L} = (\partial^\mu \psi)^\dagger (\partial^\mu \psi) - m^2 \psi^\dagger \psi \tag{5.1}$$

which has a $U(1)$ symmetry, we can change the field as $\psi(x) \to \psi(x)e^{i\alpha}$, and the Lagrangian will not be changed[1].

Since the particle charges are scalars, the components of the vector potential commute with each other, forming the $U(1)$ group and making this gauge theory Abelian. Yang and Mills worked in 1954 [171] on the generalization of a gauge theory in more complicated groups, such as $SU(2)$ and $SO(3)$. It is important because those non-Abelian gauge theories allow to describe the weak and strong interactions: the strong interaction is described by the $SU(3)$ group, and the weak interaction by the $U(1) \otimes SU(2)$ group. Even if the $SU(2)$ gauge theory developed by Yang and Mills can not describe those interactions, it was important as a first non-Abelian gauge theory. Indeed, they replaced the scalar charge by a vector charge, the isospin, with the vector potential components being the Pauli matrices that do not commute.

More recently, experiments successfully implemented emergent[2] gauge fields [173], such as the Berry curvature [126], which can be interpreted as an analogue of a magnetic field in the momentum space. The evolution along a trajectory (real or momentum space) is associated with an additional Berry phase, which means topological physics can be seen as a the result of an emergent Abelian gauge field. Such gauge fields in real space have been already been demonstrated in photonics [174]. However, no realization of emergent non-Abelian gauge fields has been reported so far. A recent work discovered a mapping between the Rashba spin-orbit coupling [175] (SOC) for massive particles and a $SU(2)$ Yang-Mills non-Abelian gauge field [176]. Since the Rashba SOC has been already well studied and implemented in solid state physics [177, 178], this mapping allows the development of analogous non-Abelian gauge field theories in these systems. Rashba SOC for photons has been proposed

[1] See Appendix C for more details about gauge theory.

[2] "The term emergent is used to evoke collective behaviour of a large number of microscopic constituents that is qualitatively different than the behaviours of the individual constituents." [172].

theoretically [18, 179] and realized experimentally using microcavities, and more precisely using polaritons [55, 56].

5.1.2 Presentation of the system

In this work [54], together with the group of Prof. D. Sanvitto from the Institute of Nanotechnology at Lecce, Italy, we investigate experimentally a Yang-Mills vector potential with space-like components. We measure the transverse acceleration of a polariton wavepacket owing to the Yang-Mills force. A precession of the pseudospin corresponding to this force is established for the propagation of the wavepacket, and it corresponds (within our analogy) to a change color of quarks in the strong interaction. Indeed, the system of the equations for the trajectory of the wavepacket and the pseudospin precession is similar to the equations of classical "two-color" chromodynamics. It makes this experiment a simplified $SU(2)$ analogue of the strongly interacting quarks with possible direct measurements.

The system is composed of a 2D fluorine-based perovskite crystal embedded in a planar microcavity with a DBR at the bottom and a metallic layer at the top, as shown in fig. 5.1.a.b (see caption for more details). The cavity is relatively thick ($\simeq 7\ \mu m$), and the cavity modes have a quality factor of $Q_f \simeq 1000$. As mentioned in chapter 2, the quantization of the wavevector k_z gives rise to a series of 2D modes, whose dispersion is parabolic in the case where $k_{x,y} \ll k_z$. Aformentioned, a non-Abelian gauge field requires a vector charge, which is in our case given by the polarization of light. The pseudospin polarization of light, whose components are determined by the Stokes vector, are directly given by the polarization degrees. As we have seen in chapter 1, the three components of the pseudospin $\mathbf{S}$ read [1]

$$S_1 = \frac{I_V - I_H}{I_V + I_H}, \quad S_2 = \frac{I_D - I_A}{I_D + I_A}, \quad S_3 = \frac{I_R - I_L}{I_R + I_L} \tag{5.2}$$

where H/V means horizontal and vertical, D/A means diagonal and antidiagonal, and R/L means right and left circular polarization. The microcavity displays a series of doublet, namely the TE and TM modes. The spin-orbit coupling comes from the energy splitting between these two modes at $k \neq 0$, where $\mathbf{k} = (k_x, k_y)$ is the in-plane wavevector. This energy splitting stems from the TE-TM splitting explained in chapter 2, where the TE and TM modes inherit different masses m_{TE} and m_{TM} as a direct consequence. The excitons of the perovskite slab are localized at 2.39 eV, and are strongly coupled with the TE and TM photonic modes of the cavity, giving rise to exciton-polariton modes. The large Rabi splitting of 208 meV allows to obtain polaritons at room temperature [180]. The fluorine part of the perovskite crystal changes the symmetry of the latter and gives rise of a strong linear birefringence. The experimental dispersion of the cavity is given in fig. 5.1, in the k_x direction with $k_y = 0$ in the panel c, and in the k_y direction with k_x direction in the panel d. Moreover, we can see in these panels that a given doublet is separated from its neighbour by 50 meV, owing to the thickness of the cavity. Indeed, we have shown in the chapter 2 that the separation between cavity modes is proportional to the inverse of the thickness of the cavity: $\Delta\nu \propto 1/L$, meaning a thick cavity results in a large number of modes in an energy

window. As we have seen[3], a polarization doublet of modes in presence of TE-TM splitting and linear birefringence can be modeled by an effective Hamiltonian written on the circular polarization basis

$$H_{eff} = \begin{pmatrix} E_0 + \frac{\hbar^2 k^2}{2m} & \beta_0 - \beta k e^{-2i\varphi} \\ \beta_0 - \beta k e^{2i\varphi} & E_0 + \frac{\hbar^2 k^2}{2m} \end{pmatrix} \tag{5.3}$$

with E_0 the energy of the modes at $k = 0$, $m = m_{TM} m_{TE}/(m_{TM} + m_{TE})$ the average mass, k is the norm of the in-plane wavevector $k = |\mathbf{k}| = \sqrt{{k_x}^2 + {k_y}^2}$ and φ is the angle of propagation defined by $k_x = k\cos\varphi$ and $k_y = k\sin\varphi$. β is the strength of the TE-TM splitting and β_0 is the birefringence term. The TE and TM modes cross in two points in the 2D reciprocal space, at $\mathbf{k}_D = (\sqrt{\beta_0/\beta}, 0) = (\pm 4.48\ \mu m^{-1}, 0)$, as shown in the fig. 5.1.c, giving rise to two Dirac points. The fit of the experimental data with the effective Hamiltonian gives $E_0 = 2.1415\ eV$, $m = 2.4 \times 10^{-5} m_e$, $\beta = 2.5 \times 10^{-4}\ eV \cdot \mu m^2$, and $\beta_0 = 10\ meV$, m_e being the free electron mass.

A crucial point of this work [54] is the possibility to rewrite the Hamiltonian, in the vicinity of the Dirac points [18], as a Rashba-like Hamiltonian [175]

$$\hat{H}_R = \frac{1}{2m}\hat{\mathbf{p}}^2 + \alpha \cdot \hat{\mathbf{p}} = \frac{1}{2m}(\hat{\mathbf{p}} + m\alpha\boldsymbol{\sigma})^2 - m\alpha^2\sigma^0 \tag{5.4}$$

where σ^0 is the identity matrix, $\mathbf{p} = \hbar\mathbf{q}$ is the momentum, with $\mathbf{q} = \mathbf{k} - \mathbf{k}_D$ the wavevector starting to a Dirac point. $\boldsymbol{\sigma}$ represents the Pauli matrices vector and $\alpha = \sqrt{\beta_0\beta/2}$. The fig. 5.1.e shows the dispersion along the k_y direction but crossing the Dirac point. It displays the typical shape of a Rashba dispersion. The pseudospin texture of the eigenstate is shown in panel f [4], it comes from the polarization degree, as we remember from eq. 5.2. We remark that the pseudospin for the different modes is pointing in opposite direction (green and dark arrows), which confirms that the system is well described by the Rashba Hamiltonian at the Dirac point.

5.1.3 Link with the Yang-Mills theory

In this section we will see how the Rasbha spin-orbit coupling can be regarded as a particular case of a Yang-Mills field. Indeed, we can derive a non-Abelian Yang-Mills Hamiltonian starting from a general relativistic Yang-Mills Lagrangian for the matter field ϕ, which is coupled with a non-Abelian field $\mathbf{F}$ [171, 181]

$$\mathcal{L} = \frac{1}{2}(D_\mu\phi)\cdot(D_\mu\phi) - \frac{m^2}{2}\phi\cdot\phi - \frac{1}{4}\mathbf{F}_{\mu\nu}\cdot\mathbf{F}^{\mu\nu} \tag{5.5}$$

with $D_\mu\phi = \partial_\mu\phi + \eta\mathbf{A}_\mu \times \phi$ the covariant derivative carrying the coupling with the vector potential $\mathbf{A}$, proportional to the coupling constant $\eta = \hbar/2$. The summation variables μ and ν denote (t, x, y, z). We remark that the two first terms are similar to the eq. 5.1, but describing here a massive *spinor* field. The Yang-Mills field stems from the third term, and we remark the vectorial nature of the elements of the field strength tensor $\mathbf{F}_{\mu\nu}$, which make

[3] See the derivation of eq. 2.30 for more details.

[4] One can wonder why this texture is different from the "usual" Rashba texture, as in Appendix A. It is because here it is a cut at constant energy, whereas usually we show the field texture for all energies.

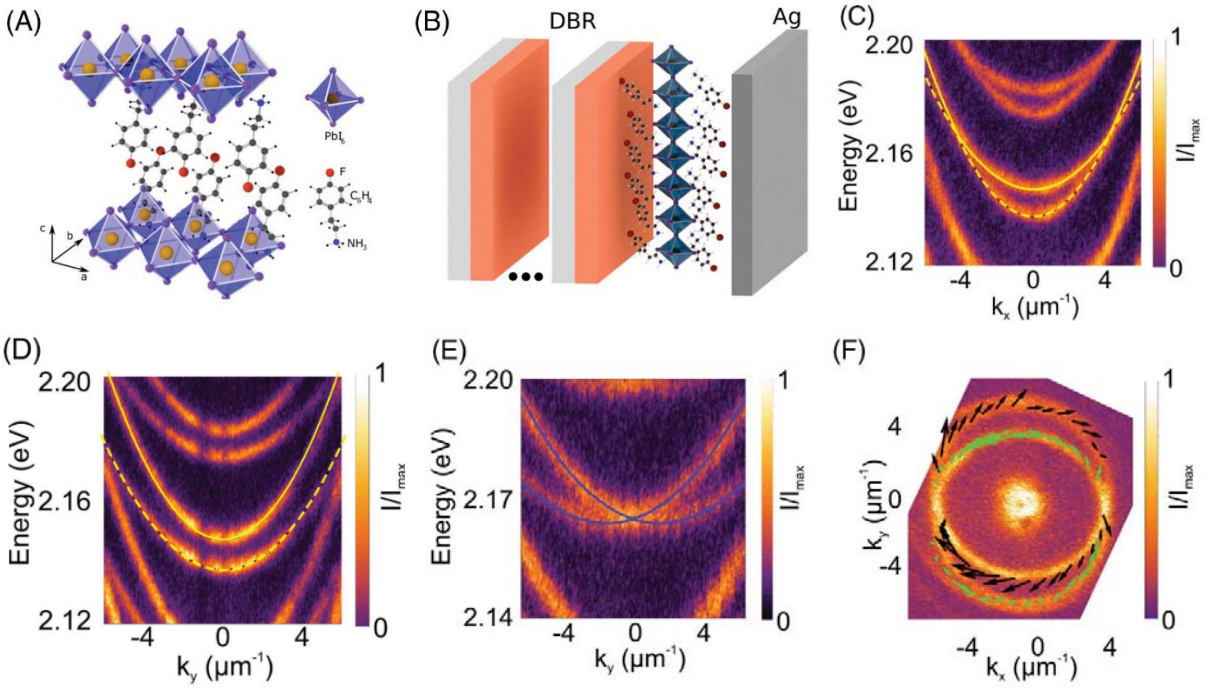

Figure 5.1: ***Experimental implementation of a non-Abelian gauge field.*** *A) Sketch of a PEAI-F (4-fluoro-phenethylammonium tetraiodoplumbate) 2D perovskite single crystal structure. B) Schematic representation of the microcavity sample. Perovskite flakes are embedded in an optical microcavity made by a DBR (seven TiO_2/SiO_2 pairs) and a 80 nm thick silver mirror. C,D) Experimental dispersions along k_x and k_y showing two Dirac points along k_x. E) Experimental dispersion along k_y for a fixed value of $k_x = 4.48\ \mu m^{-1}$ (crossing point) highlights the formation of a Rashba-type dispersion. Solid and dashed lines – dispersion fit with the parameters given in the main text. F) PL at the Dirac point energy together with the pseudo-spin orientation (arrows) obtained from polarisation measurments. The monopolar pseudospin texture around the Dirac points is another signature of the Rashba SOC.*

the Lagrangian gauge-invariant. Since our problem does not involve relativistic particles, we can separate the space and time components of the 4-vectors, which allows to write a non-relativistic Lagrangian which reads

$$L_{NR} = \frac{i\hbar}{2}\left(\dot{\phi}^\dagger\phi - \phi^\dagger\dot{\phi}\right) + \phi^\dagger\eta A_0^a\phi + \frac{1}{2m}[(\mathbf{p} - \eta\mathbf{A}^a\sigma^a)\,\phi]^\dagger\,[(\mathbf{p} - \eta\mathbf{A}^a\sigma^a)\,\phi] - \frac{1}{4}F^a_{\mu\nu}F^a_{\mu\nu} \tag{5.6}$$

A natural way to obtain the equations of motion from this point is to use the Euler-Lagrange equations

$$\frac{\partial\mathcal{L}}{\partial\phi} - \frac{\partial}{\partial x^\mu}\frac{\partial\mathcal{L}}{\partial\,(D_\mu\phi)} = 0 \tag{5.7}$$

with ϕ the matter field. It allows to obtain the following equation

$$i\hbar\frac{\partial\phi}{\partial t} = \left[\frac{1}{2m}(\mathbf{p} - \eta\mathbf{A}^a\sigma^a)^2 + \eta A_0^a\sigma^a\right]\phi \tag{5.8}$$

where the upper index a takes the values 0 to 3 and σ represents the Pauli matrices. The equation represents a spinor Schrödinger equation, describing the wavefunction of a particle with a vectorial charge, like a spin, coupled to a field acting on this charge. Hence the non-relativistic Hamiltonian of a massive particle coupled with a non-Abelian gauge field, determined by a vector potential, is expressed by

$$H_{YM} = \frac{1}{2m}(\hat{\mathbf{p}} - \eta\mathbf{A}^a\sigma^a)^2 + \eta A_0^a\sigma^a \tag{5.9}$$

The terms of the first part of this Hamiltonian can be compared with the terms of the Rashba-like Hamiltonian from eq. 5.4. It allows to identify the components of $\mathbf{A}$: $A_x^1 = A_y^2 = -m\alpha/\eta$. The last term corresponds to a Zeeman splitting which is zero in our case. We remark that the vector potential is constant, but the non-Abelian property of the field comes from the underlying symmetry group which is $SU(2)$ and not $U(1)$[5]. It results in a non-zero field strength, whose components read

$$F^a_{\mu\nu} = \partial_\mu A^a_\nu - \partial_\nu A^a_\mu - \eta\varepsilon^{abc}A^b_\nu A^c_\mu \tag{5.10}$$

It gives for the two non-zero components $F^3_{yx} = -F^3_{xy} = -m^2\alpha^2/\eta$, which couple the spatial degrees of freedom. Indeed, similar to the Lorentz force which is written as a product between the electric current and the field, the general formulation of the force given by a non-Abelian field links a unified spin-current vector J and the field strength tensor F. The equation of motion for the velocity $\mathbf{v}$ and spin (color) $\mathbf{s}$ of a classical relativistic particle coupled to the non-Abelian field read [54]

$$m\frac{dv^\mu}{d\tau} = \mathbf{J}_\nu \cdot \mathbf{F}^{\mu\nu}\,, \quad \frac{d\mathbf{s}}{d\tau} = -\eta\mathbf{A}_\mu \times \mathbf{J}^\mu \tag{5.11}$$

where $\mathbf{J}_\nu = \mathbf{s}v_\nu$ is the spin current. Solving these two coupled equations allows to obtain the particle trajectory and color dynamics in classical chromodynamics [182], studying generalized vector charges, in contrast with electrodynamics and its scalar charges. We note that

[5]The underlying symmetry group of theory of electromagnetism which is an Abelian gauge field is $U(1)$.

chromodynamics equations describing quark and gluon dynamics are based on $SU(3)$ gauge theory with three colors (spin-1), whereas the present implementation is SU(2), as in the original Yang-Mills paper [171] with two colors only (spin-1/2). The resulting acceleration components can be written under the form

$$a_x = -4m\alpha^2 J_y^3/\hbar^2\,,\quad a_y = 4m\alpha^2 J_x^3/\hbar^2 \tag{5.12}$$

with J_x^3 and J_y^3 the circular (spin-up/spin-down) components of the polariton spin current propagating along x and y, respectively. We notice that the acceleration is transverse, but, contrary to the Lorentz force which affects the charge current, here it acts on the circular component of the spin current instead. The strength of the force is given by $\alpha^2 = \beta_0\beta/2$, which is three orders of magnitude larger than in GaAs-based microcavities [56], owing to the strong anisotropy from the PEAI-F, giving a high value of β_0. We stress that the effective magnetic non-Abelian field we consider here differs crucially from a simple spin-dependent Lorentz force appearing in the presence of Abelian gauge fields different for the two spin components [55, 183], as the spin equations are not coupled in those cases.

5.1.4 Polariton propagation

To observe this effect, we use a key specificity of cavity polaritons, which is the possibility to resonantly[6] create a wavepacket with a well-defined pseudospin, centered on a specific state in reciprocal space, and then to study its real space evolution (this specificity will be used many times in this chapter). The first experiment we perform consists in exciting resonantly the vicinity of the Rashba Dirac point with a pulsed polarized laser, which in the language of Yang–Mills gauge theories corresponds to creating a color current. The energy of the laser is tuned to the Dirac point, while the wavevector is slightly detuned from it, providing a color (spin) current. The scheme of the experiment is shown in fig. 5.2.a. The blue, white and red arrows represent the σ^+, vertical and σ^- polarization states of the incident laser, respectively. The figure 5.2.b-d show the spatial intensity distribution together with the center of mass trajectories for three different excitation conditions: σ^+ ($s^1 = 0$, $s^3 = 1$), vertical ($s^1 = 1$, $s^3 = 0$) and σ_- ($s^1 = 0$, $s^3 = -1$). We can also see the difference between these three scenarios on the panel h, displaying the transverse profile of the total intensity. Ideally, the center of mass trajectory and circular polarization degree (charge vector) shown in fig. 5.2.i are expected to be reproduced theoretically (fig. 5.2.j) by the equation of motion 5.10, using the parameters m, α, β and β_0 extracted from the experiments and given above. The two colors in the figure correspond to the two s^3 spin components, σ^+ in red, and σ_- in blue, and they are strongly correlated with the trajectories. The non-Abelian magnetic-like field acts on the spin currents, which exhibit lateral deviations depending on their spin and velocity. Meanwhile, the spin itself changes depending on the propagation direction. This gives rise to opposite oscillating trajectories for red (σ^+) and blue (σ^-) wavepackets, often called Zitterbewegung oscillations [184, 185, 186]. Both effects are absent for colorless excitation (vertical polarization): the wavepacket propagates along a straight line. We note that other,

[6] Which means at a given energy: the laser is resonant with the band in energy.

qualitatively different types of behavior are possible for other parameters, including closed circular orbits, analogues of cyclotron orbits or Landau levels in an ordinary Abelian magnetic field. These represent an interesting subject for future studies.

The second experiment consists in creating an energy potential in the plane of the cavity and to launch the flow of neutral particles (vertically polarized polaritons, $s^1 = 1$, $s^3 = 0$) against the defect, as shown in fig. 5.3.A. This type of experiment in the high density regime allowed to demonstrate polariton superfluidity [90, 91, 93], the formation of oblique solitons [96], half-solitons [97], and of vortex anti-vortex pairs [187]. Here we work in the linear, low density regime, with polarised excitation at the Dirac point.

The polariton flow is in different conditions upstream and downstream of the defect. Upstream, the particle trajectory is strongly constrained by the defect potential and by the quantum pressure. The effects of the magnetic Yang-Mills force on trajectories is negligible compared to these two other contributions. However, the effects of the Yang-Mills field on the spin evolution, described by the second equation of chromodynamics 5.10, are not negligible. For upward and downward propagation, the gained s^3 components, proportional to J_y^1, have opposite signs. Opposite colors are thus generated above and below the defect, as shown in the sketch gig. 5.3.A. In the region after the defect, the magnetic Yang-Mills force becomes dominant, and the coupled chromodynamics equations 5.10 completely describe the particle trajectories and their spins. Due to the opposite colors (and therefore spin currents J_x^3) above and below the defect, the transverse force in eq. 5.10 is also opposite. This force brings the particles into the shadow of the defect. This convergent flow is clearly visible in fig. 5.3.B showing experimental spatial images of the total particle density. The results of chromodynamic simulations based on eqs. 5.10 corresponding to the wavepacket trajectories are shown as points, whose color shows the s^3 spin projection. The panel C presents the difference between the s^2 components (chosen as the new color basis), showing the best contrast due to the particular color dynamics. Dashed lines show the calculated particle trajectories (same as in panel B). It confirms that the density flows observed in total intensity in fig. 5.3.B are not due to a particular disorder pattern, but to the chromodynamics in presence of a single well-defined defect. We would like to underline that these curved trajectories have nothing in common with the recently observed anomalous Hall drift [56] of accelerated polariton wavepackets which is induced by the non-zero Berry curvature of the polariton bands when time-reversal symmetry is broken. Anomalous Hall effect caused by an emergent Abelian magnetic field in the *reciprocal* space occurs during the adiabatic motion of a wavepacket within a *single* band. On the opposite, the non-Abelian magnetic field studied in the present section acts in *real* space, and the oscillating trajectories in figs. 5.2 and 5.3 are due to beatings between *two* coherently excited eigenstates (spin precession, described by the second equation of chromodynamics).

5.1.5 Conclusion

Particle physics is the field where non-Abelian gauge theories found their application. The particles coupled with a Yang-Mills gauge field are the quarks. Their color determines their coupling to the field, and the excitations of the field are the gluons. In our analogue system,

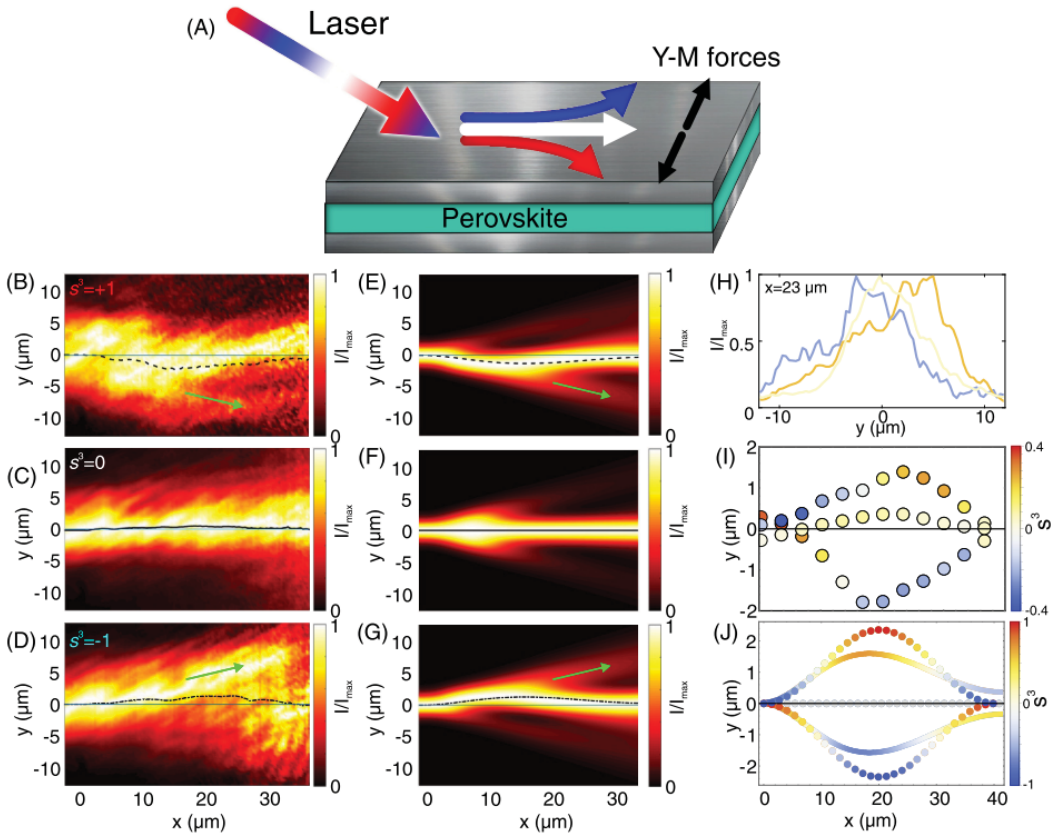

Figure 5.2: ***Polariton propagation in a non-Abelian field.*** *(a): Scheme of the experiment. A polarized laser creates a flow that is deviated by the gauge field, depending on the sign of the spin current. Polarization of the excitation: left-circular* ($s^3 = 1$)*, vertical* ($s^1 = 1, s^3 = 0$) *and right-circular* ($s^3 = 1$)*. (b-d) Spatial images of the total emission intensity for the three spin excitation conditions. Log-scale false color map is used for all images. The dashed lines are the center of mass trajectories. (b):* $s^3 = +1$*, the center of mass deviated downwards and then back. (c):* $s^3 = 0$*, the center of mass has no deviation along the in-plane propagation. (d):* $s^3 = -1$*, the center of mass deviated upwards and then back. (e-g): Calculated spatial images of the total emission intensity based on eq. 5.10 for three excitations* ($s^3 = -1, 0, 1$)*. (h): Transverse profiles of the total intensity at* $x = 20$ *μm (curve color corresponds to local* s^3 *of emission). (i) Experimentally measured center of mass trajectories extracted from panels (b-d) and spin dynamics for three excitation conditions* ($s^3 = -1, 0, 1$)*. Dot color corresponds to* s^3*. (j): Classical simulations of propagation trajectories and spin for the same initial conditions* ($s^3 = -1, 0, 1$)*. Dot color corresponds to* s^3*. Lines are extracted from the quantum simulations (e-g).*

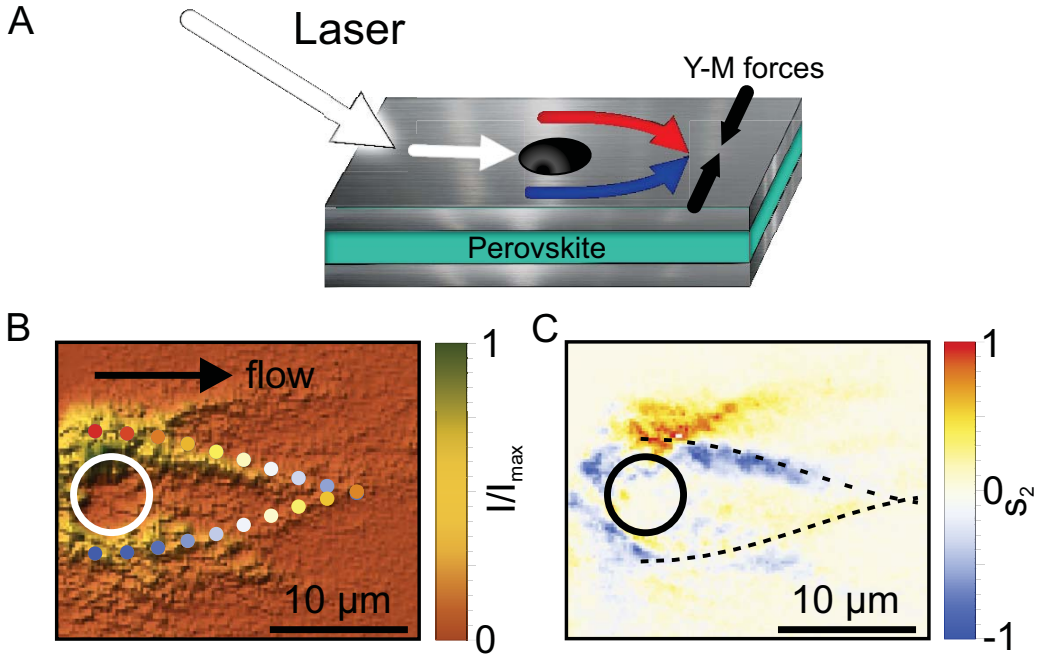

Figure 5.3: ***Chromodynamics behind a defect potential.*** *A) Scheme of the experiment. A linear polarized laser creates a propagating flow, which hits a potential and splits into circular-polarized flows deviated by the Yang-Mills field. B) Experimental image of the total emission intensity (false color). Colored dots show the theoretical results (color corresponds to the s^3 spin projection, the scale is the same as on fig. 3). The white circle shows the position of the potential defect. C) Experimental image of the difference between the diagonal polarization intensities (s^2). Dashed lines mark the theoretical trajectories.*

the field is constant and fixed externally, so there are no analogue gluons in this experiment yet. This allows to obtain a simpler, fully solvable configuration, with the advantage of the possibility of direct experimental measurements of the particle trajectories and of their isospin orientation, which is evidently impossible in the original, much more complex quark-gluon system. A very interesting outlook is provided by the polariton platform with its high non-linearities (spin-anisotropic polariton-polariton interaction). This could be used to access more complex dynamical situations, where charges self-consistently interact via the field they create. The role of vectorial charges could there be played by spinor topological charges of the polariton quantum fluid, such as half-vortices and half-solitons [97]. Both the magnetostatic-like experiment we are reporting and the outlook related to the use of polariton non-linearities make of our photonic system a valid and attractive simulation platform for quark QCD.

5.2 Semiclassical equations

5.2.1 Introduction

We will first consider the motion of a wavepacket in a crystal. The studies of lattices and their interaction with light and electrons have been extensive in the past century [15], and now form an important foundation of solid state physics. The motion of electron in a lattice described by a wavepacket has been developed by Wannier starting from 1937 [188, 189]. The electron is described by a wavefunction $\psi = \sum c_n \psi_n$, using Wannier function ψ_n, a position and a wavevector. The Hamiltonian describing the system is given by $H = \langle \psi(r,k) | H | \psi(r,k) \rangle$. To obtain the so-called semiclassical equations, we start from the Hamilton's equations

$$\frac{d\mathbf{r}}{dt} = \frac{\partial H}{\partial \mathbf{p}}, \quad \frac{d\mathbf{p}}{dt} = -\frac{\partial H}{\partial \mathbf{r}} \tag{5.13}$$

where $\mathbf{p} = h\mathbf{k}$ is the wavepacket momentum, and $\boldsymbol{r}$ is the position of its center of mass. The Ehrenfest's theory [190] demonstrates that the center of mass moves similarly to the corresponding classical Hamiltonian, if the latter is time independent [191]. Hence the wavepacket motion associated with a charge $-q$, in a perturbing Hamiltonian of the form $H_1 = -qV$ moves conforming to the equations

$$\mathbf{v}_g(\mathbf{k}) = \frac{\partial \mathbf{r}}{\partial t} = \frac{1}{\hbar}\frac{\partial E(\mathbf{k})}{\partial \mathbf{k}}, \quad \hbar\frac{\partial \mathbf{k}}{\partial t} = q\frac{\partial V}{\partial \mathbf{r}} = -q\mathbf{E} \tag{5.14}$$

with $\mathbf{v}_g$ the group velocity, and $\mathbf{F} = -q\mathbf{E}$ is the Lorentz force acting on the wavepacket. Also, $\hbar\mathbf{k}$ is an analogue of the classical momentum, and is called the crystal momentum of the wavepacket [15]. These two equations are called the semiclassical equations, which are valid in the adiabatic limit when the electron described by it is in an eigenstate and stays in this state during the propagation. It means that this theory does not allow interband transitions. The velocity and momentum at a given time t of an electron vary rapidly as it travels through the periodic potential of the crystal, so the crystal momentum is not directly given by the actual electron momentum and the wavepacket velocity should be interpreted as an average drift velocity. Also, the semiclassical equations are valid for a wavepacket size

larger than approximately ten times the lattice constant, so that it only feels the average effect of the lattice, but small enough in comparison with the length scale of the variation of the electric field. The name, semiclassical, stems from the fact that the periodic potential of the lattice is treated non-classically (via the quantum-mechanically calculated dispersion $E(\boldsymbol{k})$), but the electric field is treated classically.

5.2.2 Bloch oscillations

An important consequence of equations 5.14 is that the knowledge of the dispersion $E(\mathbf{k})$ and, in general, of the band structure, allows to obtain the motion of the particle. The Bloch oscillations, discovered by Bloch in 1929 [192], are a perfect and understandable example of non-trivial results from the semiclassical equations. We consider the 1D motion of an electron, described as a wavepacket in a single band, in a constant electric field E_{field}. In this case, the second part of the equation 5.14 reads

$$\frac{dp}{dt} = \hbar \frac{dk}{dt} = -eE_{field} \tag{5.15}$$

The trivial solution of this equation is

$$k(t) = k(0) - \frac{eE_{field}}{\hbar} t \tag{5.16}$$

The first part of equation 5.14 gives the group velocity

$$v_g(k) = \frac{1}{\hbar} \frac{dE}{dk} \tag{5.17}$$

with $E(k)$ the dispersion of the band considered. Using the tight-binding approximation, the dispersion of an electron in a 1D lattice (with only nearest neighbor couplings) can take the form

$$E(k) = \alpha \cos(ak) \tag{5.18}$$

with α is a constant and a the lattice parameter. The solution for the velocity and the position of the wavepacket is straightforward and reads

$$v_g(k) = -\frac{\alpha a}{\hbar} \sin(ak)\,, \quad x(t) = x(0) + \frac{\alpha}{eE_{field}} \cos\left(\omega_B t\right) \tag{5.19}$$

where $\omega_B = ae\left|E\right|/\hbar$ is the Bloch frequency at which the electron oscillates in the real space. Even if this effect was explained a long time ago, its experimental observation was challenging. Indeed, the impurities in natural crystals make this effect difficult to observe. Finally, the realization of semiconductor superlattices (large period of the artificial lattice a means large ω_B, with the period of the oscillations shorter than the carrier scattering times) at very low temperatures [193, 194] made the experimental measurement possible in 1992[7].

[7] This year is also the one of the observation of 2D polaritons, but more importantly, the year of my birth!

5.2.3 Anomalous Hall effect

At the end of the 19^{th} century, Edwin H. Hall discovered that opposite electric charges accumulate on the opposite sides of a conductor when a magnetic field was applied to a current in this conductor. This is now known as the Hall effect [195], one of the most important effects, and one of the most studied effects, in solid state physics. Two years later he discovered that this effect was an order of magnitude larger in ferromagnetic iron [196] than in nonmagnetic conductors[8]. This effect is called the Anomalous Hall effect (AHE), and it was, for a long time, far less understood than the "normal" Hall effect, and is still studied nowadays [197, 56]. A first attempt to describe theoretically the AHE was done by Karplus and Luttinger in 1954 [198], but a comprehensive explanation of this effect came 40 years later from topology, and more precisely from the Berry curvature concept [126]. Indeed, Niu and Sundaram re-expressed the semiclassical equations [199, 200] under the form

$$\hbar\frac{\partial \mathbf{k}}{\partial t} = \mathbf{F}\,, \quad v_g = \frac{\partial \mathbf{r}}{\partial t} = \frac{1}{\hbar}\frac{\partial E_n}{\partial \mathbf{k}} - \frac{\partial \mathbf{k}}{\partial t} \times \mathbf{B}_n(\mathbf{k}) \tag{5.20}$$

where $\mathbf{F}$ is the force, usually equal to $\mathbf{F} = -e\mathbf{E}$ in electronic systems, and B_n and E_n are the Berry curvature and the dispersion associated with the n^{th} band, respectively. We observe that there is a correction term contributing to the group velocity which is proportional to the Berry curvature of the band. This equation means that if an electron propagates along a band with a nonzero distributed Berry curvature, a lateral drift will occur. This model is valid in the adiabatic limit when the electron is in a single band. Here, contrary to topological insulators, global topology of the band is not required (e.g. nonzero Chern number). Only a local distribution of the Berry curvature is enough to observe the AHE.

5.3 Photonic anomalous Hall effect

We have introduced in chapter 4 the Quantum Geometric Tensor and its real and imaginary parts, named respectively the Quantum Metric and the Berry curvature. The extension of topological concepts from solid state physics to other classical or quantum systems has opened up possibilities for measuring the local geometrical properties of bands, not just the global properties (such as the conductivity measured in the quantum Hall effect). Several protocols have been proposed to measure the Berry curvature [201, 202]. Experimental reconstructions via indirect dynamical measurements have been reported [203, 204].

In their work, Gianfrate *et al.* [56] demonstrate a direct measurement of the Quantum Geometric tensor in the reciprocal space, which allows to obtain both the Berry curvature and the Quantum Metric. As we can see in fig. 5.4.a.b, these two quantities have a non-zero distribution over the 2D reciprocal space. They are also in good agreement with the theory, shown on panels e and f. In the same work, the polariton anomalous Hall effect (panels c and d) was experimentally observed, and the measured trajectory is in agreement with the theoretical calculations. Lastly, the panel g shows the intensity oscillations as a function of the polariton propagation the opposite polarization to that of the injected polaritons. Their

[8] Materials that are not attracted by a magnet.

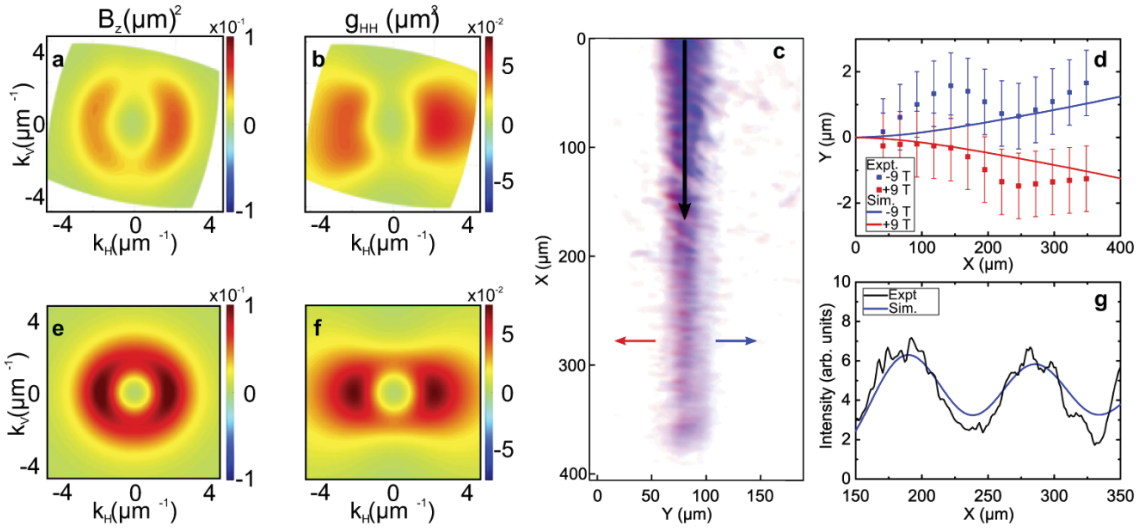

Figure 5.4: ***Quantum Geometric Tensor and polariton anomalous Hall effect.*** *(a) Experimental and (e) theoretical Berry curvature. (b) Experimental and (f) theoretical Quantum Metric. (c) Spatial distribition of emission at $+9$ T (red) and -9 T (in blue). (d) Center of mass trajectories for both initial conditions. (g) Intensity oscillations, whose contrast is determined by the Quantum Metric [56]. Figure from the review [62].*

contrast is determined by the non-adiabatic fraction, whose value is in agreement with the measured Quantum Metric.

5.4 Universal semiclassical equations based on the Quantum Metric

5.4.1 Introduction

General relativity is the first example of a geometrical theory of motion, where the particle trajectories are not governed by gravitational forces, but are found as the geodesics of the spacetime metric. In a completely different perspective, we have seen in last sections that the semiclassical theory of electron dynamics in solids was derived in the 1930s from quantum mechanics [205, 206], involving as a key element the wavevector-dependent group velocity. These equations have been corrected in 1999 [199] by Niu and Sundaram to include the impact of the Berry curvature and describe the anomalous Hall effect (AHE). The AHE was discovered in the 50s [198], but the deep understanding of the underlying physics and of its importance came with its description in terms of geometrical properties of the quantum space. The key hypothesis of the Niu-Sundaram [199, 200] equations is the adiabatic approximation, when the wavepacket remains in a single energy band, as in the original work of Berry [126]. The extension to the situation where several bands have comparable populations was done in Ref. [207], but using time-dependent components of the generalized Berry curvature tensor, which depend on initial conditions and not only on static band parameters. Multi-band Bloch oscillations with non-Abelian Berry curvature were recently studied in [208].

It is well understood that the Quantum Metric should appear in the description of tran-

sitions between quantum levels. For example, it allows to describe small non-adiabatic corrections to the AHE [209, 160, 210]. In some cases, the Quantum Metric was even found to dominate the dynamics. This occurs in systems with non-reciprocal directional dichroism [211] and also in strongly non-Hermitian systems in the vicinity of the exceptional points, where the evolution can never be adiabatic [161]. A situation of a particular interest occurs in spin-orbit-coupled systems [212, 176, 213] which can be described in terms of non-Abelian gauge potentials [214, 171, 181] with emergent vectorial charges [18, 179]. The resulting Zitterbewegung (ZBW) motion [215, 54] involves a coherent superposition of several bands. The ZBW is studied theoretically and experimentally in various electronic [216, 217, 218], atomic [219, 220, 221], and photonic systems [186, 222, 223, 224] including polaritons [185, 184]. This is an appealing situation for its description in terms of Quantum Metric, as noticed in [225], where the Quantum Metric was shown to be responsible for a contribution to the effective mass.

In this work [162], we derive semiclassical equations of motion in a two-band system using only the static band geometry encoded in the Quantum Metric. The solutions of these new equations are in complete agreement with the direct numerical solutions of the Schrödinger equations for all the cases we considered. They describe the AHE, traditionally attributed to the Berry curvature. They also describe the opposite limit, when the wavepacket is coherently distributed over the two bands, and in particular the ZBW motion induced by an emergent non-Abelian gauge field. We show that a wavepacket centered at $k = 0$ exhibits a circular trajectory in real space, with its radius given by the square root of the Quantum Metric. This quantity appears as a universal length scale, determining the uncertainty of the position of a particle involving several bands. It provides a geometrical origin of the Compton wavelength.

5.4.2 The model

We begin with the Hamilton's equations of motion for a wavepacket. Working with a 2-band system allows us to use the mapping to the pseudospin $\boldsymbol{S}$ interacting with an effective magnetic field $\boldsymbol{\Omega}$ [1, 5] (see 1^{st} chapter), with the Hamiltonian given by $H = -\hbar\boldsymbol{\Omega}\cdot\boldsymbol{S}/2$, and the associated geometry of the Bloch sphere (fig. 5.5). A general superposition of two eigenstates can be written as

$$|\psi\rangle = c_1\,|\psi_1\rangle + c_2\,|\psi_2\rangle\,, \tag{5.21}$$

with $c_1 = \cos\theta_s/2e^{-i\phi_s}$ and $c_2 = \sin\theta_s/2$, where θ_s and ϕ_s are the time-dependent angles, giving the orientation of the pseudospin on the Bloch sphere. The equations of motion for the spatial degrees of freedom are therefore accompanied with the precession equation for the pseudospin describing the wavepacket distribution within the two bands:

$$\dot{\boldsymbol{p}} = -\frac{\partial H}{\partial \boldsymbol{r}}, \quad \dot{\boldsymbol{r}} = \frac{\partial H}{\partial \boldsymbol{p}}, \quad \dot{\boldsymbol{S}} = \mathbf{S}\times\boldsymbol{\Omega} \tag{5.22}$$

Here, $\boldsymbol{r}$ is the spatial coordinate of the wavepacket center of mass, $\boldsymbol{p} = \hbar\boldsymbol{k}$ is the center of mass momentum of the wavepacket ($\boldsymbol{k}$ is the center of mass wavevector). The wavepacket is considered as a classical point-like particle and its distribution over the bands is encoded

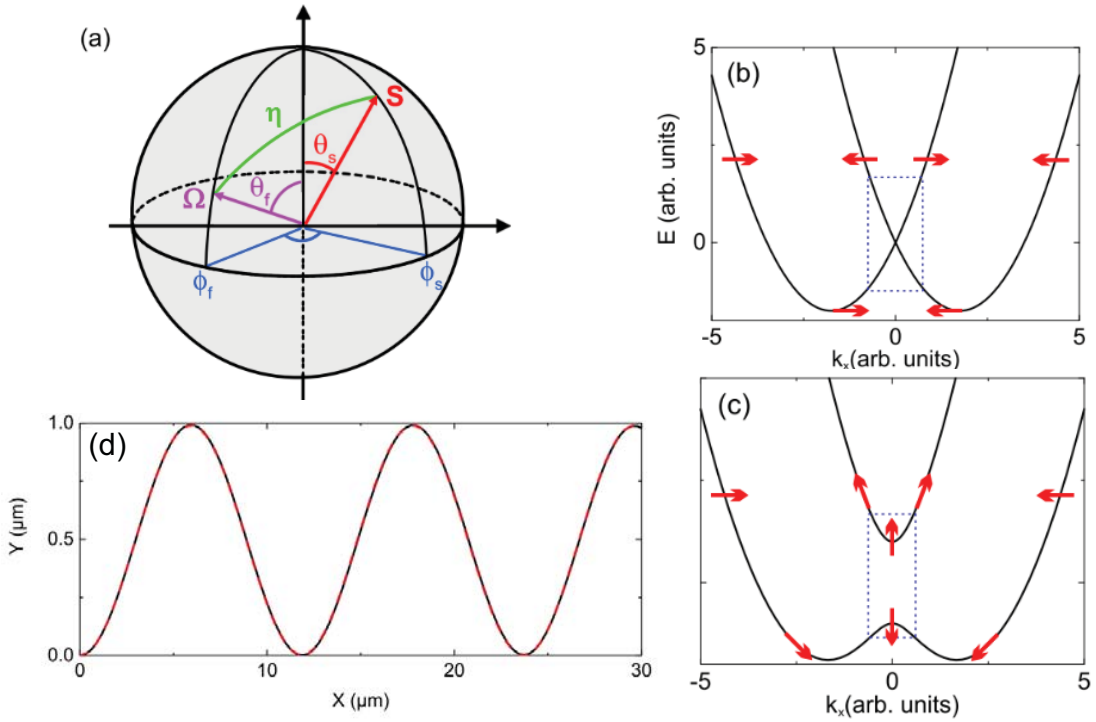

Figure 5.5: *(a) Bloch sphere representation showing the pseudospin* $\mathbf{S}$*, the effective field* $\mathbf{\Omega}$*, and their polar and azimuthal angles* θ *and* ϕ*. The angle between the spin and the field is* η*. b,c) Dispersion along* k_x *of the eigenmodes of the b) Rashba and c) Rashba+Zeeman Hamiltonians. The red arrows show the pseudo-spin orientation of the modes. Wave packet dynamics from Schrödinger equation (black solid line) and analytical solution of semiclassical Eqs. (5.28) and 5.29) (red dashed line) using the Rasbha Hamiltonian.*

in its pseudospin vector. At a given moment of time, the effective field is $\mathbf{\Omega}(\mathbf{k}(t))$ and the pseudospin is $\mathbf{S}(t)$, shown in fig. 5.5.a with violet and red arrows, respectively. While it is often possible to convert Hamilton's equations to geodesics equation in an abstract metric [226], our goal is rather to elucidate the role of the Quantum Metric, while keeping the other coordinates intact.

The first of eqns. 5.22 describes the acceleration of the wavepacket due to a spatial gradient of the potential. We will rather focus on the second of eqns. 5.22, describing the group velocity. The Hamilton's function H corresponds to the energy $E = \langle\psi|\hat{H}|\psi\rangle$ of the full wavepacket. It depends on the wavevector both directly, via the band dispersion $E_i(\mathbf{k})$, and indirectly, via the fractions $f_i = |c_i|^2$. This energy can be rewritten as $E = f_1E_1 + f_2E_2 = (f_1 + f_2)\bar{E} + (f_2 - f_1)\hbar\Omega$ where $\bar{E}$ is the spinless part of the dispersion and Ω is the absolute value of the effective field.

We characterize the pseudospin $\mathbf{S}$ and the effective field $\mathbf{\Omega}$ by the respective spherical coordinates θ_s, ϕ_s and θ_f, ϕ_f (see fig. 5.5.a). The fractions f_i are determined by the distance between these two vectors on the Bloch sphere η as $f_{1,2} = (1 \pm \cos\eta)/2$, and this distance can be found from the spherical law of cosines. Indeed, the equation for the angle η given

by the spherical cosine law reads:

$$\cos\eta = \cos\theta_s\cos\theta_f + \sin\theta_s\sin\theta_f\cos\left(\phi_f - \phi_s\right) \tag{5.23}$$

The contribution to the spin-dependent part of the energy stemming from the wavevector dependence of the coefficients f_i can be found via the wavevector dependence of the spherical coordinates θ_f, ϕ_f of the effective field:

$$\frac{\partial f_i}{\partial k_j} = \frac{\partial f_i}{\partial \phi_f}\frac{\partial \phi_f}{\partial k_j} + \frac{\partial f_i}{\partial \theta_f}\frac{\partial \theta_f}{\partial k_j} \tag{5.24}$$

and the latter are determined by the metric part of the Quantum Geometric Tensor (QGT) [118]. This is our key idea: to use the Quantum Metric as the link between the angles on the Bloch sphere and the wavevectors. By definition, the Quantum Metric provides a link between the quantum distance ds and the distance in reciprocal space:

$$ds^2 = g_{k_i,k_j}dk_i dk_j, \tag{5.25}$$

with the Quantum Metric defined by

$$g_{ij} = \mathrm{Re}\left[\left\langle\frac{\partial\psi_1}{\partial k_i}\middle|\frac{\partial\psi_1}{\partial k_j}\right\rangle - \left\langle\psi_1\middle|\frac{\partial\psi_1}{\partial k_i}\right\rangle\left\langle\frac{\partial\psi_1}{\partial k_j}\middle|\psi_1\right\rangle\right] \tag{5.26}$$

The corresponding quantum distance for the displacement $d\eta$ on the Bloch sphere is $ds^2 = (d\eta)^2/4$. This allows writing

$$\frac{\partial\theta_f}{\partial k_i} = 2\sqrt{g_{k_ik_i}}\cos\zeta, \quad \frac{\partial\phi_f}{\partial k_i} = 2\sqrt{g_{k_ik_i}}\frac{\sin\zeta}{\sin\theta_f} \tag{5.27}$$

with ζ controlled by the evolution of the effective field with k_i as $\tan\zeta = \sin\theta_f(\partial\phi_f/\partial\theta_f)_i$. Ultimately, the equations of motion read:

$$\hbar\dot{\mathbf{k}} = -\frac{\partial E}{\partial \mathbf{r}}, \quad \dot{\mathbf{S}} = \mathbf{S}\times\boldsymbol{\Omega} \tag{5.28}$$

$$\begin{aligned}\hbar\dot{\mathbf{r}} &= \frac{\partial\bar{E}}{\partial\mathbf{k}} - 2\frac{\partial\hbar\Omega}{\partial\boldsymbol{k}}\left(\cos\theta_s\cos\theta_f + \sin\theta_s\sin\theta_f\cos\left(\phi_f-\phi_s\right)\right) \\ &- \hbar\Omega\sqrt{g_{\mathbf{kk}}}\frac{\left[\left(-\cos\theta_s\sin\theta_f + \sin\theta_s\cos\theta_f\cos(\phi_f-\phi_s)\right) - \sin\theta_s\sin(\phi_f-\phi_s)\sin\theta_f\left(\frac{\partial\phi_f}{\partial\theta_f}\right)\right]}{\sqrt{1+\sin^2\theta_f\left(\frac{\partial\phi_f}{\partial\theta_f}\right)^2}}\end{aligned} \tag{5.29}$$

In these expressions, the Quantum Metric $\sqrt{g_{\boldsymbol{kk}}} = (\sqrt{g_{k_x,k_x}}, \sqrt{g_{k_y,k_y}})^T$ is that of a single band (the lowest energy band of the doublet). We see that the Quantum Metric appears as a overall factor of the corresponding term, entering 5.29 together with Ω and thus completely determining the scale of the corresponding physical effect. The physical meaning of this term is the modification of the energy of the wavepacket due to its redistribution over the two bands with the rotation of the spin, and this is controlled by the Quantum Metric.

A similar system of equations can be derived from the Hamilton's equations for an arbitrary number of bands. As in the two-band case, the terms containing the Quantum Metric appear from the variation of the fractions $\partial f_i/\partial k_j$: the variation of the overlap integral is determined by the variation of the length of the corresponding geodesic curve, which is entirely determined by the product of the Quantum Metric $g_{\boldsymbol{k},\boldsymbol{k}}$ and the projection of the displacement δk_j on the geodesic's tangent vector, according to the well-known theorem from the differential geometry [227]. We leave this for future works.

Although this equation does not include the Berry curvature explicitly, it allows to recover the semiclassical equations of Ref. [199] with the Berry curvature terms in the adiabatic limit [162] (see section 5.4.4). In spite of being written only in terms of the Quantum Metric, it entirely describes the AHE drift, and allows to go far beyond it, as we shall show below. In other words, being derived from the Hamilton's equations 5.22 without any additional approximations, the equations 5.29 are valid up to arbitrary order in the field strength, being limited only by the requirement of wavepacket localization [228]. Another advantage of Eq. 5.29 is that they contain only the static properties of the bands. These equations could also be extended to account for a magnetic field by including it into the equations for the momentum and for the pseudospin dynamics 5.28 [229, 230].

If the Hamiltonian is such that the effective field remains for all k in the equatorial plane ($\theta_f = \pi/2$, $\partial\phi_f/\partial\theta_f = \infty$), as is the case for the massless Dirac, Rashba, Dresselhaus [231], and TE-TM [52] Hamiltonians, Eq. 5.29 is considerably simplified, reducing to

$$\hbar\dot{\mathbf{r}} = \frac{\partial E}{\partial \mathbf{k}} + \hbar\Omega\sqrt{g_{\boldsymbol{kk}}}\sin\theta_s\sin(\phi_f - \phi_s) \tag{5.30}$$

with $E = \bar{E} + \hbar\Omega(\cos\theta_s\cos\theta_f + \sin\theta_s\sin\theta_f\cos(\phi_f - \phi_s))$. In what follows, we consider a Rashba Hamiltonian extensively studied in electronics, spintronics, and photonics, both with and without a Zeeman field:

$$\hat{H} = \frac{\hbar^2 k^2}{2m} + \alpha\boldsymbol{k}\cdot\boldsymbol{\sigma} + \Delta\sigma_z \tag{5.31}$$

where $\boldsymbol{\sigma}$ is a vector of Pauli matrices, α is the Rashba magnitude, and Δ the magnitude of the effective Zeeman field. When $\Delta = 0$, the eigenvalues are $E_\pm = \hbar^2k^2/(2m) \pm \alpha k$, plotted in fig 5.5.b. Close to $k = 0$, the Hamiltonian is analogous to a 2D massless Dirac Hamiltonian, with α playing the role of the speed of light c. The bands have no distributed Berry curvature. A non-zero Zeeman field opens a gap at $k = 0$ (fig 5.5.c), making appear an effective mass $m_{eff} = \hbar^2\Delta^2/\alpha^2$ (equivalence with a massive Dirac Hamiltonian). The corresponding bands show a non-zero distributed Berry curvature (see next section). We are now going to consider the wavepacket motion in these two situations.

5.4.3 Results and Discussion

Crossing bands: Rashba SOC (Dirac cone)

The equation of motion 5.30 writes explicitly:

$$\dot{\boldsymbol{r}} = \left(\frac{\hbar k}{m} + \frac{\alpha}{\hbar}\cos(\phi_s - \phi_k)\sin\theta_s\right)\begin{pmatrix}\cos\phi_k\\ \sin\phi_k\end{pmatrix} + \Omega\sin\theta_s\sin(\phi_k - \phi_s)\begin{pmatrix}\sqrt{g_{k_xk_x}}\\ \sqrt{g_{k_yk_y}}\end{pmatrix} \tag{5.32}$$

where ϕ_k is the polar angle of the wavevector, to which the effective field is antiparallel ($\phi_f = \phi_k - \pi$). This equation contains only the orientation of the spinor θ_s, ϕ_s and the center of mass wavevector k. The first part of the group velocity contains the spin-independent parabolic dispersion and a spin-dependent contribution, with the propagation direction ultimately controlled by the current orientation of the spinor. The second part of this expression, which includes the Quantum Metric $g_{\boldsymbol{kk}}$, appears because of the explicit time dependence of the spinor. The x and y projections of the velocity are controlled by the corresponding projections of the Quantum Metric.

As an illustration, we consider the case without external fields ($\dot{k} = 0$), with $\boldsymbol{k} = k_0\boldsymbol{e}_x$ ($\phi_k = 0$), and the spinor $\boldsymbol{S} = S_z\boldsymbol{e}_z$ perpendicular to the effective field at $t = 0$, so $\theta_s = 0$. The wavefunction is projected equally on both bands, and the pseudospin precession frequency is $\Omega = 2\alpha k_0/\hbar$. In this case, the x projection of the group velocity is constant. The time-dependent trajectory reads:

$$\begin{aligned} x(t) &= \frac{\hbar k_0}{m}t \\ y(t) &= (1-\cos\Omega t)\sqrt{g_{k_yk_y}} = \frac{1-\cos\Omega t}{2k_0} \end{aligned} \tag{5.33}$$

because the Quantum Metric is $g_{k_yk_y} = 1/4k_0^2$. This oscillating motion due to the pseudospin precession is the ZBW effect. The magnitude of the oscillation along y is given by $\sqrt{g_{k_yk_y}}$, which acts as a fundamental characteristic length scale of the problem, as we will discuss more in details below.

To confirm our analytical results, we perform numerical simulations, solving the time-dependent 2D spinor Schrödinger equation

$$i\hbar\frac{\partial\psi}{\partial t} = \hat{H}\psi \tag{5.34}$$

with the Rashba Hamiltonian 5.31, taking a finite-size Gaussian wavepacket defined by $\psi_0 = \exp\left(-(\boldsymbol{r}-\boldsymbol{r_0})^2/2\sigma^2\right)\exp(i\boldsymbol{k_0}\boldsymbol{r})$ with a width σ in real space (and $1/\sigma$ in reciprocal space) centered at a wavevector k_0, with its spinor part given by $(1,0)^T$ (corresponding to $\theta_s = 0$) as an initial condition. We choose the simulation parameters typical for polaritonic systems [56]: $\alpha = 1$ meV/μm^{-1}, $k_0 = 1$ μm^{-1}, $m = 2\times10^{-5}m_0$ (m_0 is the free electron mass), $\sigma = 128$ μm. We can observe a truly excellent agreement with the analytical trajectory in a substantial time window, limited only by the transient nature of the ZBW due to the finite wavepacket size in numerical simulations [228].

As said in the introduction, the Rashba Hamiltonian can be described as resulting from

the action of a non-Abelian gauge field [212, 176, 213, 214] described by the Yang-Mills Lagrangian [171]. Within this picture, it is also possible to derive a semiclassical equation of motion, where the acceleration is the result of the action of a non-Abelian magnetic force acting on (pseudo)-spin currents, as recently measured in [54]. As shown in [162], the time derivative of Eq.5.32 gives an expression of the transverse acceleration in terms of the Quantum Metric, equivalent to the results of the Yang-Mills theory [176] (see section 5.4.5). This acceleration appears because of the precession of the spin, or, in other words, because of the interband transitions described by the Quantum Metric. This provides a microscopic mechanism behind the non-Abelian Lorentz force of the Yang-Mills field, which can be interpreted as being the consequence of the geometry of the underlying quantum space.

Anticrossing bands: Rashba + Zeeman (massive Dirac)

We now consider the Rashba Hamiltonian combined with a Zeeman term. The resulting bands are non-degenerate and show a distributed Berry curvature. A wavepacket accelerated in such a system can show either AHE or ZBW, or a combination of both effects, depending on initial conditions. figure 5.6(a-c) considers the acceleration by a spatial energy gradient 2×10^{-3} meV/μm for different initial conditions. We compare the center of mass trajectories obtained by solving the spinor Schrödinger equation 5.34 and the one obtained from the semiclassical equations of motion 5.29. The Zeeman splitting is $\Delta = 0.5$ meV, other parameters as above. Panel (a) demonstrates the AHE regime, with the initial condition corresponding to an eigenstate of the system (the lowest energy band at $k = 0$): the deviation along y is the AHE drift. The correspondence between the description of the AHE in terms of Berry curvature and the one based on the use of the Quantum Metric is explicitly shown in the next section. Panel (b) corresponds to the pure ZBW, with the initial condition corresponding to the equal fraction of both branches: $f_1 = f_2$. In this case, there is no AHE drift, because the effect of the Berry curvature is completely canceled by $f_1 - f_2 = 0$. Finally, panel (c) corresponds to a particular case of $f_1 - f_2 = 0.9$, allowing to observe both the AHE drift and the large oscillations due to the ZBW. Qualitatively similar results are obtained with a TE-TM SOC (see [162]) characterized by a double winding number and typical for photonic systems. The AHE has been recently measured in an optical system with TE-TM SOC and Zeeman splitting [56].

If we consider a wavepacket with zero intial wavevector and zero external force $\dot{k} = 0$, the effective field is completely determined by the Zeeman splitting: $\theta_f = 0$. If the spin of the initial wavepacket is in the plane $\theta_s = \pi/2$ (and $\phi_s = 0$ as an example), the third equation of motion 5.28 gives that the spin will remain in the plane ($\sin\theta_s = 1$) and rotate with an angular frequency Ω ($\phi_s = \Omega t$). The equation 5.29 gives:

$$\dot{x} = \Omega\sqrt{g_{k_xk_x}}\cos\Omega t, \quad \dot{y} = \Omega\sqrt{g_{k_yk_y}}\sin\Omega t \tag{5.35}$$

where the Quantum Metric at $k = 0$ is given by $g_{k_xk_x} = g_{k_yk_y} = \alpha^2/4\Delta^2$. These equations explicitly show the wavepacket rotation in real space, with a radius determined by the value of the Quantum Metric $R = \sqrt{g_{\boldsymbol{kk}}} = \alpha/2\Delta$, as illustrated in fig. 5.6(d).

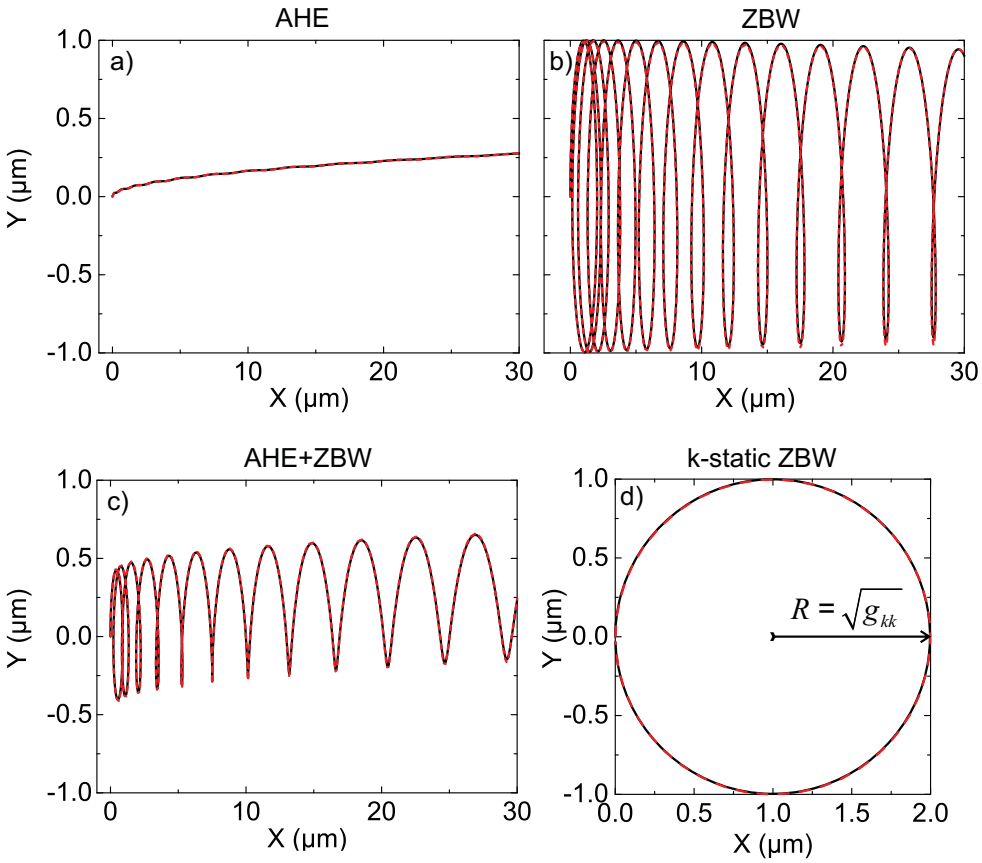

Figure 5.6: *Rashba+Zeeman Hamiltonian. Wavepacket dynamics from Schrödinger (black solid lines) and semiclassical (red dashed lines) equations: a) AHE (single-band initial excitation); b) ZBW (equal fractions of both bands); c) both effects together; d) cyclotron-like orbits at constant k (no potential gradient) with a radius determined by the metric.*

Our results show that the Quantum Metric provides a characteristic length scale $l = \sqrt{g_{max}}$ for the semiclassical behavior. This is best seen with the example of the Dirac equation, where the value of the Quantum Metric at $k = 0$ is

$$\sqrt{g_{kk}} = \frac{\hbar}{mc}, \tag{5.36}$$

which is the well-known Compton wavelength λ_C of the electron, determining a universal length scale in Physics. Indeed, it enters the expressions for the classical electron radius, the Bohr radius, the electron-proton scattering cross-section, and even determines the Planck length. We note that the full Dirac equation contains 4 components, and the Quantum Metric associated with both the particle-antiparticle and the spin degrees of freedom is the same, determined by the relativistic effects.

The physical meaning of the Compton wavelength can be understood with the Quantum Metric. Qualitatively, it limits the precision of the measurement of the electron's position. Indeed, scattering of a photon with the wavelength λ_C brings the electron into a 50% electron-positron superposition, corresponding exactly to the case of fig. 5.6(d): the electron's center of mass exhibits a cyclotron motion with the radius $R = \sqrt{g_{kk}(0)} = \lambda_C$. This rotation is what determines the uncertainty of its position. Even for Hamiltonians which do not have a single length scale, the Quantum Metric still can be used to determine the scales of the ZBW at rest or at high velocities, changing from the Compton to the de Broglie wavelength [216, 217]: indeed, $\sqrt{g_{kk}} \sim 1/k = \hbar/p$ at large k.

The maximal value of the trace of the Quantum Metric is an important physical quantity. This maximal value determines the extension of the metric in the parameter space, that is, the characteristic scale at which the changes occur (for example, level crossing), because the integral of the Quantum Metric (approximately, the product of the maximal value and the extension) is often quantized, representing a topological invariant [165] similar to the Chern number. It determines both the maximal amplitude of the ZBW oscillations and of the anomalous Hall drift (even though the latter is an integral quantity). It determines the spatial extension of the chiral edge state in topological insulators, controlling the minimal size of topological lasers and optical isolators. This will be a subject for future works.

5.4.4 Berry curvature and Quantum Metric.

The one-to-one correspondence between the Berry curvature and the Quantum Metric in two-band systems was discussed in Ref. [167, 150, 168], and this discussion was extended to three-band systems in [232]. Given the existence of such mapping, it is therefore natural that it is possible to write the semi-classical equations using either the Berry curvature or the Quantum Metric. Here, we demonstrate that the Berry curvature term responsible for the AHE drift gives exactly the same contribution to the transverse group velocity as the term written in the equation using the Quantum Metric.

In the particular case of the Rashba SOC with the Zeeman splitting we consider as an example, the AHE drift occurs in the y direction. Therefore, we need to study the y projection of the group velocity. To establish the equivalence between the equations with the Berry

curvature, containing the time derivative of the wavevector dk_y/dt and the semi-classical equations with the Quantum Metric, we will use the description of the non-adiabaticity by the Quantum Metric.

We begin by providing the explicit expressions for the Berry curvature and the Quantum Metric for the Rashba/Zeeman Hamiltonian, equivalent to the massive Dirac Hamiltonian. The Berry curvature reads:

$$B_z = \frac{\alpha^2 \Delta}{2\left(\Delta^2 + \alpha^2 k^2\right)^{3/2}} \tag{5.37}$$

and the Quantum Metric reads

$$g_{k_x,k_x} = \frac{\alpha^2\left(\Delta^2 + \alpha^2 k_y^2\right)}{4\left(\Delta^2 + \alpha^2 k^2\right)^2}, \quad g_{k_y,k_y} = \frac{\alpha^2\left(\Delta^2 + \alpha^2 k_x^2\right)}{4\left(\Delta^2 + \alpha^2 k^2\right)^2} \tag{5.38}$$

The term of the equation 5.29 of the main text responsible for the transverse anomalous Hall velocity (for a wavepacket characterized by a wavevector along x) reads:

$$\hbar v_y = \ldots + \hbar\Omega\sqrt{g_{k_y,k_y}}\sin\theta_s \sin(\phi_f - \phi_s) \tag{5.39}$$

In the quasi-adiabatic regime, $\sin\theta_s \approx \sin\theta_f = \alpha k/\hbar\Omega$ and $\sin(\phi_f - \phi_s) \approx \eta/\sin\theta_f$, which gives:

$$\hbar v_y = \ldots + \hbar\Omega\sqrt{g_{k_y,k_y}}\eta \tag{5.40}$$

The angle η here can be obtained from the wavevector change rate dk_x/dt using the fact that any non-zero change of the parameters of the Hamiltonian leads to a finite non-adiabaticity described by η and given by the Quantum Metric along the wave vector evolution direction [160, 233]:

$$f_{NA} = \frac{g_{k_x,k_x}}{\hbar^2\Omega^2}\left(\frac{dk_x}{dt}\right)^2 \tag{5.41}$$

This non-adiabatic fraction is linked with the angle between the spin and the effective field η as $f_{NA} = \eta^2/4$. This allows us to transform the expression obtained using the Quantum Metric to the familiar expression with the Berry curvature:

$$\hbar v_y = \ldots + 2\sqrt{g_{yy}g_{xx}}\frac{dk_x}{dt} = B_z\frac{dk_x}{dt} \tag{5.42}$$

where we have used the identity

$$\sqrt{\det g} = \frac{B_z}{2} \tag{5.43}$$

valid for all 2-band Hamiltonians with a Berry cuvature of a constant sign [165]. The two approaches indeed give the same contribution to the transverse velocity.

5.4.5 Link with the Yang-Mills theory

We have seen in the beggining of this chapter that a general non-relativistic Hamiltonian of a massive matter field (quantum particle) minimally coupled with a non-Abelian gauge field determined by a vector potential A_μ^a reads [171, 181, 176]

$$H_{YM} = \frac{1}{2m}\left(\hat{\boldsymbol{p}} - \eta \boldsymbol{A}^a \sigma^a\right)^2 + \eta A_t^a \sigma^a \tag{5.44}$$

The coupling constant is $\eta = \hbar/2$ (the quantum of spin). We use upper number indices $0-3$ for Pauli matrices. Comparing this expression with the Rashba Hamiltonian (eq. 5.31), one sees that only two components of the vector potential are non-zero: $A_x^1 = -m\alpha/\eta$, $A_y^2 = -m\alpha/\eta$. The non-Abelian nature of the field makes that the constant vector potential nevertheless gives rise to non-zero field strength tensor. In the case of Rashba SOC, the only non-zero components are $F_{yx}^3 = -F_{xy}^3 = -m^2\alpha^2/g$, where $g = \hbar/2$ is the Yang-Mills coupling constant (upper indices $0-3$ correspond to Pauli matrices). This non-zero field is responsible for an analogue of a Lorentz force for a non-Abelian gauge field. The Yang-Mills theory thus allows to predict an analogue of a transverse force acting on a spin current in the Rashba Hamiltonian. This force is proportional to the field strength and to the spin current, as can be seen from the second Newton's law

$$m\, dv^\mu/d\tau = \boldsymbol{J}_\nu \cdot \boldsymbol{F}^{\mu\nu} \tag{5.45}$$

The corresponding acceleration is ultimately found as $a_x = -2m\alpha^2 J_y^3/\hbar^2$, $a_y = 2m\alpha^2 J_x^3/\hbar^2$, where J_x^3, J_y^3 are the circular (spin-up/down) components of the spin current propagating along x and y respectively.

We will now compare the predictions of the Yang-Mills theory with those of the semi-classical equations that we have derived. In the particular case where the external forces are absent, the first of the equations of motion 5.28 of the main text gives that the central wavevector of the wave-packet is constant: $\dot{\mathbf{k}} = 0$. The equation 5.29 of the main text is still time-dependent, so it can be derived once again to find an analogue of the second Newton's law, similar to 5.45. We consider a parabolic band extremum characterized by an effective mass m, and define the z-projection of the spin current as $\mathbf{J} = \hbar^2 \mathbf{q}_c \cos\theta_s/2m$, which allows writing

$$m\ddot{\mathbf{r}} = \sqrt{g_{\mathbf{kk}}}\frac{4\alpha^2 km}{\hbar^2}\mathbf{e_z} \times \mathbf{J} \tag{5.46}$$

making the metric appear explicitly in the expression for the non-Abelian magnetic-like Yang-Mills force. We can therefore conclude that the QM is at the heart of the microscopic mechanism behind the Lorentz-like transverse force acting on a spin current in the static non-Abelian gauge field described by Eq. 5.45.

The covariant derivative appears in the Lagrangian to ensure the fundamental principle of gauge invariance. But the physical mechanism associated with its microscopic effect is based on the fact that the group velocity in a spinor system necessarily includes the QM describing the interband transitions due to the spin dynamics.

5.4.6 Conclusions

We derived the semiclassical equations of motion for a wavepacket in a two-band system in terms of the static band parameters, in particular, the Quantum Metric. These equations describe universally the anomalous Hall effect, the Zitterbewegung motion, and every regime

in between. The Quantum Metric turns out to determine a universal length scale for all effects beyond the simple group velocity.

5.5 Giant effective Zeeman in a monolayer semiconductor

5.5.1 Introduction

We have seen in the 3^{rd} chapter that the time-reversal symmetry can be broken in polaritonic systems owing to a Zeeman splitting, meaning in presence of a magnetic field. We will present here a particular configuration where we can obtain a giant Zeeman effect. Monolayer Molybdenum diselenide ($MoSe_2$) presents a four-band massive Dirac system for studying spin and valley pseudospin dependent interactions between electrons, excitons, and photons [234, 235]. In the presence of an appreciable free carrier density, simple neutral exciton absorption evolves into two Fermi-polaron branches, repulsive and attractive [234, 235, 236, 237]. The monolayer then plays host to a Bose-Fermi mixture consisting of excitons dressed by electrons (or holes, for p-type doping). Strong coupling of these Fermi-polaron resonances to photonic microcavity modes has been demonstrated [234, 238]. Simplistically, the repulsive and attractive polarons correspond to a spin-triplet or spin-singlet interaction, respectively, between the two-dimensional electron gas (2DEG) and the constituent electron of the exciton [234, 235, 236]. In $MoSe_2$, subject to strict spin-valley locking[9] and chiral optical selection rules, this has the consequence of tying the 2DEG degree of spin polarization to the oscillator strengths of the polaron resonances in opposite photon helicities. The extreme example of this effect is when the 2DEG becomes fully spin polarized, leading to vanishing absorption of the attractive polaron in one photon helicity [235, 236].

It has recently been reported that when the Fermi level is significantly smaller than the trion binding energy, the attractive polaron may be adequately described as a three-body charged exciton, or trion [240, 241]. Although nominally the trion exists only in the strict single particle limit, in reality the transition between these two quasiparticle regimes is unclear, and likely depends heavily on the degree of exciton and carrier spatial localization over the monolayer, especially at low densities. This is particularly true in the case of nonequilibrium scenarios such as photoluminescence experiments, in which both species may coexist [241].

Valley Zeeman splitting of these excitonic complexes has been reported under application of strong out-of-plane magnetic fields (B-fields) [235, 242, 243]. However, translating the relatively large Zeeman splitting of a purely matter-bound excitation into a photonic mode splitting remains a fundamental challenge not only in opto-valleytronics [244], but also in topological photonics. Indeed, many topological states of light have been implemented in recent years [129], including using TMD exciton-polaritons [132, 245]. The ultimate goal of real topological protection against any type of disorder scattering and back-reflection requires time-reversal symmetry breaking [134, 128], with the size of the topological gap limited by the effective Zeeman splitting of the photonic modes. Large splittings are difficult to achieve at optical frequencies, and in the existing realizations either based on the use

[9] An interesting and clear paper to understand spin-valley locking in MoS2 [239].

of magnetic proximity effects [138] or on the matter-based Zeeman splitting of exciton-polaritons [246, 135], the topological gap was < 1 meV, too small to be clearly observable.

In our work [247][10], by harnessing many-body interactions in a 2-dimensional Bose-Fermi mixture, we realise a giant effective trion-polariton Zeeman splitting, over 5 times larger than the bare (uncoupled) trion splitting, and more than double the polariton linewidths, a crucial step towards elimination of unwanted coupling between chiral modes [248]. We moreover demonstrate giant effective non-linearity $\alpha \approx 0.2 \pm 0.05$ meV$\cdot\mu$m^2 for trion-polaritons under a magnetic field. This value is one order of magnitude larger than previously reported in TMDs [249, 238] and is based on an original mechanism involving free carrier valley relaxation and strong light-matter coupling. Large photonic non-linearities, as in this work, are crucial for classical, quantum and topological photonics [128, 129].

5.5.2 MoSe2 system

Together with the group of Prof. A. I. Tartakovskii from The University of Sheffield, England, we have studied a $MoSe_2$ monolayer on a 10 nm thick film of the ferromagnetic semiconductor europium sulphide (EuS) which coats a dielectric distributed Bragg reflector (DBR). Firstly, we characterize the $MoSe_2$ monolayer in the half-cavity, or bare flake, configuration, at temperature $T = 4.2$ K. fig. 5.7.a shows circular polarization resolved reflectance contrast (RC $= (R_0 - R)/R_0$, where R and R_0 are the reflectance from the $MoSe_2$ and adjacent EuS substrate, respectively) spectra from the sample under linearly polarized broadband illumination at out-of-plane magnetic field strengths $B = -8, 0, +8$ T. We observe, at $B = 0$ T, two clear absorption peaks attributed to the neutral exciton (X_{RC}) and trion (T_{RC}) at higher and lower energy, respectively. T_{RC} displays a significant spectral weight, indicating an elevated doping level of the flake. These two resonances may be similarly described as Fermi-polarons, sharing the fundamental principle of a neutral exciton being either bound (attractive interaction, trion-like) or unbound (repulsive interaction) to itinerant carriers [237, 234, 235, 236]. The energy separation between these peaks allows us to estimate the free carrier density as 10^{12} cm^{-2} (see Supplementary Note 1 of the article [247]) [236]. We attribute this relatively high carrier density to electron doping from the EuS film, which we expect to be highly charged owing to the deposition technique (see [247]) [250, 251]. Measuring photoluminescence (PL) using a continuous wave laser at 1.946 eV, only a single peak is observed, attributed to the trion. The absence of neutral exciton PL is consistent with the high doping level in the flake, as is the significant Stokes shift of ~ 6 meV observed between T_{RC} and T_{PL} (fig. 5.7.a) [234].

When $B = \pm 8$ T, T_{RC} is only visible in one circular polarization (fig. 5.7.a). Owing to its spin-singlet or intervalley nature, the trion absorption strength of σ^+ (σ^-) light depends upon the itinerant carrier density in the $-K$ ($+K$) valley. Therefore, the electron Zeeman splitting is sufficiently large at this temperature to fully spin polarize the 2DEG (fig. 5.7.b) (see section 5.5.5) [235, 236]. Achieving complete spin polarization of a 2DEG of such high density as here may point to itinerant ferromagnetism, in which transient domains of oppositely spin polarized electrons at $B = 0$ T evolve into a spatially correlated spin polarized

[10] Reproduced with permission from Springer Nature.

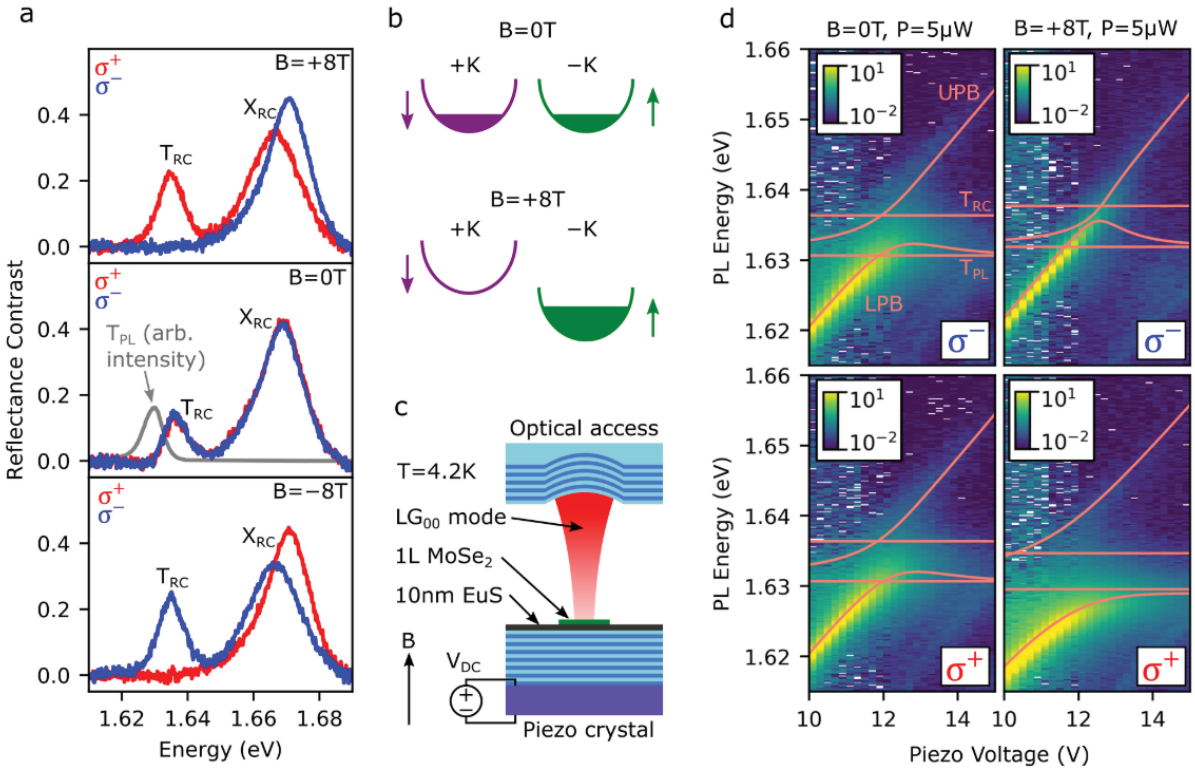

Figure 5.7: ***Excitations of a 2-dimensional electron gas strongly coupled to light in monolayer $MoSe_2$.*** *(a) Reflectance contrast $RC = (R_0 - R)/R_0$ from monolayer $MoSe_2$ (reflectance R on flake and R_0 on substrate) with raised itinerant carrier density at $T = 4.2$ K and $B = -8, 0, +8$ T. Two peaks are attributed to the neutral exciton (X_{RC}) and charged exciton or trion (T_{RC}). At high B-fields the trion absorption is completely suppressed in one or the other circular polarization of light. For comparison the trion photoluminescence T_{PL} signal at $B = 0$ T is also shown, revealing a Stokes shift of ~ 6 meV. Neutral exciton emission is absent owing to the raised doping level of the flake and rapid trion formation. (b) Sketch of the lowest conduction sub-bands of monolayer $MoSe_2$, in which the electronic spin and valley pseudospin ($+K$ or $-K$ valley of momentum space) are strictly correlated. These degrees of freedom are distinct in that the spin couples to magnetic field, while the valley pseudospin couples to light. Optical selection rules dictate that excitons and trions possess a $+K$ ($-K$) valley pseudospin when they couple, weakly or strongly, to σ^+ (σ^-) polarized photons. At $B = 0$ T, the 2DEG has zero net spin polarization. At $B = +8$ T, the 2DEG is completely spin polarized, causing the oscillator strength of the $-K$ valley trion to be suppressed owing to a lack of itinerant electrons in the $+K$ valley. (c) Schematic of the zero-dimensional open cavity structure used in this work. Applying a DC voltage to the piezo crystal decreases the cavity length (see [247]). (d) Cavity PL intensity maps (logarithmic scale) as the cavity mode is tuned through the trion resonances. Shown are the results at $B = 0$ T (left panels) and $B = +8$ T (right panels) in both photon emission helicities. The laser is linearly polarized. At $B = 0$ T, the spectra are essentially identical between both polarizations, while the near-unity spin polarization of the 2DEG at $B = +8$ T causes strong coupling to break down in σ^- polarization. A modified coupled oscillator model incorporating the trion-polariton Stokes shift was used to fit the UPB and LPB (overlaid orange curves). The energies of T_{PL} and T_{RC} in both polarizations (orange horizontal lines) are obtained directly or inferred from bare flake spectra at $B = 0$ T and $+8$ T. The UPB becomes progressively dimmer at higher energies owing to increasing absorption from the EuS film.*

state when $B > 0$ T [252, 253]. We additionally note that while EuS is ferromagnetic, we see no evidence of magnetic proximity effects in the sample (see Supplementary Note 3 of the article [247]).

For the next stage of the study, we incorporate the $MoSe_2$ / EuS structure into a tunable zero-dimensional microcavity (fig. 5.7.c), formed by introducing a downward facing top concave DBR into the optical path above the sample (as described in Ref. [254]). By control of the mirror separation using piezo nanopositioners, we tune the ground state longitudinal cavity mode (Laguerre-Gaussian LG_{00}) through resonance with both T_{PL} and T_{RC}, and perform cavity PL spectroscopy using a linearly polarized laser at power 5μW. At $B = 0$ T, we observe essentially identical PL spectra for both σ^+ and σ^- detection polarizations. As the cavity length is tuned, the observation of an anticrossing indicates strong light-matter coupling and defines upper and lower trion-polariton branches (UPB and LPB) separated by a Rabi splitting $\Omega_R \sim 9$ meV. We note here that the trion Stokes shift is comparable with the Rabi splitting, and therefore must be taken into account in order to precisely fit the polariton PL energies by going beyond the most basic coupled oscillator model (see next section). Indeed, while the anticrossing originates at the energy of T_{RC}, where cavity photons are most strongly absorbed, the polariton PL shows a finite Stokes shift causing both UPB and LPB emission to tend to the trion PL energy at vanishing photon fractions. Repeating the experiment at $B = +8$ T (fig. 5.7.d) reveals a larger anticrossing in σ^+, while the strong coupling regime breaks down in σ^- (Ω_R is smaller than the polariton linewidths and unresolvable), consistent with the weak oscillator strength of T_{RC} in σ^- (fig. 5.7.a top panel), and constituting observation of valley-specific strong light-matter coupling, in which the trion is simultaneously strongly coupled to σ^+ light while only weakly coupled to σ^- light.

5.5.3 Photoluminescence from polariton modes

We theoretically describe each circularly polarised trion-polariton mode using a standard two-coupled oscillators model. Since the broadening is significant, we include mode broadening by using an homogenous imaginary part for the bare photon and trion energies [255, 7]. The trion energies are determined by reflection experiments performed on the bare flake. The open cavity mode energy reads as $E_c = \alpha(V + V_0)$ where α the slope of the photonic mode energy versus the applied voltage V controlling the optical cavity length. The upper and lower polariton branch energies read as :

$$E^{\sigma\pm}_{U,LPB} = \frac{1}{2}\,\mathrm{Re}\left(E^{\sigma\pm}_{Ta} + E_c \pm \sqrt{\left(E^{\sigma\pm}_{Ta} - E_c + i\left(\Gamma_{Ta} - \Gamma_c\right)\right)^2 + (\Omega^{\sigma\pm})^2}\right) \qquad 5.47$$

where $E^{\sigma\pm}_{Ta}$ is the energy of the trion in absorption for a given spin component, $\Omega^{\sigma\pm}$ are the Rabi splitting values to be determined, Γ_c=0.6 meV and Γ_{Ta}=6 meV are the measured linewidth of the two modes, which we keep constant.

The trion fractions of the polaritons (square of the Hopfield coefficients) read as:

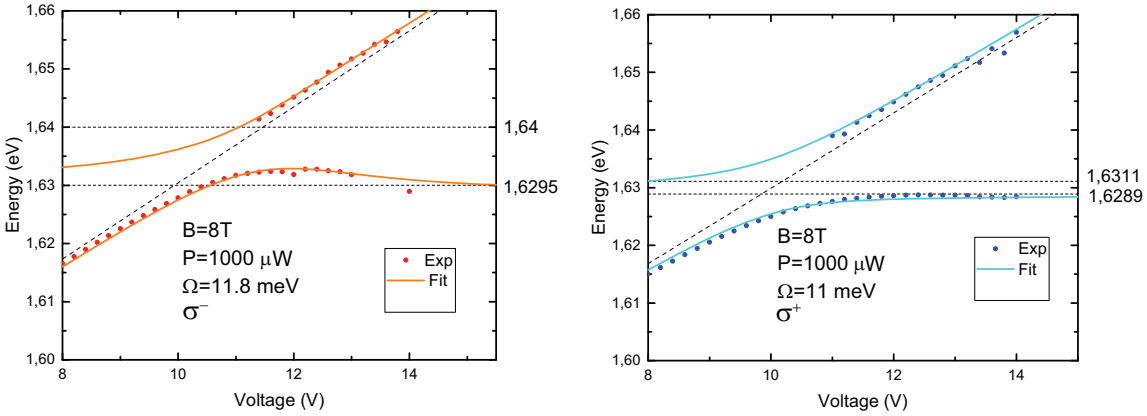

Figure 5.8: *Fit of the lower and upper polariton branches in two polarizations: dots – experiment, line – theory.*

$$\left|X_L^{\sigma\pm}\right|^2 = \frac{(\Omega^{\sigma\pm})^2}{\Omega^2 + \left(E_{UPB}^{\sigma\pm} - E_{Ta}^{\sigma\pm}\right)} \quad 5.48$$

$$\left|X_U^{\sigma\pm}\right|^2 = 1 - \left|X_L^{\sigma\pm}\right|^2 \quad 5.49$$

These energies are the one which could be measured in a transmission or absorption experiment. As for bare excitons in any media, polaritons demonstrate a finite Stokes shift. In the presence of finite random disorder, the Stokes shift is the difference between the energy of a resonance in absorption which corresponds to the maximum density of states, and in photoluminescence (PL) which corresponds to the lowest energy state of the inhomogeneous distribution of energy resonances. The Stokes shift is quite large in our sample owing to the raised itinerant electron density. Indeed, as the Fermi level increases above the bottom of the conduction band in $MoSe_2$, the Stokes shift will increase as the trion absorption feature blueshifts [234]. As shown in fig. 5.7.a, we have performed both reflection and PL measurements on the bare flakes which allows us to precisely determine the bare trion Stokes shift value, which is of the order of 6 meV. It reads

$$\Delta_S^{\sigma\pm} = E_{Ta}^{\sigma\pm} - E_{Te}^{\sigma\pm} \quad 5.50$$

where $E_{Te}^{\sigma\pm}$ is the trion energy in PL.

For polaritons, the Stokes shift is reduced with respect the case of the bare trion. The polariton Stokes shift should tend to the trion Stokes shift when the trion fraction of the polariton tends to 1. On the other hand, the Stokes shift should tend to 0 when the polariton becomes strongly photonic. We therefore choose to introduce phenomenologically a polariton Stokes shift value given by:

$$E_{U,L}^{\sigma\pm} = E_{U,LPB}^{\sigma\pm} - \Delta_S^{\sigma\pm} \left|X_{U,L}^{\sigma\pm}\right|^2 \quad 5.51$$

Using the above mentioned formula allows us to fit the voltage-dependence of the trion-polariton PL energies for different pumping powers and magnetic field strengths, with the Rabi splitting in each polarisation being the only fitting parameters. The results are shown in fig. 5.7.d and fig. 5.8. The agreement between the experiment and the phenomenological theory which we use is extremely satisfactory. The extracted dependence of the Rabi splitting values versus pumping for both spin components are shown on fig. 5.10.c of the main text.

5.5.4 Results

Fig. 5.9.a shows σ^+ and σ^- LPB PL versus piezo voltage at $B = 0$ and 8 T, where a giant effective Zeeman splitting is observed, exceeding 10 meV as cavity length decreases. The LPB Zeeman splitting is amplified by valley-specific strong light-matter coupling, whereby the near-unity spin polarization of the 2DEG at B = +8 T suppresses the oscillator strength of the trion in σ^- polarization, by transferring it to σ^+ polarization. Fig. 5.9.b compares the trion PL g-factor measured on the bare flake ($g = 3.9$) with that of the trion-polariton which is over 5 times larger ($g = 21.1$). While the LPB Zeeman splitting increases at higher voltages, this comes at the cost of increased polariton linewidths and reduced intensity. However, we note that the LPB Zeeman splitting exceeds the bare trion splitting for all B-field strengths and all cavity lengths studied here. This result is in marked contrast to the expected scenario in which the polariton Zeeman splitting is reduced relative to that of bare trion by the corresponding Hopfield coefficient [256].

Next, we show how the giant Zeeman splitting can be very effectively optically controlled. We fix $B = +8$ T and study the influence of incident laser power on the cavity PL. As can be seen in fig. 5.10.a, increased power reopens the anticrossing in σ^- which previously collapsed upon application of the B-field (fig. 5.7.d). Fig. 5.10.b shows trion-polariton PL spectra versus pumping power at fixed cavity length, where Ω_R grows in σ^- and correspondingly decays in σ^+, suggesting that non-resonant pumping efficiently transfers electrons between spin states (equivalently, between valley states). Here, qualitatively, electron-hole pairs are injected by the laser and bind to form excitons and trions on ultrafast timescales (sub-ps). The initial trion population will be highly valley polarized as the only free carriers available are from the spin polarized 2DEG, however, exciton and trion valley depolarization in $MoSe_2$ is extremely efficient (ps) owing to the Maialle-Silva-Sham (MSS) mechanism (confirmed here by transient ellipticity measurements, see Supplementary Note 4 of the article [247]) [254, 209]. Therefore, rapid intervalley scattering of trions followed by their radiative decay can result in a free electron remaining in the spin state anti-aligned to the external B-field. This means that each trion emission process results in partial transfer of electrons between spin-valley states. While trion valley relaxation occurs on ps timescales, the spin relaxation time for free electrons is $\sim$ 1000 times longer, of the order ns, as they are immune to the MSS mechanism and must undergo a large momentum transfer to scatter between spin-valley states. As such, trion intervalley scattering and subsequent photon emission can depolarize the 2DEG $\sim$ 1000 times faster than it can return to spin-polarized equilibrium. By embedding all of these processes into rate equations, we infer that laser power in the μW range is enough to fully balance the 2DEG spin populations and associated trion-polariton

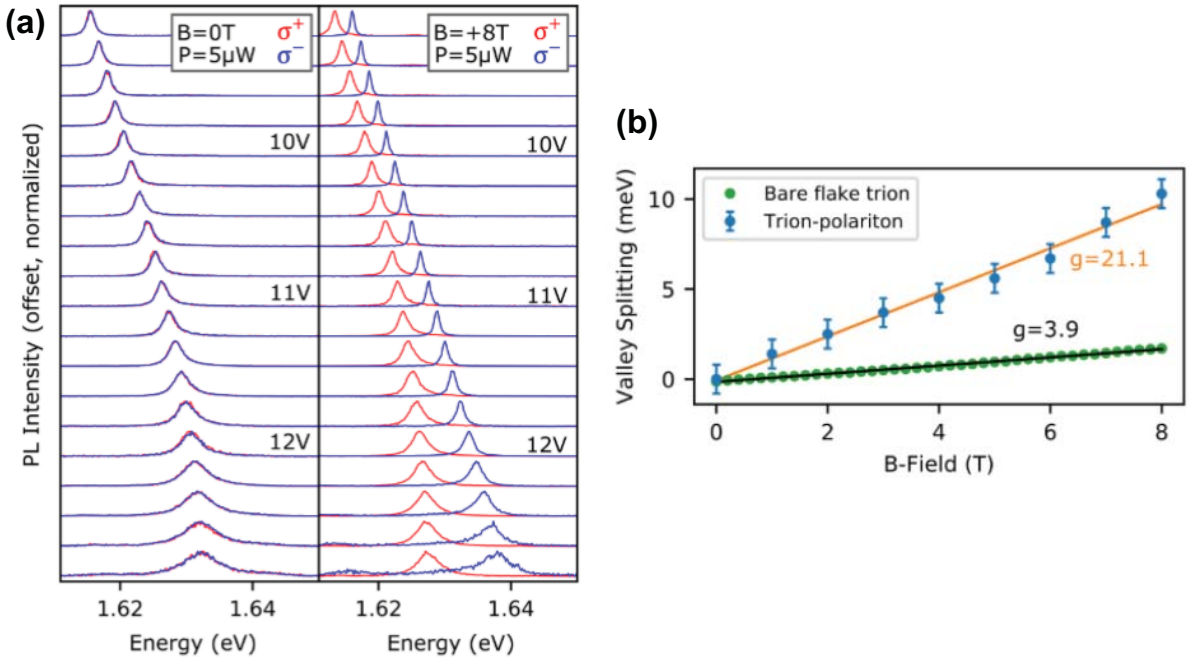

Figure 5.9: ***Giant effective trion-polariton Zeeman splitting.*** *(a) Cavity PL spectra at increasing piezo voltages (decreasing cavity length) for $B = 0$ T (left panel) and $B = +8$ T (right panel). A giant Zeeman splitting of the lower polariton branch (LPB) can be seen when the B-field is applied. Spectra normalization factors at $B = +8$ T are stable around ~ 1.2 from 9.2 V to 11.6 V, increasing to 6.6 at 12.8 V owing to onset of absorption from the EuS film, which reduces the cavity Q-factor and weakens σ^- intensity. (b) The maximum valley splitting of the trion-polariton LPB as a function of applied B-field strength. Here, we extract an effective maximum LPB Zeeman splitting at each 1 T B-field increment from our cavity fitting procedure. Error bars quantify the uncertainty arising from our cavity data fitting procedure indicated by orange curves in fig.5.7.d For comparison the valley Zeeman splitting of the bare (uncoupled) trion is also shown. The g-factors of the trion-polariton and bare trion are (21.1 ± 0.9) and (3.93 ± 0.04), respectively.*

Rabi splittings in opposite circular polarizations. Our simulations are shown in fig. 5.10.c (top panel) and are in excellent agreement with experimental data.

Lastly, we relate the computed exciton and trion densities to the energy shifts of the LPB when $B = +8$ T, and deduce effective LPB interaction strengths, in this case attractive for σ^- and repulsive for σ^+. The middle panel of fig. 5.10.c shows the LPB blueshift in σ^+ alongside the effective interaction strength, defined as $\alpha = \partial E^+_{LPB}/\partial n^+$ (see next section on the rate equation model), which corresponds to a repulsive interaction between same-spin particles since only σ^+ excitons can depolarize electrons when $B = +8$ T. The extracted value, $\alpha \approx 0.2 \pm 0.05$ meV$\cdot\mu$m^2 at $P = 5$ μW, is one order of magnitude larger than previously reported for trion-polaritons because it is based on a completely different mechanism [249]. It is based neither on oscillator strength or the Coulomb interaction between carriers, but instead on linear spin relaxation processes. The increase in the interaction strength at the lowest laser powers is accompanied by a marked increase in the effective trion-polariton Zeeman splitting, confirming their shared origin in the 2DEG spin dynamics (fig. 5.10.c bottom panel).

5.5.5 Rate equation model

In this section we present the system of rate equations we use in order to compute the free carrier spin polarisation versus pumping power. This model can be used, with different parameters, to describe the relaxation dynamics both in a bare flake and when the flake is embedded in the cavity. In this last case, the computed polarisation degree of carriers (free and those bound to excitons to form trions) allows to directly deduce the dependence of Rabi splitting values versus pumping, and to compare them with the experiment. The scheme of the processes taking place in the system is shown in fig. 5.11. When pumping starts, the resident carriers are assumed to be all spin-polarized up, because of the applied magnetic field. The pump creates excitons (exciton-polaritons), which bind with the free carriers to form trions (trion-polaritons) with correlated spin. Trions can depolarize a lot faster ($\sim$ ps) than free carriers ($\sim$ ns) because of the L-T spin-orbit coupling (Maialle-Sham mechanism[257, 209]). When these depolarized trions emit light via the exciton recombination and emission of the photon out of the cavity, the remaining free carriers have a reduced polarization. This reduced polarisation depends on the ratio between the trion (trion-polariton) decay time and the trion depolarisation time. The time needed for an electron spin to reorient parallel to the magnetic field is comparable with its depolarisation time ($\sim$ ns). Therefore, even with a small pumping (a few excitons per picosecond), the small number of trions formed by this process can efficiently depolarize a large fraction of free carriers.

The result is that, under optical pumping, we observe strong coupling in a cavity for both polarizations, because there are free carriers of both spins available in the system. The key point is that the effect of the injected exciton density on the Rabi splitting is amplified by the ratio $\tau_e^s/\tau_t^s \sim 10^3$.

Mathematically, the processes described can be modelled by rate equations involving free carriers N, excitons (exciton-polaritons) X, and trions (trion-polaritons) T:

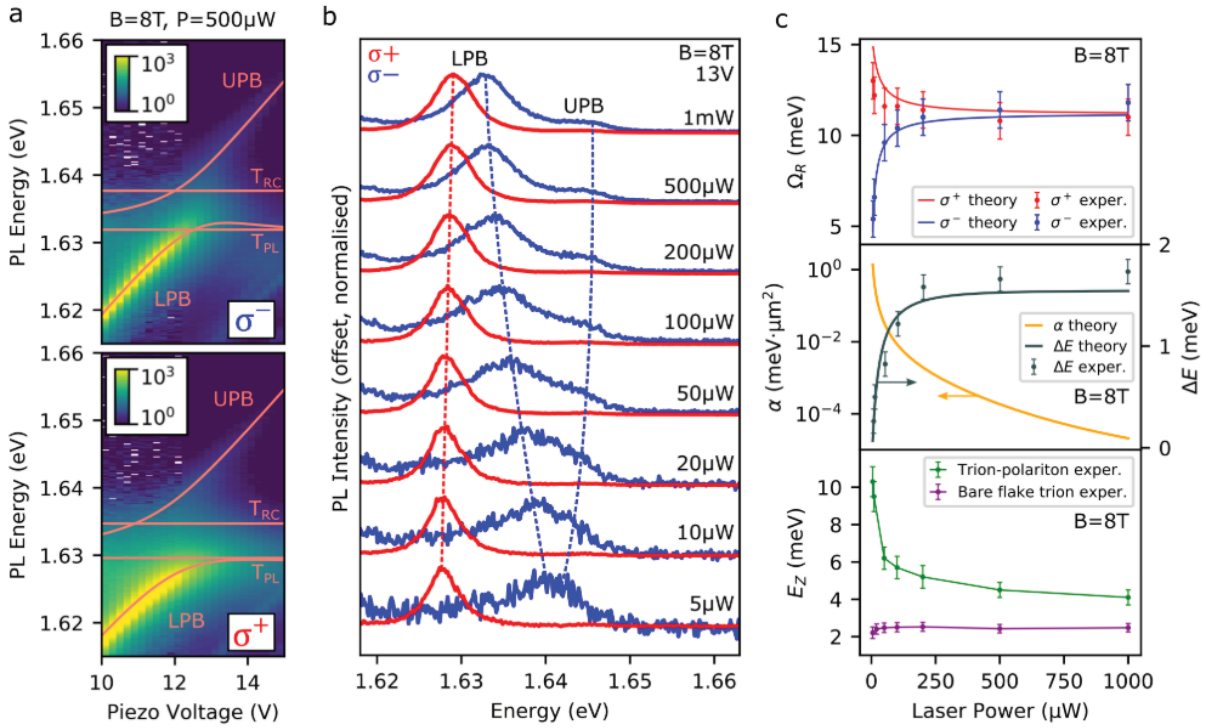

Figure 5.10: ***Trion-polariton effective nonlinearity.*** *(a) Cavity PL colormaps (logarithmic scale) in σ^+ and σ^- emission at $B = +8$ T and a high laser power $P = 500$ μW. An anticrossing is seen in both polarizations despite the strong applied B-field. Polariton fitting curves incorporating the Stokes shift are overlaid. (b) Cavity PL spectra at fixed detuning close to trion-cavity resonance, at $B = +8$ T, taken at varying incident laser powers. As the power is decreased, the 2DEG spin polarization increases and the anticrossing in σ^- is suppressed. This has the secondary effect of amplifying the effective Zeeman splitting between σ^+ and σ^- lower polaritons. (c) (top panel) Rabi splittings, Ω_R, in σ^+ and σ^- at $B = +8$ T against laser power. Nonlinear breakdown of strong coupling in σ^- is observed as the power is decreased. Solid curves are simulated results. (middle panel) The calculated effective trion-polariton interaction strength, α (see main text for definition), and the calculated and experimental blueshift, ΔE, of the LPB in σ^+ polarization, both at $B = +8$ T as a function of pump power. As there is no emission at 0 μW, the blueshift between 0 and 5 μW is assumed to be the same as between 5 and 10 μW, measured as (0.23 ± 0.12) meV. (lower panel) The maximum LPB Zeeman splitting, E_Z, at $B = +8$ T against laser power. The splitting increases drastically at the lowest powers when the 2DEG spin polarization is highest. For comparison the bare trion Zeeman splitting is shown.Error bars on experimental data points arise from our data fitting procedures and the inherent uncertainty in the spectrometer resolution.*

$$\frac{dN_\pm}{dt} = -WN_\pm X_\pm + \Gamma T_\pm \pm \frac{N_-}{\tau_e^s} \mp \frac{N_+}{\tau_e^s} e^{-\frac{\Delta}{k_b T_e}} \quad 5.52$$

$$\frac{dX_\pm}{dt} = -WN_\pm X_\pm + P_\pm - \frac{X_\pm - X_\mp}{\tau_X^s} - \frac{X_\pm}{\tau_X} \quad 5.53$$

$$\frac{dT_\pm}{dt} = WN_\pm X_\pm - \Gamma T_\pm - \frac{T_\pm - T_\mp}{\tau_T^s} \quad 5.54$$

The $\pm$ indices of N, X, and T correspond to the different spins of the free carriers, excitons (exciton-polaritons), and trions (trion-polaritons), respectively. Δ is the electron Zeeman splitting, T_e is the temperature. In all cases, we have considered linearly-polarized pumping: $P_+ = P_-$. The initial number of spin-polarized free carriers is $N_0 = 1000$ (estimated from the density 10^{12} cm^{-2}). The table below gives the parameters we used to describe the bare flake under 0 and 8 T and the cavity system. The trion-polariton decay rate toward a photon and a free electron is $\Gamma = 1/\tau_T$, where τ_T is the trion-polariton's lifetime.

Table of parameters			
Parameter	Bare flake 0T Measured experimentally	Bare flake 8T Fit parameters	Cavity 8T Fit parameters
τ_T		0.2 ps	2 ps
τ_T^s	1 ps	2.7 ps	10 ps
τ_X		0.3 ps	2 ps
τ_X^s	0.2 ps	0.7 ps	5 ps
τ_e^s	3 ns	3 ns	3 ns
Δ	0 meV	3.4 meV	3.4 meV
W		3x10^{-3} ps^{-1}	3x10^{-3} ps^{-1}

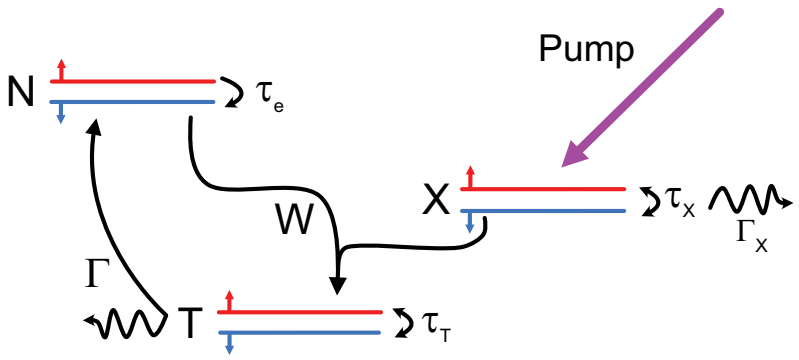

Figure 5.11: *Scheme of the population dynamics. Arrows indicate the pumping (violet), scattering and decay rates (black), spin relaxation rates (small black).*

5.5.6 Conclusion

Our experiments [247] demonstrate the simultaneous manifestation of strong and weak coupling regimes between a photonic mode and a many-body correlated matter excitation consisting of an exciton dressed by electrons in an effective ferromagnetic phase, resulting in a giant Zeeman splitting between trion-polariton modes. We additionally show that laser illumination acts to depolarize the 2DEG via a process of trion valley pseudospin relaxation and subsequent radiative recombination. The resulting Rabi splitting transfer between the two polarization components induces energy renormalisation to which we associate large effective interactions. While in this work an EuS film was used to introduce additional free electrons into the flake, similar results should be observed in any $MoSe_2$ monolayer in which the itinerant carrier density can be raised arbitrarily to give the trion sufficient oscillator strength. Magnetic 2-dimensional materials may also be used to induce 2DEG spin polarization without the need for strong external B-fields [253]. Moreover, we note that extremely high laser powers, often pulsed and quasi-resonant, are typically needed to enter regimes of polariton non-linearity, while here the strongest effective interactions occur under low power non-resonant continuous-wave laser excitation. Our work therefore highlights doped $MoSe_2$ as a flexible system in which to realize and apply ultrastrong low-threshold non-linearities, for instance towards TMD-based all-optical logic gates [258, 259], or to explore nonlinear topological photonics [260].

5.6 Chapter conclusion

In this chapter, by coherently exciting two bands near a Dirac point, we first studied a non-Abelian gauge theory, describing vector charges, in an organic microcavity. It allows to express a classical chromodynamics theory, with a coupled spatial and charge (color) polariton dynamics. It results in Zitterbewegung oscillations observable at room temperature. Then, we introduce an opposite regime of excitation, in the adiabatic limit of a single band, which allows to obtain a photonic anomalous Hall effect.

We demonstrate that both of these regimes can be described by a single formalism, resulting in universal semiclassical equations, using only the static band parameters, namely the dispersion and the Quantum Metric. The latter turns out to determine a universal length scale for all effects beyond the simple group velocity, and to provide a geometrical origin of the Compton wavelength.

This chapter ends with the study of an experimental work on a transition metal dichalcogenide semiconductor monolayer embedded in a microcavity. We show that a spin-selective strong light-matter coupling regime gives rise in unusually strong optical nonlinearity and a giant Zeeman effect, which allows to open a gap at the Dirac point in polaritonic systems, and which has direct applications in topological physics.

Chapter 6: Non-Hermitian systems

Contents

In the 6^{th} and last chapter, we demonstrate that in presence of non-Hermiticity, a Dirac point will transform into a pair of exceptional points, linked by a Fermi arc. We show that the Quantum Metric diverges at the vicinity of an exceptional point. This divergence allows to understand the complex behavior of a wavepacket centered at this point. Finally, we present the first experimental extraction of the Quantum Metric in a non-Hermitian system, exhibiting exceptional points. This thesis ends with the observation of the divergence of the Quantum Metric at the vicinity of exceptional points, accordingly with the theory.

6.1 PT-symmetric systems

Mathematically speaking, a Hermitian system is described by a Hermitian Hamiltonian H, meaning $H = H^\dagger$, with $\dagger$ the Hermitian conjugation. Physically, it guarantees eigenvalues to be real, and that the corresponding time evolution operator is unitary, thanks to which the total probability to observe a particle $\langle\psi|\psi\rangle = 1$ is conserved. On the contrary, physical systems with gain or loss can be described by a non-Hermitian Hamiltonian, which means that the probability to observe a particle is not conserved, because the time evolution is not unitary anymore. Nevertheless, it was shown that non-Hermitian Hamiltonians can also have real eigenvalues. These Hamiltonians need to be PT-symmetric [261], ensuring the commutation with the PT operator

$$[PT, H] = PTH - HPT = 0 \tag{6.1}$$

where P is the parity symmetry operator changing a system into its mirror image, and T is the time symmetry operator changing the direction of time. The two operators satisfy the

following properties

$$P^2 = 1\,,\;\; P = P^\dagger\,,\;\; T^2 = 1\,,\;\; T = T^\dagger\,,\;\; [P,T] = 0 \tag{6.2}$$

and the action of the P and T operators are defined by

$$\begin{aligned} P &: i \to i\,,\;\; \widehat{x} \to \widehat{x}\,,\;\; \widehat{p} \to -\widehat{p} \\ T &: i \to -i\,,\;\; \widehat{x} \to \widehat{x}\,,\;\; \widehat{p} \to -\widehat{p} \end{aligned} \tag{6.3}$$

where the $\hat{x}$ and $\hat{p}$ satisfy $[x,p] = xp - px = i\hbar$. Now, let us consider a 2×2 Hamiltonian describing a coupled two-level system with different loss/gain

$$H = \begin{pmatrix} E_1 - i\gamma_1 & \kappa \\ \kappa & E_2 - i\gamma_2 \end{pmatrix} \tag{6.4}$$

with κ the coupling constant and $\gamma_{1,2}$ the losses of the two different modes. It describes non-Hermitian systems with complex energies. The eigenvalues are

$$E_\pm = E_0 - i\chi \pm \sqrt{\kappa^2 + \Gamma^2} \tag{6.5}$$

with $E_0 = (E_1 + E_2)/2$ the mean energy, $\chi = (\gamma_1 + \gamma_2)/2$ the mean loss, $\Gamma = \delta + i\beta$ an important parameter defined by $\delta = (E_1 - E_2)/2$, the energy detuning, and finally $\beta = (\gamma_1 - \gamma_2)/2$, the half difference of losses. Necessary conditions to obtain real eigenvalues are

- $\chi = 0$, which gives $\gamma_1 = -\gamma_2$, meaning one correspond to gain and the other to loss.
- $\kappa^2 + \Gamma^2 \geq 0$ (implying that it's real), which, with nonzero β, is satisfied only for $\delta = 0$, meaning $E_1 = E_2$.

In this case, the Hamiltonian H' reads

$$H' = \begin{pmatrix} E' - i\gamma & \kappa \\ \kappa & E' + i\gamma \end{pmatrix} \tag{6.6}$$

with $\gamma = \gamma_1 = -\gamma_2$ and $E' = E_1 = E_2$. The resulting eigenvalues read $E'_\pm = E' \pm \sqrt{\kappa^2 - \gamma^2}$. This Hamiltonian can describe a system of two coupled resonators, one with gain (G) and one with loss (L), as shown in fig.6.1.a. This system is PT symmetric as the time operator T changes loss in gain, and vice-versa, and the parity operator P switches the two resonators. At the end of a PT operation, the system is identical to what it was before this operation. We can plot the real and imaginary parts of the eigenvalues with respect to the coupling strength κ. It is displayed in blue and red. At low coupling strength, there is a degeneracy of the real part of eigenvalues, and a splitting of the imaginary part, which means that one mode exhibits amplification and the other attenuation. When $\kappa/\gamma > 1$, we observe the opposite – a splitting of the real part of eigenvalues, and a degeneracy of the imaginary part. The eigenvalues are now purely real (and different). The transition point, at $\kappa = \gamma$, is called an exceptional point, and will be extensively studied in the following. One should

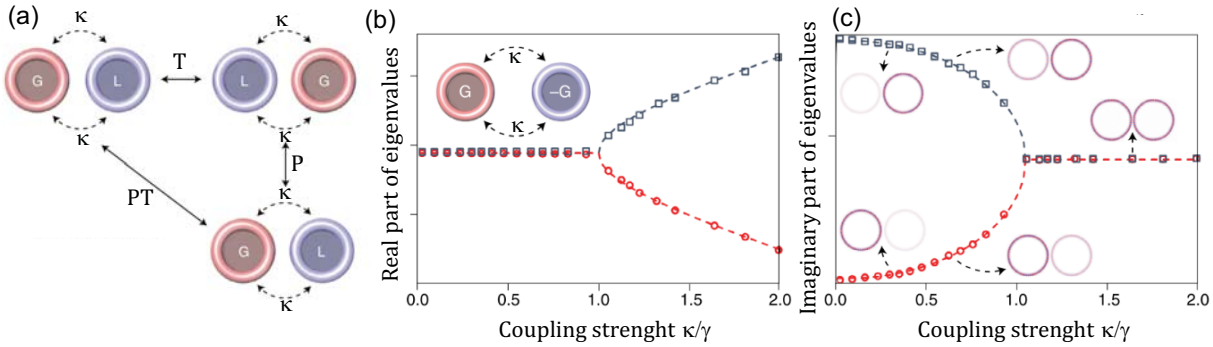

Figure 6.1: *(a) A PT-symmetric system composed of two coupled resonators, one with gain (G) and one with loss (L). A PT operation on this system leaves it unchanged. (b-c) Real and imaginary part of the eigenvalues versus the coupling constant κ. The theory is displayed with dashed lines, and a COMSOL simulation is displayed with red circles and blue squares. The exceptional point is located at $\kappa = \gamma$. At lower coupling $\kappa < \gamma$, there is a degeneracy of the real part of eigenvalues, and a splitting of the imaginary part. It is the opposite when $\kappa > \gamma$. At the exceptional point, there is a unique eigenvalue and a unique eigenstate, owing to the Hamiltonian becoming defective. Figures from [262].*

keep in mind this figure, as it is the signature of the presence of an exceptional point. An exceptional point differs from a Dirac point because not only the eigenvalues coalesce at this point, but also the eigenvectors, making the matrix describing the Hamiltonian a defective matrix (non-diagonalizable).

6.2 Exceptional points in microcavities

The losses in photonics are inevitable, and it was overall seen as an unwanted feature for quite a long time by the scientific community. But, as the reader probably understands by now, it is one of the main features that made photonic systems a central platform [263, 264, 262, 265, 266] to study non-Hermitian physics, like exceptional points. We will study in this section how to implement non-Hermiticity in a microcavity. We start by a microcavity with TE-TM splitting and linear birefringence, which, as we have shown in chapter 2, exhibits two Dirac points. As a reminder, the Hamiltonian, written in the circular basis, reads

$$H_{cav} = \begin{pmatrix} \frac{\hbar^2 k^2}{2m^*} & \beta_0 - \beta k^2 e^{-2i\varphi} \\ \beta_0 - \beta k^2 e^{2i\varphi} & \frac{\hbar^2 k^2}{2m^*} \end{pmatrix} \tag{6.7}$$

where $k = \sqrt{k_x^2 + k_y^2}$ is the in-plane wavevector, $\varphi = \arctan(k_y/k_x)$ is the in-plane polar angle of the wavevector, β_0 is the linear birefringence term, lifting the degeneracy at $k = 0$. Finally, m^* is the effective mass of the modes and β is TE-TM splitting strength given by

$$\frac{1}{m^*} = \frac{1}{2}\left(\frac{1}{m_{TE}} + \frac{1}{m_{TM}}\right), \ \beta = \frac{\hbar^2}{4}\left(\frac{1}{m_{TE}} - \frac{1}{m_{TM}}\right) \tag{6.8}$$

It allows to construct an effective Hamiltonian near a Dirac point which reads

$$H_D(\mathbf{q}) = \hbar c \begin{pmatrix} 0 & qe^{-i\varphi} \\ qe^{i\varphi} & 0 \end{pmatrix} = \hbar c \mathbf{q} \cdot \boldsymbol{\sigma} \tag{6.9}$$

where $\mathbf{q}$ is the wavevector in polar coordinates starting from the Dirac point, φ its polar angle, c is the celerity and $\boldsymbol{\sigma}$ represents the Pauli matrix vector. Plotting the eigenvalues of this Hamiltonian allows to obtain a Dirac dispersion shown in fig.6.2.a. This dispersion changes drastically in presence of non-Hermiticity. Indeed, adding a non-Hermitian term in the Hamiltonian H_D will split the Dirac point into a pair of exceptional points, linked by a Fermi arc, as shown in the panel b of the figure. We will consider the case where the distance in the reciprocal space between the two exceptional points is sufficient. In this case, we can write an effective Hamiltonian with an exceptional point centered at $q = 0$ [161], with $\hbar = 1$

$$H_1 = \begin{pmatrix} 0 & \alpha q e^{-i\varphi} + a \\ \alpha q e^{i\varphi} + a & 0 \end{pmatrix} + i \begin{pmatrix} 0 & -ia \\ ia & 0 \end{pmatrix} \tag{6.10}$$

The first part corresponds to a Rashba-like Hamiltonian with α the celerity of the waves close to this point. This Hamiltonian displays a Dirac point at $q = 0$, and a constant term a along x, shifting this point. The second part of the Hamiltonian corresponds to the non-Hermiticity, with a term proportional to σ_y. To get one of the two exceptional points at $q = 0$, it is crucial that the value a of this term is equal to the constant term along x, because this configuration allows the a terms to cancel out, as we see if we write the Hamiltonian under the form

$$H_1 = \begin{pmatrix} 0 & \alpha q e^{-i\varphi} + 2a \\ \alpha q e^{i\varphi} & 0 \end{pmatrix} \tag{6.11}$$

Due to that, the Hamiltonian becomes defective and exhibits an exceptional point at $q = 0$. The Hamiltonian H_1 describes a microcavity with TE-TM splitting, linear birefringence and linear dichroism[1], with the dichroism giving the non-Hermitian term. This Hamiltonian is similar to the gain-loss Hamiltonian [267], and is very general, as it allows to describe an arbitrary exceptional point in an arbitrary 2D parameter space. At low wavevector $\mathbf{q}$, its eigenvalues read

$$E(q) = \sqrt{2a\alpha q} e^{-i\varphi/2} \tag{6.12}$$

which gives are real and imaginary parts $\mathrm{Re}E = \sqrt{2a\alpha q}\cos\varphi/2$ and $\mathrm{Im}E = \sqrt{2a\alpha q}\sin\varphi/2$. The dispersion is shown in fig. 6.2.b and c. We can observe here an important difference between a Dirac point and an exceptional point. For the Dirac point, the dispersion at its vicinity is linear in q, meaning the group velocity is constant. However, the dispersion at the vicinity of an exceptional point is proportional the the square root of q, which results in a diverging group velocity proportional to $1/\sqrt{q}$. The imaginary parts of the eigenvalues are marked in color in the figure. Along the line in the reciprocal space defined by $\varphi = 0$ and which ends at an exceptional point, we remark that the imaginary part is zero, meaning the states are "stable". For any other point, there is a non-zero imaginary part determining

[1] Dichroism means that the absorption depends on the polarization.

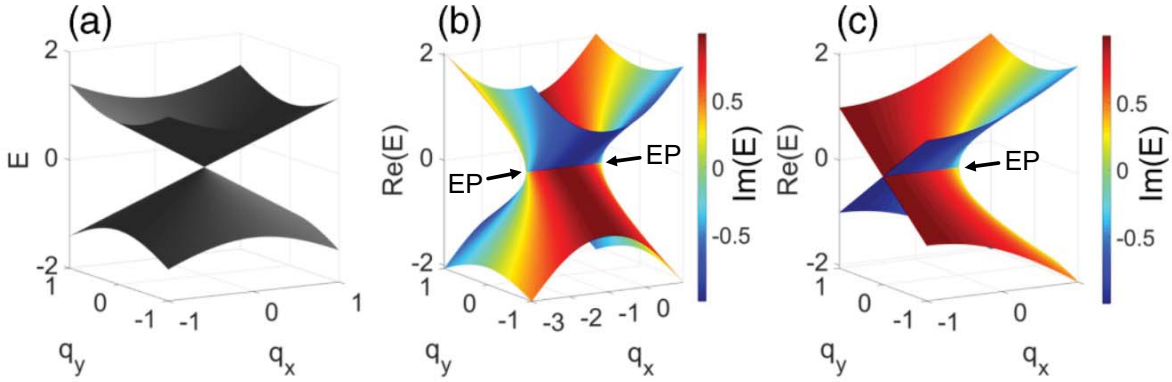

Figure 6.2: *(a) Dispersion near the Dirac point. (b) The Dirac point transforms into a pair of exceptional points, linked by a Fermi arc. (c) Zoom on an exceptional point. The color shows the imaginary part of the energy.*

either the decay (in blue) or the growth (in red) of the states.

6.3 The role of the Quantum Metric at exceptional points

6.3.1 Introduction

As a reminder, the Quantum Metric allows one to calculate the distance between two quantum states [118], and is defined in the reciprocal space[2] by

$$ds^2 = g_{ij} dk_i dk_j = 1 - |\langle \psi(\mathbf{k}) | \psi(\mathbf{k} + \boldsymbol{\delta}\mathbf{k}) \rangle|^2 \tag{6.13}$$

A crucial point is that the overlap integral between a state $|\psi_0\rangle$ and some arbitrary state $|\psi\rangle$ can be expressed using the Quantum Metric tensor g_{ij} under the form

$$I = 1 - \left(\int_{|\psi\rangle}^{|\psi_0\rangle} \sqrt{g_{ij} d\lambda_i d\lambda_j} \right)^2 \tag{6.14}$$

where the integral follows a geodesic line. It allows to obtain the behavior of the coefficients $c_l(\lambda)$, with $|c_l|^2 = I$. These coefficients allow to express an arbitrary initial state ψ as a superposition of eigenstates ψ_l used in the Schrödinger equation

$$|\psi(\lambda, t)\rangle = \sum_l c_l(\lambda) e^{-i \frac{E_l(\lambda)}{\hbar} t} |\psi_l(\lambda, t)\rangle \tag{6.15}$$

In our case, we will consider a two-band system, so only two eigenstates, and a wavepacket centered at an exceptional point in the reciprocal space. The wavepacket dynamics depends on the projection of the state on the two bands, and so on the integral I. And in our theoretical paper [161], we are interested in the dynamics of a wavepacket near an exceptional point, so we are interested in the overlap integral I. This integral depends on the Quantum

[2] Of course the Quantum Metric, as the Quantum Geometric Tensor, can be defined on any parameter space.

Metric, this is why we are interested in obtaining the Quantum Metric. This article shows that the Quantum Metric diverges near an exceptional point, and that such divergence results in a particular behavior of a wavepacket if the latter is sent at the vicinity of an exceptional point.

6.3.2 Circularly polarized wavepacket

We start by considering the Hamiltonian H_1 from eq. 6.11. At $q = 0$, meaning at the exceptional point, there is a unique eigenstate, which is $|\psi_0\rangle = (1, 0)^T$, corresponding to a circularly polarized mode. At any other point in the reciprocal space, there will be two eigenstates of H_1 noted $\psi_\pm$. We consider a circular polarized wavepacket, with a finite wavevector distribution σ_q, centered at an exceptional point. The first step is to obtain the Quantum Metric. For small wavevectors, the eigenstates of H_1 reads $|\psi_\pm(q)\rangle = \left(1 - \alpha q/4a, \sqrt{\alpha q/2a}e^{i\varphi/2}\right)^T$. Due to this result, we can compute the radial component of the Quantum Metric tensor g_{qq} which reads

$$g_{qq} \approx \frac{\alpha^2}{16a^2} + \frac{\alpha}{8aq} \tag{6.16}$$

We see that it diverges as $1/q$, with q the wavevector starting at the exceptional point. It was shown that we obtain this divergence for any second-order exceptional point [268]. The order of divergence depends on the order of the exceptional point. The angular part of the Quantum Metric tensor $g_{\varphi\varphi}$ is linear in q and reads $g_{\varphi\varphi} \approx \alpha q/8a$. For a Dirac point, this term diverges and determines the behavior of a wavepacket at its vicinity. In our case, we see that g_{qq} does not depend on φ, which allow to write the overlap integral I_{circ} between the states $|\psi_0\rangle$ and $|\psi(q)\rangle$ as

$$I_{circ} = 1 - \left(\int_{|\psi_0\rangle}^{|\psi(q)\rangle} \sqrt{g_{qq}(dq)^2}\right) \tag{6.17}$$

with $|\psi_0\rangle$ the spinor of the wavepacket, corresponding to the circular polarization, and $|\psi(q)\rangle$ the eigenstate at q. Due to the independence of the integral on φ, the wavepacket is at first equally distributed between the two modes, meaning $n_+ = n_-$. But the difference in the imaginary parts of these states will result in their growth or decay. The most important growth or decay is experienced along a line defined by $\sin\varphi/2 = 1$, meaning $\varphi = \pi$. To obtain the group velocity at a certain point in the reciprocal space, we need to calculate the derivative of the dispersion, and then fix the wavevector. The consequence is that, even if along the line $\varphi = \pi$ we have q_y equal to zero, we will calculate the group velocity before fixing its value. We start from the real part of the dispersion given by eq. 6.12. Along the line described by $\varphi = \pi$, we use the the fact that $\cos\varphi/2 = \sqrt{(1 + \cos\varphi)/2}$, and we use a Taylor expansion to finally obtain

$$E(\mathbf{q}) \approx \sqrt{2\alpha a}\left({q_x}^2 + {q_y}^2\right)^{1/4}\sqrt{\frac{1}{2} + \frac{q_x}{2\sqrt{{q_x}^2 + {q_y}^2}}} \approx \sqrt{\alpha a}\frac{q_y}{|q_x|^{1/2}} \tag{6.18}$$

From that point, we can obtain the group velocity. In the horizontal (q_x) direction, $v_x = \partial E/\partial q_x \propto q_y$ which is equal to zero along the line $\varphi = \pi$. In the vertical (q_y) direction, a

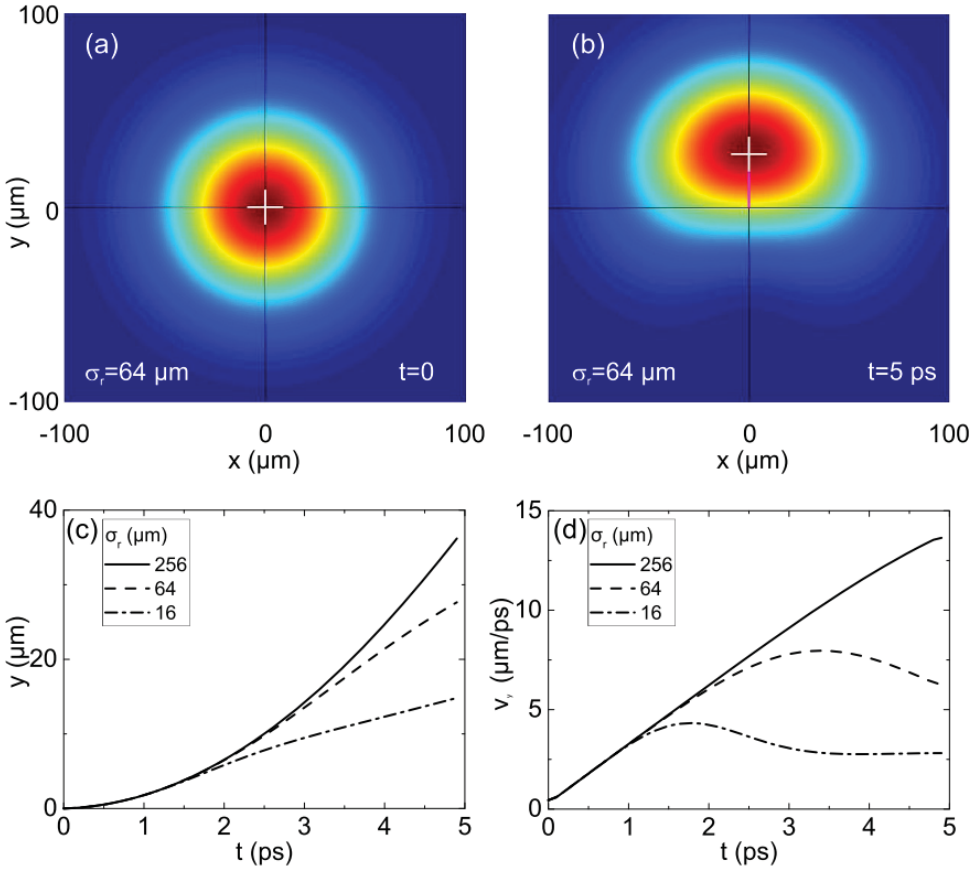

Figure 6.3: ***Circularly polarized wavepacket at an exceptional point.*** *(a) Probability density distribution* $|\psi(x,y,t)|^2$ *for a circularly polarized initial wavepacket of* $\sigma_r = 64\,\mu m$ *at* $t = 0$ *and (b)* $t = 5\,ps$*. The white cross marks the center of mass. (c) Center of mass position as a function of time. (d) Center of mass velocity as a function of time, demonstrating constant acceleration.*

non-zero group velocity $v_y = \partial E/\partial q_y$ reads

$$v_y \approx \frac{\sqrt{\alpha a}}{|q_x|^{1/2}} \tag{6.19}$$

So the group velocity $\mathbf{v}_g = (0, v_y)$ is perpendicular to the wavevector $\mathbf{q} = (q_x, 0)$ along this line. Meanwhile, the decay and the growth of the modes are given by the imaginary part of eq. 6.12 which reads $\Gamma \sim \pm {q_x}^{1/2}$. These growing (population n_+) and decaying (population n_-) fractions constitute two different parts of the wavepacket. These populations fill different modes with opposite propagation directions (along $\pm y$). What interests us is the average velocity of this wavepacket, which for small times can be written under the form

$$\langle v_y \rangle = (n_+ - n_-)v_y \approx 2v_y \Gamma t \approx 2\sqrt{2}\alpha a t \tag{6.20}$$

We remark that the $q_x^{1/2}$ terms from v_y and from γ cancel each other, resulting in the average group velocity not depending on q_x. Accordingly, one should expect a finite-size wavepacket centered at an exceptional point to demonstrate a constant acceleration in the vertical (y) direction. This constant acceleration depends linearly on the dichroism, the non-Hermitian term a, and on the celerity noted α. To validate this result, we performed numerical simulations, solving the time-dependent spinor Schrödinger equation. We used the Hamiltonian H_1 described by eq. 6.11 and we plotted the trajectory of the center of mass position of the wavepacket, for different initial sizes of the wavepacket. We used the parameters of the perovskite microcavities explained in section 5.1 [54]. For a wavepacket size of $\sigma_r = 64$ μm, two snapshots of the particle density $|\psi(x, y, t)|^2$ are displayed in fig. 6.3, describing the position of the center of mass in the real space (white cross) at $t = 0$ (panel a) and $t = 5$ ps (panel b), and showing the trajectory between these two times (pink line). We clearly see a vertical movement of the wavepacket, coming with its distortion. This distortion is less visible as the size of the wavepacket increases, such as it is not visible anymore with $\sigma_r = 256$ μm. The fig. 6.3.c. shows the time evolution of the y coordinate of the center of mass, exhibiting a quadratic dependence. Owing to this quadratic dependence, which falls off quicker for smaller wavepacket sizes, the vertical group velocity v_y shows a linear evolution. It confirms the constant acceleration, whose value corresponds well to the theoretical solution obtained earlier.

Changing the size of the wavepacket in the real space σ_r (as shown by the line style in Fig. 6.3(a,b)) also leads to a very interesting and counter-intuitive behavior. Indeed, the linear increase of the velocity occurs only while the populations of the two branches n_+ and n_- are comparable. The duration of this regime is determined by the maximal gain/loss ratio available within the wavepacket size in the reciprocal space σ_q. For high σ_q, the regime of linear increase is lost more rapidly. While the wave vector of the center of mass q_0 of the wavepacket is at this moment higher than for a smaller σ_q, the corresponding group velocity is lower, because $v_g \sim 1/\sqrt{q_0}$. So, a wavepacket which is larger in reciprocal space (dash-dotted line) exhibits a smaller final velocity and a shorter acceleration period (and, finally, a smaller total displacement for the same amount of time).

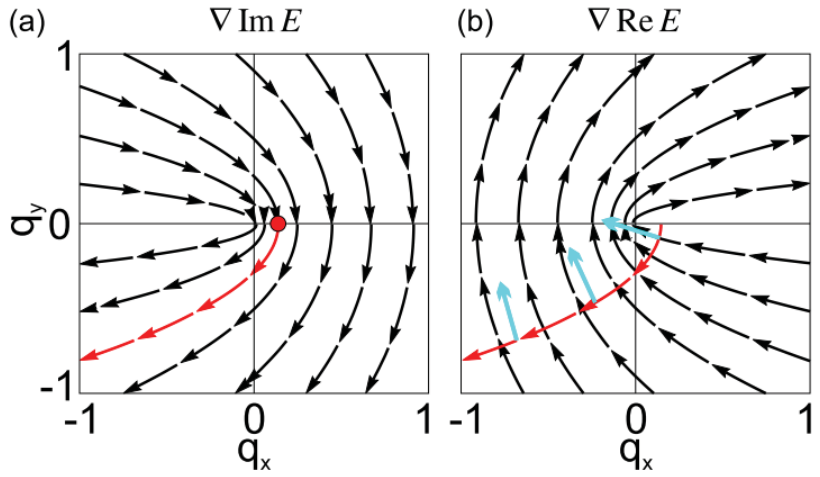

Figure 6.4: *(a) The gradient of the imaginary part of the energy* $\nabla \operatorname{Im} E$ *for one dispersion branch. The arrows show how the center of mass of the wavepacket moves in the reciprocal space due to the amplification of its components. The linear-polarized wavepacket projection of the branch is marked with a red circle. (b) The group velocity map* $\nabla \operatorname{Re} E$ *with the trajectory of the center of mass in red, and the corresponding group velocities highlighted in blue.*

6.3.3 Linearly polarized wavepacket

In the last section, we have shown that the Quantum Metric g_{qq} is independent on φ, which resulted in the circularly polarized wavepacket to overlap similarly for the two different states and so the populations were identical $n_+ = n_-$ at $t = 0$, also with a zero initial velocity. It will not be the same case if the polarization of the wavepacket is different from the one of the eigenstate of the exceptional point. The Quantum Metric allows to obtain the distance between states, so the divergent Quantum Metric g_{qq} means that the eigenstates change tremendously fast with a change of the wavevector q. Due to that, this linearly polarized wavepacket demonstrates a non-symmetrical overlap with the two modes. Indeed, from eq. 6.14, we find that the overlap between one of the eigenstates and a H-polarized wavepacket described by a spinor $|\psi_0\rangle = \left(1/\sqrt{2},\, 1/\sqrt{2}\right)^T$ can be written as

$$I_{lin} \approx \frac{1}{2} + \int_{|\psi_0\rangle}^{|\psi(q)\rangle} \sqrt{g_{qq}} dq \approx \frac{1}{2} + \sqrt{\frac{\alpha q}{2a}} \tag{6.21}$$

which is proportional to $\sqrt{q}$, leading to a rapid growth of the overlap. An interesting result is the non-zero wavevector q_0 for the center of mass of the wavepacket in each of the bands. Indeed, the equation describing the effective center of mass of the wavepacket reads

$$q_0 = \int q I_{lin} |\psi_0(q)|^2 dq \tag{6.22}$$

with $|\psi_0(q)|^2$ the excitation wavefunction, which is a Gaussian with σ_q its width (small σ_q means large σ_r). The equation 6.22 gives a non-zero value for q_0 as it reads $q_0 \sim {\sigma_q}^{3/2}\sqrt{\alpha/2a}$ for small σ_q.

In the fig. 6.4.a is plotted the gradient of the imaginary part of the energy $\nabla \mathrm{Im} E$,

with the trajectory of the center of mass due to this gradient *in the reciprocal space* in red. Indeed, the two parts of the gradient are $(\eta_x, \eta_y) = \nabla \mathrm{Im}E$ and their ratio reads $\eta_x/\eta_y = \left(-q_x + \sqrt{{q_x}^2 + {q_y}^2}\right)/q_y$. For an inital wavevector q_0, it results in a parabolic shape $q_x = -({q_y}^2 - {q_0}^2)/(2q_0)$. In the panel b of fig. 6.4, the blue arrows represent the group velocity, which is time-dependent. At the beginning, this velocity is mostly defined by the q-dependent celerity term α in the Hamiltonian H_1 given by eq. 6.11. Afterwards, the velocity decreases up to a value corresponding to the ratio of the populations n_+ and n_- of the two states. To find the x component of the group velocity v_x, we start by the dispersion calculated previously in eq. 6.18, then we derive this equation over q_y and then use a Taylor expansion over q_y, for $q_x > 0$. The solution reads $v_x \approx 3\sqrt{\alpha a}{q_y}^2/8{q_x}^2$. To obtain the time dependence of the group velocity, we need to use the center of mass wave vector $q_x(t)$, whose calculation again involves the Quantum Metric via the overlap integral I_{lin} (see supplementary of [161]). For small t, $q_x(t) \approx \alpha a q_0^2 t^2/\sqrt{2\pi}$, and finally the group velocity tends to a constant non-vanishing value

$$\langle v_x \rangle \approx 0.38\alpha \tag{6.23}$$

which does not depend on the wavepacket size. Moreover, it only depends on the celerity α of the Hermitian part of the Hamiltonian, and not on the non-Hermitian dichroism parameter a.

All this is indeed confirmed by numerical simulations. Figure 6.5(a) shows all possible trajectories for wavepackets of different polarizations. They all demonstrate a constant acceleration along y, as for a circular wavepacket. An additional polarization dependent constant velocity contribution appears. For an H-polarized wavepacket (black circles in panel (a)), it is directed along x and therefore can be studied independently from the other contribution v_y. Fig. 6.5(b) shows that the velocity v_x of an H-polarized wavepacket quickly drops from the value given by the Hermitian part of the Hamiltonian ($v_x = \alpha$) at $t = 0$ down to the constant value predicted by 6.23 and indeed independent of the dichroism a (dashed line). This finite constant velocity differs drastically from the behavoir of a gapped Dirac Hamiltonian, where the radial metric decays as $g_{qq} \sim -q^2$ and therefore does not diverge. Because of this, the associated group velocity tends to zero in the limit of a wavepacket infinitely large in real space $v_{Dirac} \sim 1/\sigma_r^2 \to 0$. Contrary to a diabolical point, associated with a localized Berry curvature (delta function), an exceptional point exhibits distributed Berry curvature [269, 270]. However, dynamical effects associated with this Berry curvature, such as the anomalous Hall effect, are practically unobservable, because the divergent group velocity dominates all possible corrections.

6.3.4 Conclusion

These results demonstrate that the Quantum Metric plays a particularly important role in the vicinity of the exceptional points, determining the dynamical behavior of wavepackets. The crucial feature is that the radial component of the Quantum Metric diverges. This, together with the divergent group velocity, leads to a non-vanishing polarization-dependent velocity for any finite-size wavepacket, centered at the exceptional point. Our studies are

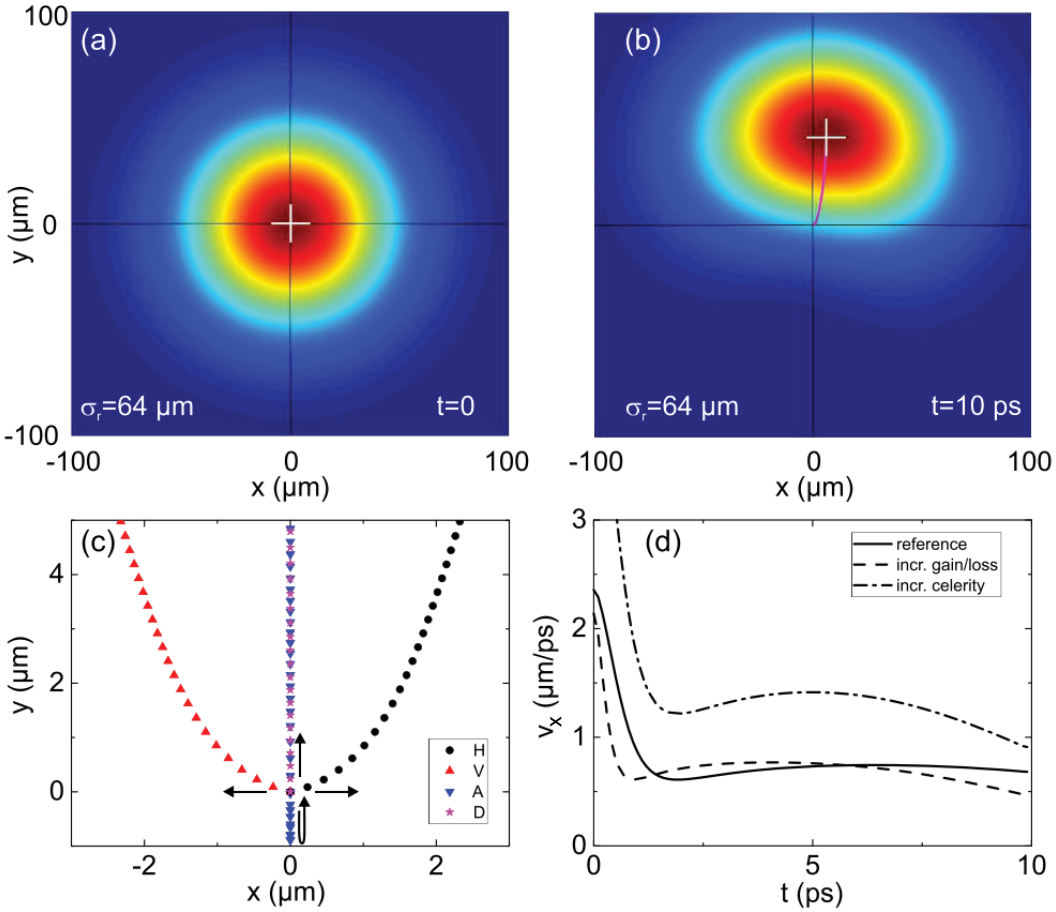

Figure 6.5: ***Linearly polarized wavepacket.*** *(a-b) Probability density distribution* $|\psi(x,y,t)|^2$ *for an initial wavepacket of* $\sigma_r = 64\,\mu m$ *at (a)* $t = 0$ *and (b)* $t = 10\,ps$*. The white cross marks the center of mass, and its trajectory is shown in pink. (c) Polarization-dependent center of mass trajectories. (d) The x-projection of the H-polarized wavepacket velocity over time, for different initial conditions.*

important for future research and applications in non-Hermitian photonics.

6.4 Experimental measurement of the Quantum Metric

6.4.1 Introduction

As we have seen in chapter 5, the recent development of experimental techniques and theoretical understanding has allowed to measure both components of the Quantum Geometric Tensor [118, 270], which are the Berry curvature and the Quantum Metric, experimentally [271, 56]. In particular, the use of optical systems allows to access the non-trivial geometry of real photonic bands and to observe the related consequences on wavepacket propagation and the anomalous Hall effect [56]. In Hermitian systems, the Quantum Metric determines the non-adiabatic corrections to the anomalous Hall effect [230, 160, 210], with the dominant role played by the Berry curvature. These measurements have inspired further research on the Quantum Metric [272], adding on top of the previous works that have demonstrated its

importance for superfluidity in flat bands [156, 157], the electronic magnetic susceptibility [230, 168], the characterization of general phase transitions [273, 274], or the exciton Lamb shift [275].

At the same time, the studies of non-Hermitian systems [276, 277, 278, 262] have also started to deal with the topology of the exceptional points. It was shown that the chiral dynamics associated with this non-Hermiticity is extremely promising for applications [279, 280, 267], together with the enhanced sensing properties [281, 282, 283], and also coherent perfect absorption [284, 285, 286]. Crucially, the good topological invariant in vicinity of these points is not anymore associated with the Berry curvature of the eigenstates, but with the winding number of the so-called effective field [287, 288] (and the associated complex eigenvalues), determined by the Hermitian and non-Hermitian parts of the Hamiltonian itself. Indeed, because of the non-Hermitian contribution, the adiabatic description of dynamics based on the Berry curvature becomes irrelevant [289, 290]. On the other hand, the Quantum Metric should exhibit a hyperbolic divergence at the exceptional points of second order (with square root topology) [268, 161]. This divergence has remarkable physical consequences, controlling the dynamics of wavepackets centered at exceptional points [161], as we have seen in the last section. Here, the Quantum Metric is not responsible for small corrections, it has a dominant role, determining a non-vanishing constant group velocity with a polarization-dependent direction. However, the Quantum Metric of a non-Hermitian system has never been measured experimentally so far, in spite of the extended studies of such points in optics [291, 262] which date back to Voigt [292], and of their recent recent observation in microcavities [293].

In this work [163], together with the group of Prof. Q. Liao from Beijing Capital University, China, we investigate the Quantum Metric of exceptional points in an organic microcavity. We study the modes of an organic microcavity [294] exhibiting a polarization-dependent strong coupling, which provides a pronounced non-Hermitian response ensuring well-defined exceptional points. We measure the Stokes parameters of the eigenmodes in vicinity of the exceptional points and extract the corresponding Quantum Metric. We demonstrate that this metric is diverging, exhibiting a scaling exponent $n = -1.01 \pm 0.08$. The coefficients of the measured hyperbola correspond to the analytical predictions based on an effective Hamiltonian.

6.4.2 Presentation of the system

The sample we study is an organic microcavity with metallic mirrors, shown in Fig. 6.6(a) [295]. The active layer is a microcrystal of an organic molecule, 4,4'-bis[4-(di-p-tolylamino) styrylbiphenyl (DPAVBi), whose structure is shown in fig. 6.6(b). The microbelt's width (Y-axis) is around 20μm, with the thickness of $2.0 - 3.0\mu$m and the length (oriented along X) is several hundreds of micrometers. The triclinic form of the DPAVBi crystal is determined by the specific arrangement of molecules. The resulting optical properties of the crystal are strongly anisotropic, with an optical axis in the XZ plane (cyan arrow) tilted by 36° [295] with respect to the Z-axis.

We start off by displaying the sample unpolarized reflectivity in the two orthogonal

directions in fig. 6.6(c,d). The light was entered and collected by using the 100× microscope objective with a high aperture (0.95), the collection angle can achieve ±70°. The momentum space of the reflectivity was located at the back focal plane of the objective lens. The reflectivity is plotted as a function of energy and wave vectors k_x and k_y. We focus on two particular eigenmodes, which exhibit the clearest behavior. First of all, we note that the two branches show very different effective masses and very different linewidths. This is due to the strongly polarized nature of excitons in DPAVBi (see [295, 296] on the anisotropy of the excitonic absorption by the microbelt). The exciton ($E_X \sim 2.7$ eV) strongly couples with the photonic modes only in the H polarization (electric field aligned along X) exhibiting a Rabi splitting of 80 meV. The V-polarized modes (electric field aligned along Y) remain unaffected by the excitonic resonance. The strongly-coupled modes exhibit a higher mass and a smaller linewidth, both because of their reduced photonic fraction.

In the two k-space directions, the behavior of the two modes is qualitatively different: a crossing of the weakly and strongly coupled polarization branches occurs along k_x direction and an anti-crossing along k_y. This anti-crossing is *not* the result of the above mentioned strong exciton-photon coupling. It is rather due to the emergent optical activity of the structure, which becomes sufficiently large at the anticrossing wave vector. Optical activity has recently been shown to emerge at the macroscopic level in cavity structures, when the linear birefringence is so high that oppositely-polarized modes of opposite parity become degenerate [55, 297]. It is therefore a coupling which occurs between the photonic part of such modes. This is illustrated by fig. 6.7, showing (with a thicker sample) that the anticrossing only appears for opposite parity branches. The direction of the OA is determined by the tilt of the optical axis [55]: it emerges in the direction Y, perpendicular to the plane XZ, containing the optical axis of the crystal.

6.4.3 Theory

From the theoretical point of view, we consider a system containing three coupled modes: two photons with polarizations H and V, and one exciton which couples to the polarization H only. Here we neglect the splitting between TE and TM polarized modes. The coupling between the H-polarized photon and the exciton is much stronger than the other couplings in the system. We therefore begin by a partial diagonalization of the Hamiltonian in the basis of these two states,

$$H_{SC} = \begin{pmatrix} E_X & \hbar\Omega_R/2 \\ \hbar\Omega_R/2 & E_{P,H} \end{pmatrix}$$

where E_X and $E_{P,H}$ are the energies of the exciton and the photon (in the H polarization) and $\hbar\Omega_R$ is the Rabi splitting (the measure of the light-matter interaction). As we have seen in chapter 2 and 3, the exciton is approximately dispersionless, while the energy of the photon depends on the wave vector parabolically (due to the confinement in the cavity):

$$E_{P,H} = E_0 + \frac{\hbar^2 k^2}{2m_P}$$

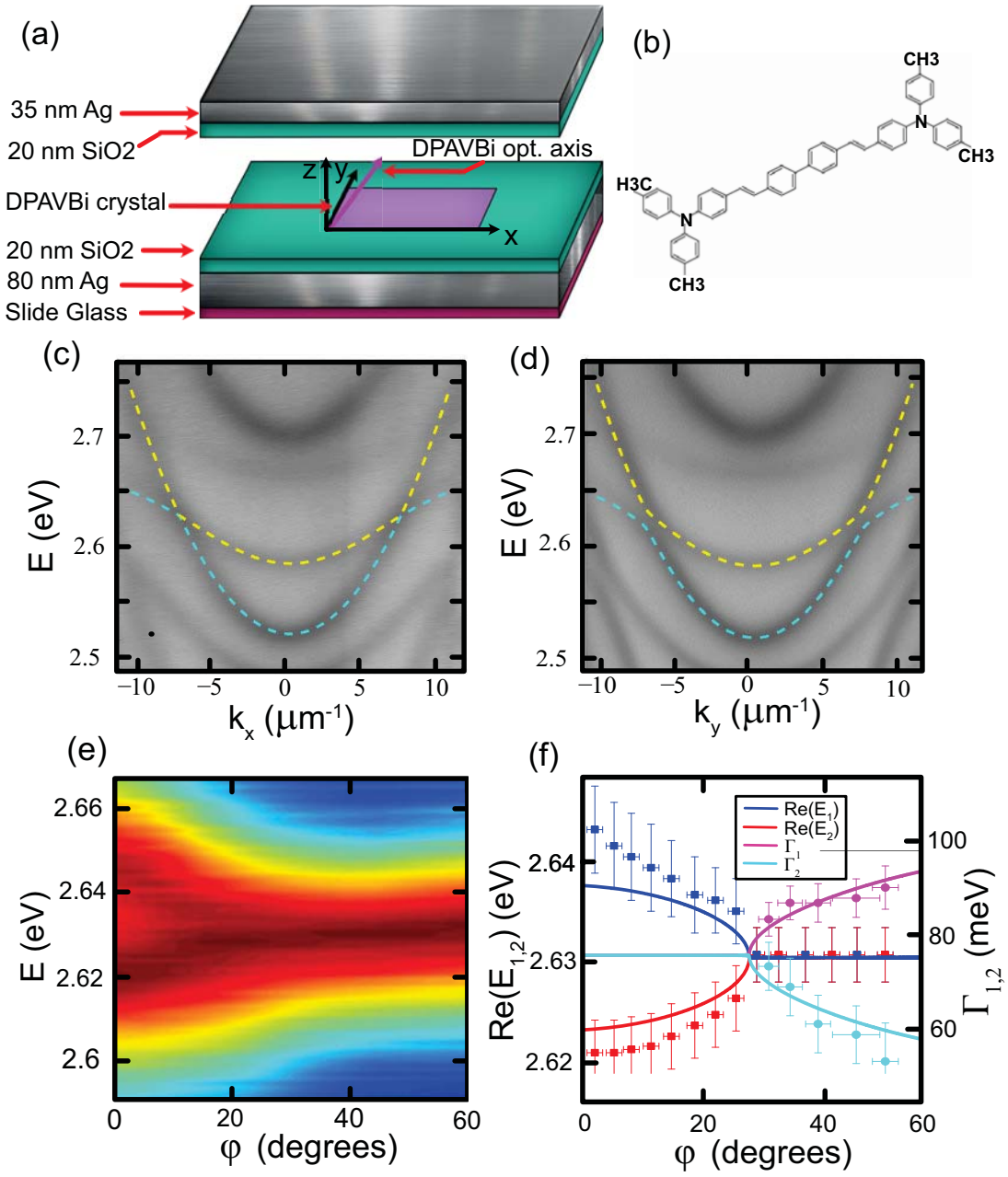

Figure 6.6: ***Reflectivity of the organic microcavity.*** *a) Scheme of the microcavity sample. b) Structure of the DPAVBi molecule. c), d) Reflectivity as a function of wave vector k_x and k_y (respectively) and energy, exhibiting anticrossing along k_y. e) Reflectivity as a function of the in-plane polar angle ϕ and energy E for $|k| = |k^*|$ (EP wave vector). f) Real and imaginary parts of the mode energies (dots with error bars – experiment, lines – theory).*

The diagonalization of the strong coupling Hamiltonian gives two H-polarized polariton eigenstates with the energies

$$E_{LPB,H} = \frac{E_X+E_{P,H}}{2} - \frac{\sqrt{\left(E_X-E_{P,H}\right)^2+\hbar^2\Omega_R^2}}{2}$$
$$E_{UPB,H} = \frac{E_X+E_{P,H}}{2} + \frac{\sqrt{\left(E_X-E_{P,H}\right)^2+\hbar^2\Omega_R^2}}{2}$$

Only the lower polariton is studied in our experiments since it is energetically well separated from the upper polariton branch. The effective mass of the lower polariton close to $k = 0$ can be found as

$$m_H = \frac{2m_P}{1-\frac{\delta}{\sqrt{\delta^2+\hbar^2\Omega^2}}} \tag{6.24}$$

where $\delta = E_0 - E_X$ is the exciton-photon detuning at zero wave vector. We see that at approximately zero detuning, the polariton mass is twice larger than the photonic mass, because of the mixing with the dispersionless excitonic mode (which has an infinite effective mass). On the other hand the photonic mode in the V-polarization keeps the bare photon mass:

$$m_V = m_P \tag{6.25}$$

For the same reason, the broadening of the polariton mode is at this detuning the average of the exciton and photon broadening. Since in our system the exciton broadening is substancially smaller than the photonic one, the polariton mode is narrower than the purely photonic mode.

Fig 6.7 shows the reflectivity spectrum along one direction in reciprocal space of a thicker cavity than the one studied in the main text and measured in both polarizations (a), and with H (b) and V polarization (c) only. These figures clearly show a series of weakly coupled Fabry-Perot modes in V-polarization and strongly to excitons in H polarizations. As visible on panel (a) these polarization modes become degenerates at some points. Half of these degenerecies give rise to an anti-crossing around which the modes become circularly polarized. These anti-crossings do not occur in the perpendicular direction of reciprocal space as illustrated with a thinner cavity on Fig. 1 of the main text. This anti-crossing occurs when modes of different parities are crossing. This effect of emergent optical activity was discovered and fully theoretically explained in [55] by solving Maxwell equations, with a qualitative explanation provided in [297]. In this case, the tilt of the optical axis of the birefringent material in the cavity shows up as an emergent optical activity in the direction determined by the direction of the tilt (if the optical axis is tilted from Z towards X, then the optical activity emerges along Y). This effect can be described as a term linear in k_y [55], which couples the two linear polarizations (H and V). Near the anticrossing point, it is possible to reduce the description of the system to two bands described by the following two by two Hamiltonian written in the *linear* polarization basis:

$$H_0 = \begin{pmatrix} \beta_0 + (\xi-\beta)(k_x^2+k_y^2) - i\Gamma - i\Gamma_0 & \chi k_y \\ \chi k_y & -\beta_0 + (\xi+\beta)(k_x^2+k_y^2) + i\Gamma - i\Gamma_0 \end{pmatrix} \tag{6.26}$$

where β_0 represents the splitting of the two modes at $k = 0$, $\xi = \hbar^2/2m^*$ with $m^* = \frac{2m_H m_V}{m_H + m_V}$, χ represents the optical activity along the k_y axis, and Γ is the difference in the broadening of the modes. Finally β describes the difference of the (inverse) effective masses of the two modes, which comes from the fact that one mode is coupled with the exciton, while there is no coupling for the other mode.

The theoretical dispersions calculated with the Hamiltonian 6.26 are shown in fig. 6.6(c,d) with dashed lines. The best fit is obtained with the following parameters: $\beta_0 = 130 \pm 9$ meV, $\Gamma = 11 \pm 4$ meV, $\beta = (1.00 \pm 0.07)$ meV/μm^{-2} , $m^* = (2.0 \pm 0.1) \times 10^{-5}$ m_e and $\chi = 1.8 \pm 0.6$ meV/μm^{-1}. The Hamiltonian is symmetric versus k_x and anti-symmetric versus k_y. Since the branches are crossing along k_x and anticrossing along k_y, there are necessarily 4 points at which the transition between the crossing and the anti-crossing occurs. These are the famous exceptional points characteristic for non-Hermitian systems. The plot of experimentally measured reflectivity spectra along a circle of constant $|k|$ passing through one of the exceptional points is shown in fig. 6.6(e). The extracted mode energies and linewidths are shown in fig. 6.6(f) with points, and the corresponding real and imaginary parts of the theoretical eigenenergies appear as solid lines. The extraction is performed by fitting the reflectivity spectra with Lorentzians (see fig. 6.7.d). In systems with perfectly balanced gain and losses, the exceptional points correspond to the transition between the PT-symmetric regime with real eigenvalues and the PT-broken regime with imaginary eigenvalues [298]. The same transition is still present in our case, in spite of the overall decay Γ_0, and the observed behavior of the modes confirms the presence of a second-order exceptional point at k^*.

6.4.4 Extraction of the Quantum Metric

We have demonstrated in chapter 4 that the eigenvalues do not tell everything about physical systems: the corresponding eigenstates are also important. While the famous Berry curvature and its integral, the Chern number, seem to be less relevant for non-Hermitian systems in the vicinity of exceptional points due to the essentially non-adiabatic behavior [289, 290], other quantities linked with the eigenstates, such as the Quantum Metric, play a key role in the wavepacket (beam) dynamics [161]. In chapter 5, we have shown that the measurement of the Stokes vector for each eigenstate in reciprocal space [160, 56] allows to extract the Quantum Metric using the definition of the Quantum Geometric Tensor (whose real part is the Quantum Metric, and the imaginary part is the Berry curvature):

$$g_{ij} = \mathrm{Re}\left[\langle\nabla\psi|\nabla\psi\rangle - \langle\psi|\nabla\psi\rangle\langle\nabla\psi|\psi\rangle\right] \tag{6.27}$$

where $|\psi\rangle$ is the eigenstate written as a spinor (similar to the Jones vector, but on the circular basis) as follows:

$$|\psi\rangle = \begin{vmatrix} \cos\frac{\theta}{2} e^{-i\phi} \\ \sin\frac{\theta}{2} \end{vmatrix} \tag{6.28}$$

and the angles $\theta = \arccos S_3$, $\phi = \arctan S_2/S_1$ characterize the orientation of the Stokes vector. We note that the gradient is taken in the parameter space (the reciprocal space).

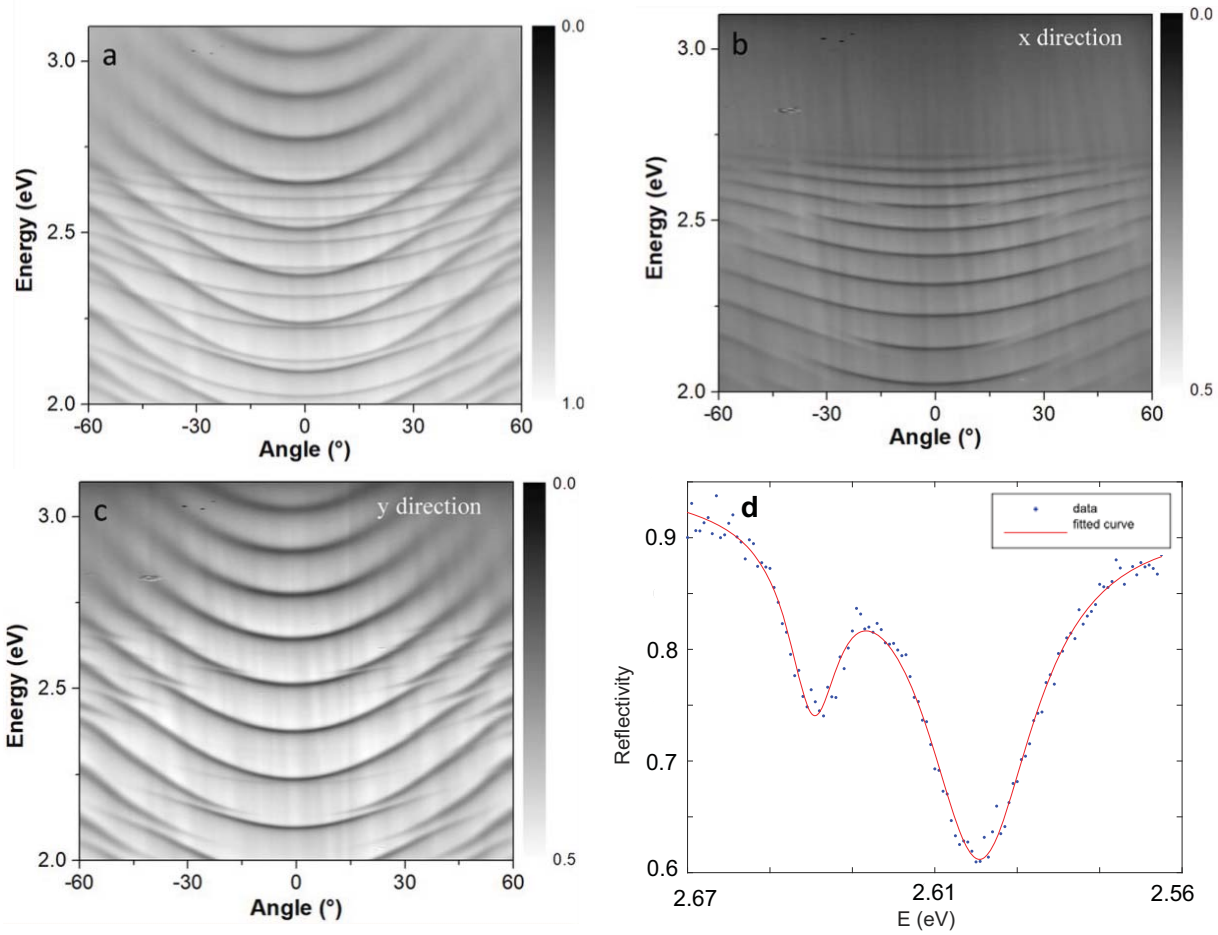

Figure 6.7: ***Branch anticrossings.*** *Anticrossing only appears for branches of opposite parity. Measured angle-resolved reflectivity spectrum of a microcavity with DPAVBi measured with both polarizations (a), (b) H-polarization and (c) V-polarization. The series of V-polarized modes are weakly coupled to photons and have comparable effective masses. The H-polarized modes are strongly coupled to excitons and shows an effective mass which is increase going to higher energy. On panel (a) one sees that H and V modes anticross each two crossings. When the measurments are performed along the perpendicular direction in reciprocal space, all anticrossing disappear, as shown in fig. 1 of the main text. Near anticrossing, modes are visible in both polarizations because they are circularly polarized. These distinct features of cavity modes are consistent with the fact of the highly ordered uniaxial alignment of DPAVBi molecules in single-crystalline microbelts. Anticrossings of the modes of opposite parity and crossings of the modes of same parity are both observed in the experiment. (d) Example of the reflectivity fit. The fit of the experimentally measured reflectivity spectrum for a particular point in the reciprocal space with a double Lorentzian, allowing to determine the real and imaginary parts of the eigenvalues.*

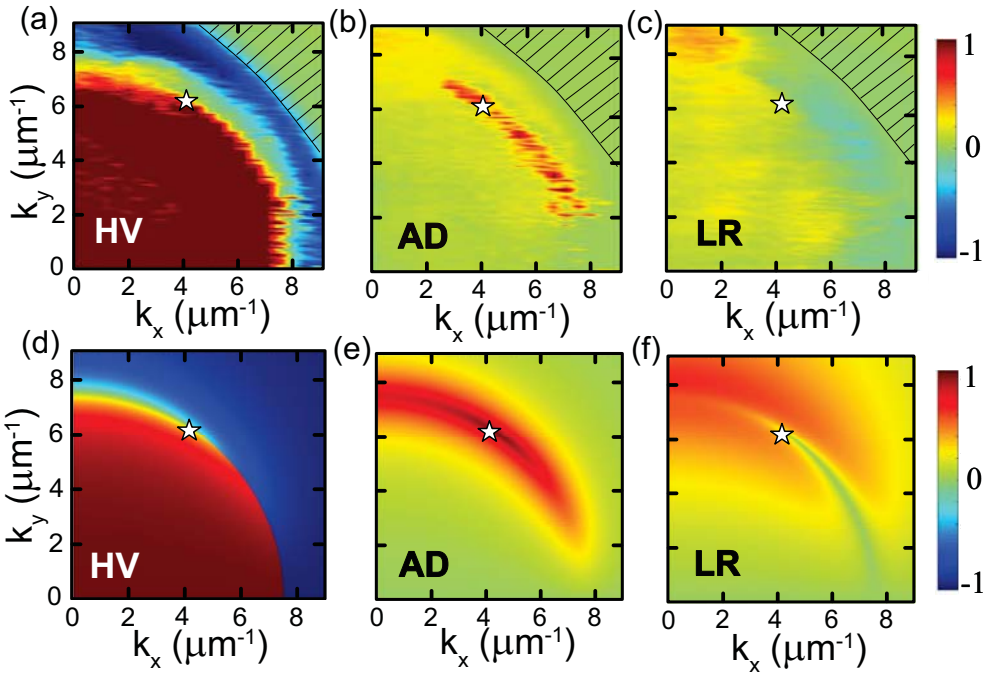

Figure 6.8: ***Stokes vector components of the lowest energy eigenstates (experiment and theory).*** *a)-c) experiment (S_1, S_2, S_3); d)-f) theory (S_1, S_2, S_3). The hatched region shows where the pseudospin could not be extracted experimentally.*

We now focus on a quarter of the reciprocal space containing a single exceptional point, and extract the Stokes vectors of the modes from polarization-resolved reflectivity measurements. In order to investigate the polarization properties, we placed a linear polarizer, half-wave plate, and a quarter-wave plate in front of the spectrometer slit to obtain the polarization state of each pixel in the k-space, horizontal-vertical (0° and 90°), diagonal (±45°) and circular ($\sigma+$ and $\sigma-$) basis. An energy spectrum is obtained in each of the six polarizations (H,V,D,A,L,R) for each point of the reciprocal space. We use a Lorentzian fit in order to get the positions, the relative intensities I, and the widths of the two modes, which permits the extraction of a 2D reciprocal space map of the Stokes vector components S_1, S_2, S_3 of the lower branch, shown in fig. 6.8(a-c). The validity of the effective 2×2 Hamiltonian 6.26 is confirmed by the good fit of the dispersions in fig. 6.6(c,d) and by the agreement between the experimentally extracted components of the Stokes vector (fig. 6.8(a-c)) and the theoretically calculated ones (fig. 6.8(d-f)). The EP located at $k_x^* = 4.01\ \mu\text{m}^{-1}$ and $k_y^* = 6.12\ \mu\text{m}^{-1}$ is shown by a white star. The two components S_1 and S_3 cancel at this point, while S_2 exhibits a maximum (similar to the circular polarization observed at the Voigt points).

Once the Stokes vectors are known, one can extract the Quantum Metric elements using Eq. 6.27, as described in details in [160]. The results of this extraction are shown as a 2D plot of the trace of the Quantum Metric $g_{xx} + g_{yy}$ in fig. 6.9(a). The uncertainty of the extracted points is of the order of 10% [56]. The part of the reciprocal space corresponding to the branch cut of the Riemann surface formed by the eigenstates is covered by a gray rectangle. The rectangular shape of the remaining regions facilitates their numerical treatment. A clear maximum is visible in the vicinity of the EP. The global behavior of the metric is in a

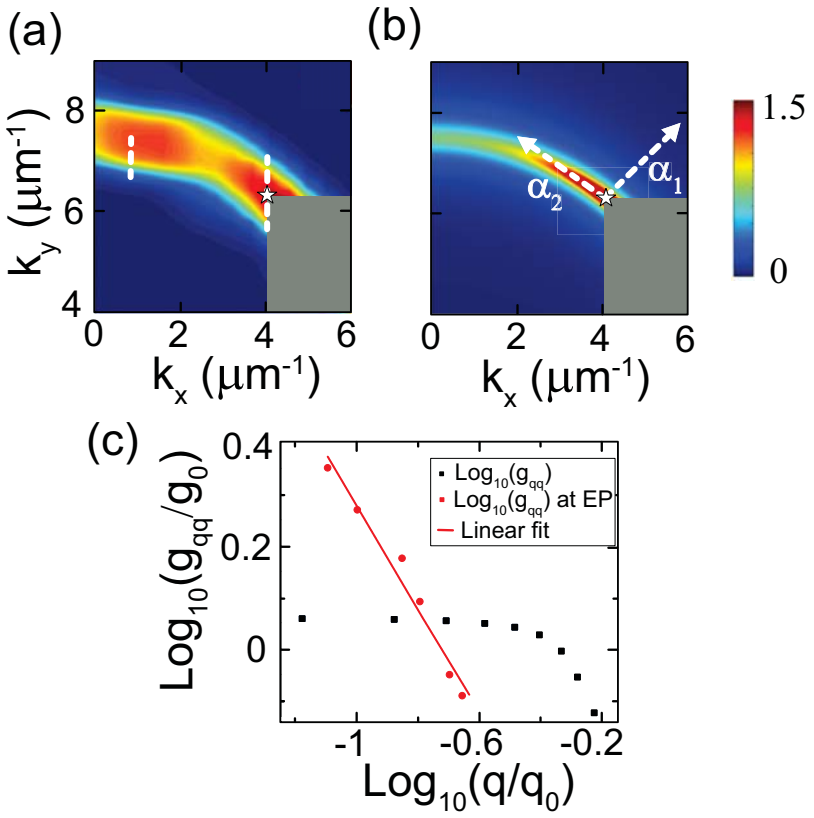

Figure 6.9: ***Quantum metric of an exceptional point.*** *2D maps of the trace of the Quantum Metric in the vicinity of an EP marked as a star: a) experiment; b) theory. The gray region covers the discontinuity of the wavefunction (branch cut). c) A log-log plot of the experimentally extracted Quantum Metric g_{qq} near $k_x = 0$ (black dots) and near the EP (red dots) and its fit (red line), giving the scaling exponent $n = -1.01 \pm 0.08$. The metric is extracted along the white dashed lines shown in panel a).*

good agreement with theoretical predictions based on the eigenstates of the Hamiltonian 6.26 (fig. 6.9b).

The Quantum Metric is known to diverge hyperbolically at the exceptional points of the second order (with 2 crossing branches) [268, 161], and an explicit expression for the metric in the vicinity of the exceptional point can be written as:

$$g_{qq} = \frac{\sqrt{{\alpha_1}^2\cos^2\phi' + {\alpha_2}^2\sin^2\phi'}}{8\Gamma q} + \frac{{\alpha_1}^2\cos'^2\phi + {\alpha_2}^2\sin^2\phi'}{16\Gamma^2} \qquad 6.29$$

where q is the wave vector measured from the exceptional point, and $\alpha_{1,2}$ (orientation shown by white arrows in fig. 6.9(b)) are proportional to the difference of the group velocities at the crossing point (the celerity of the effective Dirac Hamiltonian, see [296] for details). Experimentally, the values of the Quantum Metric are obtained only for a finite number of pixels in the reciprocal space, which can be close to the exceptional point, but never fall on it exactly. In order to demonstrate the hyperbolic divergence, we choose a particular direction in the reciprocal space, where the experimental resolution is the highest (k_y), and plot in fig. 6.9(c) the Quantum Metric in log-log scale for several experimental points (red

dots) closest to the exceptional point as a function of $q = |k_y - k_y^*|$ (using $q_0 = 1\ \mu\text{m}^{-1}$ and $g_0 = 1\ \mu\text{m}^2$ as characteristic scales). A fit with a power law $g_{qq} \sim q^n$ (black line) allows to determine the scaling of the Quantum Metric $n = -1.01 \pm 0.08$. The divergent behavior is best visible in comparison with another region, which exhibits a finite maximum (black points in fig. 6.9(c)) appearing as a horizontal asymptotic in log-log scale. Both regions are shown in fig. 6.9(a) as white lines. We can therefore conclude that we have observed the hyperbolic divergence of the Quantum Metric of a second-order exceptional point experimentally.

The agreement between the experiment and the theory can be checked further, by extracting the second (constant) term from the trace of the Quantum Metric and comparing it with the parameters of the effective Hamiltonian 6.26 obtained from the dispersions shown in fig. 6.6(c,d). For this, we fit the experimentally extracted values of the Quantum Metric with a function $f(q)$ corresponding to the reduced expression 6.29 of the Quantum Metric tensor g_{qq}:

$$f = \frac{\eta}{q} + 4\eta^2 \tag{6.30}$$

The fit of the metric gives $\eta = 0.173 \pm 0.004\ \mu m$. On the other hand, $\eta \approx \sqrt{\alpha_1^2 + \alpha_2^2}/8\sqrt{2}\Gamma$. We take the parameters of the Hamiltonian extracted from the fit of the experimental dispersion in fig. 6.6: $\Gamma = 11 \pm 0.4$ meV and the celerity parameter $\sqrt{\alpha_1^2 + \alpha_2^2}/\sqrt{2} = 14 \pm 2$ meV$/\mu\text{m}^{-1}$, which gives $\eta_{exp} = 0.16 \pm 0.06 \mu m$. This agreement validates both the metric extraction procedure and the theoretical analysis of the Hamiltonian and its eigenstates.

Our results demonstrate the advantages of the optical systems for the studies of advanced quantum-mechanical effects, such as the properties of exceptional points in non-Hermitian systems. We have managed not only to extract the real and imaginary parts of the eigenenergies, which determine the topology of the exceptional point, but also studied the eigenstates and their variation with parameters. The main property of exceptional points is the divergence of the characteristic derivatives in their vicinity. This divergence is responsible for enhanced sensing properties of these points. While it is very well known that the derivative of the real part of the energy diverges as $q^{-1/2}$, the hyperbolic q^{-1} divergence of the eigenstates measured by the Quantum Metric is much less known. Yet, it determines the overlap integrals and therefore the possibilities to excite and to measure the states in vicinity of exceptional points, and, ultimately, to benefit from the enhanced sensing.

The possibilities of extraction of the eigenstates and their metric are determined by the experimental resolution in the reciprocal space. In our case, we had to use the axis with the smallest experimental step in order to get sufficiently close to the exceptional point and to be able to evidence the particular power law of the divergence. The observation of this power law on a larger scale would require smaller steps and higher stability of the experimental platform, in order to avoid the broadening in the k-space. Disorder-induced mixing of the wave vectors also restrains the possibilities of approaching the exceptional point. The same considerations apply to enhanced sensing: enhancement applies not only to the useful signal, but also to the noise [299], which therefore must be reduced as much as possible.

6.4.5 Conclusion

To conclude, we have studied exceptional points in an organic microcavity. We have extracted the Stokes vectors of the eigenstates in the vicinity of the exceptional point and then calculated the Quantum Metric tensor. Our measurements confirm that the Quantum Metric of a second-order exceptional point exhibits a hyperbolic divergence. This is expected to affect the dynamics of wavepacket (the trajectories of optical beams) at exceptional points.

6.5 Chapter conclusion

In this last chapter, we have investigated non-Hermitian physics. In photonics, losses are naturally present, and the difference of losses between two eigenstates results in non-Hermiticity in the system. We have demonstrated that it happens with effects such as polarization-dependent absorption (dichroism), and polarization-selective strong coupling. This non-Hermiticity transforms a Dirac point into a pair of exceptional points, linked by a Fermi arc. We have theoretically demonstrated the $1/q$ divergence of the Quantum Metric at exceptional points of 2^{nd} order, where q is the wavevector starting to this point. Shortly after this result was confirmed experimentally, in the first extraction of the Quantum Geometric Tensor in a non-Hermitian system. The divergence of the Quantum Metric results in a polarization-dependent dynamics of a wavepacket centered at the exceptional point. This complex dynamics can be expressed with Quantum Metric terms.

Conclusion and perspectives

In this thesis, we have studied the quantum geometry of different photonic Dirac systems. First of all, we have provided a general introduction in the first four chapters. In the 5^{th} Chapter, we first presented a peculiar system which allows to simulate a non-Abelian Yang-Mills theory by exciting coherently two bands near the Dirac point. The spin precession is coupled with the spatial dynamics, and the wavepacket exhibits Zitterbewegung oscillations. It is the opposite limit of a prior work, describing the adiabatic excitation of a single band, and exhibiting a photonic anomalous Hall effect. Nevertheless, we have developed universal semiclassical equations, based on the Quantum Metric, describing both these effects, and every regime in between. The square root of the Quantum Metric appears as a universal length scale, and provide a geometrical origin of the Compton wavelength. This chapter ends with the study of an experimental work on a semiconductor monolayer embedded in a microcavity. We show that a spin-selective strong light-matter coupling regime results in unusually strong optical nonlinearity and a giant Zeeman effect, which allows to open a gap at the Dirac point in polaritonic systems, and which has direct applications in topological physics.

Finally, we have investigated non-Hermitian physics in the 6^{th} Chapter. The losses, which appear naturally in photonic systems, are a crucial feature to obtain non-Hermiticity. Different losses for different eigenstates transform a Dirac point into a pair of exceptional points linked by a Fermi arc. We have demonstrated that the dynamics of a wavepacket centered at an exceptional point can be expressed with Quantum Metric terms. In the last part of the Chapter we presented the first experimental measurement of the Quantum Metric in a non-Hermitian system, where the non-Hermiticity comes from selective polarization strong-coupling. We demonstrated the divergence of the Quantum Metric, accordingly to the theory, near the 2^{nd} order exceptional point.

Our works have shed light on the role of the quantum metric in Physics, which has turned out to be much deeper than found in the first studies. And there is surely much more to be discovered.

These results appeal for further studies. First, a system of universal semiclassical equations can be derived from the Hamilton's equations for an arbitrary number of bands. As in the two-band case, the terms containing the Quantum Metric appear from the variation of the overlap integral, which is determined by the variation of the length of the corresponding geodesic curve, which is entirely determined by the product of the Quantum Metric g_{kk} and the projection of the displacement δk_j on the geodesic's tangent vector. Deriving such equations for n-band systems might be an important step forward.

Also, the maximal value of the trace of the Quantum Metric is an important physical quantity. This maximal value determines the extension of the metric in the parameter space, that is, the characteristic scale at which the changes occur (for example, level crossing), because the integral of the Quantum Metric is often quantized, representing a topological invariant similar to the Chern number. It determines both the maximal amplitude of the Zitterbewegung oscillations and of the anomalous Hall drift. One could demonstrate that it

determines the spatial extension of the chiral edge state in topological insulators, controlling the minimal size of topological lasers and optical isolators. Thus, the quantum metric will be an important quantity for future applications based on quantum geometry.

Finally, the divergence of the Quantum Metric can be different for higher-order exceptional points. Similar polarization dependent trajectories can be expected, and the dynamics of wavepackets (lightbeams) centered around these points could also be understood with Quantum Metric terms. The knowledge of the Quantum Metric allows to understand how fast the states change near exceptional points, that is to say the sensitivity of the system to a small perturbation near this singularity. It will be important in the future in order to build enhanced (exceptional) sensors.

Bibliography

[1] R. P. Feynman, F. L. Vernon, and R. W. Hellwarth, "Geometrical representation of the schrödinger equation for solving maser problems," *J. Appl. Phys.*, vol. 28, no. 1, pp. 49–52, Jan. 1957. [Online]. Available: http://aip.scitation.org/doi/10.1063/1.1722572 (cited on pages 15, 16, 43, 61, and 73)

[2] C. Leblanc, G. Malpuech, and D. D. Solnyshkov, "High-frequency exciton-polariton clock generator," *Phys. Rev. B: Condens. Matter Mater. Phys.*, vol. 101, no. 11, p. 115418, Mar. 2020. [Online]. Available: https://link.aps.org/doi/10.1103/PhysRevB.101.115418 (cited on pages 15 and 38)

[3] I. I. Rabi, N. F. Ramsey, and J. Schwinger, "Use of rotating coordinates in magnetic resonance problems," *Rev. Mod. Phys.*, vol. 26, no. 2, pp. 167–171, Apr. 1954. [Online]. Available: https://link.aps.org/doi/10.1103/RevModPhys.26.167 (cited on page 16)

[4] F. Bloch, "Nuclear induction," *Physical Review*, vol. 70, no. 7-8, pp. 460–474, Oct. 1946. [Online]. Available: https://link.aps.org/doi/10.1103/PhysRev.70.460 (cited on page 16)

[5] C. Tannoudji, B. Diu, and F. Laloë, *Mécanique Quantique*, CNRS/EDP Sciences, Ed., 2018. (cited on pages 16 and 73)

[6] B. Schumacher, "Quantum coding," *Phys. Rev. A*, vol. 51, no. 4, pp. 2738–2747, Apr. 1995. [Online]. Available: https://link.aps.org/doi/10.1103/PhysRevA.51.2738 (cited on page 16)

[7] A. Kavokin and G. Malpuech, *Cavity Polaritons*. Elsevier, 2003. (cited on pages 16, 38, and 86)

[8] R. Saito, G. Dresselhaus, and M. S. Dresselhaus, *Physical Properties of Carbon Nanotubes*. Press, Imperial College, 1998. [Online]. Available: https://www.worldscientific.com/worldscibooks/10.1142/p080 (cited on page 17)

[9] R. Bistritzer and A. H. MacDonald, "Moiré bands in twisted double-layer graphene," *Proceedings of the National Academy of Sciences*, vol. 108, no. 30, pp. 12 233–12 237, Jul. 2011. [Online]. Available: https://pnas.org/doi/full/10.1073/pnas.1108174108 (cited on page 17)

[10] K. S. Novoselov, A. K. Geim, S. V. Morozov, D. Jiang, M. I. Katsnelson, I. V. Grigorieva, S. V. Dubonos, and A. A. Firsov, "Two-dimensional gas of massless dirac fermions in graphene," *Nature*, vol. 438, no. 7065, pp. 197–200, 2005. [Online]. Available: https://www.nature.com/articles/nature04233 (cited on pages 17 and 24)

[11] K. S. Novoselov, S. V. Morozov, A. K. Geim, V. V. Khotkevich, T. J. Booth, F. Schedin, and D. Jiang, "Two-dimensional atomic crystals," *Phys. Today*, vol. 58, no. 9, pp. 9–9,

2005. [Online]. Available: https://physicstoday.scitation.org/doi/10.1063/1.4797258 (cited on page 17)

[12] K. S. Novoselov, A. K. Geim, S. V. Morozov, D. Jiang, Y. Zhang, S. V. Dubonos, I. V. Grigorieva, and A. A. Firsov, "Electric field effect in atomically thin carbon films," *Science*, vol. 306, no. 5696, pp. 666–669, Oct. 2004. [Online]. Available: https://www.science.org/doi/10.1126/science.1102896 (cited on page 17)

[13] J. H. Chen, C. Jang, S. Xiao, M. Ishigami, and M. S. Fuhrer, "Intrinsic and extrinsic performance limits of graphene devices on SiO 2," *Nat. Nanotechnol.*, vol. 3, no. 4, pp. 206–209, 2008. [Online]. Available: http://dx.doi.org/10.1038/nnano.2008.58 (cited on page 17)

[14] A. H. Castro Neto, F. Guinea, N. M. R. Peres, K. S. Novoselov, and A. K. Geim, "The electronic properties of graphene," *Rev. Mod. Phys.*, vol. 81, no. 1, pp. 109–162, Jan. 2009. [Online]. Available: https://link.aps.org/doi/10.1103/RevModPhys.81.109 (cited on pages 17, 19, and 21)

[15] N. W. Ashcroft and N. D. Mermin, *Solid State Physic*, C. Brooks, Ed. EDP Sciences, 1976. (cited on pages 18, 49, 52, and 69)

[16] P. R. Wallace, "The band theory of graphite," *Physical Review*, vol. 71, no. 9, pp. 622–634, May 1947. [Online]. Available: https://link.aps.org/doi/10.1103/PhysRev.71.622 (cited on pages 19 and 21)

[17] E. I. Rashba and V. I. Sheka, "Symmetry of energy bands in crystals of wurtzite type II. symmetry of bands with Spin-Orbit interaction included," *New J. Phys.*, vol. 17, no. 1, pp. 50 202–50 368, 1959. (cited on pages 21 and 153)

[18] H. Terças, H. Flayac, D. D. Solnyshkov, and G. Malpuech, "Non-Abelian gauge fields in photonic cavities and photonic superfluids," *Phys. Rev. Lett.*, vol. 112, no. 6, p. 66402, 2014. (cited on pages 21, 34, 61, 62, and 73)

[19] G. Dresselhaus, "Spin-Orbit coupling effects in zinc blende structures," *Physical Review*, vol. 100, no. 2, pp. 580–586, Oct. 1955. [Online]. Available: https://link.aps.org/doi/10.1103/PhysRev.100.580 (cited on pages 21 and 153)

[20] H. Graham Flegg, *From Geometry to Topology*. Dover Publications, 1974. (cited on page 21)

[21] D. S. Simon, "Topology and physics: a historical overview," in *Tying Light in Knots: Applying topology to optics*. Morgan & Claypool Publishers, Nov. 2018. [Online]. Available: https://iopscience.iop.org/book/mono/978-1-64327-234-4/chapter/bk978-1-64327-234-4ch1.pdf (cited on pages 21 and 49)

[22] M. Epple, "Topology, matter, and space, i: Topological notions in 19th-century natural philosophy," *Arch. Hist. Exact Sci.*, vol. 52, no. 4, pp. 297–392, Feb. 1998. [Online]. Available: https://doi.org/10.1007/s004070050019 (cited on pages 21 and 49)

[23] H. Poincaré, "Analysis situs," *Journal de l'école Polytechnique*, 1895. [Online]. Available: http://utenti.quipo.it/base5/fano/Fano_topologia_1.pdf (cited on pages 21 and 49)

[24] K. von Klitzing, "The quantized hall effect," *Rev. Mod. Phys.*, vol. 58, no. 3, pp. 519–531, Jul. 1986. [Online]. Available: https://link.aps.org/doi/10.1103/RevModPhys.58.519 (cited on pages 21 and 49)

[25] C.-H. Park and N. Marzari, "Berry phase and pseudospin winding number in bilayer graphene," *Phys. Rev. B: Condens. Matter Mater. Phys.*, vol. 84, no. 20, p. 205440, Nov. 2011. [Online]. Available: https://link.aps.org/doi/10.1103/PhysRevB.84.205440 (cited on page 22)

[26] P. Delplace, D. Ullmo, and G. Montambaux, "Zak phase and the existence of edge states in graphene," *Phys. Rev. B: Condens. Matter Mater. Phys.*, vol. 84, no. 19, p. 195452, Nov. 2011. [Online]. Available: https://link.aps.org/doi/10.1103/PhysRevB.84.195452 (cited on page 22)

[27] G. Montambaux, F. Piéchon, J.-N. Fuchs, and M. O. Goerbig, "Merging of dirac points in a two-dimensional crystal," *Phys. Rev. B: Condens. Matter Mater. Phys.*, vol. 80, no. 15, p. 153412, Oct. 2009. [Online]. Available: https://link.aps.org/doi/10.1103/PhysRevB.80.153412 (cited on page 22)

[28] L. Tarruell, D. Greif, T. Uehlinger, G. Jotzu, and T. Esslinger, "Creating, moving and merging dirac points with a fermi gas in a tunable honeycomb lattice," *Nature*, vol. 483, no. 7389, pp. 302–305, Mar. 2012. [Online]. Available: http://www.nature.com/articles/nature10871 (cited on page 22)

[29] P. A. M. Dirac, "The quantum theory of the electron," *Proceedings of the Royal Society of London. Series A, Containing Papers of a Mathematical and Physical Character*, vol. 117, no. 778, pp. 610–624, 1928. [Online]. Available: https://royalsocietypublishing.org/doi/10.1098/rspa.1928.0023 (cited on page 23)

[30] ——, "Quantised singularities in the electromagnetic field„" *Proc. R. Soc. Lond.*, vol. 133, no. 821, pp. 60–72, Sep. 1931. [Online]. Available: https://royalsocietypublishing.org/doi/10.1098/rspa.1931.0130 (cited on pages 23 and 49)

[31] G. W. Semenoff, "Condensed-Matter simulation of a Three-Dimensional anomaly," *Phys. Rev. Lett.*, vol. 53, no. 26, pp. 2449–2452, Dec. 1984. [Online]. Available: https://link.aps.org/doi/10.1103/PhysRevLett.53.2449 (cited on page 24)

[32] A. K. Geim and K. S. Novoselov, "The rise of graphene," *Nat. Mater.*, vol. 6, no. 3, pp. 183–191, Mar. 2007. [Online]. Available: http://www.nature.com/articles/nmat1849 (cited on page 24)

[33] A. Rycerz, J. Tworzydło, and C. W. J. Beenakker, "Valley filter and valley valve in graphene," *Nat. Phys.*, vol. 3, no. 3, pp. 172–175, 2007. [Online]. Available: https://www.nature.com/articles/nphys547 (cited on page 24)

[34] H. Kim, K.-Y. Park, J. Hong, and K. Kang, "All-graphene-battery: bridging the gap between supercapacitors and lithium ion batteries," *Sci. Rep.*, vol. 4, no. 1, p. 5278, May 2015. [Online]. Available: http://www.nature.com/articles/srep05278 (cited on page 24)

[35] L. Lavagna, G. Meligrana, C. Gerbaldi, A. Tagliaferro, and M. Bartoli, "Graphene and Lithium-Based battery electrodes: A review of recent literature," *Energies*, vol. 13, no. 18, p. 4867, Sep. 2020. [Online]. Available: https://www.mdpi.com/1996-1073/13/18/4867 (cited on page 24)

[36] "Graphene opens up to new applications," *Nat. Nanotechnol.*, vol. 10, no. 5, p. 381, May 2015. [Online]. Available: http://dx.doi.org/10.1038/nnano.2015.110 (cited on page 24)

[37] J.-H. Ahn and B. H. Hong, "Graphene for displays that bend," *Nat. Nanotechnol.*, vol. 9, no. 10, pp. 737–738, Oct. 2014. [Online]. Available: http://dx.doi.org/10.1038/nnano.2014.226 (cited on page 24)

[38] "Things you could do with graphene," *Nat. Nanotechnol.*, vol. 9, no. 10, pp. 737–737, Oct. 2014. [Online]. Available: https://www.nature.com/articles/nnano.2014.245 (cited on page 24)

[39] F. Schedin, A. K. Geim, S. V. Morozov, E. W. Hill, P. Blake, M. I. Katsnelson, and K. S. Novoselov, "Detection of individual gas molecules adsorbed on graphene," *Nat. Mater.*, vol. 6, no. 9, pp. 652–655, Sep. 2007. [Online]. Available: http://www.nature.com/articles/nmat1967 (cited on page 24)

[40] M. J. Molaei, M. Younas, and M. Rezakazemi, "A comprehensive review on recent advances in Two-Dimensional (2d) hexagonal boron nitride," *ACS Applied Electronic Materials*, vol. 3, no. 12, pp. 5165–5187, Dec. 2021. [Online]. Available: https://pubs.acs.org/doi/10.1021/acsaelm.1c00720 (cited on page 24)

[41] S. Shree, I. Paradisanos, X. Marie, C. Robert, and B. Urbaszek, "Guide to optical spectroscopy of layered semiconductors," *Nature Reviews Physics*, vol. 3, no. 1, pp. 39–54, Jan. 2021. [Online]. Available: http://www.nature.com/articles/s42254-020-00259-1 (cited on page 24)

[42] Y. Li, M. Amado, T. Hyart, G. P. Mazur, and J. W. A. Robinson, "Topological valley currents via ballistic edge modes in graphene superlattices near the primary dirac point," *Communications Physics*, vol. 3, no. 1, p. 224, Dec. 2020. [Online]. Available: http://www.nature.com/articles/s42005-020-00495-y (cited on page 24)

[43] M. V. Berry and M. R. Jeffrey, "Chapter 2 conical diffraction: Hamilton's diabolical point at the heart of crystal optics," *Progress in Optics*, vol. 50, no. 07, pp. 13–50, 2007. [Online]. Available: http://dx.doi.org/10.1016/S0079-6638(07)50002-8 (cited on pages 27 and 29)

[44] L. D. Landau and E. M. Lifshitz, *Electrodynamics of Continuous Media -Volume 8 of Theoretical Physics*. Oxford, 1984. (cited on page 28)

[45] W. R. Hamilton, "Third supplement to an essay on the theory of systems of rays," *Royal Irish Academy*, vol. 17, no. 1837, pp. 1–144, 1837. (cited on page 28)

[46] H. Lloyd, "On the phenomena presented by light in its passage along the axes of biaxal crystals," *The Transactions of the Royal Irish Academy*, pp. 145–157, 1831. (cited on page 28)

[47] M. V. Berry, M. R. Jeffrey, and J. G. Lunney, "Conical diffraction: Observations and theory," *Proceedings of the Royal Society A: Mathematical, Physical and Engineering Sciences*, vol. 462, no. 2070, pp. 1629–1642, 2006. [Online]. Available: http://dx.doi.org/10.1098/rspa.2006.1680 (cited on page 28)

[48] E. Rosencher and B. Vinter, *Optoelectronics*. Cambridge University Press, 2004. [Online]. Available: https://www.cambridge.org/core/books/optoelectronics/86B6621671230A798D5BFBE24266EE3F (cited on pages 31 and 32)

[49] A. Kuther, M. Bayer, T. Gutbrod, A. Forchel, P. A. Knipp, T. L. Reinecke, and R. Werner, "Confined optical modes in photonic wires," *Phys. Rev. B: Condens. Matter Mater. Phys.*, vol. 58, no. 23, pp. 15 744–15 748, Dec. 1998. [Online]. Available: https://link.aps.org/doi/10.1103/PhysRevB.58.15744 (cited on page 33)

[50] G. Panzarini, L. C. Andreani, A. Armitage, D. Baxter, M. S. Skolnick, V. N. Astratov, J. S. Roberts, A. V. Kavokin, M. R. Vladimirova, and M. A. Kaliteevski, "Cavity-polariton dispersion and polarization splitting in single and coupled semiconductor microcavities," *Phys. Solid State*, vol. 41, no. 8, pp. 1223–1238, Aug. 1999. [Online]. Available: http://link.springer.com/10.1134/1.1130973 (cited on page 33)

[51] ——, "Exciton-light coupling in single and coupled semiconductor microcavities: Polariton dispersion and polarization splitting," *Phys. Rev. B: Condens. Matter Mater. Phys.*, vol. 59, no. 7, pp. 5082–5089, Feb. 1999. [Online]. Available: https://link.aps.org/doi/10.1103/PhysRevB.59.5082 (cited on page 33)

[52] A. Kavokin, G. Malpuech, and M. Glazov, "Optical spin hall effect," *Phys. Rev. Lett.*, vol. 95, no. 13, pp. 2–5, 2005. [Online]. Available: http://dx.doi.org/10.1103/PhysRevLett.95.136601 (cited on pages 33, 43, 44, and 76)

[53] Ł. Kłopotowski, M. D. Martín, A. Amo, L. Viña, I. A. Shelykh, M. M. Glazov, G. Malpuech, A. V. Kavokin, and R. André, "Optical anisotropy and pinning of the linear polarization of light in semiconductor microcavities," *Solid State Commun.*, vol. 139, no. 10, pp. 511–515, Sep. 2006. [Online]. Available: https://linkinghub.elsevier.com/retrieve/pii/S0038109806006211 (cited on page 34)

[54] L. Polimeno, A. Fieramosca, G. Lerario, L. De Marco, M. De Giorgi, D. Ballarini, L. Dominici, V. Ardizzone, M. Pugliese, C. T. Prontera, V. Maiorano,

G. Gigli, C. Leblanc, G. Malpuech, D. D. Solnyshkov, and D. Sanvitto, "Experimental investigation of a non-abelian gauge field in 2D perovskite photonic platform," *Optica*, vol. 8, no. 11, p. 1442, Nov. 2021. [Online]. Available: https://opg.optica.org/optica/fulltext.cfm?uri=optica-8-11-1442&id=464680 (cited on pages 34, 61, 62, 64, 73, 78, and 102)

[55] K. Rechcinska, M. Król, R. Mazur, P. Morawiak, R. Mirek, K. Łempicka, W. Bardyszewski, M. Matuszewski, P. Kula, W. Piecek, P. G. Lagoudakis, B. Pietka, and J. Szczytko, "Engineering spin-orbit synthetic hamiltonians in liquid-crystal optical cavities : supplementary," *Science*, vol. 366, no. 6466, pp. 727–730, 2019. [Online]. Available: http://dx.doi.org/10.1126/science.aay4182 (cited on pages 34, 61, 65, 107, and 109)

[56] A. Gianfrate, O. Bleu, L. Dominici, V. Ardizzone, M. De Giorgi, D. Ballarini, G. Lerario, K. W. West, L. N. Pfeiffer, D. D. Solnyshkov, D. Sanvitto, and G. Malpuech, "Measurement of the quantum geometric tensor and of the anomalous hall drift," *Nature*, vol. 578, no. 7795, pp. 381–385, 2020. [Online]. Available: http://dx.doi.org/10.1038/s41586-020-1989-2 (cited on pages 34, 43, 58, 61, 65, 66, 71, 72, 77, 78, 105, 110, and 112)

[57] A. Gelfert, "Manipulative success and the unreal," *Int. Stud. Philos. Sci.*, vol. 17, no. 3, pp. 245–263, Oct. 2003. [Online]. Available: http://www.tandfonline.com/doi/abs/10.1080/0269859032000169451 (cited on page 37)

[58] L. Venema, B. Verberck, I. Georgescu, G. Prando, E. Couderc, S. Milana, M. Maragkou, L. Persechini, G. Pacchioni, and L. Fleet, "The quasiparticle zoo," *Nat. Phys.*, vol. 12, no. 12, pp. 1085–1089, Dec. 2016. [Online]. Available: http://www.nature.com/articles/nphys3977 (cited on page 37)

[59] J. J. Hopfield, "Theory of the contribution of excitons to the complex dielectric constant of crystals," *Physical Review*, vol. 112, no. 5, pp. 1555–1567, 1958. [Online]. Available: http://dx.doi.org/10.1103/PhysRev.112.1555 (cited on page 38)

[60] V. M. Agranovich, "Dispersion of electromagnetic waves in crystals," *Sov. Phys. JETP*, vol. 37, no. 2, pp. 307–313, 1960. (cited on page 38)

[61] C. Weisbuch, M. Nishioka, A. Ishikawa, and Y. Arakawa, "Observation of the coupled exciton-photon mode splitting in a semiconductor quantum microcavity," *Phys. Rev. Lett.*, vol. 69, no. 23, pp. 3314–3317, 1992. [Online]. Available: http://link.aps.org/doi/10.1103/PhysRevLett.69.3314 (cited on page 38)

[62] D. D. Solnyshkov, G. Malpuech, P. St-Jean, S. Ravets, J. Bloch, and A. Amo, "Microcavity polaritons for topological photonics [invited]," *Opt. Mater. Express*, vol. 11, no. 4, p. 1119, Apr. 2021. [Online]. Available: https://opg.optica.org/abstract.cfm?URI=ome-11-4-1119 (cited on pages 38, 44, 46, and 72)

[63] D. D. Solnyshkov, C. Leblanc, S. V. Koniakhin, O. Bleu, and G. Malpuech, "Quantum analogue of a kerr black hole and the penrose effect in a Bose-Einstein condensate," *Phys. Rev. B: Condens. Matter Mater. Phys.*, vol. 99, p. 214511, 2019. [Online]. Available: https://journals.aps.org/prb/pdf/10.1103/PhysRevB.99.214511 (cited on pages 38 and 42)

[64] D. D. Solnyshkov, C. Leblanc, I. Septembre, and G. Malpuech, "Domain-Wall topology induced by spontaneous symmetry breaking in polariton graphene," *Phys. Rev. Lett.*, vol. 129, no. 6, p. 066802, Aug. 2022. [Online]. Available: http://dx.doi.org/10.1103/PhysRevLett.129.066802 (cited on pages 38, 41, and 53)

[65] P. G. Savvidis, J. J. Baumberg, R. M. Stevenson, M. S. Skolnick, D. M. Whittaker, and J. S. Roberts, "Angle-Resonant stimulated polariton amplifier," *Phys. Rev. Lett.*, vol. 84, no. 7, pp. 1547–1550, Feb. 2000. [Online]. Available: https://link.aps.org/doi/10.1103/PhysRevLett.84.1547 (cited on pages 38 and 43)

[66] A. Baas, J. P. Karr, H. Eleuch, and E. Giacobino, "Optical bistability in semiconductor microcavities," *Phys. Rev. A*, vol. 69, no. 2, p. 023809, Feb. 2004. [Online]. Available: https://link.aps.org/doi/10.1103/PhysRevA.69.023809 (cited on pages 38 and 43)

[67] D. Ballarini, M. De Giorgi, E. Cancellieri, R. Houdré, E. Giacobino, R. Cingolani, A. Bramati, G. Gigli, and D. Sanvitto, "All-optical polariton transistor," *Nat. Commun.*, vol. 4, 2013. [Online]. Available: http://dx.doi.org/10.1038/ncomms2734 (cited on page 38)

[68] J. Kasprzak, M. Richard, S. Kundermann, A. Baas, P. Jeambrun, J. M. J. Keeling, F. M. Marchetti, M. H. Szymańska, R. André, J. L. Staehli, V. Savona, P. B. Littlewood, B. Deveaud, and L. S. Dang, "Bose–Einstein condensation of exciton polaritons," *Nature*, vol. 443, no. 7110, pp. 409–414, Sep. 2006. [Online]. Available: http://www.nature.com/articles/nature05131 (cited on pages 38 and 41)

[69] R. Balili, V. Hartwell, D. Snoke, L. Pfeiffer, and K. West, "Bose-Einstein condensation of microcavity polaritons in a trap," *Science*, vol. 316, no. 5827, pp. 1007–1010, May 2007. [Online]. Available: https://www.science.org/doi/10.1126/science.1140990 (cited on page 38)

[70] D. Sanvitto and S. Kéna-Cohen, "The road towards polaritonic devices," *Nat. Mater.*, vol. 15, no. 10, pp. 1061–1073, Oct. 2016. [Online]. Available: https://www.nature.com/articles/nmat4668 (cited on page 38)

[71] A. Einstein, "Quantentheorie des einatomigen idealen gases," in *Albert Einstein: Akademie-Vorträge*. Wiley, Dec. 2005, pp. 237–244. [Online]. Available: https://onlinelibrary.wiley.com/doi/10.1002/3527608958.ch27 (cited on page 40)

[72] S. N. Bose, "Plancks gesetz und lichtquantenhypothese," *Zeitschrift for Physik*, vol. 26, no. 1, pp. 178–181, Dec. 1924. [Online]. Available: http://link.springer.com/10.1007/BF01327326 (cited on page 40)

[73] L. Pitaevskii and S. Stringari, *Bose-Einstein Condensation and Superfluidity*. Oxford University Press, Jan. 2016. [Online]. Available: https://oxford.universitypressscholarship.com/view/10.1093/acprof:oso/9780198758884.001.0001/acprof-9780198758884 (cited on pages 40 and 41)

[74] N. N. Bogolyubov, "On the theory of superfluidity," *J. Phys. (USSR)*, vol. 11, pp. 23–32, 1947. (cited on page 40)

[75] E. P. Gross, "Structure of a quantized vortex in boson systems," *Nuovo Cimento: C: Geophys. Space Phys.*, vol. 20, no. 3, pp. 454–477, May 1961. [Online]. Available: http://link.springer.com/10.1007/BF02731494 (cited on page 41)

[76] L. Pitaevskii, "Vortex lines in an imperfect bose gas," *J. Exptl. Theoret. Phys. (USSR)*, vol. 40, pp. 646–651, 1961. [Online]. Available: http://jetp.ras.ru/cgi-bin/dn/e_013_02_0451.pdf (cited on page 41)

[77] I. Georgescu, "25 years of BEC," *Nature Reviews Physics*, vol. 2, no. 8, pp. 396–396, Aug. 2020. [Online]. Available: http://www.nature.com/articles/s42254-020-0211-7 (cited on page 41)

[78] A. Imamoglu, R. J. Ram, S. Pau, and Y. Yamamoto, "Nonequilibrium condensates and lasers without inversion: Exciton-polariton lasers," *Phys. Rev. A*, vol. 53, no. 6, pp. 4250–4253, Jun. 1996. [Online]. Available: https://link.aps.org/doi/10.1103/PhysRevA.53.4250 (cited on page 41)

[79] H. Deng, G. Weihs, D. Snoke, J. Bloch, and Y. Yamamoto, "Polariton lasing vs. photon lasing in a semiconductor microcavity," *Proceedings of the National Academy of Sciences*, vol. 100, no. 26, pp. 15 318–15 323, Dec. 2003. [Online]. Available: https://pnas.org/doi/full/10.1073/pnas.2634328100 (cited on page 41)

[80] D. D. Solnyshkov, H. Terças, K. Dini, and G. Malpuech, "Hybrid Boltzmann–Gross-Pitaevskii theory of Bose-Einstein condensation and superfluidity in open driven-dissipative systems," *Phys. Rev. A*, vol. 89, no. 3, p. 033626, Mar. 2014. [Online]. Available: https://link.aps.org/doi/10.1103/PhysRevA.89.033626 (cited on page 41)

[81] L. Pitaevskii, "Phenomenological theory of superfluidity near the λ point," *J. Exptl. Theoret. Phys. (USSR)*, vol. 35, pp. 408–415, 1958. (cited on page 41)

[82] H. Flayac, I. A. Shelykh, D. D. Solnyshkov, and G. Malpuech, "Topological stability of the half-vortices in spinor exciton-polariton condensates," *Phys. Rev. B: Condens. Matter Mater. Phys.*, vol. 81, no. 4, p. 045318, Jan. 2010. [Online]. Available: https://link.aps.org/doi/10.1103/PhysRevB.81.045318 (cited on page 41)

[83] I. A. Shelykh, Y. G. Rubo, G. Malpuech, D. D. Solnyshkov, and A. Kavokin, "Polarization and propagation of polariton condensates," *Phys. Rev. Lett.*, vol. 97, no. 6, p. 066402, Aug. 2006. [Online]. Available: https://link.aps.org/doi/10.1103/PhysRevLett.97.066402 (cited on page 41)

[84] D. S. Hall, M. R. Matthews, J. R. Ensher, C. E. Wieman, and E. A. Cornell, "Dynamics of component separation in a binary mixture of Bose-Einstein condensates," *Phys. Rev. Lett.*, vol. 81, no. 8, pp. 1539–1542, Aug. 1998. [Online]. Available: https://link.aps.org/doi/10.1103/PhysRevLett.81.1539 (cited on page 41)

[85] T.-L. Ho and V. B. Shenoy, "Binary mixtures of bose condensates of alkali atoms," *Phys. Rev. Lett.*, vol. 77, no. 16, pp. 3276–3279, Oct. 1996. [Online]. Available: https://link.aps.org/doi/10.1103/PhysRevLett.77.3276 (cited on page 41)

[86] S. Christopoulos, G. B. H. von Högersthal, A. J. D. Grundy, P. G. Lagoudakis, A. V. Kavokin, J. J. Baumberg, G. Christmann, R. Butté, E. Feltin, J.-F. Carlin, and N. Grandjean, "Room-Temperature polariton lasing in semiconductor microcavities," *Phys. Rev. Lett.*, vol. 98, no. 12, p. 126405, Mar. 2007. [Online]. Available: https://link.aps.org/doi/10.1103/PhysRevLett.98.126405 (cited on page 42)

[87] R. Su, C. Diederichs, J. Wang, T. C. H. Liew, J. Zhao, S. Liu, W. Xu, Z. Chen, and Q. Xiong, "Room-temperature polariton lasing in all-inorganic perovskite nanoplatelets," *Nano Lett.*, vol. 17, no. 6, pp. 3982–3988, 2017. (cited on page 42)

[88] D. G. Lidzey, D. D. C. Bradley, M. S. Skolnick, T. Virgili, S. Walker, and D. M. Whittaker, "Strong exciton–photon coupling in an organic semiconductor microcavity," *Nature*, vol. 395, no. 6697, pp. 53–55, Sep. 1998. [Online]. Available: http://www.nature.com/articles/25692 (cited on page 42)

[89] I. Carusotto and C. Ciuti, "Quantum fluids of light," *Rev. Mod. Phys.*, vol. 85, no. 1, pp. 299–366, Feb. 2013. [Online]. Available: https://link.aps.org/doi/10.1103/RevModPhys.85.299 (cited on page 42)

[90] A. Amo, J. Lefrère, S. Pigeon, C. Adrados, C. Ciuti, I. Carusotto, R. Houdré, E. Giacobino, and A. Bramati, "Superfluidity of polaritons in semiconductor microcavities," *Nat. Phys.*, vol. 5, no. 11, pp. 805–810, Nov. 2009. [Online]. Available: http://www.nature.com/articles/nphys1364 (cited on pages 42 and 66)

[91] A. Amo, D. Sanvitto, F. P. Laussy, D. Ballarini, E. d. Valle, M. D. Martin, A. Lemaître, J. Bloch, D. N. Krizhanovskii, M. S. Skolnick, C. Tejedor, and L. Viña, "Collective fluid dynamics of a polariton condensate in a semiconductor microcavity," *Nature*, vol. 457, no. 7227, pp. 291–295, Jan. 2009. [Online]. Available: http://www.nature.com/articles/nature07640 (cited on pages 42 and 66)

[92] E. Wertz, L. Ferrier, D. D. Solnyshkov, R. Johne, D. Sanvitto, A. Lemaître, I. Sagnes, R. Grousson, A. V. Kavokin, P. Senellart, G. Malpuech, and J. Bloch, "Spontaneous formation and optical manipulation of extended polariton condensates," *Nat. Phys.*, vol. 6, no. 11, pp. 860–864, Nov. 2010. [Online]. Available: http://www.nature.com/articles/nphys1750 (cited on page 42)

[93] G. Lerario, A. Fieramosca, F. Barachati, D. Ballarini, K. S. Daskalakis, L. Dominici, M. De Giorgi, S. A. Maier, G. Gigli, S. Kéna-Cohen, and D. Sanvitto, "Room-temperature superfluidity in a polariton condensate," *Nat. Phys.*, vol. 13, no. 9, pp.

837–841, Sep. 2017. [Online]. Available: http://www.nature.com/articles/nphys4147 (cited on pages 42 and 66)

[94] K. G. Lagoudakis, M. Wouters, M. Richard, A. Baas, I. Carusotto, R. André, L. S. Dang, and B. Deveaud-Plédran, "Quantized vortices in an exciton–polariton condensate," *Nat. Phys.*, vol. 4, no. 9, pp. 706–710, Sep. 2008. [Online]. Available: http://www.nature.com/articles/nphys1051 (cited on page 42)

[95] K. G. Lagoudakis, T. Ostatnický, A. V. Kavokin, Y. G. Rubo, R. André, and B. Deveaud-Plédran, "Observation of Half-Quantum vortices in an Exciton-Polariton condensate," *Science*, vol. 326, no. 5955, pp. 974–976, Nov. 2009. [Online]. Available: https://www.science.org/doi/10.1126/science.1177980 (cited on page 42)

[96] A. Amo, S. Pigeon, D. Sanvitto, V. G. Sala, R. Hivet, I. Carusotto, F. Pisanello, G. Leménager, R. Houdré, E. Giacobino, C. Ciuti, and A. Bramati, "Polariton superfluids reveal quantum hydrodynamic solitons," *Science*, vol. 332, no. 6034, pp. 1167–1170, 2011. [Online]. Available: https://science.sciencemag.org/content/332/6034/1167 (cited on pages 42 and 66)

[97] R. Hivet, H. Flayac, D. D. Solnyshkov, D. Tanese, T. Boulier, D. Andreoli, E. Giacobino, J. Bloch, A. Bramati, G. Malpuech, and A. Amo, "Half-solitons in a polariton quantum fluid behave like magnetic monopoles," *Nat. Phys.*, vol. 8, no. 10, pp. 724–728, Oct. 2012. [Online]. Available: http://www.nature.com/articles/nphys2406 (cited on pages 42, 66, and 69)

[98] Q. Fontaine, D. Squizzato, F. Baboux, I. Amelio, A. Lemaître, M. Morassi, I. Sagnes, L. Le Gratiet, A. Harouri, M. Wouters, I. Carusotto, A. Amo, M. Richard, A. Minguzzi, L. Canet, S. Ravets, and J. Bloch, "Kardar-Parisi-Zhang universality in a one-dimensional polariton condensate," *Nature*, vol. 608, no. 7924, pp. 687–691, Aug. 2022. [Online]. Available: http://dx.doi.org/10.1038/s41586-022-05001-8 (cited on page 42)

[99] D. D. Solnyshkov, H. Flayac, and G. Malpuech, "Black holes and wormholes in spinor polariton condensates," *Phys. Rev. B: Condens. Matter Mater. Phys.*, vol. 84, no. 23, p. 233405, Dec. 2011. [Online]. Available: https://link.aps.org/doi/10.1103/PhysRevB.84.233405 (cited on page 42)

[100] H. S. Nguyen, D. Gerace, I. Carusotto, D. Sanvitto, E. Galopin, A. Lemaître, I. Sagnes, J. Bloch, and A. Amo, "Acoustic black hole in a stationary hydrodynamic flow of microcavity polaritons," *Phys. Rev. Lett.*, vol. 114, no. 3, p. 036402, Jan. 2015. [Online]. Available: https://link.aps.org/doi/10.1103/PhysRevLett.114.036402 (cited on page 42)

[101] T. Byrnes, N. Y. Kim, and Y. Yamamoto, "Exciton–polariton condensates," *Nat. Phys.*, vol. 10, no. 11, pp. 803–813, Nov. 2014. [Online]. Available: http://www.nature.com/articles/nphys3143 (cited on page 42)

[102] I. A. Shelykh, A. V. Kavokin, Y. G. Rubo, T. C. H. Liew, and G. Malpuech, "Polariton polarization-sensitive phenomena in planar semiconductor microcavities," *Semicond. Sci. Technol.*, vol. 25, no. 1, p. 13001, 2009. (cited on page 42)

[103] L. Ferrier, E. Wertz, R. Johne, D. D. Solnyshkov, P. Senellart, I. Sagnes, A. Lemaître, G. Malpuech, and J. Bloch, "Interactions in confined polariton condensates," *Phys. Rev. Lett.*, vol. 106, no. 12, p. 126401, Mar. 2011. [Online]. Available: https://link.aps.org/doi/10.1103/PhysRevLett.106.126401 (cited on page 43)

[104] J. M. Gérard, D. Barrier, J. Y. Marzin, R. Kuszelewicz, L. Manin, E. Costard, V. Thierry-Mieg, and T. Rivera, "Quantum boxes as active probes for photonic microstructures: The pillar microcavity case," *Appl. Phys. Lett.*, vol. 69, no. 4, pp. 449–451, Jul. 1996. [Online]. Available: http://aip.scitation.org/doi/10.1063/1.118135 (cited on page 43)

[105] D. Bajoni, P. Senellart, E. Wertz, I. Sagnes, A. Miard, A. Lemaître, and J. Bloch, "Polariton laser using single micropillar GaAs - GaAlAs semiconductor cavities," *Phys. Rev. Lett.*, vol. 100, no. 4, p. 047401, Jan. 2008. [Online]. Available: https://link.aps.org/doi/10.1103/PhysRevLett.100.047401 (cited on page 43)

[106] U. Fano, "Precession equation of a spinning particle in nonuniform fields," *Physical Review*, vol. 133, no. 3B, pp. B828–B830, Feb. 1964. [Online]. Available: https://link.aps.org/doi/10.1103/PhysRev.133.B828 (cited on page 43)

[107] H.-J. Stöckmann and D. Dubbers, "Generalized spin precession equations," *New J. Phys.*, vol. 16, no. 5, p. 053050, May 2014. [Online]. Available: https://iopscience.iop.org/article/10.1088/1367-2630/16/5/053050 (cited on page 43)

[108] C. Leyder, M. Romanelli, J. P. Karr, E. Giacobino, T. C. H. Liew, M. M. Glazov, A. V. Kavokin, G. Malpuech, and A. Bramati, "Observation of the optical spin hall effect," *Nat. Phys.*, vol. 3, no. 9, pp. 628–631, Sep. 2007. [Online]. Available: http://www.nature.com/articles/nphys676 (cited on page 44)

[109] A. V. Kavokin, M. R. Vladimirova, M. A. Kaliteevski, O. Lyngnes, J. D. Berger, H. M. Gibbs, and G. Khitrova, "Resonant faraday rotation in a semiconductor microcavity," *Phys. Rev. B: Condens. Matter Mater. Phys.*, vol. 56, no. 3, pp. 1087–1090, Jul. 1997. [Online]. Available: https://link.aps.org/doi/10.1103/PhysRevB.56.1087 (cited on page 46)

[110] M. J. Snelling, E. Blackwood, C. J. McDonagh, R. T. Harley, and C. T. B. Foxon, "Exciton, heavy-hole, and electron g factors in type-i GaAs/ al x ga 1 - x as quantum wells," *Phys. Rev. B: Condens. Matter Mater. Phys.*, vol. 45, no. 7, pp. 3922–3925, Feb. 1992. [Online]. Available: https://link.aps.org/doi/10.1103/PhysRevB.45.3922 (cited on page 46)

[111] M. Król, R. Mirek, D. Stephan, K. Lekenta, J.-G. Rousset, W. Pacuski, A. V. Kavokin, M. Matuszewski, J. Szczytko, and B. Piętka, "Giant spin meissner

effect in a nonequilibrium exciton-polariton gas," *Phys. Rev. B: Condens. Matter Mater. Phys.*, vol. 99, no. 11, p. 115318, Mar. 2019. [Online]. Available: https://link.aps.org/doi/10.1103/PhysRevB.99.115318 (cited on page 46)

[112] P. Walker, T. C. H. Liew, D. Sarkar, M. Durska, A. P. D. Love, M. S. Skolnick, J. S. Roberts, I. A. Shelykh, A. V. Kavokin, and D. N. Krizhanovskii, "Suppression of zeeman splitting of the energy levels of Exciton-Polariton condensates in semiconductor microcavities in an external magnetic field," *Phys. Rev. Lett.*, vol. 106, no. 25, p. 257401, Jun. 2011. [Online]. Available: https://link.aps.org/doi/10.1103/PhysRevLett.106.257401 (cited on page 46)

[113] C. Sturm, D. Solnyshkov, O. Krebs, A. Lemaître, I. Sagnes, E. Galopin, A. Amo, G. Malpuech, and J. Bloch, "Nonequilibrium polariton condensate in a magnetic field," *Phys. Rev. B: Condens. Matter Mater. Phys.*, vol. 91, no. 15, p. 155130, Apr. 2015. [Online]. Available: https://link.aps.org/doi/10.1103/PhysRevB.91.155130 (cited on page 46)

[114] I. A. Shelykh, G. Pavlovic, D. D. Solnyshkov, and G. Malpuech, "Proposal for a mesoscopic optical Berry-Phase interferometer," *Phys. Rev. Lett.*, vol. 102, no. 4, p. 046407, Jan. 2009. [Online]. Available: https://link.aps.org/doi/10.1103/PhysRevLett.102.046407 (cited on pages 46 and 54)

[115] A. Rahimi-Iman, C. Schneider, J. Fischer, S. Holzinger, M. Amthor, S. Höfling, S. Reitzenstein, L. Worschech, M. Kamp, and A. Forchel, "Zeeman splitting and diamagnetic shift of spatially confined quantum-well exciton polaritons in an external magnetic field," *Phys. Rev. B Condens. Matter*, vol. 84, no. 16, p. 165325, Oct. 2011. [Online]. Available: https://link.aps.org/doi/10.1103/PhysRevB.84.165325 (cited on page 46)

[116] B. Piętka, D. Zygmunt, M. Król, M. R. Molas, A. A. L. Nicolet, F. Morier-Genoud, J. Szczytko, J. Łusakowski, P. Zięba, I. Tralle, P. Stępnicki, M. Matuszewski, M. Potemski, and B. Deveaud, "Magnetic field tuning of exciton-polaritons in a semiconductor microcavity," *Phys. Rev. B*, vol. 91, no. 7, p. 075309, Feb. 2015. [Online]. Available: https://journals.aps.org/prb/abstract/10.1103/PhysRevB.91.075309 (cited on page 47)

[117] M. Gell-Mann and M. Lévy, "The axial vector current in beta decay," *Il Nuovo Cimento (1955-1965)*, vol. 16, no. 4, pp. 705–726, May 1960. [Online]. Available: https://doi.org/10.1007/BF02859738 (cited on page 49)

[118] J. P. Provost and G. Vallee, "Riemannian structure on manifolds of quantum states," *Commun. Math. Phys.*, vol. 76, no. 3, pp. 289–301, Sep. 1980. [Online]. Available: http://link.springer.com/10.1007/BF02193559 (cited on pages 50, 75, 99, and 105)

[119] F. Wilczek and A. Shapere, *Geometric Phases in Physics*, ser. Advanced Series in Mathematical Physics. WORLD SCIENTIFIC, Jul. 1989, vol. 5. [Online]. Available: https://www.worldscientific.com/worldscibooks/10.1142/0613 (cited on page 50)

[120] S. Pancharatnam, "Generalized theory of interference, and its applications," *Proceedings of the Indian Academy of Sciences - Section A*, vol. 44, no. 5, pp. 247–262, Nov. 1956. [Online]. Available: http://link.springer.com/10.1007/BF03046050 (cited on page 50)

[121] E. Cohen, H. Larocque, F. Bouchard, F. Nejadsattari, Y. Gefen, and E. Karimi, "Geometric phase from Aharonov–Bohm to Pancharatnam–Berry and beyond," *Nature Reviews Physics*, vol. 1, no. 7, pp. 437–449, Jul. 2019. [Online]. Available: http://www.nature.com/articles/s42254-019-0071-1 (cited on page 50)

[122] C. Cisowski, J. B. Götte, and S. Franke-Arnold, "Colloquium : Geometric phases of light: Insights from fiber bundle theory," *Rev. Mod. Phys.*, vol. 94, no. 3, p. 031001, Jul. 2022. [Online]. Available: https://link.aps.org/doi/10.1103/RevModPhys.94.031001 (cited on page 50)

[123] J. H. Hannay, "Angle variable holonomy in adiabatic excursion of an integrable hamiltonian," *J. Phys. A Math. Gen.*, vol. 18, no. 2, pp. 221–230, Feb. 1985. [Online]. Available: https://iopscience.iop.org/article/10.1088/0305-4470/18/2/011 (cited on page 50)

[124] A. Khein and D. F. Nelson, "Hannay angle study of the foucault pendulum in action-angle variables," *Am. J. Phys.*, vol. 61, no. 2, pp. 170–174, Feb. 1993. [Online]. Available: http://aapt.scitation.org/doi/10.1119/1.17332 (cited on page 50)

[125] D. J. Griffiths and D. F. Schroeter, *Introduction to Quantum Mechanics*. Cambridge University Press, Aug. 2018. [Online]. Available: https://www.cambridge.org/core/product/identifier/9781316995433/type/book (cited on page 51)

[126] M. V. Berry, "Quantal phase factors accompanying adiabatic changes," *Proc. R. Soc. Lond. A Math. Phys. Sci.*, vol. 392, no. 1802, pp. 45–57, Mar. 1984. [Online]. Available: https://royalsocietypublishing.org/doi/10.1098/rspa.1984.0023 (cited on pages 51, 60, 71, and 72)

[127] M. Z. Hasan and C. L. Kane, "Colloquium : Topological insulators," *Rev. Mod. Phys.*, vol. 82, no. 4, pp. 3045–3067, Nov. 2010. [Online]. Available: https://link.aps.org/doi/10.1103/RevModPhys.82.3045 (cited on pages 52 and 54)

[128] L. Lu, J. D. Joannopoulos, and M. Soljačić, "Topological photonics," *Nat. Photonics*, vol. 8, no. 11, pp. 821–829, 2014. (cited on pages 52, 54, 55, 83, and 84)

[129] T. Ozawa, H. M. Price, A. Amo, N. Goldman, M. Hafezi, L. Lu, M. C. Rechtsman, D. Schuster, J. Simon, O. Zilberberg, and I. Carusotto, "Topological photonics," *Rev. Mod. Phys.*, vol. 91, no. 1, p. 15006, Mar. 2019. [Online]. Available: https://link.aps.org/doi/10.1103/RevModPhys.91.015006 (cited on pages 52, 55, 83, and 84)

[130] R. Jackiw and C. Rebbi, "Solitons with fermion number $\frac{1}{2}$," *Phys. Rev. D Part. Fields*, vol. 13, no. 12, pp. 3398–3409, Jun. 1976. [Online]. Available: https://link.aps.org/doi/10.1103/PhysRevD.13.3398 (cited on pages 53 and 54)

[131] T. X. Tran, H. M. Nguyen, and D. C. Duong, "Jackiw-Rebbi states in interfaced binary waveguide arrays with kerr nonlinearity," *Phys. Rev. A*, vol. 100, no. 5, p. 053849, Nov. 2019. [Online]. Available: https://link.aps.org/doi/10.1103/PhysRevA.100.053849 (cited on page 53)

[132] M. Li, I. Sinev, F. Benimetskiy, T. Ivanova, E. Khestanova, S. Kiriushechkina, A. Vakulenko, S. Guddala, M. Skolnick, V. M. Menon, D. Krizhanovskii, A. Alù, A. Samusev, and A. B. Khanikaev, "Experimental observation of topological Z2 exciton-polaritons in transition metal dichalcogenide monolayers," *Nat. Commun.*, vol. 12, no. 1, p. 4425, Dec. 2021. [Online]. Available: http://www.nature.com/articles/s41467-021-24728-y (cited on pages 53 and 83)

[133] F. D. M. Haldane and S. Raghu, "Possible realization of directional optical waveguides in photonic crystals with broken Time-Reversal symmetry," *Phys. Rev. Lett.*, vol. 100, no. 1, p. 013904, Jan. 2008. [Online]. Available: https://link.aps.org/doi/10.1103/PhysRevLett.100.013904 (cited on page 54)

[134] Z. Wang, Y. Chong, J. D. Joannopoulos, and M. Soljačić, "Observation of unidirectional backscattering-immune topological electromagnetic states," *Nature*, vol. 461, no. 7265, pp. 772–775, Oct. 2009. [Online]. Available: http://www.nature.com/articles/nature08293 (cited on pages 54, 56, and 83)

[135] S. Klembt, T. H. Harder, O. A. Egorov, K. Winkler, R. Ge, M. A. Bandres, M. Emmerling, L. Worschech, T. C. H. Liew, M. Segev, and Others, "Exciton-polariton topological insulator," *Nature*, vol. 562, no. 7728, p. 552, 2018. (cited on pages 54 and 84)

[136] D. D. Solnyshkov, A. V. Nalitov, and G. Malpuech, "Kibble-Zurek mechanism in topologically nontrivial zigzag chains of polariton micropillars," *Phys. Rev. Lett.*, vol. 116, no. 4, pp. 1–6, Jan. 2016. [Online]. Available: http://dx.doi.org/10.1103/PhysRevLett.116.046402 (cited on page 54)

[137] P. St-Jean, V. Goblot, E. Galopin, A. Lemaître, T. Ozawa, L. Le Gratiet, I. Sagnes, J. Bloch, and A. Amo, "Lasing in topological edge states of a one-dimensional lattice," *Nat. Photonics*, vol. 11, no. 10, pp. 651–656, Oct. 2017. [Online]. Available: http://www.nature.com/articles/s41566-017-0006-2 (cited on page 55)

[138] B. Bahari, A. Ndao, F. Vallini, A. El Amili, Y. Fainman, and B. Kanté, "Nonreciprocal lasing in topological cavities of arbitrary geometries," *Science*, vol. 358, no. 6363, pp. 636–640, Nov. 2017. [Online]. Available: http://dx.doi.org/10.1126/science.aao4551 (cited on pages 55 and 84)

[139] U. Kuhl, S. Barkhofen, T. Tudorovskiy, H.-J. Stöckmann, T. Hossain, L. de Forges de Parny, and F. Mortessagne, "Dirac point and edge states in a microwave

realization of tight-binding graphene-like structures," *Phys. Rev. B: Condens. Matter Mater. Phys.*, vol. 82, no. 9, p. 094308, Sep. 2010. [Online]. Available: https://link.aps.org/doi/10.1103/PhysRevB.82.094308 (cited on page 55)

[140] M. Bellec, U. Kuhl, G. Montambaux, and F. Mortessagne, "Tight-binding couplings in microwave artificial graphene," *Phys. Rev. B: Condens. Matter Mater. Phys.*, vol. 88, no. 11, p. 115437, Sep. 2013. [Online]. Available: https://link.aps.org/doi/10.1103/PhysRevB.88.115437 (cited on page 55)

[141] ——, "Topological transition of dirac points in a microwave experiment," *Phys. Rev. Lett.*, vol. 110, no. 3, p. 033902, Jan. 2013. [Online]. Available: https://link.aps.org/doi/10.1103/PhysRevLett.110.033902 (cited on page 55)

[142] ——, "Manipulation of edge states in microwave artificial graphene," *New J. Phys.*, vol. 16, no. 11, p. 113023, Nov. 2014. [Online]. Available: https://iopscience.iop.org/article/10.1088/1367-2630/16/11/113023 (cited on page 55)

[143] Y. Ota, K. Takata, T. Ozawa, A. Amo, Z. Jia, B. Kante, M. Notomi, Y. Arakawa, and S. Iwamoto, "Active topological photonics," *Nanophotonics*, vol. 9, no. 3, pp. 547–567, 2020. [Online]. Available: http://dx.doi.org/10.1515/nanoph-2019-0376 (cited on page 55)

[144] M. Reisner, M. Bellec, U. Kuhl, and F. Mortessagne, "Microwave resonator lattices for topological photonics [invited]," *Opt. Mater. Express*, vol. 11, no. 3, p. 629, Mar. 2021. [Online]. Available: https://opg.optica.org/abstract.cfm?URI=ome-11-3-629 (cited on page 55)

[145] A. Marsh, *Mathematics for Physics*. WORLD SCIENTIFIC, Jan. 2018. [Online]. Available: https://www.worldscientific.com/worldscibooks/10.1142/10816 (cited on page 55)

[146] S. Hassani, *Mathematical physics: A modern introduction to its foundations, second edition*. Springer, 2013. [Online]. Available: http://dx.doi.org/10.1007/978-3-319-01195-0 (cited on pages 55 and 155)

[147] E. Gourgoulhon, *Relativité restreinte*. EDP Sciences, Nov. 2020. [Online]. Available: https://www.degruyter.com/document/doi/10.1051/978-2-7598-0923-3/html (cited on pages 56 and 155)

[148] ——, *Relativité Générale*. CEL, 2014. [Online]. Available: https://cel.archives-ouvertes.fr/cel-00366315v6/file/relatM2.pdf (cited on page 57)

[149] P. Zanardi, P. Giorda, and M. Cozzini, "Information-Theoretic differential geometry of quantum phase transitions," *Phys. Rev. Lett.*, vol. 99, no. 10, p. 100603, Sep. 2007. [Online]. Available: https://link.aps.org/doi/10.1103/PhysRevLett.99.100603 (cited on page 58)

[150] R. Roy, "Band geometry of fractional topological insulators," *Phys. Rev. B: Condens. Matter Mater. Phys.*, vol. 90, no. 16, p. 165139, Oct. 2014. [Online]. Available: https://link.aps.org/doi/10.1103/PhysRevB.90.165139 (cited on pages 58 and 80)

[151] A. Abouelkomsan, K. Yang, and E. J. Bergholtz, "Quantum metric induced phases in moiré materials," *arXiv*, vol. 2, pp. 1–15, 2022. [Online]. Available: http://arxiv.org/abs/2202.10467 (cited on page 58)

[152] G. E. Topp, C. J. Eckhardt, D. M. Kennes, M. A. Sentef, and P. Törmä, "Light-matter coupling and quantum geometry in moiré materials," *Phys. Rev. B: Condens. Matter Mater. Phys.*, vol. 104, no. 6, p. 064306, Aug. 2021. [Online]. Available: https://link.aps.org/doi/10.1103/PhysRevB.104.064306 (cited on page 58)

[153] P. Törmä, S. Peotta, and B. A. Bernevig, "Superconductivity, superfluidity and quantum geometry in twisted multilayer systems," *Nature Reviews Physics*, Jun. 2022. [Online]. Available: https://www.nature.com/articles/s42254-022-00466-y (cited on page 58)

[154] A. Julku, G. M. Bruun, and P. Törmä, "Excitations of a Bose-Einstein condensate and the quantum geometry of a flat band," *Phys. Rev. B: Condens. Matter Mater. Phys.*, vol. 104, no. 14, pp. 1–15, 2021. [Online]. Available: http://dx.doi.org/10.1103/physrevb.104.144507 (cited on page 58)

[155] P. Törmä, L. Liang, and S. Peotta, "Quantum metric and effective mass of a two-body bound state in a flat band," *Phys. Rev. B: Condens. Matter Mater. Phys.*, vol. 98, no. 22, p. 220511, Dec. 2018. [Online]. Available: https://link.aps.org/doi/10.1103/PhysRevB.98.220511 (cited on page 58)

[156] S. Peotta and P. Törmä, "Superfluidity in topologically nontrivial flat bands," *Nat. Commun.*, vol. 6, no. 1, p. 8944, Dec. 2015. [Online]. Available: http://www.nature.com/articles/ncomms9944 (cited on pages 58 and 106)

[157] L. Liang, S. Peotta, A. Harju, and P. Törmä, "Wave-packet dynamics of bogoliubov quasiparticles: Quantum metric effects," *Phys. Rev. B: Condens. Matter Mater. Phys.*, vol. 96, no. 6, p. 064511, Aug. 2017. [Online]. Available: https://link.aps.org/doi/10.1103/PhysRevB.96.064511 (cited on pages 58 and 106)

[158] A. Julku, S. Peotta, T. I. Vanhala, D.-H. Kim, and P. Törmä, "Geometric origin of superfluidity in the Lieb-Lattice flat band," *Phys. Rev. Lett.*, vol. 117, no. 4, p. 45303, 2016. [Online]. Available: http://link.aps.org/doi/10.1103/PhysRevLett.117.045303 (cited on page 58)

[159] A. Julku, G. M. Bruun, and P. Törmä, "Quantum geometry and flat band Bose-Einstein condensation," *Phys. Rev. Lett.*, vol. 127, no. 17, p. 170404, Oct. 2021. [Online]. Available: https://link.aps.org/doi/10.1103/PhysRevLett.127.170404 (cited on page 58)

[160] O. Bleu, G. Malpuech, Y. Gao, and D. D. Solnyshkov, "Effective theory of nonadiabatic quantum evolution based on the quantum geometric tensor," *Phys. Rev. Lett.*, vol. 121, no. 2, p. 020401, Jul. 2018. [Online]. Available: https://link.aps.org/doi/10.1103/PhysRevLett.121.020401 (cited on pages 58, 73, 81, 105, 110, and 112)

[161] D. D. Solnyshkov, C. Leblanc, L. Bessonart, A. Nalitov, J. Ren, Q. Liao, F. Li, and G. Malpuech, "Quantum metric and wave packets at exceptional points in non-hermitian systems," *Phys. Rev. B: Condens. Matter Mater. Phys.*, vol. 103, no. 12, p. 125302, Mar. 2021. [Online]. Available: https://link.aps.org/doi/10.1103/PhysRevB.103.125302 (cited on pages 58, 73, 98, 99, 104, 106, 110, and 113)

[162] C. Leblanc, G. Malpuech, and D. D. Solnyshkov, "Universal semiclassical equations based on the quantum metric for a two-band system," *Phys. Rev. B: Condens. Matter Mater. Phys.*, vol. 104, no. 13, p. 134312, Oct. 2021. [Online]. Available: https://link.aps.org/doi/10.1103/PhysRevB.104.134312 (cited on pages 58, 73, 76, and 78)

[163] Q. Liao, C. Leblanc, J. Ren, F. Li, Y. Li, D. Solnyshkov, G. Malpuech, J. Yao, and H. Fu, "Experimental measurement of the divergent quantum metric of an exceptional point," *Phys. Rev. Lett.*, vol. 127, no. 10, p. 107402, Sep. 2021. [Online]. Available: http://dx.doi.org/10.1103/PhysRevLett.127.107402 (cited on pages 58 and 106)

[164] T. Ozawa and B. Mera, "Relations between topology and the quantum metric for chern insulators," *Phys. Rev. B: Condens. Matter Mater. Phys.*, vol. 104, no. 4, pp. 1–13, 2021. [Online]. Available: http://dx.doi.org/10.1103/PhysRevB.104.045103 (cited on page 58)

[165] B. Mera and T. Ozawa, "Kähler geometry and chern insulators: Relations between topology and the quantum metric," *Phys. Rev. B: Condens. Matter Mater. Phys.*, vol. 104, no. 4, p. 045104, Jul. 2021. [Online]. Available: https://link.aps.org/doi/10.1103/PhysRevB.104.045104 (cited on pages 58, 80, and 81)

[166] B. Mera, A. Zhang, and N. Goldman, "Relating the topology of dirac hamiltonians to quantum geometry: When the quantum metric dictates chern numbers and winding numbers," *SciPost Phys.*, vol. 12, no. 1, Jan. 2022. [Online]. Available: http://dx.doi.org/10.21468/SciPostPhys.12.1.018 (cited on page 58)

[167] Y.-Q. Ma, S.-J. Gu, S. Chen, H. Fan, and W.-M. Liu, "The euler number of bloch states manifold and the quantum phases in gapped fermionic systems," *EPL*, vol. 103, no. 1, p. 10008, Jul. 2013. [Online]. Available: https://iopscience.iop.org/article/10.1209/0295-5075/103/10008 (cited on pages 58 and 80)

[168] F. Piéchon, A. Raoux, J.-N. Fuchs, and G. Montambaux, "Geometric orbital susceptibility: Quantum metric without {B}erry curvature," *Phys. Rev. B Condens.*

Matter, vol. 94, no. 13, p. 134423, Oct. 2016. [Online]. Available: https://link.aps.org/doi/10.1103/PhysRevB.94.134423 (cited on pages 58, 80, and 106)

[169] J. C. Maxwell, "VIII. a dynamical theory of the electromagnetic field," *Philosophical Transactions of the Royal Society of London*, vol. 155, pp. 459–512, Dec. 1865. [Online]. Available: https://royalsocietypublishing.org/doi/10.1098/rstl.1865.0008 (cited on page 60)

[170] T. Lancaster and S. J. Blundell, *Quantum Field Theory for the Gifted Amateur*. Oxford, May 2016, vol. 69. [Online]. Available: http://physicstoday.scitation.org/doi/10.1063/PT.3.3173 (cited on pages 60, 157, and 158)

[171] C. N. Yang and R. L. Mills, "Conservation of isotopic spin and isotopic gauge invariance," *Phys. Rev.*, vol. 96, no. 1, pp. 191–195, Oct. 1954. [Online]. Available: https://link.aps.org/doi/10.1103/PhysRev.96.191 (cited on pages 60, 62, 65, 73, 78, and 81)

[172] S. Kivelson and S. A. Kivelson, "Defining emergence in physics," *npj Quantum Materials 2016 1:1*, vol. 1, no. 1, pp. 1–2, Nov. 2016. [Online]. Available: https://www.nature.com/articles/npjquantmats201624 (cited on page 60)

[173] M. Aidelsburger, S. Nascimbene, and N. Goldman, "Artificial gauge fields in materials and engineered systems," *C. R. Phys.*, vol. 19, no. 6, pp. 394–432, Sep. 2018. [Online]. Available: https://linkinghub.elsevier.com/retrieve/pii/S1631070518300318 (cited on page 60)

[174] F. Liu, T. Xu, S. Wang, Z. H. Hang, and J. Li, "Polarization beam splitting with gauge field metamaterials," *Advanced Optical Materials*, vol. 7, no. 12, p. 1801582, Jun. 2019. [Online]. Available: https://onlinelibrary.wiley.com/doi/10.1002/adom.201801582 (cited on page 60)

[175] Y. A. Bychkov and É. I. Rashba, "Properties of a 2D electron gas with lifted spectral degeneracy," *Soviet Journal of Experimental and Theoretical Physics Letters*, vol. 39, p. 78, 1984. (cited on pages 60 and 62)

[176] P.-Q. Jin, Y.-Q. Li, and F.-C. Zhang, "SU (2) × U (1) unified theory for charge, orbit and spin currents," *J. Phys. A Math. Gen.*, vol. 39, no. 22, pp. 7115–7123, Jun. 2006. [Online]. Available: https://iopscience.iop.org/article/10.1088/0305-4470/39/22/022 (cited on pages 60, 73, 78, and 81)

[177] S. Lee, H. Koike, M. Goto, S. Miwa, Y. Suzuki, N. Yamashita, R. Ohshima, E. Shigematsu, Y. Ando, and M. Shiraishi, "Synthetic rashba spin–orbit system using a silicon metal-oxide semiconductor," *Nat. Mater.*, vol. 20, no. 9, pp. 1228–1232, Sep. 2021. [Online]. Available: https://www.nature.com/articles/s41563-021-01026-y (cited on page 60)

[178] A. Manchon, H. C. Koo, J. Nitta, S. M. Frolov, and R. A. Duine, "New perspectives for rashba spin-orbit coupling," *Nat. Mater.*, vol. 14, no. 9, pp. 871–882, 2015. [Online]. Available: http://dx.doi.org/10.1038/nmat4360 (cited on page 60)

[179] Y. Chen, R.-Y. Zhang, Z. Xiong, Z. Hong Hang, J. Li, J. Q. Shen, and C. T. Chan, "Non-Abelian gauge field optics," *Nat. Commun.*, vol. 10, p. 3125, 2019. (cited on pages 61 and 73)

[180] A. Fieramosca, L. De Marco, M. Passoni, L. Polimeno, A. Rizzo, B. L. T. Rosa, G. Cruciani, L. Dominici, M. De Giorgi, G. Gigli, and Others, "Tunable out-of-plane excitons in 2D single-crystal perovskites," *ACS Photonics*, vol. 5, no. 10, pp. 4179–4185, 2018. (cited on page 61)

[181] L. H. Ryder, *Quantum Field Theory*. Cambridge University Press, Jun. 1996. [Online]. Available: https://www.cambridge.org/core/product/identifier/9780511813900/type/book (cited on pages 62, 73, and 81)

[182] A. D. Boozer, "Classical Yang-Mills theory," *Am. J. Phys.*, vol. 79, no. 9, pp. 925–931, 2011. [Online]. Available: https://doi.org/10.1119/1.3606478 (cited on page 64)

[183] M. C. Beeler, R. A. Williams, K. Jimenez-Garcia, L. J. LeBlanc, A. R. Perry, and I. B. Spielman, "The spin hall effect in a quantum gas," *Nature*, vol. 498, p. 201, 2013. (cited on page 65)

[184] E. S. Sedov, I. E. Sedova, S. M. Arakelian, and A. V. Kavokin, "Magnetic control over the zitterbewegung of exciton-polaritons," *New J. Phys.*, vol. 22, no. 8, 2020. [Online]. Available: http://dx.doi.org/10.1088/1367-2630/aba731 (cited on pages 65 and 73)

[185] E. S. Sedov, Y. G. Rubo, and A. V. Kavokin, "Zitterbewegung of exciton-polaritons," *Phys. Rev. B: Condens. Matter Mater. Phys.*, vol. 97, no. 24, Jun. 2018. [Online]. Available: http://dx.doi.org/10.1103/PHYSREVB.97.245312 (cited on pages 65 and 73)

[186] F. Dreisow, M. Heinrich, R. Keil, A. Tünnermann, S. Nolte, S. Longhi, and A. Szameit, "Classical simulation of relativistic zitterbewegung in photonic lattices," *Phys. Rev. Lett.*, vol. 105, no. 14, p. 143902, Sep. 2010. [Online]. Available: https://link.aps.org/doi/10.1103/PhysRevLett.105.143902 (cited on pages 65 and 73)

[187] L. Dominici, R. Carretero-González, A. Gianfrate, J. Cuevas-Maraver, A. S. Rodrigues, D. J. Frantzeskakis, G. Lerario, D. Ballarini, M. De Giorgi, G. Gigli, P. G. Kevrekidis, and D. Sanvitto, "Interactions and scattering of quantum vortices in a polariton fluid," *Nat. Commun.*, vol. 9, no. 1, Dec. 2018. [Online]. Available: http://dx.doi.org/10.1038/S41467-018-03736-5 (cited on page 66)

[188] G. H. Wannier, "The structure of electronic excitation levels in insulating crystals," *Physical Review*, vol. 52, no. 3, pp. 191–197, Aug. 1937. [Online]. Available: https://link.aps.org/doi/10.1103/PhysRev.52.191 (cited on page 69)

[189] ——, "Dynamics of band electrons in electric and magnetic fields," *Rev. Mod. Phys.*, vol. 34, no. 4, pp. 645–655, Oct. 1962. [Online]. Available: https://link.aps.org/doi/10.1103/RevModPhys.34.645 (cited on page 69)

[190] P. Ehrenfest, "Bemerkung über die angenäherte gültigkeit der klassischen mechanik innerhalb der quantenmechanik," *Zeitschrift für Physik*, vol. 45, no. 7-8, pp. 455–457, Jul. 1927. [Online]. Available: http://link.springer.com/10.1007/BF01329203 (cited on page 69)

[191] A. I. M. Rae and J. Napolitano, *Quantum Mechanics*. CRC Press, Dec. 2015. [Online]. Available: https://www.taylorfrancis.com/books/9781482299212 (cited on page 69)

[192] F. Bloch, "Über die quantenmechanik der elektronen in kristallgittern," *Zeitschrift fûr Physik*, vol. 52, no. 7-8, pp. 555–600, Jul. 1929. [Online]. Available: http://link.springer.com/10.1007/BF01339455 (cited on page 70)

[193] J. Feldmann, K. Leo, J. Shah, D. A. B. Miller, J. E. Cunningham, T. Meier, G. von Plessen, A. Schulze, P. Thomas, and S. Schmitt-Rink, "Optical investigation of bloch oscillations in a semiconductor superlattice," *Phys. Rev. B: Condens. Matter Mater. Phys.*, vol. 46, no. 11, pp. 7252–7255, Sep. 1992. [Online]. Available: https://linkinghub.elsevier.com/retrieve/pii/S0749603683710116 (cited on page 70)

[194] K. Leo, P. H. Bolivar, F. Brüggemann, R. Schwedler, and K. Köhler, "Observation of bloch oscillations in a semiconductor superlattice," *Solid State Commun.*, vol. 84, no. 10, pp. 943–946, Dec. 1992. [Online]. Available: https://linkinghub.elsevier.com/retrieve/pii/003810989290798E (cited on page 70)

[195] E. H. Hall, "On a new action of the magnet on electric currents," *Amer. J. Math.*, vol. 2, no. 3, p. 287, Sep. 1879. [Online]. Available: https://www.jstor.org/stable/2369245?origin=crossref (cited on page 71)

[196] ——, "XVIII. on the "rotational coefficient" in nickel and cobalt," *The London, Edinburgh, and Dublin Philosophical Magazine and Journal of Science*, vol. 12, no. 74, pp. 157–172, Sep. 1881. [Online]. Available: https://www.tandfonline.com/doi/full/10.1080/14786448108627086 (cited on page 71)

[197] N. Nagaosa, J. Sinova, S. Onoda, A. H. MacDonald, and N. P. Ong, "Anomalous hall effect," *Rev. Mod. Phys.*, vol. 82, no. 2, pp. 1539–1592, May 2010. [Online]. Available: https://link.aps.org/doi/10.1103/RevModPhys.82.1539 (cited on page 71)

[198] R. Karplus and J. M. Luttinger, "Hall effect in ferromagnetics," *Physical Review*, vol. 95, no. 5, pp. 1154–1160, Sep. 1954. [Online]. Available: https://link.aps.org/doi/10.1103/PhysRev.95.1154 (cited on pages 71 and 72)

[199] G. Sundaram and Q. Niu, "Wave-packet dynamics in slowly perturbed crystals: Gradient corrections and berry-phase effects," *Phys. Rev. B: Condens. Matter*

Mater. Phys., vol. 59, no. 23, pp. 14 915–14 925, Jun. 1999. [Online]. Available: https://link.aps.org/doi/10.1103/PhysRevB.59.14915 (cited on pages 71, 72, and 76)

[200] M.-C. Chang and Q. Niu, "Berry curvature, orbital moment, and effective quantum theory of electrons in electromagnetic fields," *J. Phys. Condens. Matter*, vol. 20, no. 19, p. 193202, May 2008. [Online]. Available: https://iopscience.iop.org/article/10.1088/0953-8984/20/19/193202 (cited on pages 71 and 72)

[201] P. Hauke, M. Lewenstein, and A. Eckardt, "Tomography of band insulators from quench dynamics," *Phys. Rev. Lett.*, vol. 113, no. 4, p. 045303, Jul. 2014. [Online]. Available: https://journals.aps.org/prl/abstract/10.1103/PhysRevLett.113.045303 (cited on page 71)

[202] L.-K. Lim, J.-N. Fuchs, and G. Montambaux, "Geometry of bloch states probed by stückelberg interferometry," *Phys. Rev. A*, vol. 92, no. 6, p. 063627, Dec. 2015. [Online]. Available: https://link.aps.org/doi/10.1103/PhysRevA.92.063627 (cited on page 71)

[203] N. Fläschner, B. S. Rem, M. Tarnowski, D. Vogel, D.-S. Lühmann, K. Sengstock, and C. Weitenberg, "Experimental reconstruction of the {B}erry curvature in a {F}loquet {B}loch band," *Science*, vol. 352, no. 6289, pp. 1091–1094, 2016. (cited on page 71)

[204] M. Wimmer, H. M. Price, I. Carusotto, and U. Peschel, "Experimental measurement of the berry curvature from anomalous transport," *Nat. Phys.*, vol. 13, no. 6, pp. 545–550, Jun. 2017. [Online]. Available: http://www.nature.com/articles/nphys4050 (cited on page 71)

[205] C. Ze and J. E. Lennard-Jones, "The general proof of certain fundamental equations in the theory of metallic conduction," *Proceedings of the Royal Society of London. Series A, Containing Papers of a Mathematical and Physical Character*, vol. 144, no. 851, pp. 101–117, Mar. 1934. [Online]. Available: https://royalsocietypublishing.org/doi/10.1098/rspa.1934.0036 (cited on page 72)

[206] J. Zak, "Dynamics of electrons in solids in external fields," *Physical Review*, vol. 168, no. 3, p. 686, Apr. 1968. [Online]. Available: https://journals.aps.org/pr/abstract/10.1103/PhysRev.168.686 (cited on page 72)

[207] D. Culcer, Y. Yao, and Q. Niu, "Coherent wave-packet evolution in coupled bands," *Phys. Rev. B: Condens. Matter Mater. Phys.*, vol. 72, no. 8, p. 085110, Aug. 2005. [Online]. Available: http://link.aps.org/doi/10.1103/PhysRevB.72.085110 (cited on page 72)

[208] M. Di Liberto, N. Goldman, and G. Palumbo, "Non-Abelian bloch oscillations in higher-order topological insulators," *Nat. Commun.*, vol. 11, no. 1, p. 5942, Dec. 2020. [Online]. Available: http://www.nature.com/articles/s41467-020-19518-x (cited on page 72)

[209] M. M. Glazov, T. Amand, X. Marie, D. Lagarde, L. Bouet, and B. Urbaszek, "Exciton fine structure and spin decoherence in monolayers of transition metal dichalcogenides," *Phys. Rev. B: Condens. Matter Mater. Phys.*, vol. 89, no. 20, p. 201302, May 2014. [Online]. Available: https://link.aps.org/doi/10.1103/PhysRevB.89.201302 (cited on pages 73, 88, and 90)

[210] T. Holder, D. Kaplan, and B. Yan, "Consequences of time-reversal-symmetry breaking in the light-matter interaction: Berry curvature, quantum metric, and diabatic motion," *Physical Review Research*, vol. 2, no. 3, p. 033100, Jul. 2020. [Online]. Available: https://journals.aps.org/prresearch/abstract/10.1103/PhysRevResearch.2.033100 (cited on pages 73 and 105)

[211] Y. Gao and D. Xiao, "Nonreciprocal directional dichroism induced by the quantum metric dipole," *Phys. Rev. Lett.*, vol. 122, no. 22, p. 227402, Jun. 2019. [Online]. Available: https://journals.aps.org/prl/abstract/10.1103/PhysRevLett.122.227402 (cited on page 73)

[212] S.-Q. Shen, "Spin transverse force on spin current in an electric field," *Phys. Rev. Lett.*, vol. 95, no. 18, p. 187203, Oct. 2005. [Online]. Available: https://link.aps.org/doi/10.1103/PhysRevLett.95.187203 (cited on pages 73 and 78)

[213] N. Hatano, R. t. t. Shirasaki, and H. Nakamura, "Non-Abelian gauge field theory of the spin-orbit interaction and a perfect spin filter," *Phys. Rev. A*, vol. 75, no. 3, p. 32107, Mar. 2007. [Online]. Available: https://link.aps.org/doi/10.1103/PhysRevA.75.032107 (cited on pages 73 and 78)

[214] J.-S. Yang, X.-G. He, S.-H. Chen, and C.-R. Chang, "Spin precession due to a non-abelian spin-orbit gauge field," *Phys. Rev. B Condens. Matter*, vol. 78, no. 8, p. 85312, 2008. [Online]. Available: https://link.aps.org/doi/10.1103/PhysRevB.78.085312 (cited on pages 73 and 78)

[215] Y. Yang, C. Peng, D. Zhu, H. Buljan, J. D. Joannopoulos, B. Zhen, and M. Soljačić, "Synthesis and observation of non-abelian gauge fields in real space," *Science*, vol. 365, no. 6457, pp. 1021–1025, Sep. 2019. [Online]. Available: http://dx.doi.org/10.1126/SCIENCE.AAY3183 (cited on page 73)

[216] R. Winkler, U. Zülicke, and J. Bolte, "Oscillatory multiband dynamics of free particles: The ubiquity of zitterbewegung effects," *Phys. Rev. B*, vol. 75, no. 20, p. 205314, May 2007. [Online]. Available: https://journals.aps.org/prb/abstract/10.1103/PhysRevB.75.205314 (cited on pages 73 and 80)

[217] W. Zawadzki and T. M. Rusin, "Zitterbewegung (trembling motion) of electrons in semiconductors: a review," *J. Phys. Condens. Matter*, vol. 23, no. 14, p. 143201, Mar. 2011. [Online]. Available: https://iopscience.iop.org/article/10.1088/0953-8984/23/14/143201 (cited on pages 73 and 80)

[218] S. A. Tarasenko, A. V. Poshakinskiy, E. L. Ivchenko, I. Stepanov, M. Ersfeld, M. Lepsa, and B. Beschoten, "Zitterbewegung of spin split electrons," *JETP Lett.*, vol. 108, no. 5, pp. 326–328, Aug. 2018. [Online]. Available: https://link.springer.com/article/10.1134/S0021364018170022 (cited on page 73)

[219] R. Gerritsma, G. Kirchmair, F. Zähringer, E. Solano, R. Blatt, and C. F. Roos, "Quantum simulation of the dirac equation," *Nature*, vol. 463, no. 7277, pp. 68–71, Jan. 2010. [Online]. Available: https://www.nature.com/articles/nature08688 (cited on page 73)

[220] L. J. Leblanc, M. C. Beeler, K. Jiménez-García, A. R. Perry, S. Sugawa, R. A. Williams, and I. B. Spielman, "Direct observation of zitterbewegung in a Bose–Einstein condensate," *New J. Phys.*, vol. 15, no. 7, p. 073011, Jul. 2013. [Online]. Available: https://iopscience.iop.org/article/10.1088/1367-2630/15/7/073011 (cited on page 73)

[221] C. Qu, C. Hamner, M. Gong, C. Zhang, and P. Engels, "Observation of zitterbewegung in a spin-orbit-coupled Bose-Einstein condensate," *Phys. Rev. A*, vol. 88, no. 2, p. 021604, Aug. 2013. [Online]. Available: https://journals.aps.org/pra/abstract/10.1103/PhysRevA.88.021604 (cited on page 73)

[222] Q. Guo, W. Gao, J. Chen, Y. Liu, and S. Zhang, "Line degeneracy and strong Spin-Orbit coupling of light with bulk bianisotropic metamaterials," *Phys. Rev. Lett.*, vol. 115, no. 6, p. 067402, Aug. 2015. [Online]. Available: https://journals.aps.org/prl/abstract/10.1103/PhysRevLett.115.067402 (cited on page 73)

[223] R.-P. Guo, Q.-H. Guo, L.-T. Wu, J. Chen, and D. Fan, "Optical spin-sensitive zitterbewegung in bianisotropic metamaterials," *Opt. Express*, vol. 24, no. 13, p. 13788, Jun. 2016. [Online]. Available: http://dx.doi.org/10.1364/OE.24.013788 (cited on page 73)

[224] T. L. Silva, E. R. F. Taillebois, R. M. Gomes, S. P. Walborn, and A. T. Avelar, "Optical simulation of the free dirac equation," *Phys. Rev. A*, vol. 99, no. 2, p. 022332, Feb. 2019. [Online]. Available: https://journals.aps.org/pra/abstract/10.1103/PhysRevA.99.022332 (cited on page 73)

[225] M. Iskin, "Geometric mass acquisition via a quantum metric: An effective-band-mass theorem for the helicity bands," *Phys. Rev. A*, vol. 99, no. 5, p. 53603, 2019. [Online]. Available: https://doi.org/10.1103/PhysRevA.99.053603 (cited on page 73)

[226] L. Casetti, M. Pettini, and E. G. D. Cohen, "Geometric approach to hamiltonian dynamics and statistical mechanics," *Phys. Rep.*, vol. 337, no. 3, pp. 237–341, Oct. 2000. [Online]. Available: http://dx.doi.org/10.1016/S0370-1573(00)00069-7 (cited on page 74)

[227] P. Rashevski, "Riemannian geometry and tensor analysis," *Nauka, Moscow*, 1967. (cited on page 76)

[228] J. A. Lock, "The zitterbewegung of a free localized dirac particle," *Am. J. Phys.*, vol. 47, no. 9, pp. 797–802, Sep. 1979. [Online]. Available: https://aapt.scitation.org/doi/abs/10.1119/1.11697 (cited on pages 76 and 77)

[229] D. Xiao, Y. Yao, Z. Fang, and Q. Niu, "Berry-phase effect in anomalous thermoelectric transport," *Phys. Rev. Lett.*, vol. 97, no. 2, p. 026603, Jul. 2006. [Online]. Available: https://journals.aps.org/prl/abstract/10.1103/PhysRevLett.97.026603 (cited on page 76)

[230] Y. Gao, S. A. Yang, and Q. Niu, "Field induced positional shift of {B}loch electrons and its dynamical implications," *Phys. Rev. Lett.*, vol. 112, no. 16, p. 166601, 2014. [Online]. Available: https://link.aps.org/doi/10.1103/PhysRevLett.112.166601 (cited on pages 76, 105, and 106)

[231] B. A. Bernevig, J. Orenstein, and S.-C. Zhang, "Exact SU(2) symmetry and persistent spin helix in a spin-orbit coupled system," *Phys. Rev. Lett.*, vol. 97, no. 23, p. 236601, Dec. 2006. [Online]. Available: http://dx.doi.org/10.1103/PhysRevLett.97.236601 (cited on pages 76 and 153)

[232] L. Liang, T. I. Vanhala, S. Peotta, T. Siro, A. Harju, and P. Törmä, "Band geometry, berry curvature, and superfluid weight," *Phys. Rev. B: Condens. Matter Mater. Phys.*, vol. 95, no. 2, p. 024515, Jan. 2017. [Online]. Available: https://link.aps.org/doi/10.1103/PhysRevB.95.024515 (cited on page 80)

[233] O. Bleu, D. D. Solnyshkov, and G. Malpuech, "Measuring the quantum geometric tensor in two-dimensional photonic and exciton-polariton systems," *Phys. Rev. B: Condens. Matter Mater. Phys.*, vol. 97, no. 19, p. 195422, May 2018. [Online]. Available: https://link.aps.org/doi/10.1103/PhysRevB.97.195422 (cited on page 81)

[234] M. Sidler, P. Back, O. Cotlet, A. Srivastava, T. Fink, M. Kroner, E. Demler, and A. Imamoglu, "Fermi polaron-polaritons in charge-tunable atomically thin semiconductors," *Nat. Phys.*, vol. 13, no. 3, pp. 255–261, Mar. 2017. [Online]. Available: http://www.nature.com/articles/nphys3949 (cited on pages 83, 84, and 87)

[235] P. Back, M. Sidler, O. Cotlet, A. Srivastava, N. Takemura, M. Kroner, and A. Imamoğlu, "Giant Paramagnetism-Induced valley polarization of electrons in Charge-Tunable monolayer MoSe2," *Phys. Rev. Lett.*, vol. 118, no. 23, p. 237404, Jun. 2017. [Online]. Available: http://link.aps.org/doi/10.1103/PhysRevLett.118.237404 (cited on pages 83 and 84)

[236] J. G. Roch, G. Froehlicher, N. Leisgang, P. Makk, K. Watanabe, T. Taniguchi, and R. J. Warburton, "Spin-polarized electrons in monolayer MoS2," *Nat. Nanotechnol.*, vol. 14, no. 5, pp. 432–436, May 2019. [Online]. Available: http://www.nature.com/articles/s41565-019-0397-y (cited on pages 83 and 84)

[237] D. K. Efimkin and A. H. MacDonald, "Many-body theory of trion absorption features in two-dimensional semiconductors," *Phys. Rev. B: Condens. Matter*

Mater. Phys., vol. 95, no. 3, p. 035417, Jan. 2017. [Online]. Available: https://link.aps.org/doi/10.1103/PhysRevB.95.035417 (cited on pages 83 and 84)

[238] L. B. Tan, O. Cotlet, A. Bergschneider, R. Schmidt, P. Back, Y. Shimazaki, M. Kroner, and A. İmamoğlu, "Interacting Polaron-Polaritons," *Physical Review X*, vol. 10, no. 2, p. 021011, Apr. 2020. [Online]. Available: https://link.aps.org/doi/10.1103/PhysRevX.10.021011 (cited on pages 83 and 84)

[239] D. Xiao, G.-B. Liu, W. Feng, X. Xu, and W. Yao, "Coupled spin and valley physics in monolayers of MoS2 and other group-VI dichalcogenides," *Phys. Rev. Lett.*, vol. 108, no. 19, p. 196802, May 2012. [Online]. Available: http://dx.doi.org/10.1103/PhysRevLett.108.196802 (cited on page 83)

[240] M. M. Glazov, "Optical properties of charged excitons in two-dimensional semiconductors," *J. Chem. Phys.*, vol. 153, no. 3, p. 034703, Jul. 2020. [Online]. Available: http://aip.scitation.org/doi/10.1063/5.0012475 (cited on page 83)

[241] A. Imamoglu, O. Cotlet, and R. Schmidt, "Exciton–polarons in two-dimensional semiconductors and the Tavis–Cummings model," *C. R. Phys.*, vol. 22, no. S4, pp. 89–96, Mar. 2022. [Online]. Available: https://comptes-rendus.academie-sciences.fr/physique/articles/10.5802/crphys.47/ (cited on page 83)

[242] J. Klein, A. Hötger, M. Florian, A. Steinhoff, A. Delhomme, T. Taniguchi, K. Watanabe, F. Jahnke, A. W. Holleitner, M. Potemski, C. Faugeras, J. J. Finley, and A. V. Stier, "Controlling exciton many-body states by the electric-field effect in monolayer MoS2," *Physical Review Research*, vol. 3, no. 2, p. L022009, Apr. 2021. [Online]. Available: https://link.aps.org/doi/10.1103/PhysRevResearch.3.L022009 (cited on page 83)

[243] D. MacNeill, C. Heikes, K. F. Mak, Z. Anderson, A. Kormányos, V. Zólyomi, J. Park, and D. C. Ralph, "Breaking of valley degeneracy by magnetic field in monolayer MoSe2," *Phys. Rev. Lett.*, vol. 114, no. 3, p. 037401, Jan. 2015. [Online]. Available: https://link.aps.org/doi/10.1103/PhysRevLett.114.037401 (cited on page 83)

[244] F. Langer, C. P. Schmid, S. Schlauderer, M. Gmitra, J. Fabian, P. Nagler, C. Schüller, T. Korn, P. G. Hawkins, J. T. Steiner, U. Huttner, S. W. Koch, M. Kira, and R. Huber, "Lightwave valleytronics in a monolayer of tungsten diselenide," *Nature*, vol. 557, no. 7703, pp. 76–80, May 2018. [Online]. Available: http://www.nature.com/articles/s41586-018-0013-6 (cited on page 83)

[245] W. Liu, Z. Ji, Y. Wang, G. Modi, M. Hwang, B. Zheng, V. J. Sorger, A. Pan, and R. Agarwal, "Generation of helical topological exciton-polaritons," *Science*, vol. 370, no. 6516, pp. 600–604, Oct. 2020. [Online]. Available: https://www.science.org/doi/10.1126/science.abc4975 (cited on page 83)

[246] A. V. Nalitov, D. D. Solnyshkov, and G. Malpuech, "Polariton Z topological insulator," *Phys. Rev. Lett.*, vol. 114, no. 11, p. 116401, Mar. 2015. [Online]. Available: http://dx.doi.org/10.1103/PhysRevLett.114.116401 (cited on page 84)

[247] T. P. Lyons, D. J. Gillard, C. Leblanc, J. Puebla, D. D. Solnyshkov, L. Klompmaker, I. A. Akimov, C. Louca, P. Muduli, A. Genco, M. Bayer, Y. Otani, G. Malpuech, and A. I. Tartakovskii, "Giant effective zeeman splitting in a monolayer semiconductor realized by spin-selective strong light–matter coupling," *Nat. Photonics*, pp. 1–7, Jul. 2022. [Online]. Available: http://arxiv.org/abs/2109.05859 (cited on pages 84, 85, 86, 88, and 93)

[248] W. Song, W. Sun, C. Chen, Q. Song, S. Xiao, S. Zhu, and T. Li, "Breakup and recovery of topological zero modes in finite Non-Hermitian optical lattices," *Phys. Rev. Lett.*, vol. 123, no. 16, p. 165701, Oct. 2019. [Online]. Available: https://link.aps.org/doi/10.1103/PhysRevLett.123.165701 (cited on page 84)

[249] R. P. A. Emmanuele, M. Sich, O. Kyriienko, V. Shahnazaryan, F. Withers, A. Catanzaro, P. M. Walker, F. A. Benimetskiy, M. S. Skolnick, A. I. Tartakovskii, I. A. Shelykh, and D. N. Krizhanovskii, "Highly nonlinear trion-polaritons in a monolayer semiconductor," *Nat. Commun.*, vol. 11, no. 1, 2020. [Online]. Available: http://dx.doi.org/10.1038/s41467-020-17340-z (cited on pages 84 and 90)

[250] J. Keller, J. S. Parker, J. Stankiewicz, D. E. Read, P. A. Stampe, R. J. Kennedy, P. Xiong, and S. von Molnar, "Controlling the magneto-transport properties of EuS thin films," *IEEE Trans. Magn.*, vol. 38, no. 5, pp. 2673–2675, Sep. 2002. [Online]. Available: http://ieeexplore.ieee.org/document/1042311/ (cited on page 84)

[251] M. Grzeszczyk, M. R. Molas, K. Nogajewski, M. Bartoš, A. Bogucki, C. Faugeras, P. Kossacki, A. Babiński, and M. Potemski, "The effect of metallic substrates on the optical properties of monolayer MoSe2," *Sci. Rep.*, vol. 10, no. 1, p. 4981, Dec. 2020. [Online]. Available: http://www.nature.com/articles/s41598-020-61673-0 (cited on page 84)

[252] J. G. Roch, D. Miserev, G. Froehlicher, N. Leisgang, L. Sponfeldner, K. Watanabe, T. Taniguchi, J. Klinovaja, D. Loss, and R. J. Warburton, "First-Order magnetic phase transition of mobile electrons in monolayer MoS2," *Phys. Rev. Lett.*, vol. 124, no. 18, p. 187602, May 2020. [Online]. Available: https://link.aps.org/doi/10.1103/PhysRevLett.124.187602 (cited on page 86)

[253] T. P. Lyons, D. Gillard, A. Molina-Sánchez, A. Misra, F. Withers, P. S. Keatley, A. Kozikov, T. Taniguchi, K. Watanabe, K. S. Novoselov, J. Fernández-Rossier, and A. I. Tartakovskii, "Interplay between spin proximity effect and charge-dependent exciton dynamics in MoSe2/CrBr3 van der waals heterostructures," *Nat. Commun.*, vol. 11, no. 1, p. 6021, Dec. 2020. [Online]. Available: http://www.nature.com/articles/s41467-020-19816-4 (cited on pages 86 and 93)

[254] S. Dufferwiel, T. P. Lyons, D. D. Solnyshkov, A. A. P. Trichet, F. Withers, S. Schwarz, G. Malpuech, J. M. Smith, K. S. Novoselov, M. S. Skolnick, D. N. Krizhanovskii, and A. I. Tartakovskii, "Valley-addressable polaritons in atomically thin semiconductors,"

Nat. Photonics, vol. 11, no. 8, pp. 497–501, Aug. 2017. [Online]. Available: http://www.nature.com/articles/nphoton.2017.125 (cited on pages 86 and 88)

[255] V. Savona, L. C. Andreani, P. Schwendimann, and A. Quattropani, "Quantum well excitons in semiconductor microcavities: Unified treatment of weak and strong coupling regimes," *Solid State Commun.*, vol. 93, no. 9, pp. 733–739, 1995. [Online]. Available: http://dx.doi.org/10.1016/0038-1098(94)00865-5 (cited on page 86)

[256] N. Lundt, M. Klaas, E. Sedov, M. Waldherr, H. Knopf, M. Blei, S. Tongay, S. Klembt, T. Taniguchi, K. Watanabe, U. Schulz, A. Kavokin, S. Höfling, F. Eilenberger, and C. Schneider, "Magnetic-field-induced splitting and polarization of monolayer-based valley exciton polaritons," *Phys. Rev. B: Condens. Matter Mater. Phys.*, vol. 100, no. 12, p. 121303, Sep. 2019. [Online]. Available: https://link.aps.org/doi/10.1103/PhysRevB.100.121303 (cited on page 88)

[257] M. Z. Maialle, E. A. De Andrada E Silva, and L. J. Sham, "Exciton spin dynamics in quantum wells," *Phys. Rev. B: Condens. Matter Mater. Phys.*, vol. 47, no. 23, pp. 15 776–15 788, 1993. [Online]. Available: http://dx.doi.org/10.1103/PHYSREVB.47.15776 (cited on page 90)

[258] A. Amo, T. C. H. Liew, C. Adrados, R. Houdré, E. Giacobino, A. V. Kavokin, and A. Bramati, "Exciton–polariton spin switches," *Nat. Photonics*, vol. 4, no. 6, pp. 361–366, Jun. 2010. [Online]. Available: http://www.nature.com/articles/nphoton.2010.79 (cited on page 93)

[259] F. Chen, H. Li, H. Zhou, S. Luo, Z. Sun, Z. Ye, F. Sun, J. Wang, Y. Zheng, X. Chen, H. Xu, H. Xu, T. Byrnes, Z. Chen, and J. Wu, "Optically controlled femtosecond polariton switch at room temperature," *Phys. Rev. Lett.*, vol. 129, no. 5, p. 057402, Jul. 2022. [Online]. Available: http://dx.doi.org/10.1103/PhysRevLett.129.057402 (cited on page 93)

[260] D. Smirnova, D. Leykam, Y. Chong, and Y. Kivshar, "Nonlinear topological photonics," *Applied Physics Reviews*, vol. 7, no. 2, p. 021306, Jun. 2020. [Online]. Available: http://aip.scitation.org/doi/10.1063/1.5142397 (cited on page 93)

[261] C. M. Bender, "Introduction to PT-symmetric quantum theory," *Contemporary Physics*, vol. 46, no. 4, pp. 277–292, Jul. 2005. [Online]. Available: http://www.tandfonline.com/doi/abs/10.1080/00107500072632 (cited on page 95)

[262] K. Özdemir, S. Rotter, F. Nori, and L. Yang, "Parity–time symmetry and exceptional points in photonics," *Nat. Mater.*, vol. 18, no. 8, pp. 783–798, 2019. [Online]. Available: http://dx.doi.org/10.1038/s41563-019-0304-9 (cited on pages 97 and 106)

[263] A. Ruschhaupt, F. Delgado, and J. G. Muga, "Physical realization of PT-symmetric potential scattering in a planar slab waveguide," *J. Phys. A Math. Gen.*, vol. 38, no. 9, p. L171, Feb. 2005. [Online]. Available: https://iopscience.iop.org/article/10.1088/0305-4470/38/9/L03/meta (cited on page 97)

[264] A. Szameit, M. C. Rechtsman, O. Bahat-Treidel, and M. Segev, "PT-symmetry in honeycomb photonic lattices," *Phys. Rev. A*, vol. 84, no. 2, p. 021806, Aug. 2011. [Online]. Available: https://link.aps.org/doi/10.1103/PhysRevA.84.021806 (cited on page 97)

[265] M. A. Miri and A. Alù, "Exceptional points in optics and photonics," *Science*, vol. 363, no. 6422, 2019. [Online]. Available: http://dx.doi.org/10.1126/science.aar7709 (cited on page 97)

[266] E. J. Bergholtz, J. C. Budich, and F. K. Kunst, "Exceptional topology of non-hermitian systems," *Rev. Mod. Phys.*, vol. 93, no. 1, p. 015005, Feb. 2021. [Online]. Available: https://link.aps.org/doi/10.1103/RevModPhys.93.015005 (cited on page 97)

[267] J. Doppler, A. A. Mailybaev, J. Böhm, U. Kuhl, A. Girschik, F. Libisch, T. J. Milburn, P. Rabl, N. Moiseyev, and S. Rotter, "Dynamically encircling an exceptional point for asymmetric mode switching," *Nature*, vol. 537, no. 7618, pp. 76–79, Sep. 2016. [Online]. Available: http://www.nature.com/articles/nature18605 (cited on pages 98 and 106)

[268] D. C. Brody and E. M. Graefe, "Information geometry of complex hamiltonians and exceptional points," *Entropy*, vol. 15, no. 9, pp. 3361–3378, 2013. [Online]. Available: http://dx.doi.org/10.3390/e15093361 (cited on pages 100, 106, and 113)

[269] Q. Zhang and B. Wu, "Non-Hermitian quantum systems and their geometric phases," *Phys. Rev. A*, vol. 99, no. 3, p. 32121, Mar. 2019. [Online]. Available: https://link.aps.org/doi/10.1103/PhysRevA.99.032121 (cited on page 104)

[270] M. V. Berry, "The quantum phase, five years after," in *Geometric phases in physics*. World Scientific, Singapore, 1989, p. 7. (cited on pages 104 and 105)

[271] X. Tan, D.-W. Zhang, Z. Yang, J. Chu, Y.-Q. Zhu, D. Li, X. Yang, S. Song, Z. Han, Z. Li, Y. Dong, H.-F. Yu, H. Yan, S.-L. Zhu, and Y. Yu, "Experimental measurement of the quantum metric tensor and related topological phase transition with a superconducting qubit," *Phys. Rev. Lett.*, vol. 122, no. 21, p. 210401, May 2019. [Online]. Available: https://link.aps.org/doi/10.1103/PhysRevLett.122.210401 (cited on page 105)

[272] M. V. Berry and P. Shukla, "Quantum metric statistics for random-matrix families," *J. Phys. A: Math. Theor.*, vol. 53, no. 27, p. 275202, Jun. 2020. [Online]. Available: https://iopscience.iop.org/article/10.1088/1751-8121/ab91d6/meta (cited on page 105)

[273] U. Marzolino and D. Braun, "Precision measurements of temperature and chemical potential of quantum gases," *Phys. Rev. A*, vol. 88, no. 6, p. 063609, Dec. 2013. [Online]. Available: https://link.aps.org/doi/10.1103/PhysRevA.88.063609 (cited on page 106)

[274] D. Braun, G. Adesso, F. Benatti, R. Floreanini, U. Marzolino, M. W. Mitchell, and S. Pirandola, "Quantum-enhanced measurements without entanglement," *Rev. Mod. Phys.*, vol. 90, no. 3, p. 035006, Sep. 2018. [Online]. Available: https://link.aps.org/doi/10.1103/RevModPhys.90.035006 (cited on page 106)

[275] A. Srivastava and A. Imamoglu, "Signatures of {b}loch-band geometry on excitons: Nonhydrogenic spectra in Transition-Metal dichalcogenides," *Phys. Rev. Lett.*, vol. 115, no. 16, p. 166802, Oct. 2015. [Online]. Available: http://link.aps.org/doi/10.1103/PhysRevLett.115.166802 (cited on page 106)

[276] N. Moiseyev, *Non-Hermitian Quantum Mechanics*. Cambridge University Press, Feb. 2011. [Online]. Available: https://www.cambridge.org/core/product/identifier/9780511976186/type/book (cited on page 106)

[277] V. V. Konotop, J. Yang, and D. A. Zezyulin, "Nonlinear waves in PT-symmetric systems," *Rev. Mod. Phys.*, vol. 88, no. 3, p. 035002, Jul. 2016. [Online]. Available: https://link.aps.org/doi/10.1103/RevModPhys.88.035002 (cited on page 106)

[278] R. El-Ganainy, K. G. Makris, M. Khajavikhan, Z. H. Musslimani, S. Rotter, and D. N. Christodoulides, "Non-Hermitian physics and PT symmetry," *Nat. Phys.*, vol. 14, no. 1, pp. 11–19, Jan. 2018. [Online]. Available: http://www.nature.com/articles/nphys4323 (cited on page 106)

[279] B. Peng, Ş. K. Özdemir, F. Lei, F. Monifi, M. Gianfreda, G. L. Long, S. Fan, F. Nori, C. M. Bender, and L. Yang, "Parity–time-symmetric whispering-gallery microcavities," *Nat. Phys.*, vol. 10, no. 5, pp. 394–398, May 2014. [Online]. Available: http://www.nature.com/articles/nphys2927 (cited on page 106)

[280] T. J. Milburn, J. Doppler, C. A. Holmes, S. Portolan, S. Rotter, and P. Rabl, "General description of quasiadiabatic dynamical phenomena near exceptional points," *Phys. Rev. A*, vol. 92, no. 5, p. 052124, Nov. 2015. [Online]. Available: https://link.aps.org/doi/10.1103/PhysRevA.92.052124 (cited on page 106)

[281] W. Chen, Ş. Kaya Özdemir, G. Zhao, J. Wiersig, and L. Yang, "Exceptional points enhance sensing in an optical microcavity," *Nature*, vol. 548, no. 7666, pp. 192–196, Aug. 2017. [Online]. Available: http://www.nature.com/articles/nature23281 (cited on page 106)

[282] J. Wiersig, "Response strengths of open systems at exceptional points," *Physical Review Research*, vol. 4, no. 2, p. 023121, May 2022. [Online]. Available: https://link.aps.org/doi/10.1103/PhysRevResearch.4.023121 (cited on page 106)

[283] ——, "The distance between exceptional points and diabolic points and its implication for the response strength of non-hermitian systems," *arXiv*, May 2022. [Online]. Available: http://dx.doi.org/10.48550/arXiv.2205.15685 (cited on page 106)

[284] W. R. Sweeney, C. W. Hsu, S. Rotter, and A. D. Stone, "Perfectly absorbing exceptional points and chiral absorbers," *Phys. Rev. Lett.*, vol. 122, no. 9, p.

093901, Mar. 2019. [Online]. Available: https://journals.aps.org/prl/abstract/10.1103/PhysRevLett.122.093901 (cited on page 106)

[285] C. Wang, W. R. Sweeney, A. D. Stone, and L. Yang, "Coherent perfect absorption at an exceptional point," *Science*, vol. 373, no. 6560, pp. 1261–1265, Sep. 2021. [Online]. Available: https://www.science.org/doi/10.1126/science.abj1028 (cited on page 106)

[286] S. Suwunnarat, Y. Tang, M. Reisner, F. Mortessagne, U. Kuhl, and T. Kottos, "Non-linear coherent perfect absorption in the proximity of exceptional points," *Communications Physics 2022 5:1*, vol. 5, no. 1, pp. 1–7, Jan. 2022. [Online]. Available: https://www.nature.com/articles/s42005-021-00782-2 (cited on page 106)

[287] D. Leykam, K. Y. Bliokh, C. Huang, Y. D. Chong, and F. Nori, "Edge modes, degeneracies, and topological numbers in Non-Hermitian systems," *Phys. Rev. Lett.*, vol. 118, no. 4, p. 40401, Jan. 2017. [Online]. Available: https://link.aps.org/doi/10.1103/PhysRevLett.118.040401 (cited on page 106)

[288] H. Shen, B. Zhen, and L. Fu, "Topological band theory for Non-Hermitian hamiltonians," *Phys. Rev. Lett.*, vol. 120, no. 14, p. 146402, Apr. 2018. [Online]. Available: http://dx.doi.org/10.1103/PhysRevLett.120.146402 (cited on page 106)

[289] M. V. Berry, "Optical polarization evolution near a non-hermitian degeneracy," *J. Opt.*, vol. 13, no. 11, p. 115701, 2011. [Online]. Available: http://dx.doi.org/10.1088/2040-8978/13/11/115701 (cited on pages 106 and 110)

[290] M. V. Berry and R. Uzdin, "Slow non-hermitian cycling: exact solutions and the stokes phenomenon," *J. Phys. A: Math. Theor.*, vol. 44, no. 43, p. 435303, Oct. 2011. [Online]. Available: https://iopscience.iop.org/article/10.1088/1751-8113/44/43/435303 (cited on pages 106 and 110)

[291] M. V. Berry and M. R. Dennis, "The optical singularities of birefringent dichroic chiral crystals," *Proc. R. Soc. Lond. A Math. Phys. Sci.*, vol. 459, p. 1261, 2003. (cited on page 106)

[292] W. Voigt, "On the behaviour of pleochroitic crystals along directions in the neighbourhood of an optic axis," *Philosophical Magazine Series*, vol. 4, p. 90, 1902. (cited on page 106)

[293] S. Richter, H.-G. Zirnstein, J. Zúñiga-Pérez, E. Krüger, C. Deparis, L. Trefflich, C. Sturm, B. Rosenow, M. Grundmann, and R. Schmidt-Grund, "Voigt exceptional points in an anisotropic ZnO-Based planar microcavity: Square-Root topology, polarization vortices, and circularity," *Phys. Rev. Lett.*, vol. 123, no. 22, p. 227401, Nov. 2019. [Online]. Available: https://link.aps.org/doi/10.1103/PhysRevLett.123.227401 (cited on page 106)

[294] A. V. Kavokin, J. J. Baumberg, G. Malpuech, and F. P. Laussy, *Microcavities*. Oxford University Press, Aug. 2017, vol. 1. [Online]. Avail-

able: http://www.oxfordscholarship.com/view/10.1093/oso/9780198782995.001.0001/oso-9780198782995 (cited on page 106)

[295] J. Ren, Q. Liao, H. Huang, Y. Li, T. Gao, X. Ma, S. Schumacher, J. Yao, S. Bai, and H. Fu, "Efficient bosonic condensation of exciton polaritons in an H-Aggregate organic Single-Crystal microcavity," *Nano Lett.*, vol. 20, no. 10, pp. 7550–7557, Oct. 2020. [Online]. Available: https://pubs.acs.org/doi/10.1021/acs.nanolett.0c03009 (cited on pages 106 and 107)

[296] Q. Liao, C. Leblanc, J. Ren, F. Li, Y. Li, D. Solnyshkov, G. Malpuech, J. Yao, and H. Fu, "Supplementary material: Experimental measurement of the divergent quantum metric of an exceptional point," *Phys. Rev. Lett.*, vol. 127, no. 10, p. 107402, Sep. 2021. [Online]. Available: http://dx.doi.org/10.1103/PhysRevLett.127.107402 (cited on pages 107 and 113)

[297] J. Ren, Q. Liao, F. Li, Y. Li, O. Bleu, G. Malpuech, J. Yao, H. Fu, and D. Solnyshkov, "Nontrivial band geometry in an optically active system," *Nat. Commun.*, vol. 12, no. 1, p. 689, Dec. 2021. [Online]. Available: http://www.nature.com/articles/s41467-020-20845-2 (cited on pages 107 and 109)

[298] C. M. Bender and S. Boettcher, "Real spectra in Non-Hermitian hamiltonians having PT symmetry," *Phys. Rev. Lett.*, vol. 80, no. 24, pp. 5243–5246, 1998. [Online]. Available: https://link.aps.org/doi/10.1103/PhysRevLett.80.5243 (cited on page 110)

[299] J.-H. Park, A. Ndao, W. Cai, L. Hsu, A. Kodigala, T. Lepetit, Y.-H. Lo, and B. Kanté, "Symmetry-breaking-induced plasmonic exceptional points and nanoscale sensing," *Nat. Phys.*, vol. 16, no. 4, pp. 462–468, Apr. 2020. [Online]. Available: http://www.nature.com/articles/s41567-020-0796-x (cited on page 114)

[300] M. Kepenekian, R. Robles, C. Katan, D. Sapori, L. Pedesseau, and J. Even, "Rashba and dresselhaus effects in hybrid Organic–Inorganic perovskites: From basics to devices," *ACS Nano*, vol. 9, no. 12, pp. 11 557–11 567, Dec. 2015. [Online]. Available: https://pubs.acs.org/doi/10.1021/acsnano.5b04409 (cited on page 153)

Appendices

Appendix A: Pseudospin texture

"A method is more important than a discovery, since the right method will lead to new and even more important discoveries." Lev Landau

We will consider a simple case: an Hamiltonian with a momentum term of energy E_C and a Rashba contribution H_R [17]. The Hamiltonian reads

$$H = E_C + H_R = \frac{\hbar^2 k_{/\!/}^2}{2m} + \alpha \left(k_y \sigma_x - k_x \sigma_y\right) \tag{A.1}$$

with $k_{/\!/} = \sqrt{{k_x}^2 + {k_y}^2}$, α the Rashba coefficient and m the mass of the particle. The eigenvalues are

$$E_1 = \frac{\hbar^2 k_{/\!/}^2}{2m} + \alpha k_{/\!/}, \quad E_2 = \frac{\hbar^2 k_{/\!/}^2}{2m} - \alpha k_{/\!/} \tag{A.2}$$

and are plotted in fig. A.1.a. We consider the angle φ of the wavevector $\mathbf{k}$ in the reciprocal space. This angle is given by

$$k_x = k_{/\!/} \cos(\varphi)\,, \quad k_y = k_{/\!/} \sin(\varphi) \tag{A.3}$$

Hence, the eigenstates of the Hamiltonian H can be described by

$$\psi_1 = \begin{pmatrix} {\psi_+}^1 \\ {\psi_-}^1 \end{pmatrix} = \begin{pmatrix} 1 \\ -ie^{i\varphi} \end{pmatrix}, \quad \psi_2 = \begin{pmatrix} {\psi_+}^2 \\ {\psi_-}^2 \end{pmatrix} = \begin{pmatrix} 1 \\ ie^{i\varphi} \end{pmatrix} \tag{A.4}$$

As mentioned in the Chapter 1, the equation to obtain the pseudospin components reads

$$S_i = (\psi_+ \;\; \psi_-)^* \sigma_i \begin{pmatrix} \psi_+ \\ \psi_- \end{pmatrix} = \langle \sigma_i \rangle \tag{A.5}$$

with $i = x, y, z$ and σ_i the Pauli matrices. This gives the results for the mode 1 and 2

$$\begin{aligned} {S_x}^1 &= \sin\varphi\,, & {S_x}^2 &= -\sin\varphi \\ {S_y}^1 &= -\cos\varphi\,, & {S_y}^2 &= \cos\varphi \\ {S_z}^1 &= 0\,, & {S_z}^2 &= 0 \end{aligned} \tag{A.6}$$

We will study the pseudospin texture of $(S_x,\ S_y)$. We consider a $2D$ cut at a given energy ϵ, as shown in fig. A.1.a, and we display the pseudospin texture along the respective mode energies in the panel b. We remark that the pseudospin rotates clockwise for the mode number 2 and anticlockwise for the mode number 1. This pseudospin texture is the signature of a Rashba Hamiltonian [300]. In the same manner, one could obtain the pseudospin texture of a Dresselhaus Hamilonian which reads [19, 231]

$$H = E_C + H_D = \frac{\hbar^2 k_{/\!/}^2}{2m} + \lambda_D \left(k_x \sigma_x - k_y \sigma_y\right) \tag{A.7}$$

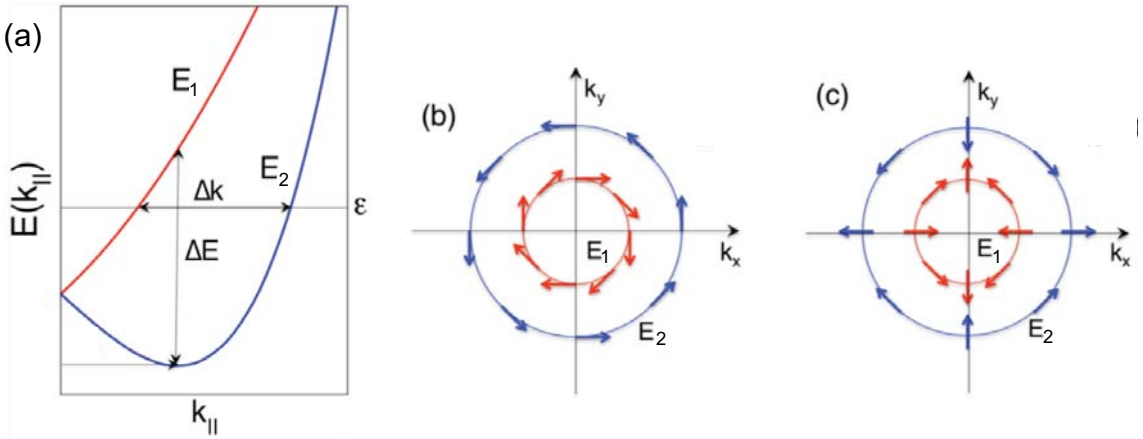

Figure A.1: *(a) Dispersion of the mode* 1 *and* 2*. (b) Scheme of the pseudospin texture of Rashba Hamiltonian at a given energy* ϵ *represented on the two corresponding modes. (c) Same but for a Dresselhaus Hamiltonian.*

The texture, also a typical pseudospin texture for a Dresselhaud Hamiltonian, is represented in the panel c. The dispersion is the same as in the case of the Rashba Hamiltonian, hence the pseudospin texture is a convenient tool to understand systems beyond their dispersion relation.

"Do not worry about your difficulties in Mathematics. I can assure you mine are still greater." Albert Einstein

B.1 Metrics

We will work with $\mathcal{E}$ the spacetime, E the vectorial space associated and g a bilinear form which is symmetrical and not degenerated [147].

- A bilinear form g is an application $E \times E \to \mathbb{R}$ linear compared to each of his arguments (meaning that $g(\lambda\vec{x}, \vec{y}) = \lambda g(\vec{x}, \vec{y})$ and so on).
- g is symmetric meaning that $\forall(\vec{x}, \vec{y}) \in E^2,\ g(\vec{x}, \vec{y}) = g(\vec{y}, \vec{x})$.
- g is not degenerated meaning that if we consider $x \in E$, then:

$$\forall \vec{y} \in E \quad g(x, y) = 0 \iff \vec{x} = \vec{0}$$

- g have a signature $(-, +, +, +)$ meaning that a base of E exist where $g(u, v)$ can be expressed compared to the components u^α, u^β in this base such that:

$$g(\vec{u}, \vec{v}) = -u^0 v^0 + u^1 v^1 + u^2 v^2 + u^3 v^3$$

B.2 Manifold

Mathematician have invented the theory of differentiable manifolds, which unifies the common features of all space together. A definition of a differentiable manifold (called usually just manifold) reads [146]: *A differentiable manifold is a collection of objects called points that are connected to each other in a smooth fashion such that the neighborhood of each point looks like the neighborhood of an n-dimensional (Cartesian) space, where n is the dimension of the manifold.*

So any surface with sharp edges or points cannot be a manifold, meaning that a cone or a cylinder are not manifold. Some examples of differentiable manifolds:

- The space $\mathbb{R}^n$ is an n-dimensional manifold.
- The surface of a sphere is a two-dimensional manifold.
- A torus (used in the main text) is a two-dimensional manifold as well.

"Well, gauge theory is very fundamental to our understanding of physical forces these days. But they are also dependent on a mathematical idea, which has been around for longer than gauge theory has." Roger Penrose

C.1 Gauge field

As mentioned in the chapter 5, we can start by writing the Lagrangian for a massless scalar field under the form

$$\mathcal{L} = (\partial^\mu \psi)^\dagger (\partial^\mu \psi) - m^2 \psi^\dagger \psi \tag{C.1}$$

which has a $U(1)$ symmetry. By choosing $\psi(x) \to \psi(x)e^{i\alpha}$, we can trivially demonstrate that the equation C.1, as the equations of motions which are derived from it, does not change. Note here that the transformation is said to be a global $U(1)$ transformation, because it does not depend on a space parameter. Now, if we consider a more complex transformation such as $\psi(x) \to \psi(x)e^{i\alpha(x)}$, where $\alpha(x)$ transform the field differently in space, things get a little more complicated. Indeed, the derivation gives

$$\begin{aligned} \partial_\mu \psi(x) &\to \partial_\mu \psi(x) e^{i\alpha(x)} \\ &= e^{i\alpha(x)} \partial_\mu \psi(x) + \psi(x) e^{i\alpha(x)} i \partial_\mu \alpha(x) \\ &= e^{i\alpha(x)} \left[\partial_\mu + i\partial_\mu \alpha(x)\right] \psi(x) \end{aligned} \tag{C.2}$$

Hence, the Lagrangian now reads

$$\mathcal{L} = (\partial^\mu \psi)^\dagger (\partial^\mu \psi) - i (\partial^\mu \alpha) \psi^\dagger (\partial^\mu \psi) + i \left(\partial^\mu \psi^\dagger\right) (\partial_\mu \alpha) \psi + (\partial^\mu \alpha) (\partial_\mu \alpha) \psi^\dagger \psi - m^2 \psi^\dagger \psi \tag{C.3}$$

which is, without a doubt, different from the initial Lagrangian. We say that it is not invariant with respect to local $U(1)$ transformation. The idea of gauge theory, is that we can restore this symmetry by adding a new field term $A^\mu(x)$ which would be designed to cancel terms making this theory non-invariant. We proceed by introducing a new object D_μ known as the covariant derivative [170], written as

$$D_\mu = \partial_\mu + iqA_\mu(x) \tag{C.4}$$

where the q parameter is the coupling strength between A_μ and other fields. The two conditions for the local transformation to be invariant can be written under the form

$$\begin{aligned} &\psi(x) \to \psi(x) e^{i\alpha(x)} \\ &A_\mu(x) \to A_\mu(x) - \tfrac{1}{q} \partial_\mu \alpha(x) \end{aligned} \tag{C.5}$$

From this field, a derivation similar to C.3 will give the initial Lagrangian from eq.C.1. A theory where a field A^μ is introduced to get an invariance with respect to a local transformation is called a gauge theory, and the field A^μ is a gauge field.

C.2 Electromagnetism as a gauge theory

The theory of electromagnetism can be described by a vector field $A^\mu(x) = (V(x), \mathbf{A}(x))$ which allows to write a Lagrangian under the form

$$\mathcal{L} = -\frac{1}{4}\left(\partial_\mu A_\nu - \partial_\nu A_\mu\right)\left(\partial^\mu A^\nu - \partial^\nu A^\mu\right) - J^\mu_{em} A^\mu \tag{C.6}$$

which is used to obtain the equations of motion

$$\partial^2 A^\nu - \partial^\nu\left(\partial_\mu A^\mu\right) = J^\nu_{em} \tag{C.7}$$

One important point about this formulation is that both the Lagrangian and the equations of motions are unchanged if we add to the vector field

$$A_\mu(x) \to A_\mu(x) - \partial_\mu \chi(x) \tag{C.8}$$

meaning that its components transform unto

$$\begin{aligned} V &\to V - \partial_0 \chi \\ \mathbf{A} &\to \mathbf{A} + \boldsymbol{\nabla}\chi \end{aligned} \tag{C.9}$$

Of course, usually we chose χ so the physics is described as simple as possible. We could chose χ in such a way that

$$\boldsymbol{\nabla} \cdot \mathbf{A} = 0 \tag{C.10}$$

which is known as the Coulomb gauge. We could also chose χ so

$$\partial_\mu A^\mu(x) = 0 \tag{C.11}$$

which is called the Lorenz gauge. This gauge is useful because in the absence of current J^ν_{em} it gives the massless Klein-Gordon equation $\partial^2 A^\mu = 0$. By writing $\chi(x) = \alpha(x)/q$, we can remark that the conditions from eq. C.5 are satisfied, making electromagnetism a gauge theory [170].

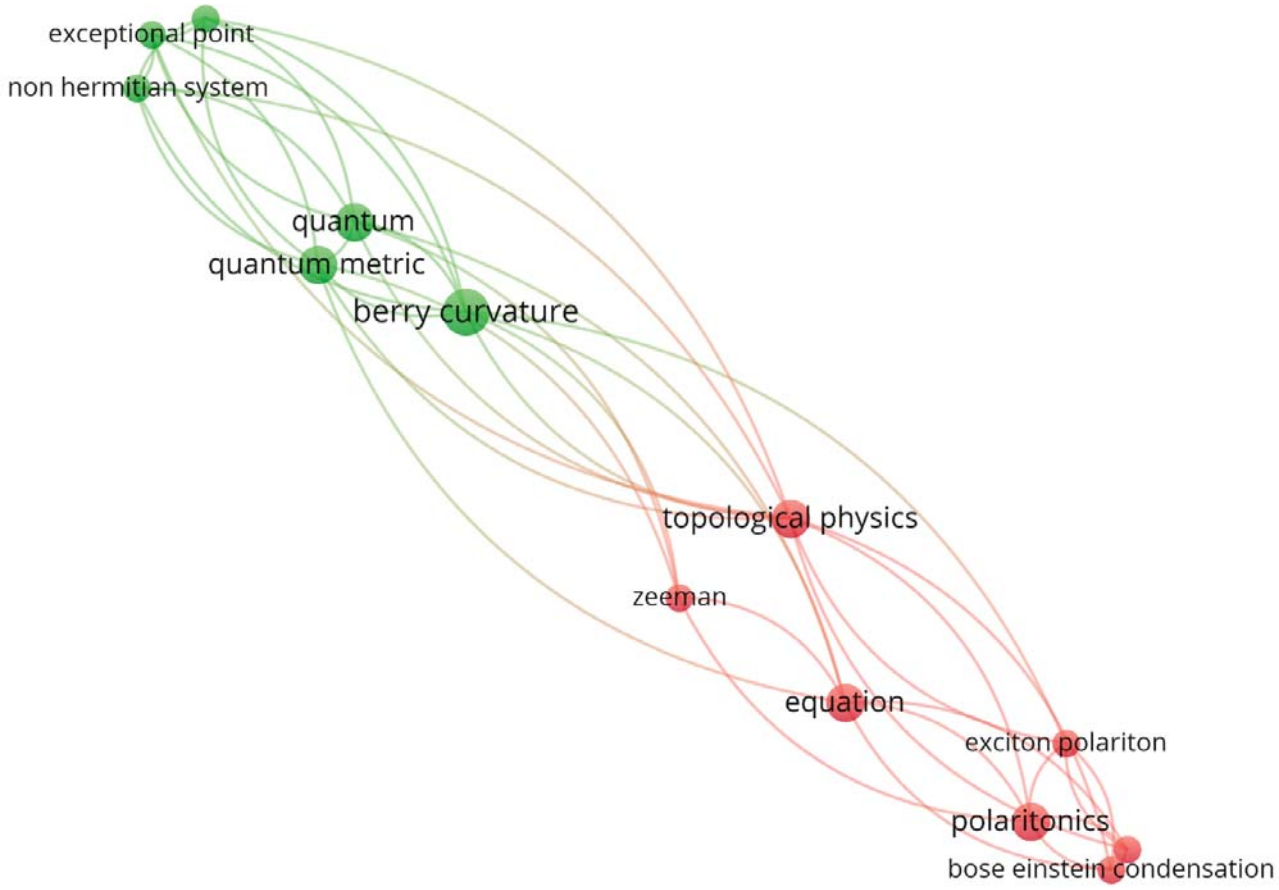

Figure D.1: *Co-occurence of words in the abstract of my articles, using VOSviewer.*

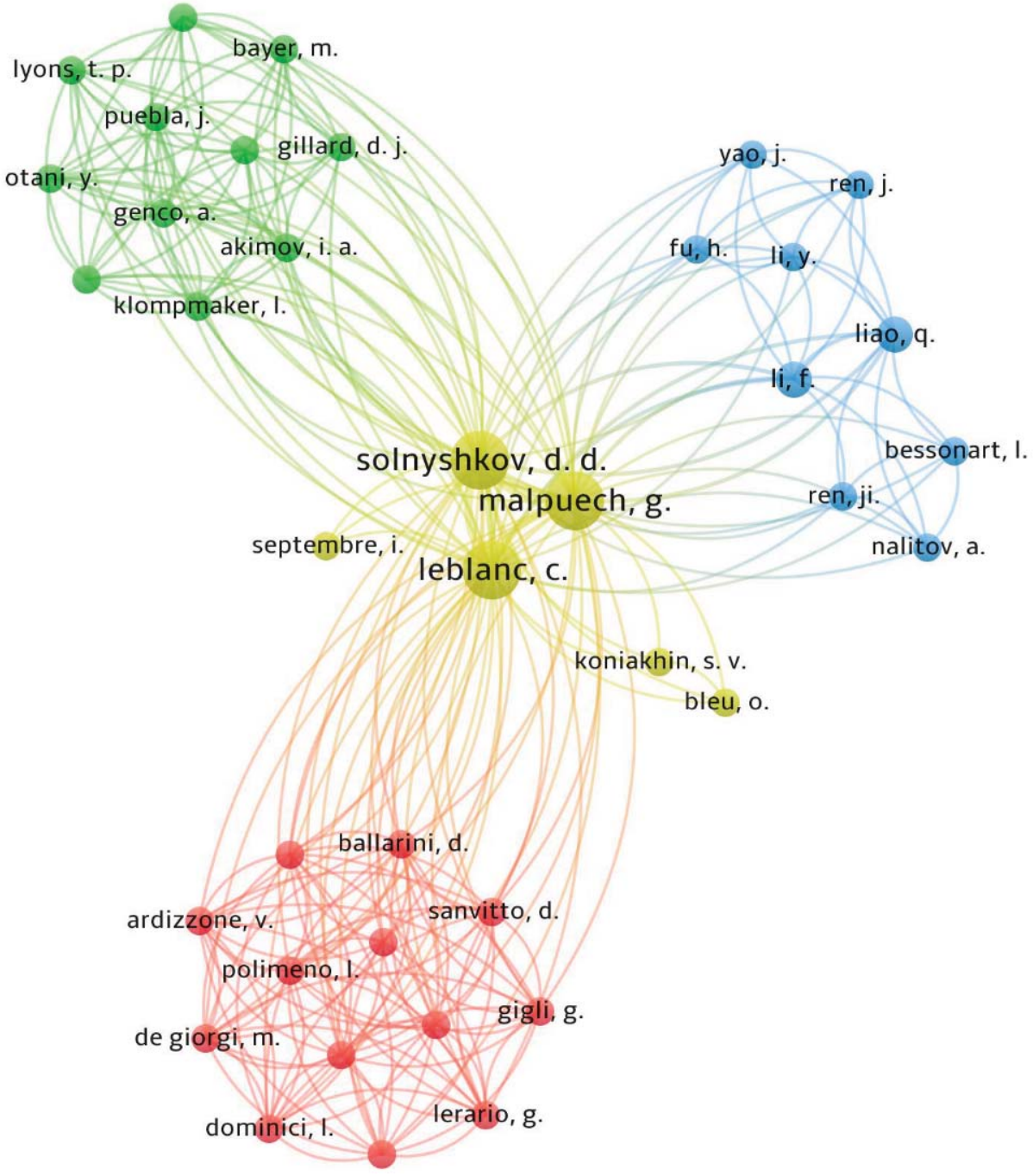

Figure D.2: *Co-authorship analysis of all my articles, using VOSviewer.*

2DEG	Two-dimensional electron gaz
AHE	Anomalous Hall effect
BEC	Bose-Einstein condensate
BN	Boron Nitride
DBR	Distributed Bragg reflector
DPAVBi	4,4'-bis[4-(di-p-tolylamino)styryl] biphenyl
EP	Exceptional point
EuS	Europium sulphide
GPE	Gross Pitaevskii equation
LPB	Lower polariton branch
$MoSe_2$	Monolayer Molybdenum diselenide
MSS	Maialle-Silva-Sham
OA	Optical activity
PEAI-F	4-fluoro-phenethylammonium tetraiodoplumbate
PL	Photoluminescence
PT	Parity-Time
QGT	Quantum Geometric Tensor
QM	Quantum Metric
SOC	Spin-orbit coupling
TE	Transverse-electric
TM	Transverse-magnetic
TMD	Transition metal dichalcogenide
UPB	Upper polariton branch

Charly Leblanc

PHD CANDIDATE IN PHYSICS · QUANTUM OPTOELECTRONICS AND NANOPHOTONICS

(+33) 650615256 | charly.Leblanc@uca.fr | www.charlyleblanc.net

Publications

1^{st} author

Clermont-Ferrand, France

PEER-REVIEWED JOURNAL PAPERS AND PREPRINTS — *March 2019 - Present*

- **Giant effective Zeeman splitting in a monolayer semiconductor realized by spin-selective strong light-matter coupling.**
  Nature Photonics, 16, 632–636 (2022)
- **Universal semiclassical equations based on the quantum metric for a two-band system.**
  Physical Review B, 104, 134312 (2021)
- **Experimental measurement of the divergent quantum metric of an exceptional point.**
  Physical Review Letters, 127, 107402 (2021)
- **High-frequency exciton-polariton clock generator.**
  Physical Review B, 101, 115418 (2020)

Other publications

Clermont-Ferrand, France

PEER-REVIEWED JOURNAL PAPERS AND PREPRINTS — *March 2019 - Present*

- **Domain-wall topology induced by spontaneous symmetry breaking in polariton graphene.**
  Physical Review Letters, 129, 066802 (2022)
- **Quantum metric and wave packets at exceptional points in non-Hermitian systems.**
  Physical Review B, Editor's suggestion, 103, 125302 (2021)
- **Experimental investigation of a Non-Abelian gauge field in 2D perovskite photonic platform.**
  Optica, 427088 (2021)
- **Quantum analogue of a Kerr black hole and the Penrose effect in a Bose-Einstein condensate.**
  Physical Review B, 99, 214511 (2019)

Experiences

PhD in physics

Aubière, France

INSTITUT PASCAL - UNIVERSITÉ CLERMONT AUVERGNE / CNRS — *Oct. 2019 - Sep. 2022*

- Thesis: Quantum Metric and Topology in the exploration of photonic Dirac systems.
- Thesis advisors: G. Malpuech, D. Solnyshkov. Quantum Optoelectronics and Nanophotonics.
- The goal of this thesis is to propose a realistic scheme of a topological polariton laser and circuits for integrated photonics using topologically protected states.
- I worked also on TMDs, organics, perovskites, quantum metric, non-Hermitian systems (Exceptional points) and Moiré superlattices.
- Tools: Comsol, Matlab, Mathematica, OriginLab, Lumerical, Affinity Designer, Blender, MathType and LateX.

Graduate Teaching Assistant

Clermont-Ferrand, France

UNIVERSITÉ CLERMONT AUVERGNE — *Sep. 2020 - Aug. 2022*

- Undergraduate lectures, tutorials and laboratory courses in physics.
- Tools: Discord, Zoom, Microsoft Office and LibreOffice.

Research internship

Aubière, France

INSTITUT PASCAL - UNIVERSITÉ CLERMONT AUVERGNE / CNRS — *Feb. 2019 - Jun. 2019*

- High-frequency exciton-polariton clock generator.
- Grant: I-SITE CAP 20-25 Fellowship.
- Theoretical implementation of a high-frequency generator (100GHz) based on cavity polariton for photonic integrated circuits.
- Tools: Matlab, Mathematica, LateX, MathType, Inkscape.

Research internship

Aubière, France

INSTITUT PASCAL - UNIVERSITÉ CLERMONT AUVERGNE / CNRS — *Apr. 2018 - June 2018*

- Quantum analogue of a Kerr black hole and the Penrose effect in a Bose-Einstein condensate.
- Implementation of an acoustic Kerr black hole with quantized angular momentum in a Bose-Einstein condensate. Analytical demonstration that the black hole exhibits a horizon and an ergosphere.
- Tools: Matlab, Mathematica, LateX, MathType, LibreOffice Draw.

Research internship

Aubière, France

Laboratoire de Physique des particules - Université Blaise Pascal / CNRS

Jul. 2016 - June 2016

- The limits of the Standard Model.
- As part of "Graine de Chercheur".

Education

PhD in Physics

Aubière, France

Institut Pascal - Clermont Auvergne University / CNRS

Oct. 2019 - Sep. 2022

- Thesis: Quantum Metric and Topology in the exploration of photonic Dirac systems.
- Thesis advisors: G. Malpuech, D. Solnyshkov. Quantum Optoelectronics and Nanophotonics.

Master's degree in Physics

Clermont-Ferrand, France

Clermont Auvergne University

Sept. 2017 - June 2019

- Major in Fundamental Physics.
- Minor in Nanophysics.
- Obtained with honor: rank #1.

Bachelor's degree in Physics

Clermont-Ferrand, France

Blaise Pascal University

Sept. 2015 - June 2017

- Major in Fundamental Physics.
- Minor in Applied Physics.

Classe Préparatoire aux Grandes Ecoles

Clermont-Ferrand, France

Blaise Pascal University

Sept. 2011 - June 2013

- Two-year intensive course in mathematics and physics to prepare for nationwide competitive examination.
- Major in Mathematics and Physics.
- Minor in Computer Science.

Skills

Research skills

- Theoretical modeling with Mathematica and Matlab.
- Data analysis with OriginLab and Matlab.
- Simulations of complex systems with Matlab, Comsol (FEM), Lumerical (FDTD) and Mathematica.
- Advance knowledge of vector graphics and 3D software: Affinity Designer, Blender.
- Collaboration with international teams in England, China, Italy, Japan, Germany and Russia.
- Native language in French, working knowledge of English.
- Article writing with LateX (Overleaf) and MathType.
- Knowledge of research funding and call for projects.

Programming Language & software

- Advanced level: Matlab, Mathematica, Comsol, OriginLab and LateX.
- Intermediate level: Lumerical, Python, Go and C.
- Beginner level: Labview and Arduino.

Subjects of work

- Topology : quantum metric, topological edge states, domain walls.
- Polaritonics : exciton-polaritons, strong coupling, Bose-Einstein condensates.
- Integrated photonics : 2D lasers, microcavities, photonic crystals.
- Non-Hermitian systems : Exceptional (Voigt) points.
- Materials physics : perovskite, TMDs, organics.
- Analog physics : rotating black holes, classical chromodynamics, Moiré superlattices.

Teaching and Mentoring

- Mentoring of 1 PhD student (I. Septembre) and 5 undergraduate students in a Master's degree in Physics.
- 6h of undergraduate lectures on Measurement and Uncertainty.
- 12h of undergraduate tutorials in Computing tools.
- 30h of undergraduate tutorials in Thermodynamics.
- 36h of undergraduate tutorials in Electrostatics.
- 44h of undergraduate laboratory courses : Mechanics, Electrostatics, Magnetostatics.
- More than 100h of personal courses: Mathematics and Physics at high-school and undergraduate level.

Community involvement

Dissemination articles

- Physics World contributor: I write articles for the condensed matter section of Physics World, an internationally leading physics magazine of the Institute of Physics (IOP), that reports on news and exciting developments in the field. The articles are listed below:
- Photonic fractals open a new area of topological physics. (Editor's choice)
- Ultrafast switch takes a big step towards the terahertz regime.
- Experimental investigation of a universal law for out-of-equilibrium systems.

Community outreach

- Presentation of a workshop about "Theoretical Physics" at *Fête de la Science*: a national general public event with lab visits and scientific hands-on demonstrations.
- Popularising physical concepts and writing guides for PhD Students on my personal website.
- Portfolio of my 2D and 3D scientific illustrations on my personal website.

Reviewing

- Reviewer of: Physical Review Letters (x2), Physica Scripta (x2).
- Most reviews can be found at: Orcid - Charly Leblanc.
- I obtained the "Institute of Physics (IOP) trusted reviewer" certification.

Talks & posters at conferences

Talks

Contributed Talks

- **Condensed Matter Days - Topology, waves and matter** (JMC2022) - "Universal semiclassical equations based on the quantum metric for a two-band system". Lyon, France. 08/2022
- **Physics of Light-Matter Coupling in Nanostructures** (PLMCN2022) - "Universal semiclassical equations based on the quantum metric". Varadero, Cuba. 04/2022
- **Optics of Excitons in Confined Systems** (OECS17) - "Quantum metric and wavepackets in exceptional points in non-Hermitian systems". Online. 08/2021
- **C'Nano Auvergne-Rhone-Alpes 2021** (AURA21) - "Quantum metric and wavepackets in exceptional points in non-Hermitian systems". Online. 06/2021
- **GDR ondes GT1** - "Quantum metric and wavepackets in exceptional points in non-Hermitian systems". Online. 05/2021

Invited Colloquia/Seminars

- **University of Warsaw** (Faculty of Physics) - "Quantum metric and wavepackets in Hermitian and non-Hermitian photonic systems". Online. 05/2022
- **Institute of Nanotechnology** (CNR-Nanotec) - "Quantum metric and wavepackets in Hermitian and non-Hermitian photonic systems". Lecce, Italy. 05/2022
- **Stockholm University** (Department of Physics) - "Quantum metric and wavepackets in Hermitian and non-Hermitian photonic systems". Stockholm, Sweden. 04/2022

Posters

- **Topological Matter School 2021** - "Experimental measurement of the divergent quantum metric of an exceptional point." Online. 09/2021
- **Wavecomplexity International Networking Event** (WINE) - "Experimental measurement of the divergent quantum metric of an exceptional point." Online. 07/2021
- **Cargese School of Quantum Information and Quantum Technology** - "Experimental measurement of the divergent quantum metric of an exceptional point." Cargèse, Corsica. 06/2021
- **Physics of Light-Matter Coupling in Nanostructures** (PLMCN2020) - "High-frequency exciton-polariton clock generator". Online. 05/2020

Fellowships & Awards

- "**I-Site CAP20-25**" Fellowship to initiate research on innovative technology.
  Subject: High-frequency exciton-polariton clock generator.
- "**Graine de Chercheur**" laureate.
  Subject: The limits of the Standard Model.

Relevant coursework

Summer Schools

Topological matter school 2021

- Topological quantum chemistry and symmetry indicators.
- Correlations and topology in the magic angle twisted bilayer graphene narrow bands.
- Topology Bands from homotopy theory.
- Interaction-driven insulators in flat-band moire superlattices.

IEEE quantum

- Quantum engineering: photonics in quantum computing and quantum network.

Cargese school of quantum information and quantum technology

- Photonic integrated circuits.
- Light Matter interaction with nanophotonics.
- Solid state light matter interface for quantum information.

Graduate courses

Between 2019 and 2022

- Advance Quantum Mechanics.
- Plasma Physics.
- How to finance research - Call for funding.
- Ethics of Science.
- Teaching at University.

Master's degree

Between 2017 and 2019

- Light-Matter interaction and Symmetries.
- Nanostructures and nanomaterials.
- Numerical simulations (COMSOL, matlab, LabView, FDTD).
- Statistics and machine learning.
- Solid-state physics.
- Epitaxy and Surfaces/Interfaces.
- Experimental techniques.